Theses and Dissertations

2016

Synthesis And Utility Of Bis-Urea Macrocycles As Nanoreactors And As Ligands For Metal Organic Materials

Sahan R. Salpage
University of South Carolina

Recommended Citation

SYNTHESIS AND UTILITY OF *BIS*-UREA MACROCYCLES AS NANOREACTORS AND
AS LIGANDS FOR METAL ORGANIC MATERIALS

by

Sahan R. Salpage

Bachelor of Science
Institute of Chemistry Ceylon, 2008

Submitted in Partial Fulfillment of the Requirements

For the Degree of Doctor of Philosophy in

Chemistry

College of Arts and Sciences

University of South Carolina

2016

Accepted by:

Linda S. Shimizu, Major Professor

John J. Lavigne, Chairman, Examining Committee

Daniel L. Reger, Committee Member

Christopher T. Williams, Committee Member

Lacy Ford, Senior Vice Provost and Dean of Graduate Studies

DEDICATION

This work dedicated to Randima, Father Ariyapala Salpage, Aunt Indrani Salpage, Mother Lalitha Salpage and my little sister Vimarsha Salpage, without those unwavering support this could not have been possible.

ACKNOWLEDGEMENTS

ABSTRACT

"Supramolecular chemistry" powered by non-covalent interactive forces forms the crux in the area of host-guest chemistry. Supramolecular assemblies often have different chemical and physical properties than that of its individual molecular entities and are used to develop novel functional materials. Our expertise involves making functional materials from macrocycles, which contain two urea groups and two rigid C shaped spacer groups. These individual macrocyclic components can self-assemble through hydrogen bonding and other non-covalent interactions to form porous supramolecular assemblies that can be used as confined reaction environments and as ligands to synthesize novel metal organic materials.

This dissertation focuses on studying the self-assembly, and the utility of three *bis*-urea macrocyclic systems, namely phenylethynylene, pyridine-phenylethylene, and bipyridine. My major research effort focuses on the scope and applications of the phenylethynylene *bis*-urea and its pyridine counterpart pyridine-phenylethylene macrocycles as confined environments for studying the absorption and diffusion of guests and investigating their reactivity in confinement. The second research project is based on bipyridine *bis*-urea macrocycle, which is a great candidate to study the architectures formed by interplay of metal ligand coordination and hydrogen bonds in the presence of suitable metallic guests. This dissertation consists of six chapters. The introductory chapter is devoted to discuss the structure and reactivity of organic solid-state host-guest

systems as reaction media to carryout photoreactions. The work described in chapters two and three has been focused on our efforts to use phenylethynylene *bis*-urea as a nanoreactor to modulate [2+2] photodimerization of series of benzopyrones. We went beyond studying dimerizations with the reactor built from pyridine-phenylethylene *bis*-urea where we were able to facilitate photoinduced polymerization reactions of isoprene which is detailed in chapter four. Chapter five describes the structure, electrochemistry and photophysical properties of an *exo* di-ruthenium complex synthesized using the bipyridine *bis*-urea macrocycle. It extends to a description of its application as a photosensitizer to carryout electronically mismatched Diels-Alder reaction of isoprene and *trans*-anethole using visible light. The chapter six reports the solid state structures and subsequent Hirshfeld surface analysis of 6-substituted chromones, which were used as guest molecules in chapter three.

TABLE OF CONTENTS

LIST OF TABLES

LIST OF FIGURES

xv

LIST OF SCHEMES

CHAPTER I

INTRODUCTION

1

1.1 Structure and reactivity of organic inclusion compounds: As reaction media for [2+2] photodimerization and polymerization reactions.

Inclusion compounds have been demonstrated as powerful and fruitful media to probe the solid-state host-guest chemistry. Early work by Sir Humphrey in 1811, reported the first inclusion compound known as chlorine clathrate, which results from chlorine gas trapped in water-ice sockets. The term inclusion compound was then introduced by W. Schlenk to describe the crystalline adduct where the host molecule leads to isolation of the guest molecule into well-defined cavities *via* the crystallization of host molecules in a matrix.[1] In 1945, H. M. Powell coined the synonym clathrate derived from the Latin word clathratus which means "to fit with bars".[2] In addition, inclusion compounds with more than one kind of discrete molecules in the crystal lattice have also been described using the term "cocrystal". Solid-state inclusion chemistry has proven useful for the separation of mixtures, in the storage of gases and toxic substances, in the stabilization of reactive compounds, in the control of release profile of a drugs under physiological conditions, and for modulating reaction pathways by using as a molecular vessels.[3] This chapter focuses on solid inclusion in which guest molecule are embedded in the host lattice structure.

The cavity free crystalline host is often referred to as the alpha phase. The empty host (beta phase or apohost) is the host crystallized in a different crystal form that contains cavities but is free of guest molecules. The cavities provide "inclusion space" that can span a range of sizes and shapes. The interior geometry of inclusion spaces include tunnels, isolated cages, inter-lamellar regions within layered hosts, interconnected cages, and networks of intersecting tunnels.[3,4] The apohost is considered to be a

2

metastable form marked by its low density, which can be easily converted back to its alpha phase. Guests can exist in the form of a solid, a liquid or even a gas. In contrast to the solution state host-guest chemistry, in the solid-state, the aggregation of single molecules builds up the host crystal. Here, the crystal itself is considered as the unit entity. Therefore, the cavity for binding guest or guests does not need to be an intrinsic property of the individual host molecules. When host molecules are crystalized with suitable guest molecules, the guest may be trapped within the host.

Chemistry of solution state host-guest complexes, can be monitored in solution by a range of techniques that are taught in the undergraduate level. Solid-state characterization techniques are more typically seen in upper level courses. These techniques range from the powerfully elucidating technique of single crystal X-ray, which gives atomic resolution. In the absence of single crystals a number of solid state material characterization material characterization methods must be applied to elucidate information about the structure of the host-guest complex and to probe the key interactions that occur to trap the guest within the host. Such characterization methods include Single Crystal X-Ray Diffraction (SCXRD), Powder X-Ray Diffraction (PXRD), solid state: NMR, IR, Raman spectroscopy, UV-vis, diffuse reflectance, X-ray Photoelectron Spectroscopy (XPS), porosity analysis (BET), optical microscopy, and thermochemical methods such as Thermogravimetric Analysis (TGA) and Differential Scanning Calorimetry (DSC).

The host framework imposes structural and geometrical constraints on confined guests within the inclusion compound, rendering the confined guests to display different chemical reactivity from its free state. The guests within the complex are comparatively

3

less mobile than in solution but may have sufficient mobility in order to undergo a reaction with the nearest neighboring molecule. These reactions proceed according to the "topochemical principle"[5,6] where a minimum amount of molecular motion is required. In other words, both regiochemistry and stereochemistry of the reaction product may be governed by the relative position and the orientation of two reactant molecules within the inclusion space. Therefore, the relative energies of the transition states within the solid host could be very different from the relative energies for the corresponding reactions in free state.[4] Hence, the reactions occur in the inclusion space may favor a particular reaction pathway. This affords more control over the reactivity and the reaction selectivity by limiting the side reactions and often leads to the formation of one major product.

Chapter 4 focuses on the polymerization of isoprene within confined channels of assembled *bis*-urea macrocycles. Thus, it is expedient for us to consider the example of polymerization of isoprene by conventional means.[7] Free radical polymerization methods yield polyisoprene that has multiple stereoisomers within its microstructure (Scheme 1.1).
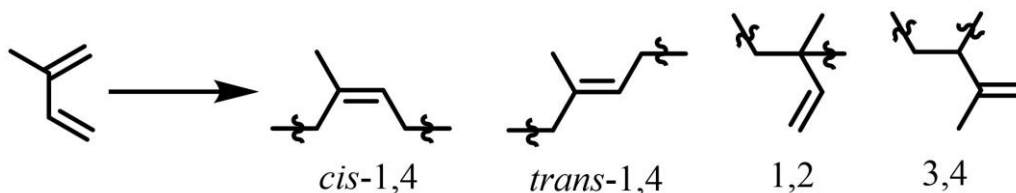
Scheme 1.1. Addition modes of isoprene during conventional polymerization leads to multiple isomers.

In comparison, when isoprene is constrained into small one dimensional channels of within tunnels of clathrates formed by tris(o-phenylenedioxy)cyclotriphosphazene,

inclusion polymerization can selectively yield the linear form *trans*-1,4-isomer.[8] Also advantageous, the use of host•isoprene inclusion complex as a medium for polymerization removes the need for radical initiators, solvents, and specialized handling procedures, which are necessary for conventional polymerization. This method employs mild initiation techniques that are sufficient to generate the initial radicals needed for polymerization. Polymers generated often are well defined and in some occasions have low polydispersities. It is indicative of a controlled radical polymerization inside the one dimensional channels of the host structure. Most importantly, after removing the resultant polymer molecules the host materials can be recovered and reused. The sustainability of the host crystals may make this approach more environmentally friendly.

This introductory chapter discusses the functionality of solid-state inclusion compounds in terms of their ability to act as molecular scale vessels to carry out photoreactions in high selectivity and conversion efficiency. We will limit our discussion to [2+2] photodimerizations and polymerizations as model reactions to understand how solid state host-guest complexes can alter the reactivity of guest and control the regio and stereo selectivity of the reaction. The structural features of corresponding inclusion complex/host molecules will also be discussed.

5
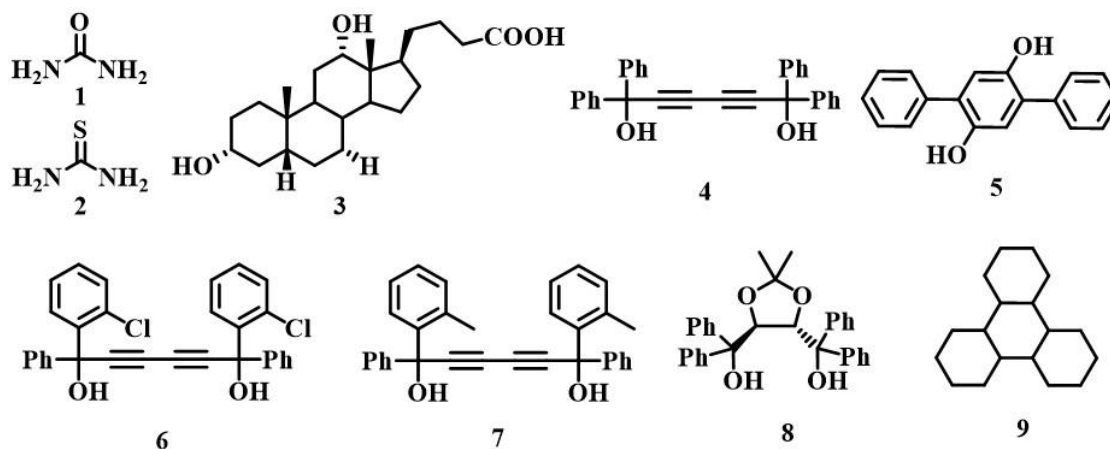
Figure 1.1. Organic hosts that are used in solid-state host-guest chemistry discussed in this chapter

1.2 Urea and thiourea based inclusion compounds

Urea and its sulfur analogue thiourea (1 and 2 in Figure 1.1) are known to form solid-state clathrates with variety of hydrocarbons. Both compounds form chiral helical hollow structures, which are stabilized by intermolecular hydrogen bonds between NH_2 protons and oxygen or sulphur atom of the adjacent molecule (Figure 1.2). Although they have similar bonding pattern, the structures formed by both urea and thiourea has its own subtle differences probably arising from the chemical nature of oxygen and sulphur. Urea forms helical tunnel like hexagonal shaped channels also known as β-urea with channel diameters around 5.5 Å whereas thiourea has a more cage like cavity with diameters about 7 Å (Figure 1.2).[3,4,9-12] Furthermore, Figure 1.3 illustrates a comparison of channel diameters of urea vs thiourea.
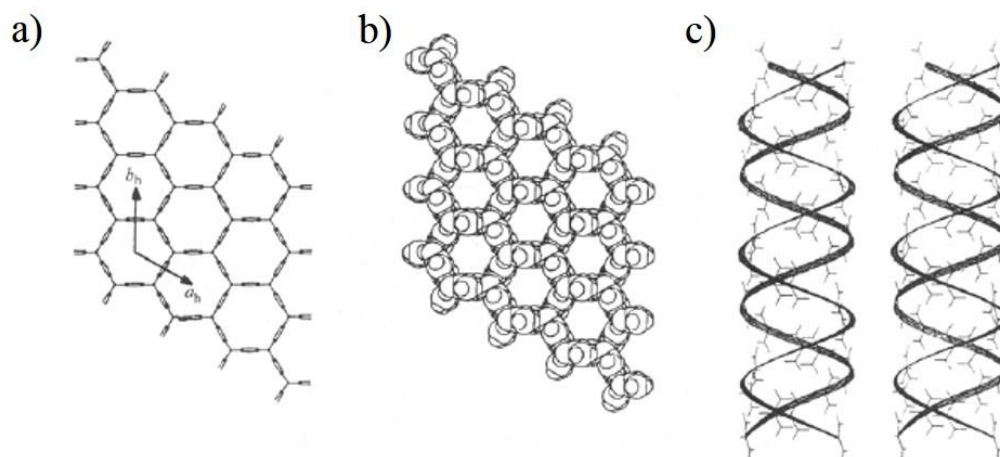
Figure 1.2. Structures of conventional urea host structure. (a) Hexagonal channels parallel to the channel axis (b) Similar view showing van der Waals radii of the host molecules (c) Helical ribbon structure.

Urea tunnel structures are known to have smooth internal surfaces in comparison to cavities formed by thiourea.[3] The differences in the structure and nature of the cavities dictate the binding of guests to form the corresponding clathrate. Urea tends to absorb linear hydrocarbons where as thiourea has the ability to absorb branched hydrocarbons. In host-guest chemistry studies, both urea and thiourea based clathrates have been widely explored.[13-17] Since urea does not have an auxiliary hydrogen bonding site for guest molecules, the clathrates often show nonstoichiometric guest binding and substantial guest disorder.
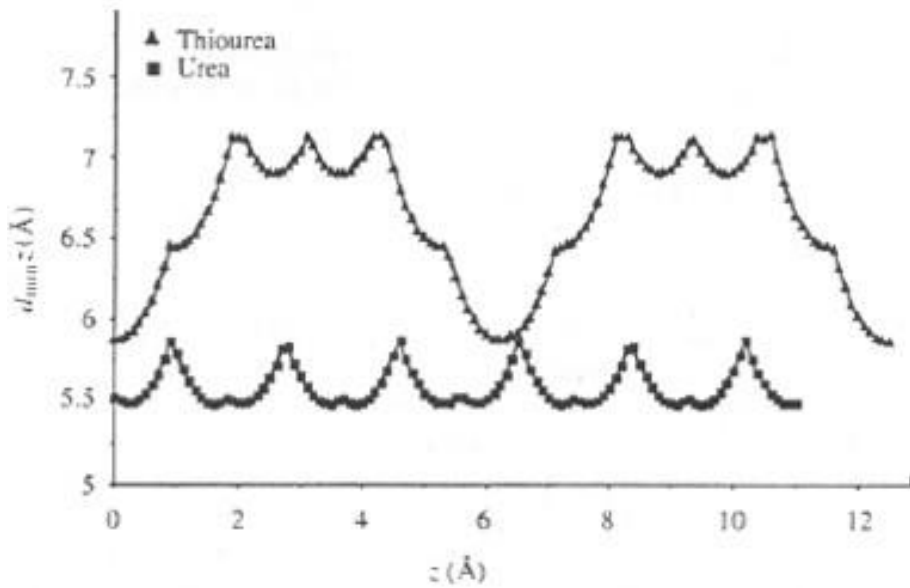
Figure 1.3. Compression of Minimum tunnel diameter (d_{min}) of urea and thiourea as a function of crystallographic axis z.

Urea and based clathrates have been used to conduct inclusion polymerization reactions that employ a range of monomers. The first polymerization was reported by Clasen and coworkers in 1956.[18] They observed that the inclusion compound formed between thiourea and 2,3-dimethylbutadiene undergoes spontaneous polymerization overtime without any initiation. Since then a number of groups have investigated the polymerization reactions in urea and thiourea. These findings are summarized in the table 1.1.

Table 1.1. Summary of the polymerization reactions done in urea and thiourea based inclusion compounds.

Entry	Host	Monomer	Polymer	Reference
1	Urea	1,3-butadiene	*trans*-1,4-polybutadiene	19
2	Urea	vinyl chloride	syndiotactic polyvinylchloride	19
3	Urea	acrylonitrile	polyacrylonitrile	20
4	Urea	acrylonitrile	isotactic polyacrylonitrile	20
5	Thiourea	2,3-dimethylbutadiene	*trans*-1,4-polydimethylbutadiene	22
6	Thiourea	2,3-dichlorobutadiene	*trans*-1,4-polydichlorobutadiene	22
7	Thiourea	1,3-cyclohexadiene	*trans*-1,4-polycyclohexadiene	22

White and co-workers polymerized 1,3-butadiene and vinyl chloride in urea inclusion complexes.[19] Gamma irradiation of urea•1,3-butadiene selectively produced the *trans*-1,4-polybutadiene (100%) (Table 1.1 entry 1) and urea•vinyl chloride yielded the highly stereo regular syndiotactic polyvinylchloride (Table 1.1 entry 2). Tonelli and coworkers have reported the polymerization of acrylonitrile in urea matrix under two different conditions.[20] At room temperature, photoirradiation of urea•acrylonitrile complex yielded polyacrylonitrile (Table 1.1 entry 3) while polymerization at low temperatures produced isotactic polyacrylonitrile with >80% m-diad content (Table 1.1 entry 4).[19,21] Thiourea inclusion complexes have also been investigated to drive polymerizations. Brown and White reported the polymerization of 2,3-dimethylbutadiene, 2,3-dichlorobutadiene, and 1,3-cyclohexadiene with thiourea to selectively produce *trans*-1,4-polymer (Figure 1.4) in each case (Table 1.1 entry 5, 6, and 7).[22] In 2008, Cataldo and coworkers analyzed the microstructure of polydimethylbutadiene polymers obtain from thiourea inclusion complex and bulk

9

polymerization.[23-25] The polymers from inclusion polymerizations showed high *trans* content (97%) when compared to polymers obtained from bulk polymerization, which yielded very low *trans* content and high percentages of 1,2-units.
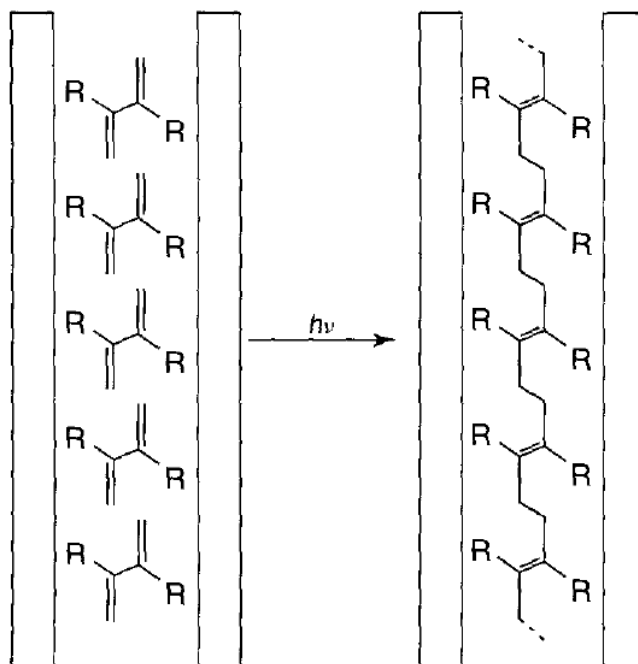
Figure 1.4. Packing of individual diene monomer molecules inside the channels formed by urea and thiourea. (R = H, 1,3-butadiene; R = CH₃, 2,3-dimethylbutadiene; R = Cl, 2,3-dichlorobutadiene)

1.3 Acid based inclusion compounds

Discovery of clathrates with fatty acid derivatives dates back to early 1910 when Wieland discovered a series of crystalline compounds known as "choleric acids". Clathrates formed by fatty acid Deoxycholic Acid (DCA) (3 in Figure 1.1) have been particularly well studied. In the solid state, DCA molecules assemble into bilayer helical type structure held together by hydrogen bonding between two hydroxyl groups.[26] These bilayers consist of alternating stacks of hydrophobic and lipophilic layers. The bent molecular shape of DCA provides one dimensional channels running through the

10

lipophilic layer with the channel diameters of 2.6 x 7.0 Å (Figure 1.5).[27,28] The first account of solid state polymerization within DCA was reported by Miyata and coworkers.[29] They investigated the DCA•2,3-dimethyl butadiene and DCA•2,3-dichlorobutadiene to form the corresponding well defined polymers with high trans content.[30] Since then a number of groups have investigated the polymerization in DCA. These findings are summarized in the table 1.2.
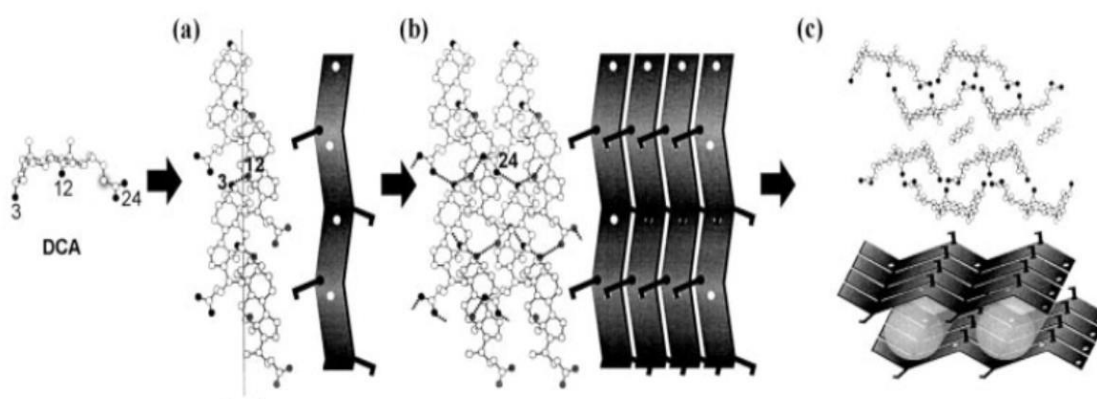
Figure 1.5. Structure of the DCA. (a) Individual DCA molecules held together by hydrogen bonding to form chains. (b) Stacking pattern of chains to form layers. (c) Bilayers consist of alternating stacks of hydrophobic and lipophilic layers with the channel diameters of 2.6 x 7.0 Å.

Table 1.2. Summary of the polymerization reactions done in DCA based inclusion compounds.

Entry	Monomer	Polymer	Reference
1	*cis*-1,3-pentadiene	*trans*-1,4-polypentadiene	31
2	*trans*-1,3-pentadiene	*trans*-1,4-polypentadiene	31
3	2,3-dimethylbutadiene	*trans*-1,4-polydimethylbutadiene	33
4	3-methyl-1,4-pentadiene	*trans*-1,4-poly(3-methyl-1,4-pentadiene)	35

11

Audisio and coworkers discovered that in the presence of DCA polymerization of *cis*-1,3-pentadiene and *trans*-1,3-pentadiene yield *trans*-1,4-polypentadiene.[31] This polymerization was induced by gamma irradiation and the *cis*-1,3-pentadiene shows the highest stereospecificity. Further investigations showed that the stereospecificity is controlled by the van der Waals interactions between the host tunnels and the monomer molecules.[32] Miyata and coworkers have reported the polymerization of 2,3-dimethylbutadiene in DCA and variety of DCA derivatives such as apocholic acid (ACA), cholic acid (CA), and chenodeoxycholic acid (CDCA).[33] The DCA and ACA having the similar channel diameter gave the highest selectivity for *trans*-1,4-polydimethylbutadiene (>99%). The CA and CDCA, which have larger channel diameters compared to DCA and ACA produced polymers with less *trans*-content (54%) with 38-42% *cis*-1,4- and 4-8% of 1,2- addition product. The polymerization of 3-methyl-1,4-pentadiene was reported by Cataldo and coworkers in 2010 using DCA. They were able to synthesize *trans*-1,4-poly(3-methyl-1,4-pentadiene) in very high selectivity.[34,35] Stereoregular polymers have a tendency to pack efficiently, rendering highly crystalline materials with improved mechanical properties. Particularly stereoregular polymers produced from diene monomers such as isoprene and 1,3-butadiene are heavily used in the synthetic elastomer industry.

1.4 Diol based clathrates

Solid state inclusion compounds based on alcohol containing host molecules have been investigated. Figure 1.1 illustrates the molecular structures of such host molecules (**4-8**), which have been applied to control [2+2] photodimerization reactions in solid state. Guest molecules investigated with these systems contain hydrogen bond donor or

12

acceptor moieties. Therefore, the inclusion complex is held together by hydrogen bonding interactions that organize and position the reactive alkenes in the solid-state. This organization defines relative orientation of the nearest neighboring guest molecule and controls the stereo and regiochemistry of the product.
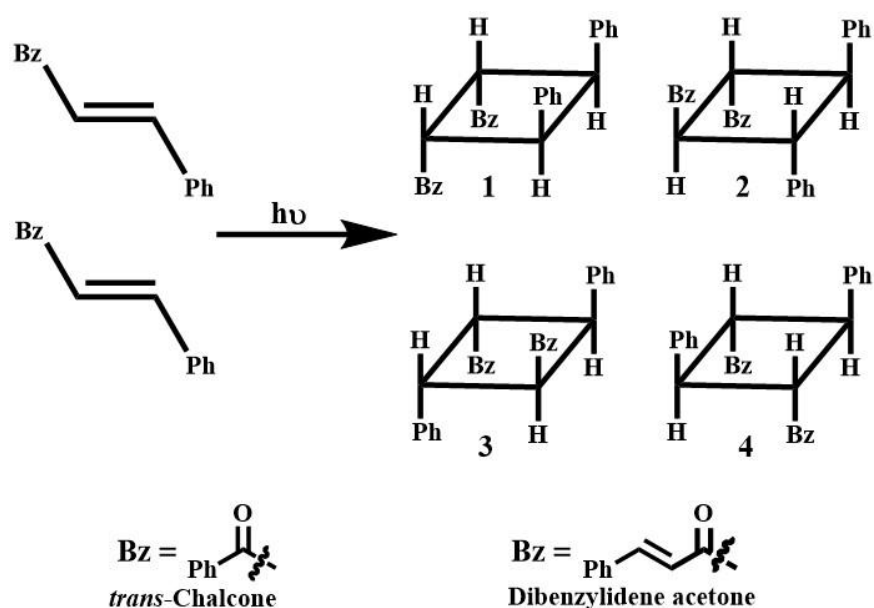
Scheme 1.2. Possible dimer products from the [2+2] photodimerization of chalcone and dibenzylidene.

Photodimerization of chalcone and dibenzylidene acetone have been extensively studied with the hosts **4** and **5**. In solid state they both can form four possible dimer products under UV- irradiation (Scheme 1.2).[36-39] UV-irradiation of neat *trans*-chalcone results in the formation of mixture of [2+2] dimer products in low product selectivity (Table 1.3 entry 1). As reported by Kaftory and coworkers, the irradiation of *trans*-Chalcone with host **4** produced product **3** exclusively (Table 1.3 entry 2).[40] Dibenzylidene acetone on the other hand forms complex with host **5**, which selectively yields the dimer product **3** exclusively under UV irradiation (Table 1.3 entry 3). The

control experiments without the host molecules shows no product formation (Table 1.3 entry 4).[40] Host molecules **6**, **7**, and **8** have been investigated in terms of facilitating the [2+2] dimerization of coumarin. In the presence of UV light coumarin has the possibility to form four different dimer products (Scheme 1.3).

Table 1.3. Summary of the [2+2] photodimerization of chalcone and dibenzylidene acetone using hots 4 and 5.

Entry	Media	Guest molecule	Product 1	Product 2	Product 3	Product 4	Reference
1	Neat solid	*trans-*Chalcone	x	x	x	x	36
2	4	*trans-*Chalcone			x		40
3	Neat solid	Dibenzylidene acetone					37
4	5	Dibenzylidene acetone			x		40
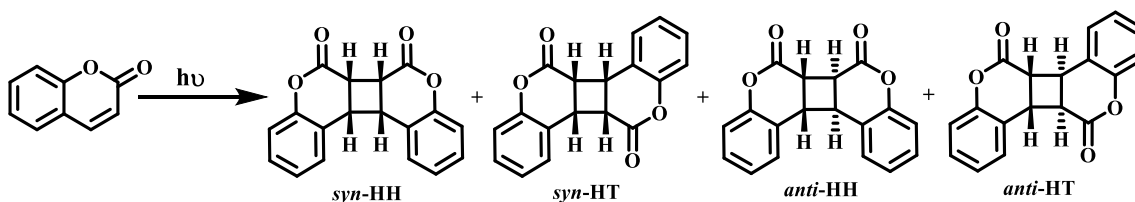
Scheme 1.3. Possible dimer products from the [2+2] photodimerization of coumarin.

Reaction of host **6**•coumarin selectively produces the *syn*-HH product exclusively (Table 1.4 entry 2) while the reaction of host **7**•coumarin yields a different dimer product namely *anti*-HT (Table 1.4 entry 3).[38] Toda and coworkers analyzed the effects of host **8** on the dimerization of coumarin.[39] Interestingly the outcome of the reaction was depended on the solvent used for the crystallization of the inclusion compound. The complex host **8**•coumarin crystallized from ethyl acetate/hexane gives the product *anti*-HH (Table 1.4 entry 4), while its gives *syn*-HH when crystalized from toluene/hexane

(Table 1.4 entry 5).[39] In addition Venkatesan and coworkers have used host **6** to drive the photodimerization of several coumarin derivatives including 7-methylcoumarin, 7-methoxycoumarin, 4,7-dimethylcoumarin, 4,6-dimethylcoumarin, and 4-chlorocoumarin. Photoirradiation of the inclusion compound, host **6**•7-methylcoumarin yielded the *syn*-HH in 90% and host **6**•7-methoxycoumarin proceed to form *syn*-HH in 66%. No reactions were observed with 4,7-dimethylcoumarin, 4,6-dimethylcoumarin, and 4-chlorocoumarin with the host **6**.[41]

Table 1.4. Summary of the [2+2] photodimerization of coumarin done using hots 6, 7, and 8.

Entry	Media	*syn*-HH	*syn*-HT	*anti*-HH	*anti*-HT	Reference
1	Neat solid	x	x	x	x	
2	6	x				38
3	7				x	38
4	8			x		39
5	8	x				39

1.5 Perhydrotriphenylene (PHTP)

The host molecule perhydrotriphenylene was synthesized by Sohrauth and Gorig in 1923.[42] The compound exists in two stereoisomeric forms. The isomer **9** appears to be the most stable form due to high symmetry (Figure 1.1). Isomer **9** can exist in optically active enantiomers in spite of its high symmetry. PHTP forms channels that are nearly cylindrical in shape with diameters in the range of 5.25-5.50 A.[27,43,44] Their aliphatic interior makes the channel surface more nonpolar compared to urea and thiourea

channels. Farina and co-workers have used the tunnel hosts to facilitate inclusion polymerization of a wide range of monomers.[45,46]
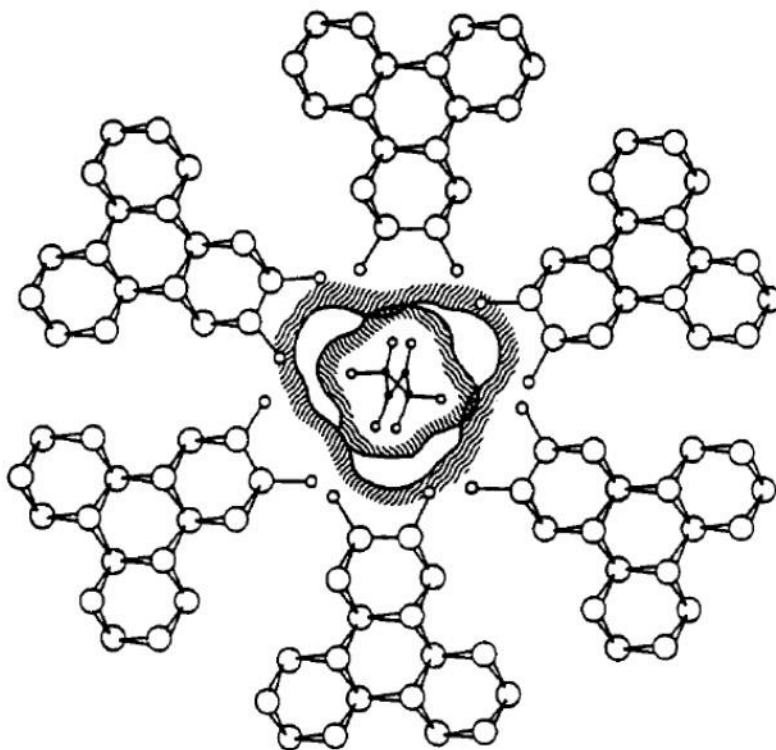
Figure 1.6. Schematic drawing of the *trans*-1,4-polybutadiene in the channels of its inclusion compound with PHTP.

The monomers such as 1,3-butadiene, 2,3-dimethylbutadiene, *trans*-pentadiene, and *cis*-pentadiene have been investigated as complexes with PHTP. All these monomers form the *trans*-1,4 polymer exclusively upon irradiation of their PHTP inclusion complexes. The radical molecule serving as the initiator needed for the polymerization was produced using gamma rays and the polymer was extracted using a suitable solvent under refluxing conditions. The same group reported the first example of asymmetric polymerization of *trans*-1,3-pentadiene to obtain isotactic *trans*-1,4-polypentadiene

(Figure 1.6). The investigations showed that the optical activity arises from the chiral environment of the (-)(R)-PHTP host structure.[43,47,48]

The research thrust of Shimizu group lies on solid-state host-guest chemistry, which is introduced in the above description. The solid host is formed by *bis*-urea macrocycles. The succeeding chapters focus on three *bis*-urea macrocyclic systems, namely phenylethynylene, pyridine-phenylethylene, and bipyridine with an emphasis on self-assembly and their utility to complex guests and modulate the reactivity of the included guests. The chapters 2 and 3 describe studies done on the scope and applications of the self-assembled phenylethynylene *bis*-urea macrocycle as a nanoreactor for selective [2+2] photodimerization reactions. The chapter 4 discusses the synthesis and utility of pyridine-phenylethylene macrocycles as confined environment for producing stereo-regular polymers. The chapter 5 provides a concise account of utility of bipyridine *bis*-urea macrocycle as a candidate to study the architectures formed by metal ligand coordination and hydrogen bonds in the self-assembled system.

1.6 References

(1) Schlenk, W. *Liebigs Ann. Chem.* **1949**, *564*, 204-240.

(2) Palin, D. E., Powell, H. M. *Nature* **1945**, 156, 334-335.

(3) Steed, J. W.; Atwood, J. L.: Solid-State Inclusion Compounds. In *Supramolecular Chemistry*; John Wiley & Sons, Ltd, 2009; pp 385-440.

(4) Hollingsworth, M. D.; Harris, K. D. M. Comprehensive Supramolecular Chemistry, eds. Toda, F.; MacNicol, D. D.; Bishop, R. Pergamon Press, 1996, vol. 6, pp. 177.

(5) Elizabé, L.; Kariuki, B. M.; Harris, K. D. M.; Tremayne, M.; Epple, M.; Thomas, J. M. Topochemical Rationalization of the Solid-State Polymerization Reaction of Sodium

Chloroacetate: Structure Determination from Powder Diffraction Data by the Monte Carlo Method. *The Journal of Physical Chemistry B* **1997**, *101*, 8827-8831.

(6) Kohlschütter, V.; Tüscher, J. L. Zur Kenntnis topochemischer Reaktionen. Über Bildung und Verhalten von Kupferhydroxyd. *Zeitschrift für anorganische und allgemeine Chemie* **1920**, *111*, 193-236.

(7) Jitchum, V.; Perrier, S. Living Radical Polymerization of Isoprene via the RAFT Process. *Macromolecules* **2007**, *40*, 1408-1412.

(8) Allcock, H. R.; Silverberg, E. N.; Dudley, G. K.; Pucher, S. R. Inclusion Polymerization within a Tris(2,3-naphthylenedioxy)cyclotriphosphazene Clathrate. *Macromolecules* **1994**, *27*, 7550-7555.

(9) Fetterly, L. C. Non-Stochiometric Compounds, ed. Mandelcorn, L. Academic Press, New York, 1964, pp. 491.

(10) Harris, K. D. M. Structural and dynamic properties of urea and thiourea inclusion compounds. *Journal of Molecular Structure* **1996**, *374*, 241-250.

(11) Harris, K. D. M. Meldola Lecture: understanding the properties of urea and thiourea inclusion compounds. *Chemical Society Reviews* **1997**, *26*, 279-289.

(12) Harris, K. D. M.; Palmer, B. A.; Edwards-Gau, G. R.: Reactions in Solid-State Inclusion Compounds. In *Supramolecular Chemistry*; John Wiley & Sons, Ltd, 2012.

(13) Chao, M.-H.; Kariuki, B. M.; Harris, K. D. M.; Collins, S. P.; Laundy, D. Design of a Solid Inclusion Compound with Optimal Properties as a Linear Dichroic Filter for X-ray Polarization Analysis. *Angewandte Chemie* **2003**, *115*, 3090-3093.

(14) Guillaume, F. Des cristaux organiques d'intercroissance incommensurables 1-D : les composés d'inclusion de l'urée. *J. Chim. Phys.* **1999**, *96*, 1295-1315.

18

(15) Harris, K. D. M. Investigating the Structure and Dynamics of a Family of Organic Solids: The Alkane/Urea Inclusion Compounds. *Journal of Solid State Chemistry* **1993**, *106*, 83-98.

(16) Harris, K. D. M. Fundamental and Applied Aspects of Urea and Thiourea Inclusion Compounds. *Supramolecular Chemistry* **2007**, *19*, 47-53.

(17) Hollingsworth, M. D. Crystal Engineering: From Structure to Function. *Science* **2002**, *295*, 2410-2413.

(18) Clasen, H. Elektrochem. **1956**, *60*, 982-987.

(19) White, D. M. Stereospecific Polymerization in Urea Canal Complexes1. *Journal of the American Chemical Society* **1960**, *82*, 5678-5685.

(20) Yang, H.; El-Shafei, A.; Schilling, F. C.; Tonelli, A. E. Why is Stereoregular Polyacrylonitrile Obtained by Polymerization in Urea Canals Isotactic? *Macromolecular Theory and Simulations* **2007**, *16*, 797-809.

(21) Minagawa, M.; Ute, K.; Kitayama, T.; Hatada, K. Determination of Stereoregularity of .gamma.-Irradiation Canal Polymerized Polyacrylonitrile by 1H 2D J-Resolved NMR Spectroscopy. *Macromolecules* **1994**, *27*, 3669-3671.

(22) Brown, J. F.; White, D. M. Stereospecific Polymerization in Thiourea Canal Complexes1. *Journal of the American Chemical Society* **1960**, *82*, 5671-5678.

(23) Chatani, Y.; Kuwata, S. Structural Investigation of Radiation-Induced Urea Canal Polymerization of 1,3-Butadiene. *Macromolecules* **1975**, *8*, 12-18.

(24) Chatani, Y.; Nakatani, S. Structural Evidence of Radiation-Induced Thiourea Canal Polymerization of 2,3-Disubstituted 1,3-Butadienes. *Macromolecules* **1972**, *5*, 597-604.

(25) Chatani, Y.; Nakatani, S.; Tadokoro, H. Structural Study of the Polymerization of 2,3-Dichlorobutadiene in the Thiourea Canal Complex. Structural Change during Canal Polymerization and the Crystal Structure of the Resultant Polymer. *Macromolecules* **1970**, *3*, 481-486.

(26) Kato, K.; Sugahara, M.; Tohnai, N.; Sada, K.; Miyata, M. Drastic Increase in the Flexibility of Open Host Frameworks of a Steroidal Host Compound upon Shortening Its Spacer. *European Journal of Organic Chemistry* **2004**, *2004*, 981-994.

(27) Giglio, E. I. c., eds. Atwood, J. L.; Davies, J. E. D. MacNicol, Academic Press, New York, 1984, 207.

(28) Miyata, M. S., K. Comprehensive Supramoleculer Chemistry, eds. Toda, F.; MacNicol, D. D.; Bishop, R. Pergamon Press, 1996, vol. 6, pp. 147.

(29) Miyata, M.; Takemoto, K. Radiation-induced polymerization of 2,3-disubstituted butadienes in deoxycholic acid inclusion compounds. *Journal of Polymer Science: Polymer Letters Edition* **1975**, *13*, 221-223.

(30) Miyata, M.; Takemoto, K. Radiation-induced polymerization of vinyl and diene monomers in deoxycholic acid inclusion compounds. *Journal of Polymer Science: Polymer Symposia* **1976**, *55*, 279-285.

(31) Audisio, G.; Silvani, A. Inclusion asymmetric polymerization of penta-1,3-dienes in deoxycholic acid. *Journal of the Chemical Society, Chemical Communications* **1976**, 481-482.

(32) Audisio, G.; Silvani, A.; Zetta, L. Inclusion asymmetric polymerization in deoxycholic acid by "through-space" asymmetric induction. *Macromolecules* **1984**, *17*, 29-32.

(33) Nakano, K.; Sada, K.; Miyata, M. Inclusion Polymerization in Polymorphic Crystals of Cholic Acid. *Polym J* **2001**, *33*, 172-176.

(34) Cataldo, F.; Angelini, G.; Iglesias-Groth, S.; Manchado, A. Solid state radiolysis of amino acids in an astrochemical perspective. *Radiation Physics and Chemistry* **2011**, *80*, 57-65.

(35) Cataldo, F.; Ursini, O.; Ragni, P.; Rosati, A. Radiation-induced polymerization of 2,3-dimethyl-1,3-butadiene clathrate in deoxycholic acid. *Journal of Radioanalytical and Nuclear Chemistry* **2009**, *280*, 99-106.

(36) Lewis, F. D.; Barancyk, S. V. Lewis acid catalysis of photochemical reactions. 8. Photodimerization and cross-cycloaddition of coumarin. *Journal of the American Chemical Society* **1989**, *111*, 8653-8661.

(37) Moorthy, J. N.; Venkatesan, K.; Weiss, R. G. Photodimerization of coumarins in solid cyclodextrin inclusion complexes. *The Journal of Organic Chemistry* **1992**, *57*, 3292-3297.

(38) Tanaka, K.; Mochizuki, E.; Yasui, N.; Kai, Y.; Miyahara, I.; Hirotsu, K.; Toda, F. Single-Crystal-to-Single-Crystal Enantioselective [2+2] Photodimerization of Coumarin, Thiocoumarin and Cyclohex-2-enone in the Inclusion Complexes with Chiral Host Compounds. *Tetrahedron* **2000**, *56*, 6853-6865.

(39) Tanaka, K.; Toda, F. Selective photodimerisations of coumarin in crystalline inclusion compounds. *Journal of the Chemical Society, Perkin Transactions 1* **1992**, 943-944.

(40) Kaftory, M. Reactions in the solid state : III. Structural aspects of photochemical reactions in crystalline inclusion compounds1. *Tetrahedron* **1987**, *43*, 1503-1511.

21

(41) Moorthy, J. N.; Venkatesan, K. Stereospecific photodimerization of coumarins in crystalline inclusion complexes. Molecular and crystal structure of 1:2 complex of (S,S)-(-)-1,6-bis(o-chlorophenyl)-1,6-diphenyl-hexa-2,4-diyne-1,6-diol and coumarin. *The Journal of Organic Chemistry* **1991**, *56*, 6957-6960.

(42) Sohrauth, W. G., K. Ber. **1923**, *56*, 2024.

(43) Farina, M.; Di Silvestro, G.; Sozzani, P. Optically active block copolymers by inclusion polymerization: Evidence for 'through-space' asymmetric induction. *Die Makromolekulare Chemie, Rapid Communications* **1981**, *2*, 51-54.

(44) Farina, M. in 'Inclusion Compounds' (Eds J. L. Atwood et al.), Vol. 2, Academic, New York, 1984, p. 69

(45) Farina, M.; Natta, G.; Allegua, G.; Löffelholz, M. Inclusion compounds of linear polymers and polymerization of monomers included in perhydrotriphenylene. *Journal of Polymer Science Part C: Polymer Symposia* **1967**, *16*, 2517-2524.

(46) Farina, M.; Pedretti, U.; Gramegna, M. T.; Audisio, G. Stereospecific and Asymmetric Inclusion Polymerization I. Polymerization of trans- and cis-1,3-Pentadiene Included in Racemic Perhydrotriphenylene. *Macromolecules* **1970**, *3*, 475-480.

(47) Colombo, A.; Allegra, G. Single Crystal to Single Crystal Transformation of Perhydrotriphenylene Inclusion Compounds during Canal Polymerization of Butadiene. *Macromolecules* **1971**, *4*, 579-584.

(48) Farina, M.; Audisio, G.; Natta, G. Asymmetric synthesis. Radiation polymerization of trans-1,3-pentadiene included in optically active perhydrotriphenylene. *Journal of the American Chemical Society* **1967**, *89*, 5071-5071.

CHAPTER II

APPLICATIONS OF A *BIS*-UREA PHENYLETHYNYLENE SELF-ASSEMBLED
NANOREACTOR FOR [2+2] PHOTODIMERIZATIONS*

2.1 Abstract

Confined environments can be used to alter the selectivity of a reaction by influencing the organization of the reactants, altering the mobility of trapped molecules, facilitating one reaction pathway or selectively stabilizing the products. This chapter utilizes a series of potentially photoreactive guests to interrogate the utility of the one-dimensional nanochannels of a porous host to absorb and to facilitate the reaction of encapsulated guests. The host is a columnar self-assembled phenylethynylene *bis*-urea macrocycle, which absorbs guests including coumarin, 6-methyl coumarin, 7-methyl coumarin, 7-methoxy coumarin, acenaphthylene, *cis*-stilbene, *trans*-stilbene and *trans*-β-methyl styrene to afford crystalline inclusion complexes. We examine the structure of the host:guest complexes using powder X-ray diffractions, which suggests that they are well-ordered highly crystalline materials. Investigations using solid state cross-polarized magic angle spinning $^{13}C\{^1H\}$CP-MAS NMR spectroscopy indicate that the guests are mobile relative to the host. Upon UV-irradiation, we observed selective photodimerization reactions for coumarin, 6-methyl coumarin, 7-methyl coumarin, and acenaphthylene, while the other substrates were unreactive even under prolonged UV-irradiation. Grand Canonical Monte Carlo simulations suggest that the reactive guests were close paired and preorganized in configurations that facilitate the photodimerization with high selectivity while the unreactive guests did not exhibit similar close pairing. A greater understanding of the factors that control diffusion and reaction in confinement could lead to the development of better catalysts.

24

2.2 Introduction

Confined environments can potentially be used to modulate the chemical reactivity of encapsulated guests with the goal of controlling their reactions and inducing selectivity.[1,2] A host that provides a confinement environment for reaction is popularly termed a 'nanoreactor'.[3] A few of the chemical processes that are facilitated within nanoreactors include unimolecular aza-cope rearrangements,[4,5] bimolecular Diels-Alder reactions,[6,7] oxidations,[8,9] and [2+2] photodimerization reactions.[10,11] They have also been used to stabilize reactive substances[12,13] and intermediates.[14-17] In many cases, the encapsulated guest molecules interact both with the walls of the host and with each other and can be constrained to adopt a particular orientation within these small spaces.[18] The interactions that orient these guests depend on their chemical nature and on the specific structure of the hosts and occur between the host and guests and between neighboring guests. The strength, directionality and reversibility of these interactions guide the structure of these complexes both before and after reaction. A greater understanding of the factors that control reaction in confinement could lead to the development of better catalysts.

Recently, we reported *bis*-urea phenylethynylene macrocycle **1** (Figure 2.1a), which assembles into columnar structures from several solvents.[19] These columns pack together to afford micron sized porous crystals with nanometer range channels. The crystallization solvent could be removed by heating, and the empty host displayed permanent porosity by gas adsorption and showed a surface area of ~ 350 m^2/g. From the X-ray structure of host 1•nitrobenzene (Figure 2.1c), one can see that the accessible columns are lined with ureas and aryl groups. This manuscript explores the absorption of a series of guests (Figure 2.1b), which have a propensity to undergo light driven reactions, into these

porous crystals. We examine the structure of these crystalline inclusion complexes by both solid-state and computational studies using Grand Canonical Monte Carlo (GCMC) simulations. The simulations were able to differentiate between the guests that undergo reactions within the columnar channels (coumarin, 6-methyl coumarin, 7-methyl coumarin and acenaphthylene) versus guests that were unreactive within the channels (7-methoxy coumarin, stilbenes and styrene). Guests that were reactive were bound in close proximity within the channels in relative geometries that were close to those required for photoreaction. In contrast, unreactive guests were not close paired but were randomly distributed within the tubes and displayed few contacts with neighboring guests.
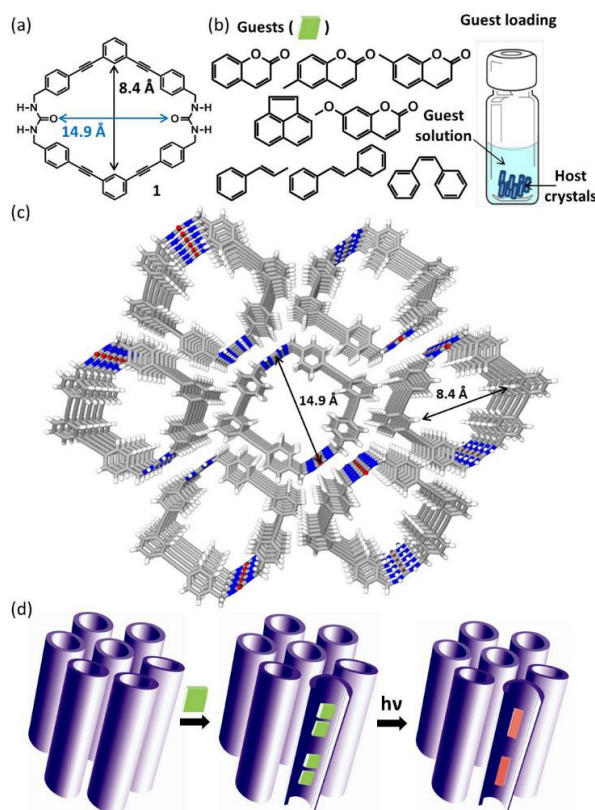
Figure 2.1. Columnar assembled host **1** forms porous crystals with accessible channels for binding guests. a). Structure of macrocycle **1**. b). Guests that load into the crystals from solution. c). View from the X-ray structure of **1**•nitrobenzene shows the packing of aligned one-dimensional channels (disorder solvent removed for clarity). d). Schematic of guest loading and subsequent reaction in the simple tubular channels.

26

The uptake of reactants into open cavities, pores, and channels or the formation of co-crystals results in complexes where the guests display restricted motion, altered mobility or preorganization that can lead to selective conversions or facilitate pathways and products that are not observed in solution.[20] It is the organization of reactants within this confined space or 'reaction cavity'[21-23] which are key to understanding the product distribution for a given transformation. Imagination and synthetic accessibility are a few of the limits when it comes to designing a confined space. The confined space may consist of a discrete cavity or pore in a small molecular host in solution such as cyclodextrins,[24] calixarenes,[25] or cucurbiturils.[26] It could be the larger interiors of small to medium sized assembled structures, such as cavitands[27] or Gibbs Octa acids,[28] as well as nanoscale structures such as coordination spheres,[1] proteins and polymers.[29] Reaction cavities are not limited to soluble hosts in solution, but can also be voids in solids or templated and preorganized asssemblies in co-crystals such as the innovative work from Toda,[30] and MacGillivray.[31]

In comparison, host **1** presents a high density of aligned, one-dimensional channels with ~ 9 Å diameter (Figure 2.1a), which are accessible to guests. Previously, we have loaded coumarin into these channels. Figure 2.2a illustrates a view of half of the channel from the X-ray structure to highlight the aryl, ethynylene, and urea groups that line the channels. Our hypothesis is the ureas are unable to participate in further hydrogen bonding interactions with the guests as the three centered urea hydrogen bonding motif is used to construct the columnar framework. Molecular modeling with Scienomics MAPS[32] of the host **1**•coumarin complex suggests that the encapsulated guests form aryl stacking and dipole interactions between the coumarin and the phenyls that line the

27

channel as well as dipole interactions between the coumarin oxygen and the urea groups (Figure 2.2b).
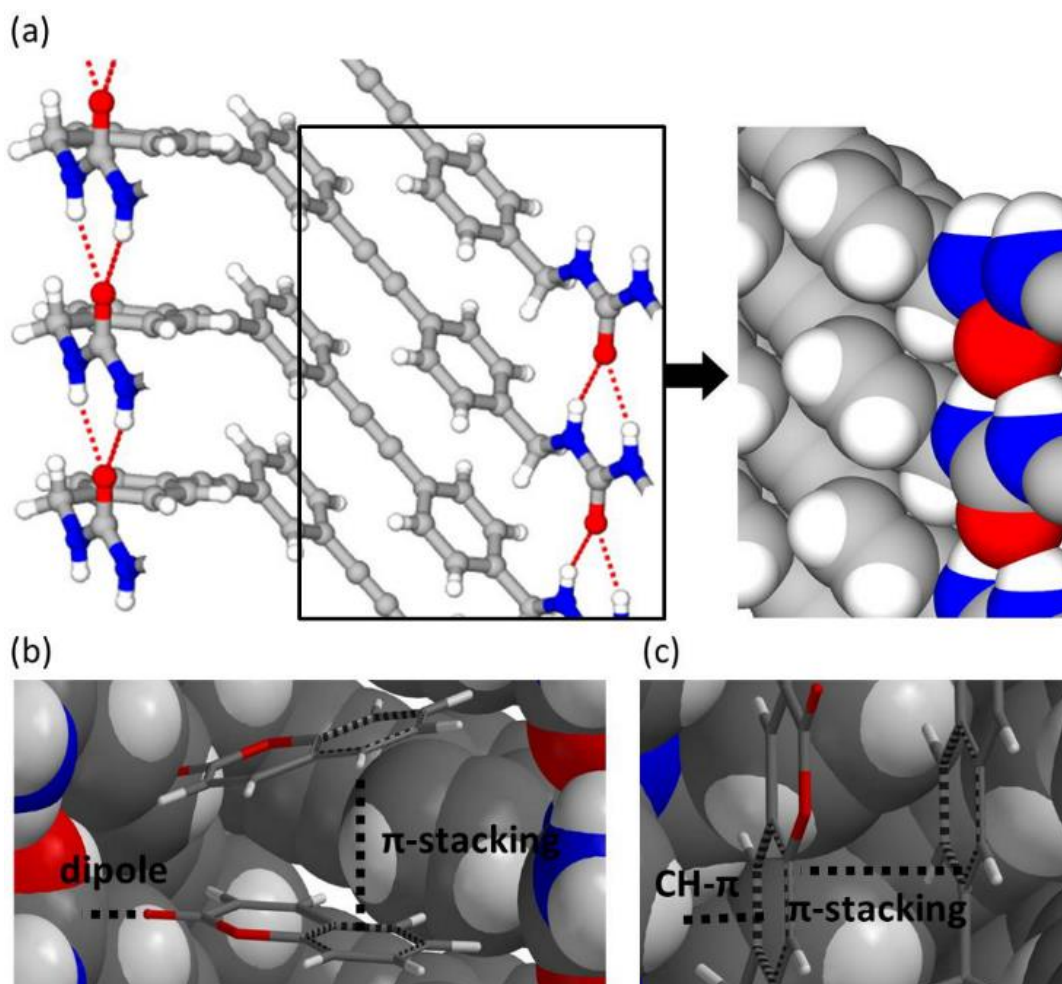
Figure 2.2. Views of host **1** and host **1** complexes: a) View of half of the channel illustrating the aryl, ethynyl and hydrogen bonded urea groups that line the interior. b) Molecular models of the host **1**•coumarin inclusion complexes generated with Scienomic's MAPS illustrate the aryl stacking interactions that can occur between the neighboring coumarins as well as the dipole-dipole interactions between coumarin and the column walls. c) Aryl stacking and CH-л aid in binding of 6-methyl coumarin in the channel's interior.

We chose to test seven different of guests: those that undergo [2+2] photocycloadditions (6-methyl and 7-methyl coumarin, 7-methoxy coumarin and acenaphthylene) and three that undergo photo-isomerization reactions (*cis-* and *trans-*

stilbene and *trans*-β-methyl styrene) (Table 3.1). In addition, *trans*-β-methyl styrene can also act as a probe to test if the host itself can be a photosensitizer, as it will only undergo isomerization in the presence of a medium energy sensitizer, such as chrysene or 1-acetylnaphthalene.[33] We evaluated the absorption of these guests by host **1** and characterized the structure of their inclusion complexes by solid-state methods. We then investigated if these encapsulated guests would undergo photochemical reactions upon UV-irradiation. Some of the guests underwent photochemical reactions within the solid complex in moderate to good yields with high selectivity while others were unreactive within these solid inclusion complexes. Molecular modeling studies allowed us to probe the fit of the guests inside the channel of the host. These studies were directed at understanding the following questions: Are certain orientations of the guest molecules stabilized by the confinement? Are they appropriately oriented to undergo photodimerization or photoisomerization reaction?

2.3 Results and discussion

In our previous work, we reported the X-ray structure of host **1** from DMSO/nitrobenzene (host **1**•nitrobenzene) and demonstrated that the structure of the host is similar when crystallized from DMSO (host **1**•DMSO). The encapsulated solvent can be removed from the channels of each of these complexes to give the same empty host as indicated by their identical PXRD pattern. The channels can subsequently be reloaded with either solvent or alternatively with a different guest. Figure 2.1c highlights the channel of this host, which is approximately ~ 9 Å in diameter. The channel is lined with polar urea groups that are occupied in the hydrogen bonding scheme that runs along the channel's frame (Figure 2.2a). Aryl and ethynyl groups also line the channel. This

29

manuscript investigates the loading of a series of guests within the channel of these pores through both experimental and computational methods. These guests were chosen for their similarity in polarity to coumarin. Furthermore, these guests were selected based on their size, shape and potential photoreactivity.

Host **1** was synthesized and characterized by ^{1}H and ^{13}C NMR in DMSO-d_6 solution. After crystallization from DMSO, the host 1•DMSO solvate was further characterized by PXRD, solid-state NMR and TGA. The channel of the newly recrystallized material was filled with DMSO solvent, which needed to be removed before a new guest could be loaded. Figure 2.3 illustrates the process of desorption and adsorption of guests schematically. Host **1**•DMSO crystals show a two step curve (TGA 1) with corresponding weight loss of 9.1% between 30 and 80 °C and an 4.9% weight loss between 80 and 130 °C. Previous work with the 'empty' host demonstrated a type 1 gas adsorption isotherm with CO_2 (g) with an apparent surface area of 349 m^2/g at 273 K. For absorption of new guests, the 'empty' host obtained by TGA was cooled under helium gas then transferred directly to a solution containing guest (method A) or to an aliquot of liquid guest (method B). The channels are guest accessible and the crystals could be reused many times. For example, after removal of the DMSO (Figure 2.3, TGA 1) the crystals were treated with DMSO (method B). TGA 2 (Figure 2.3) shows a nearly identical two step desorption curve with a weight loss of 8.3% between 30 and 80 °C and a 5.2% weight loss between 80 and 130 °C. These empty crystals were reloaded again with DMSO and also showed a similar two step desorption curve (Figure 2.3, TGA 3). Different batches and sizes of crystals showed reversible absorption with similar

host:DMSO ratios. These experiments demonstrate that guests can be reversibly bound by host 1 and suggest that they are bound in discrete binding sites.
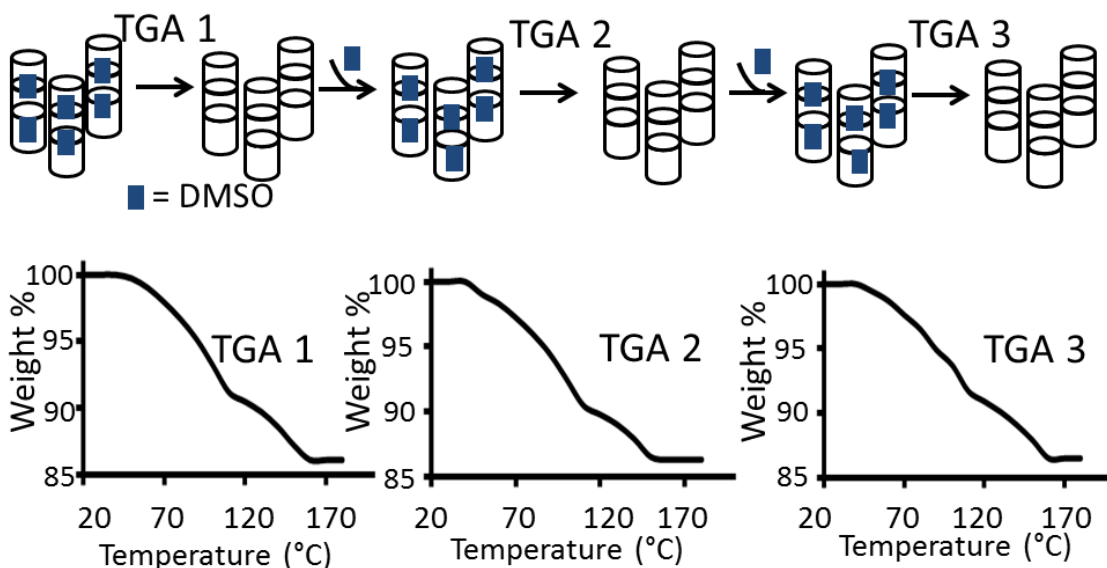
Figure 2.3. Reversible absorption/desorption of guests: (Top) Schematic depicting of desorption and reabsorption of DMSO. (Bottom) Three successive cycles showing TGA desorption for host 1•DMSO.

As the channel of host **1** is much larger than our earlier hosts, we focused on guests that were similar or larger in volume than the parent coumarin. A series of coumarins (coumarin, 6-methyl coumarin, 7-methyl coumarin, and 7-methoxy coumarin) were loaded into the porous host by method A. Loading experiments were carried out a minimum of 3 times on different batches and sizes of host **1** crystals and gave similar binding ratios. The reproducibility of the loading ratio suggests that guests are absorbed into discrete binding sites and are not merely surface absorbed. For example, host **1** (30 mg) was soaked in a solution of 6-methyl coumarin (0.1 mM CH_3CN) for 0-12 h. The depletion of 6-methyl coumarin from solution was monitored by absorbance spectroscopy at 273 nm (Figure 3.4a). The absorbance reached a plateau by 3 h, suggesting that we reached an equilibrium and no further 6-methyl coumarin was absorbed. Assuming that

31

the loss of guest from solution corresponds to the binding of guest in host **1**, we compared the final absorbance to Lambert-Beer plots of known concentrations of the guest in CH_3CN. This gave calculated host:guest ratio of 1:1, and an average ratio of 1:1.0 from 5 loading experiments. Coumarin (0.1 mM CH_3CN), 7-methyl coumarin (0.1 mM CH_3CN) and 7-methoxy coumarin (0.5 mM in hexanes at 35 °C) were loaded similarly. Figure 2.4a shows the decrease in absorbance versus time as each of these coumarin guests are separately equilibrated with fresh crystalline host **1**. The guests were monitored at slightly different wavelengths depending on their absorption maxima. Comparison of the absorbance at the plateau to a Lambert-Beer plot gave a calculated host:guest ratio for a specific guest. Table 2.1 compares the guest structure, dimensions, volume and polarity with the observed host:guest binding ratio. For coumarin derivatives, the smallest coumarin, displayed the highest binding ratio (1:1.4) while the largest derivative 7-methoxy coumarin showed the smallest binding ratio (1:0.5). The 6- and 7-methyl derivatives had similar sizes and gave similar ratios (~ 1:1). Overall, the coumarin and methyl coumarins have similar polarities and their size appears to be the primary determinant in their uptake into the channels of the host. In the case of 7-methoxy coumarin, polarity appears to play a greater role in determining guest absorption. This coumarin derivative is more polar than 7-methyl coumarin (7.1 versus 5.8 D) but only slightly larger and was bound in the lowest ratio 1:0.5.

32
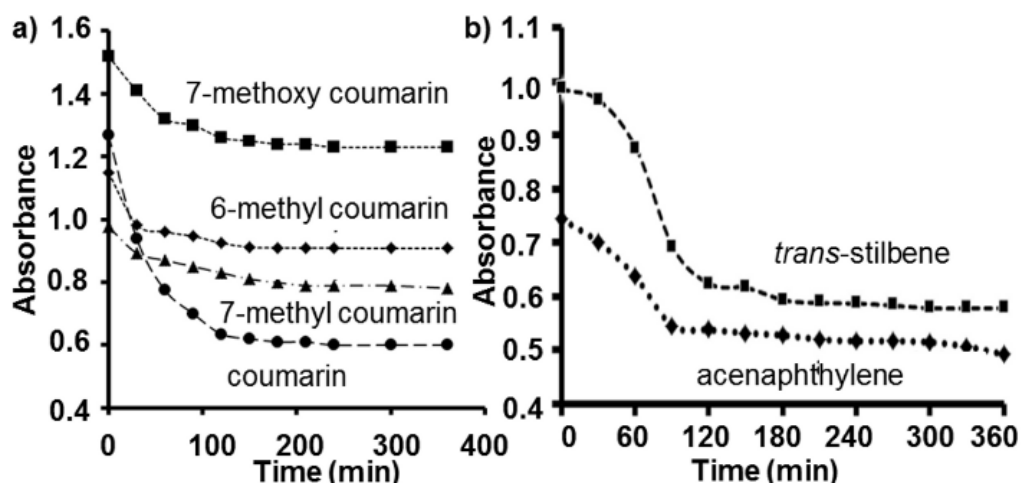
Figure 2.4. Absorption of guests by host **1**: a) Coumarin derivatives: The depletion of 6-methyl coumarin from solution (0.1 mM in CH_3CN) monitored at 273 nm. The depletion of 7-methyl coumarin from solution (0.1 mM in CH_3CN) monitored at 276 nm. The depletion of 7-methoxy coumarin (0.5 mM in hexanes) was monitored at 315 nm. The depletion of coumarin was reported previously.[19] b) The depletion of acenaphthylene from solution (0.1 mM in CH_3CN) monitored at 322 nm. The depletion of *trans*-stilbene (0.1 mM in CH_3CN) monitored at 295 nm.

As Figures 2.1 and 2.2 illustrate, the interior channel of the host is lined with aromatic groups and polar urea groups that provide a suitable space to absorb the polar coumarin derivatives of complementary size. We next investigated aromatic hydrocarbons, which are less polar than the coumarins but still offer aryl surfaces that may form aryl stacking interactions with the sides of the channels. Acenaphthylene, *cis-* and *trans*-stilbene and *trans*-β-methyl styrene are not polar based on their dielectric constants, but contain a quadrupole and are polarizable according the л* scale.[34] Method A was used to load acenaphthylene (0.1 mM in CH_3CN) and *trans*-stilbene (0.1 mM CH_3CN). Figure 3.4b shows the depletion of *trans*-stilbene from solution as (0.1 mM in CH_3CN) was monitored at 295 nm. Acenapthylene was loaded similarly and its concentration in solution was monitored at 322 nm. Again, the loading ratios were calculated by comparison of the absorbance at the plateau to a Lambert-Beer plot and are summarized

33
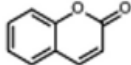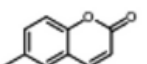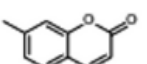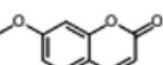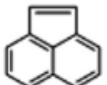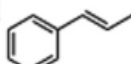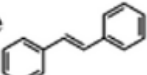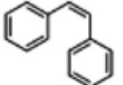
in Table 3.1. Two guests *cis*-stilbene and *trans*-β-methyl styrene did not load appreciably by method A and were instead loaded by soaking host 1 in the respective liquid guests (Method B). The complexes were air dried (6 h) and the loading was estimated by TGA (Figure 3.5). The small *trans*-β-methyl styrene is similar in size to coumarin and gave a similar loading ratio. In contrast, although acenaphthylene's volume (~ 170 $Å^3$) is close to the volume of 7-methoxy coumarin, it loaded in a higher ratio (1:0.8), perhaps due its lower polarity (2.9 D versus 7.1 D).[35,36] The loading of the stilbenes strongly favors the smaller isomer, and *cis*-stilbene was bound in a 1:1.7 host:guest ratio while the larger *trans*-stilbene was bound in a 1:0.5 host:guest ratio.
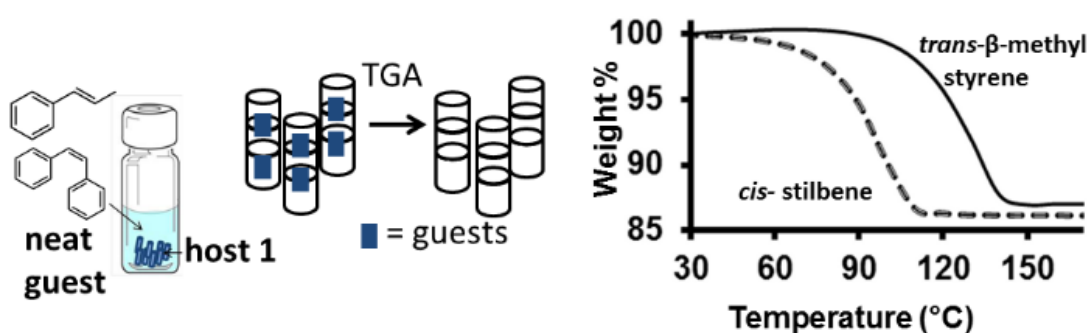
Figure 2.5. Formation of host•guest complexes: Schematic of loading guests via method B (left) Comparison of TGA desorption curves for host **1**•*cis*-stilbene and host **1**•*trans*-β-methyl styrene (right).

34

Table 2.1. Guests absorbed by host **1**.

Guest		Dimensions (Å)	Volume (Å³)	Polarity (D)	Host: Guest ratio
coumarin		7.6 x 3.2	147.1	5.2[a]	1:1.4[A]
6-methyl coumarin		8.2 x 3.2	167.2	5.8[a]	1:1.0[A]
7-methyl coumarin		7.7 x 3.2	167.3	5.6[a]	1:1.1[A]
7-methoxy coumarin		8.3 x 3.3	171.2	7.1[a]	1:0.5[A]
ace-naphthylene		7.1 x 3.9	170.3	2.9[b]	1:0.8[A]
trans-β-methyl styrene		8.2 x 3.3	149.9	2.3[b]	1:1.3[B]
trans-stilbene		11.6 x 3.4	215.5	2.5[b]	1:0.45[A]
cis-stilbene		8.1 x 6.2	198.7	2.9[b]	1:1.7[B]

[a]reference 35, [b]reference 36, The Host:Guest ratio superscript denotes the loading method (A or B).

In summary, host **1** appears to form stable host guest complexes with host:guest ratios ranging from 1:0.5 to nearly 1:2 for a variety of polar and/or aromatic guests with volumes that range in size from 140-220 Å³. Two guests, 7-methoxy coumarin and *trans*-stilbene, were bound in relatively low host:guest ratios (~ 1:0.5). Next, we sought to

evaluate the structures of these solid inclusion complexes using solid-state methods. The complexes were pressed to powder form and examined by powder X-ray diffraction. Figure 3.6a compares the PXRD patterns of host 1•DMSO (pattern I) and the empty host 1 (pattern II) with host **1**•guests complexes. Upon removal of DMSO by TGA, the empty host 1 showed generation of new peaks at low 2θ range. Relative intensity of the peaks at 5.3 and 6.8 degrees were increased due to solvent removal and new peaks were observed at 9.8 and 11.7 degrees. But in the higher 2θ values (above 20 degrees) a number of peaks disappeared. These observations indicate that the host maintains crystallinity upon solvent removal. All the complexes (Figure 3.6a, patterns III-V) exhibit different and sharp PXRD patterns in the 2θ range of 5 to 20 degree, suggesting that each of these host 1•guests complexes forms a different crystalline structure. The PXRD pattern of host 1•coumarin (Figure 3.6a, patterns III) shows disappearance of sharp peaks at 5.3 and 6.8 degrees of the empty host 1 pattern and generation of number of peaks above 12 to 25 degrees. This result suggests after incorporating solid guest coumarin, a structural change occurred, but the complex managed to stay crystalline as a whole. Similar observations were also made for other two coumarin derivatives, 6-and 7-methyl coumarin complexes with host **1** (Figure 3.6a, patterns IV-V respectively). All these observations suggest incorporation of coumarin or its derivatives kept the overall material crystalline but induced changes in their overall structure due to presence of these guests. The host **1**•7-methoxy coumarin complex has the lowest host:guest ratio (~1:0.5). Its PXRD pattern showed the presence of the crystalline host and possibly the guest (Figure 3.6a, pattern VI). The presence of similar peaks to those of the host in the range of 5 to 20 degrees supports the existence of the crystalline host. The presence of the guest, on the other

36

hand, appeared to be arranged in less ordered manner as indicated by the presence of new broad peak in 20 to 27 degrees.
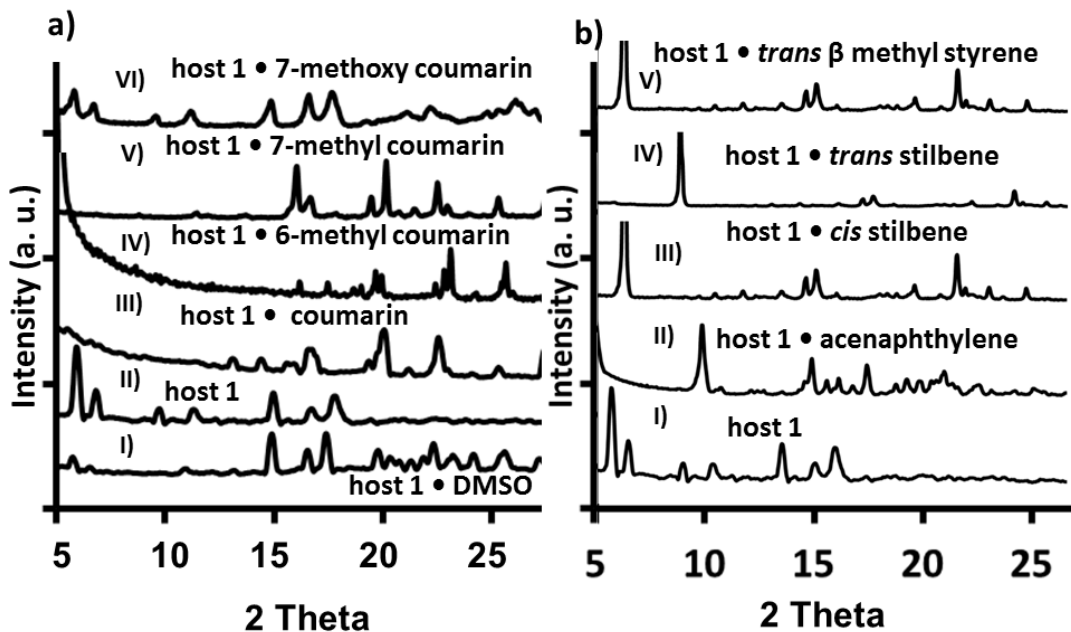
Figure 2.6. Comparison of the observed PXRD of host **1** and its host•guest complexes: a) Host **1** and its complexes with coumarin: I) Host **1**•DMSO, II) Host **1**, III) Host **1**•coumarin, IV) Host **1**•6-methyl coumarin, V) Host **1**•7-methyl coumarin, and IV) host **1**•7-methoxy coumarin. b) Host **1** and its complexes. I) host **1**, II) host •acenaphthylene, III) host **1**•*cis*-stilbene, IV) host **1**•*trans*-stilbene, V) host **1**•*trans*-β-methyl styrene.

In the other set of host **1**•guest complexes, similar general trends were also observed (Figure 2.6b, patterns II-V). The PXRD pattern of host 1•acenaphthylene complex (Figure 2.6b, pattern II) showed a sharp peak at 10.2 degrees and a number of sharp peaks above 15 degrees indicating formation of a new crystalline structure. The host **1** complexes with *cis* and *trans* stilbenes (Figure 2.6b, pattern III and IV, respectively) showed distinct PXRD patterns. The host **1**•*cis*-stilbene complex displayed sharp peaks at 6.1, 16.6, 17.2, and 17.9 degrees 2θ. The host **1**• *trans*-β-methyl styrene also gives a sharp PXRD pattern that is distinct from the empty host (Figure 2.6b pattern V). Overall each complex displayed markedly different 2θ peaks as compared to those of

37

the host **1**, which suggests that during the host **1**•guest complexes formation the structure of the host **1** undergoes structural changes upon guest absorption while maintaining crystallinity. The one exception was the 7-methoxy coumarin, which loaded in the lowest ratio. Its PXRD pattern suggested that the inclusion occurs without changing the overall crystalline structure of the empty host.

The PXRD patterns probe the order and crystallinity of the complexes. To further investigate the mobility of the guests within these crystals, we turned to solid-state NMR experiments. Solid-state cross-polarized magic angle spinning $^{13}C\{^{1}H\}$CP-MAS (125.79 MHz) NMR spectra of solid complexes can probe the mobility of the guests. If the guests are well ordered and incorporated within the pore of the tubes, the cross-polarization behavior of the guests would be very similar to that of the host and new distinguished peaks from the guest should be observed in the spectra. Spectra I in Figure 2.7 shows the previously reported CP-MAS NMR of the solid empty crystals of the host 1 that shows the urea carbonyl peak at 159 ppm, aromatic region 125-140 ppm, ethynylene (sp C) peaks at 85-90 ppm and -CH- (sp^3 C) peaks at 40 ppm.[19] In comparison, the host **1**•coumarin complex (spectra II, Figure 2.7) displays a shift of these signature peaks of the host and/or appearance of additional peaks in the spectra. The carbons of coumarin overlap with the host in the aromatic and carbonyl regions. However, comparison of the two spectra shows the appearance of new peaks at 160-165 ppm and change in pattern at the aromatic carbonyl.

The new complexes: host **1**•6-methyl coumarin (spectra III) host **1**•7-methyl coumarin (spectra IV), and host **1**•7-methoxy coumarin (spectra V) show very similar shifting of the host resonances with little contributions from the guests, suggesting that

38

the guests do not effectively cross-polarize probably due to their greater mobility than the host. Relatively small resonances were observed for the methyl groups in the complexes of host **1** with 6-methyl and 7-methyl coumarin between 31-34 ppm, Similar shifts in the host were also observed in the complex with acenaphthylene (spectra VI), suggesting that all these guests have similar effects on the host structure.
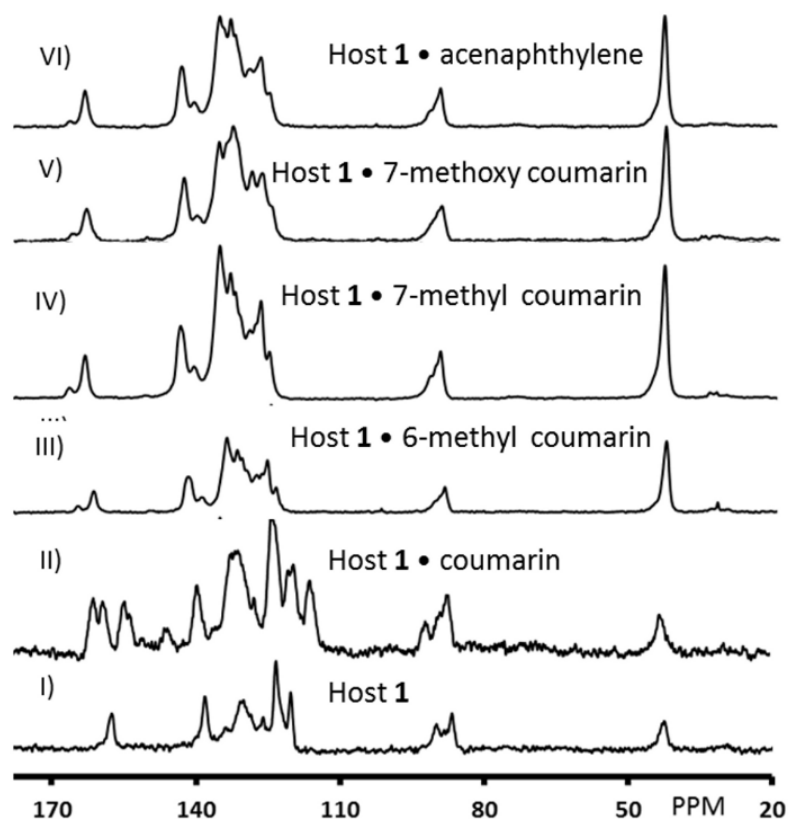
Figure 2.7. Comparison of solid-state ^{13}C{^{1}H}CP-MAS NMR spectra for I) host **1**, II) host **1**•coumarin. with the new complexes III) host **1**•6-methyl coumarin, IV) host **1**•7-methylcoumarin, V) host **1**•7-methoxy coumarin and VI) host **1**•acenaphthylene.

Solid-state characterization by PXRD and NMR indicate that the host•guest complexes are well ordered crystalline materials. Next, we wanted to investigate the effect of the encapsulation on the photoreactivity of these compounds. It is especially

39

advantageous that the photophysical and photochemical properties of coumarin derivatives, stilbenes and *trans*-β-methyl styrene are well studied and that their respective photoproducts are readily characterized by NMR. Here, we use these potentially photoreactive guests as probes to investigate the ability of the one-dimensional channel to facilitate photochemical transformations and to influence the product distribution and selectivity.

To test the photoreactivity, a sample of each host•guest complex (30 mg) was placed in a Norell S-5-500-7 NMR tube (with 100% transmittance up to 400 nm) and UV-irradiated at room temperature under argon atmosphere using a Hanovia 450 W medium pressure mercury arc lamp. Samples (5 mg) were removed from the NMR tube after 12, 24, 96 h for analysis, and the reactions were done in triplicate. The photoproducts were isolated from the host by extraction with CDCl$_3$ and analyzed by ^{1}H NMR spectroscopy. Samples were also directly dissolved in DMSO-*d$_6$* to confirm that the guests could be fully removed from the crystals. The photodimers are well studied and can be readily differentiated by their characteristic cyclobutane resonances in their ^{1}H NMR spectra. For acenaphthylene, coumarin, and the methylcoumarins, the conversion was estimated by comparison of the starting material to the cyclobutyl CH's. Specifically, we monitored the disappearance of the peaks that correspond to the H's attached to the reacting double bond and compared them to the newly formed cyclobutyl -CH peaks. As a control, the pure solid guests were also UV-irradiated under identical condition.

Table 2.2 summarizes the data from the photoreactions.   First, let us compare coumarin and its derivatives.   The table shows that most but not all encapsulated guest undergo reaction in the solid:host inclusion complexes. Coumarin and its derivatives

40

undergo photolysis reactions that can potentially afford four products, although three products are mainly observed: the *syn*-HH, *syn*-HT, and *anti*-HH (Scheme 2.1).[37,38] We observed that host 1 facilitated the [2+2] photocycloaddition of coumarin in high selectivity for its corresponding *anti*-HH photodimer (97%, entry 3). Longer reaction times afforded an increase in conversion (entry 4-5), which is unusual as under photolysis the cycloaddition is reversible and shows limited conversion (<5%, entry 1).[39] Thus, we tested the host 1 complexes of other coumarin derivatives to see if they show similar reactivity and selectivity as host 1•coumarin.

Coumarin $R_1 = R_2 = $ -H
6-methyl coumarin $R_1 = $ -CH$_3$, $R_2 = $ -H
7-methyl coumarin $R_1 = $ -H, $R_2 = $ -CH$_3$
7-methoxy coumarin $R_1 = $ -H, $R_2 = $ -OCH$_3$
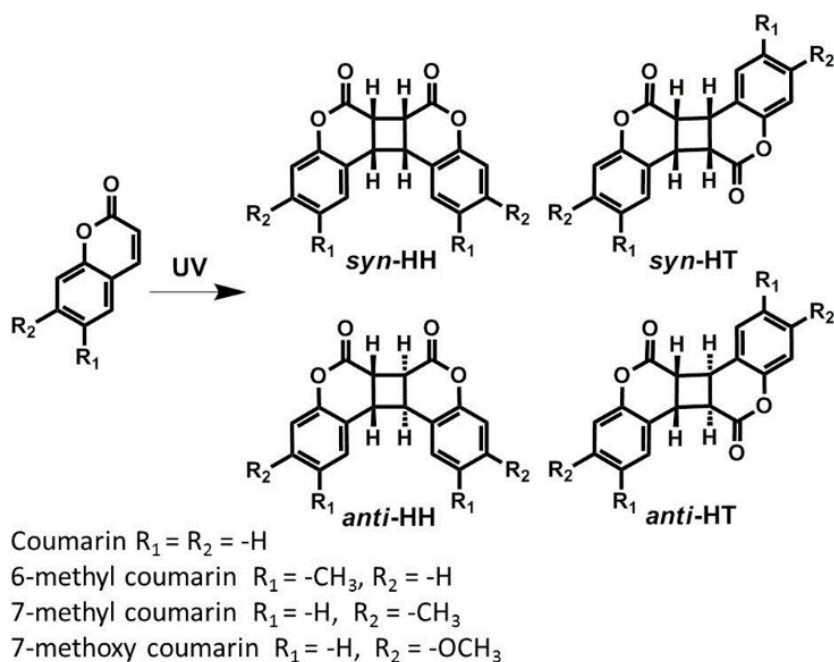
Scheme 2.1 Photolysis of Coumarin derivatives.

41

Table 2.2. Summary of photolysis reactions.

Guest	Entry	Host	Time h	Conv. %	syn-HH	syn-HT	anti-HH	anti-HT
Coumarin	1	-----	96	<5	30	20	30	10
	2	Pd nanocage[a]	10	8	90	mixture of others		
	3	1[b]	12	19	1	0	97	1
	4	1[b]	24	26	1	0	97	1
	5	1[b]	96	55	1	0	97	1
6-methyl coumarin	6	-----	96	<5	30	20	30	10
	7	CB [8][c]	1	76	69	31	0	0
	8	1	12	11	14	0	84	2
	9	1	24	21	13	0	84	3
	10	1	96	46	14	0	84	2
7-methyl coumarin	11	------	96	<5	30	20	30	10
	12	CB [8][c]	12	12	>99%			
	13	1	12	14	2	0	97	1
	14	1	24	22	2	0	97	1
	15	1	96	51	2	0	97	1
7-methoxy coumarin	16	-----	96	12	0	>99%	----	-----
	17	Pd nanocage[d]	10	55	>90%	----	-----	-----
	18	1	96	0	----	-----	-----	-----
						syn	anti	
Acenaph-thylene	19	----	96	<5		25	75	
	20	Octa acid[e]	2	24		>99		
	21	1	12	16		98	2	
	22	1	24	27		98	2	
	23	1	96	51		98	2	

[a]reference 49, [b]reference 19, [c]reference 43, [d]reference 49, [e]reference 54.

Upon UV-irradiation of the host **1**•6-methyl coumarin complex, we observed formation of the *anti*-HH dimer (84%) along with some of *syn*-HH dimer (14%) after 12 h in ~ 11% conversion (Table 2.2, entry 8). Samples of the UV-irradiated host **1**•6-methyl coumarin complex were directly dissolved in DMSO-d_6 or the guests were extracted into CDCl$_3$ and displayed new peaks that correspond to *syn*-HH dimer in the 4.0-4.1 ppm range and peaks for *anti*-HH dimer in the 3.8-3.9 ppm range. Similar to coumarin, increasing the UV-irradiation time (24 h, entry 9 and 96 h, entry 10) gave an increase in conversion of 6-methyl coumarin to 21% at 24 h with 84% *anti*-HH dimer and to 46% by

96 h with similar selectivity for the *anti*-HH dimer. In comparison, UV-irradiation of solid 6-methyl coumarin showed a mixture of the four possible dimers (Table 2.2, entry 6) at low conversion (< 5%) due to the reversibility of this photoreaction. In solution, others observed selective photoreaction of 6-methyl coumarin in the presence of cucurbit[8]urils,[40-42] cyclodextrins,[43] micelles,[44,45] and complexes with optically active hosts,[46] with the *anti*-dimers postulated as originating from the triplet state.[47] A Pd nanocage[48] facilitated 15% conversion to the *syn*-HH dimer with >85% selectivity.

Similarly, UV-irradiation of host **1**•7-methyl coumarin complex also facilitated a more selective photodimerization, yielding the *anti*-HH dimer in 14% conversion in 97% selectivity after 12 h of UV-irradiation (Table 2.2, entry 13). Again, increased reaction time afforded an increased conversion (22% at 24 h and 51% at 96 h; entries 14 and 15) with similar high selectivity for the *anti*-HH product. The minor product (<2%) was the *syn*-HH dimer. Such high yield and selectivity was not observed upon the similar UV-irradiation of solid 7-methyl coumarin, which gave low conversion (<5%) after 96 h to afford four photodimers (Table 2.2, entry 11). Solid-state inclusion complexes of 7-methyl coumarin in cyclodextrin favor the *syn*-HH dimer in 99% selectivity (entry 12).[44] In solution, the conversion and selectivity depends on the polarity of the solvent, with the *anti*-HH observed in methanol.[49] Exclusive formation of the *syn*-HH dimer was observed in water with complexation by cucurbit[8]uril.

We found that the host **1**•7-methoxy coumarin complex was stable to prolonged UV-irradiation (96 h). This is in contrast to what occurs in the solid 7-methoxy coumarin (entry 16), which shows low conversion (12% at 96 h) to the *syn*-HT photodimer. In

solution (chloroform, methanol or water), 7-methoxy coumarin favors *syn* products (*syn*-HH and/or *syn*-HT) with >99% selectivity.[48,49]

Next, we investigated the reactivity of other complexes including acenaphthylene, *cis*- and *trans*-stilbene and *trans*-β-methyl styrene in the presence of host **1** using a similar protocol. UV-irradiation of host **1**•acenaphthylene crystals facilitated high selectivity for the *syn*-photodimer of acenaphthylene (Table 3.2 entry 21) in 16% conversion after 12 h. When we increase the irradiation time, we observed increased conversion (27% at 24 h and 51% at 96 h (entries 22 and 23) with similar high selectivity for the *syn* product. Acenaphthylene is known to undergo photoreactions in both solution and in the solid state. In the solid state, we observed a 1:3 ratio of *syn* and *anti* (<5% conv., entry 19). In solution, the excited singlet state of acenaphthylene undergoes [2+2] photodimerization to yield the *syn*-dimer.[50,51] In contrast, the triplet sensitized route yields both *syn* and *anti* products.[49] Ramamurthy's group investigated the use of Gibb's "octa acid" capsule in water to facilitate the photoreaction of acenaphthylene to favor the *syn*-dimer in >99% selectivity (24 % conversion, entry 20).[52] The origin of their selectivity appeared to be due to the fit of the product as the capsule could only accommodate the smaller *syn*-dimer with its dimensions of 7.2 x 6.6 Å versus the comparatively larger *anti*-dimer (6.8 x 11.8 Å).[54]

The host **1** complexes of *cis*-stilbene, *trans*-stilbene and *trans*-β-methyl styrene were all found to be stable to prolonged UV-irradiation and were recovered after 96 h of UV-irradiation time. This is similar to our controls in which no conversion was observed even after 96 h of UV-irradiation time. Crystallographic studies suggest that the photodimerization of stilbene is suppressed in the crystalline solid-state likely due to the

44

large distance and non-parallel orientation of the olefinic double bonds of stilbenes in the crystal lattice.[53] Others have preorganized stilbenes in molecular hosts,[54-58] surfactant assemblies,[59] clays,[60] or employed co-crystals to organize stilbene derivatives to facilitate selective reactions. Finally, *trans*-β-methyl styrene typically requires the presence of low to medium energy triplet sensitizers to undergo a photoisomerization. We have observed this photoisomerization using the benzophenone containing *bis*-urea host, which contains a triplet sensitizer.[61] The lack of reactivity in host 1 suggests that either this host cannot act as a sensitizer or that the guest is too constrained within the channels to undergo reaction.

Clearly, the guests within the columns displayed either reactivity or selectivity differences or both versus the controlled solids. For coumarin and its methyl derivatives, the selectivity for the *anti*-HH photodimers were very different than observed in other confined environments and these products are more typically observed in the presence of a sensitizer. For acenaphthylene, the host facilitated the reaction in similar selectivity to what is observed for Gibbs Octa-acid, a selectivity whose origin is likely guided by a favorable fit of the *syn*-product within the confined space.[54] Our hypothesis is that the origin of both the different reactivity and the selectivity of these reactions within their host **1** complexes is due to the confinement of the guests within the confined one-dimensional channel of host **1**. To test this hypothesis, we turned to molecular simulations.

The earlier simulations of the host **1**•coumarin complexes were done using Spartan[62] by importing the atomic coordinates from the host **1**•nitrobenzene crystal structure and deleting the guests. In those calculations, a truncated column of 4 macrocycles was

45

'frozen' and guests were added sequentially and minimized until additional guests were ejected during the minimization process. Monte Carlo searching of the conformer distributions at the ground state with molecular mechanics (MMFF) afforded 450 conformers. From analysis of the ten lowest energy conformers, we concluded that 1) the guests were paired in close proximity within the distance (< 4.2 Å) required for the [2+2] photocycloaddition, 2) the guests have room to move relative to their neighbors and to the channel framework, and 3) the guests do not appear to be preorganized to favor only one photodimer selectively. Disadvantages of this calculation include intensive computational time, truncated model (only 4 macrocycles were used), and observations of some distortion of the urea hydrogen bond motif. Our experimental data suggests that the structure of the columns do not change significantly structure during guest absorption, subsequent guest reaction and product removal. Therefore, we sought to reexamine our system using additional GCMC simulations.

We investigated methods to apply Monte Carlo for Complex Chemical Systems (MCCCS) Towhee plug-in built into Scienomics' Materials Processes and Simulations (MAPS) platform. The direct modeling of a single column, analogous to the prior procedure, did not produce columns with paired guests. Instead, a new procedure was required. The simulation cell (Figure 3.8a) was generated by importing the atomic coordinates from the single crystal X-ray structure of host 1•nitrobenzene and omitting the coordinates of the guest atoms. The GCMC simulation on the crystalline host **1**•coumarin complex was conducted for 1×10^6 steps. We analyzed significant configurations of these simulations to probe the movement/mobility and orientation of the guest molecules within the simulation cell.

Figure 2.8b, shows the coumarins load into the columns and pair together, similar to the earlier Spartan predictions. The two coumarins interact through aryl stacking interactions (Figure 2.2b) and the reacting alkenes are in close proximity (4 Å), although not optimally aligned. Both simulations show the coumarins closely paired; however, the alignment in the MAPS simulation suggests that they are preorganized to favor formation of an *anti*-HH dimer product (Figure 2.8c). Interestingly, the simulation also predicted that some coumarin guests load in between the neighboring columns (Fig. 2.8b), much like alcohol guests in our pyridyl systems;[63] however, these coumarins are not paired and are spaced at distances and geometries that are unfavorable for reactions. This exterior loading may arise from the way the simulation cell has been constructed (Fig. 2.8a), although we have no experimental data to suggest that guests are loaded in such exterior binding sites.
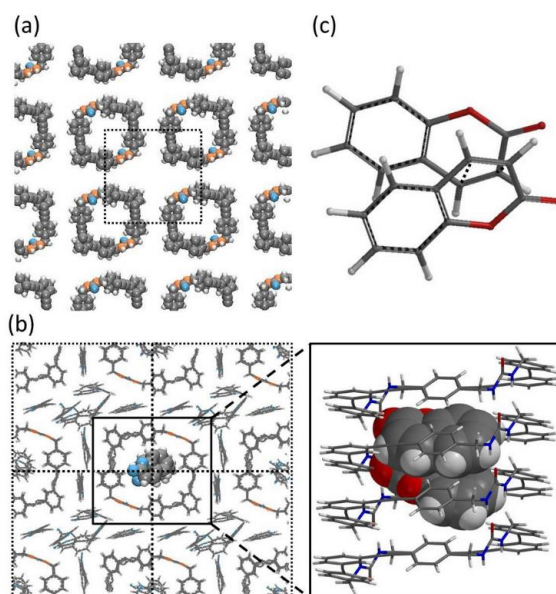
Figure 2.8. GCMC simulations for the host **1**•coumarin complex. a) The periodic simulation cell used for GCMC simulations. b) Simulations indicate coumarin guests are paired in the channel (shown in space filling models). Simulations also suggest that guests may fit in between columns, although no close contacts were predicted between the reactive alkenes. c) Orientation of two coumarin molecules paired in the channel.

We next applied this same method to analyze other guests. Watching the simulation frames from the loading of 6-methyl coumarin, we observed two molecules of 6-methyl coumarin enter the simulation cell, move towards the center and pair together even before reaching to the step number 1×10^5. The two guests rapidly orient themselves in the *anti* orientation to each other where their carbonyl head groups are pointing to the same direction (Figure 2.9a). This pairing is stabilized by CH-л (Figure 2.2c) and aryl stacking interactions between the guests and the channel walls. The paired coumarins also interact by aryl stacking interactions (3.4 Å) and remain close together throughout the remaining simulation. In the minimized structure, the paired 6-methyl coumarins are offset from each other by 1.4 Å, and the olefinic double bonds are located approximately 4.0 Å apart. Although the reactive double bonds are organized at a favorable distance, they are not in the optimal parallel alignment. Others have observed the [2+2] photodimerization from non-parallel orientations in the solid-state.[64,65] Given the orientation in Figure 2.9a, there is a high probability that the photodimerization will afford the *anti*-HH dimer, which is in agreement with the experimental results.

After the reactants are paired in the center column, we focused on what the other molecules do in the extended system, keeping in mind that the rest of the simulation cell shows the edges of the columns or partial columns. The next two molecules enter into the host macrocycle from opposite ends of the simulation cell and have no pair within the simulation cell. Throughout the simulation the stand-alone 6-methyl coumarin molecules are on the edges of our simulated cell, where they have the ability to rotate and adopt a number of configurations, a pattern that emerges in subsequent calculations. This indicates not all the guest molecules that are absorbed by the host are present in an

48

orientation to form dimers, and the yield of dimer forming reaction is expected to be lower. This could account for the observed conversion limit of ~ 50% even after 96 h of photoirradiation; however, other facts such as inefficient light penetration or non-uniform UV-irradiation could also play a role. Taken together, the simulation suggests that there is room within the host macrocycle for the 6-methyl coumarin molecules to rotate and change between configurations until two neighboring 6-methyl coumarins are paired, which fixes them in a configuration that favors *anti*-HH dimer formation.

A similar approach was used to investigate the 7-methyl coumarin guests, which is similar in dimension to its isomer 6-methyl coumarin (table 2.1). Here, again we observe a fast pairing of two guests in the central channel, which occurs within the first 1×10^5 steps. After minimization (Figure 2.9b), the pairs are located 3.2 Å away from each other and offset from each other in the by 3.0 Å with their olefinic double bond is located 3.8 Å apart, although they are not exactly aligned and suprafacial for the subsequent photoreaction. While some movement is required for a dimerization to occur, the two closely paired molecules are preorganized to primarily product the *anti*-HH photodimer, which is experimentally observed with 97% selectivity.
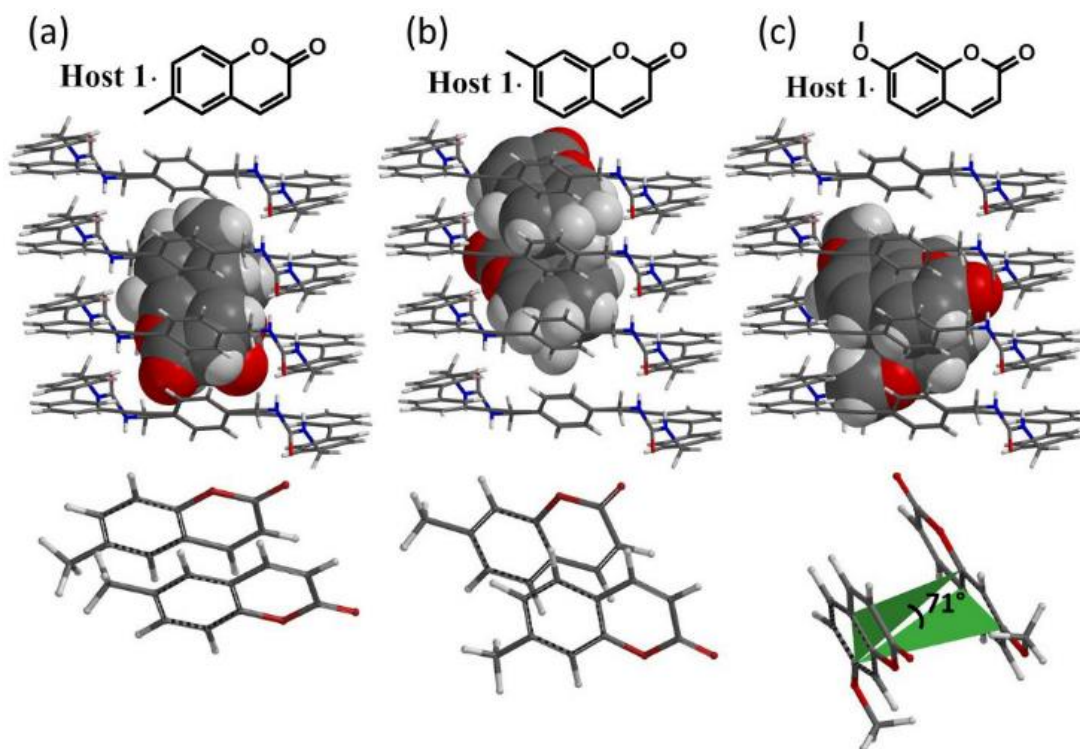
Figure 2.9. GCMC simulation results for coumarin derivatives. (Partial guest molecules omitted for clarity). a) Orientation of 6-methyl coumarin molecules inside the channel of host **1**. b) Orientation of 7-methyl coumarin molecules inside the channel. c) Orientation of 7-methoxy coumarin molecules inside the channel.

The same procedure was used to analyze the unreactive host **1**•7-methoxy coumarin complex. This coumarin derivative was the largest and most polar tested (table 2.1) and was absorbed in the lowest ratio (1:0.5). The simulations suggest that each 7-methoxy coumarin guest interacts with the walls of the channel through edge to face aryl stacking interactions (Figure 2.9c). The distance from the aryl H of the phenyl rings on the host to the center of the aryl ring of the coumarin guests range is ~ 2.7 Å. Two neighboring coumarins approach each other but are not as closely paired as in the previous examples. The planes of the neighboring coumarins are rotated 71.3° with respect to each other and the closest approach is 3.7 Å (plane to plane). Simulation results after 1×10^6 steps showed the olefinic double bonds of two molecules located ~5.7 Å apart. This suggests

50

that the two guest molecules are not oriented to favor the dimer formation, which was also observed experimentally.

Acenaphthylene is slightly larger than the methylcoumarins (170 Å^3 versus 167 Å^3) and is bound in an ~ 1:1 host:guest ratio. The simulation of host **1**•acenapthylene suggests thee acenaphthylenes will be quickly bound in the central channel of our periodic cell (Figure 2.10a). Two are close packed and the third is at the end of the simulated tube roughly perpendicular and interacts with its neighbor through edge to face aryl- stacking interactions. This perpendicular orientation is not preorganized for reaction and may be a contributing factor in the observed moderate conversion (51%). Additional insight was obtained by analyzing the compiled 'snapshots' over course of the minimization. During the minimization process, it appears that the perpendicular acenapthylene is frequently observed often before its neighbor's bind and may provide additional contacts for organizing the pair. Closer inspection of this pair shows they are oriented in a configuration that should favor the *syn*-photodimer, which is the experimentally observed product.
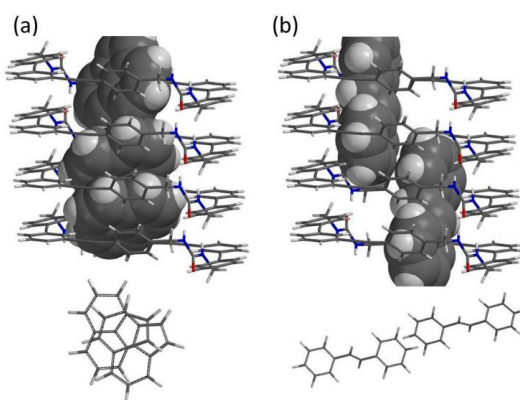
Figure 2.10. GCMC simulation results of host **1**•acenaphthylene and host **1**•*trans*-stilbene. (Partial guest molecules omitted for clarity). a) Predicted orientation of acenaphthylene molecules inside the channel of host **1**. b) Orientation of *trans*-stilbene molecules inside the channel.

GCMC simulations of the host **1** complexes with *cis*-stilbene, *trans*-stilbenes (Figure 2.10b) and β-methyl styrene predicted these guests are randomly distributed within the tubes with limited close contacts with neighboring guests. Similar to the models of the host **1**•coumarin, some loading of these guests was also predicted to occur in an exterior binding site between neighboring tubes. These exterior absorbed guests also lacked proximity to neighboring guests and displayed geometries that were not conducive for further reaction.

2.4 Examination of Xenon diffusion in host **1** and comparison with diffusion studies in the phenylether *bis*-urea host.[68,69]

Hyperpolarized Xe-129 NMR is employed to study the packing effects, internal electronic environment, and Xe diffusion in the nanochannels of host 1 in comparison with smaller phenylether *bis*-urea host (Figure 2.11 and 2.12). The nanochannels formed by the phenylether *bis*-urea macrocycle are elliptical shaped with minor and major axes of approximately ~0.37×0.48 nm, while the channels formed by the phenylethynylene *bis*-urea (host 1) affords a large pore with a diameter of ~0.9 nm. In agreement with expectations based on the collision diameter of the Xe atom relative to the differing internal diameters of the two types of macrocycles, hyperpolarized spin tracer exchange data indicate single-file diffusion of Xe in the narrow channels of the phenylether *bis*-urea macrocyle and normal, Fickian diffusion in the larger *bis*-urea channels. The small elliptically shaped pores formed by stacking of the phenylether *bis*-urea macrocycle produce a Xe-129 powder pattern characteristic of an asymmetric shielding tensor with three different principal shielding components which scale different with Xe pressure. In contrast, the wider channels formed by phenylethynylene *bis*-urea macrocycle yield an

52

approximately symmetric Xe-129 NMR peak, reflecting an isotropic dynamically averaged electronic environment. At low loading and room temperature, the Xe-129 powder pattern extends to well-over 300 ppm with respect to the gas phase reference at zero ppm, an observation that is attributed to the extreme confinement of Xe in the channels of the phenylether bis urea. The results establish the self-assembled *bis*-urea macrocycles as nanoporous materials as a new class of porous nanotubular materials with tunable geometry, which are ideally suited for the study of single-file diffusion and diffusion control on the micrometer length scale.
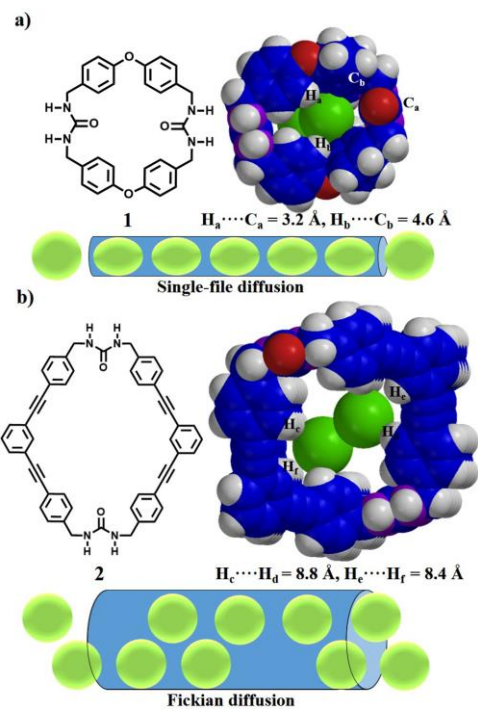
Figure 2.11. Two *bis*-urea macrocycles studied using Hyperpolarized Xe-129 NMR with a side view of the packing arrangement of adjacent channels. (a) Phenylether *bis*-urea macrocycle displays a single file diffusion of Xe molecules, (b) Phenylethynylene *bis*-urea macrocycle displays a Fickian type diffusion of Xe molecules.
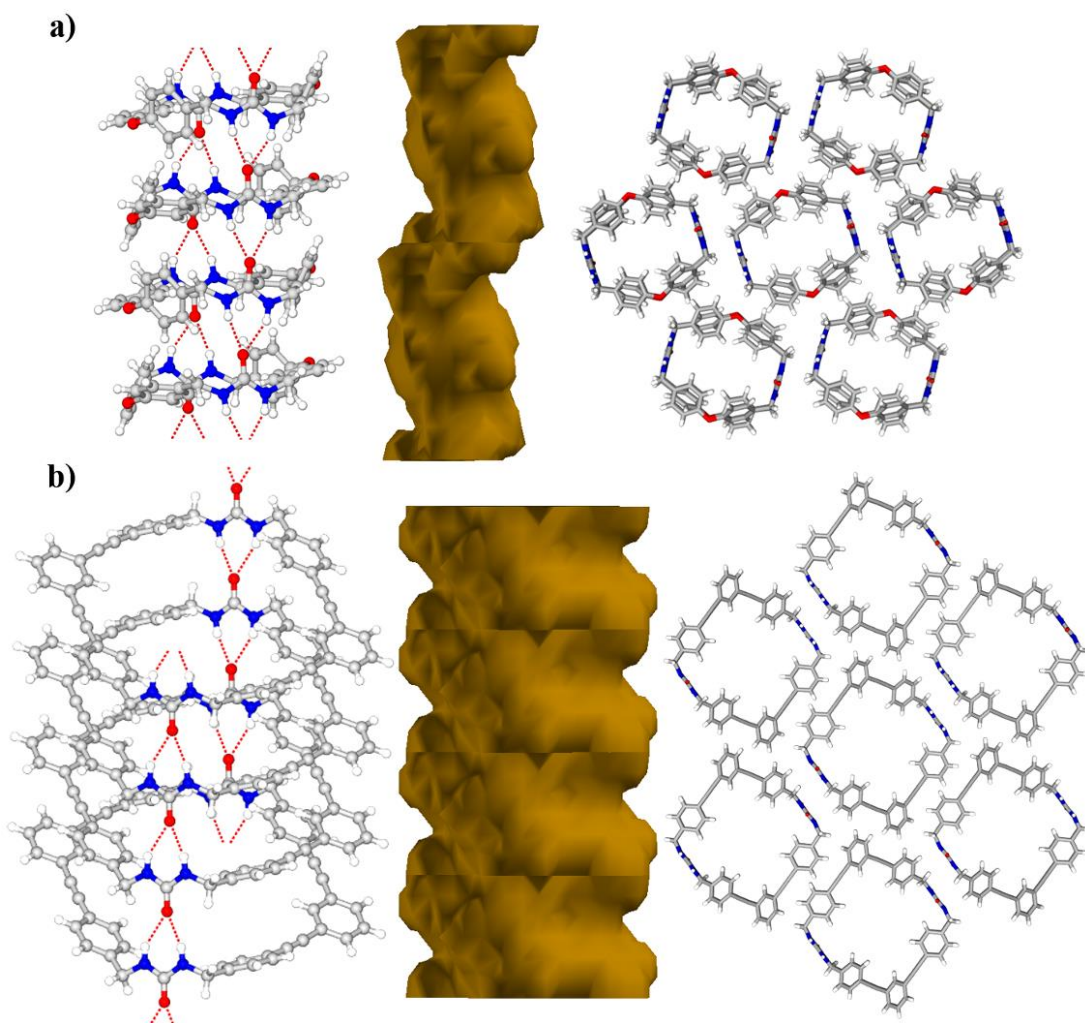
Figure 2.12. Two *bis*-urea macrocycles studied using Hyperpolarized Xe-129 NMR with a side view of the packing arrangement of adjacent channels. (a) Phenylether *bis*-urea host (b) Phenylethynylene *bis*-urea macrocycle host.

2.5 Conclusions

This chapter demonstrates the utility of our self-assembled phenylethynylene *bis*-urea host to absorb a range of aromatic guests and form well-ordered crystalline complexes as indicated by PXRD. Subsequent solid-state $^{13}C\{^{1}H\}$CP-MAS NMR studies suggest that the encapsulated guests have a greater mobility within the solid than the assembled host. The guests were chosen based on their propensity to undergo photochemical reactions and were used to probe the ability of the one-dimensional channel to influence or direct

photochemical transformations. Upon UV-irradiation, we observed selective photodimerization reactions for coumarin, 6-methyl coumarin, and 7-methyl coumarin to afford their corresponding *anti*-HH photodimers with good to excellent selectivity (84-97%) in moderate conversion. Acenaphthylene also reacted selectively in the solid host **1**•acenaphthylene complex to afford exclusive production of the syn-photodimer. Not all the guests reacted in the presence of host 1. No isomerization reactions were observed for the *cis*-stilbene, *trans*-stilbene, or *trans*-β-methylstyrene complexes, which indicates that host 1 is not able to act as a sensitizer. Also, no [2+2]-photocycloadditions were observed for these guests, suggesting that either they were bound in geometries that were not conducive for reactions or that the photoproducts were too large for the channel.

The most important aspect of this work was the development of a protocol to examine these host guest complexes by GCMC simulations. These were carried out with Monte Carlo for Complex Chemical Systems (MCCCS) Towhee plug-in built into Scienomics' MAPS. The simulations were not only able to explain the observed reactivity of these guests, but also correctly predicted the product selectivity. Indeed, in the simulations the reactive guests (coumarin, 6-methyl coumarin, 7-methyl coumarin and acenaphthylenes) appeared to be closely paired within the channels and were preorganized with respect to each other to most easily form their respective *anti*-HH or *syn* photodimers. These were also the experimentally observed products. Thus, our simulations suggest that the selectivity is due to the pre-organization of the starting materials within the channels of host **1**.

Our simulations also predicted that there could potentially be loading of guests in sites on the exterior in between neighboring one-dimensional columns, although these

55

guests were positioned in geometries and at distances that were unfavorable for subsequent reactions. Thus far, we have no experimental evidence of such binding modes; however, such binding could provide an alternative explanation for the apparent conversion limit of ~55%. This limit could also due to inefficient light penetration or lack of uniform irradiation of the crystals.

We next tried to refine these simulations and apply this method to more broadly to predict the loading and potential reactive of new guests within this porous host. As described in chapter 3, we future utilized this method to model chromone and four mono-substituted derivatives namely 6-fluorochromone, 6-bromochromone, 7-hydroxy-4-chromone, and 3-cyanochromone inside the host 1 channel. Please see chapter 3 for detailed investigation. We expect this synergy between experiment and simulations to guide our future studies.

2.6 Experimental

Macrocycle **1** was prepared as previously described. Crystals were obtained by slow cooling a DMSO solution of **1** (50 mg/ 10 mL) from 140 °C at 1 °C / h. Small needle crystals of **1**•DMSO were observed in 2-3 days and displayed a 1:2 host 1:DMSO stoichiometry. Host **1** was obtained by heating the 1•DMSO crystals using thermogravimetric analysis (TGA). Freshly obtained crystals (15 mg) were heated from 25 to 170 °C (4 °C/min). A two-step desorption curve was observed with a total weight loss of 18.3%, corresponding to removal of the DMSO. The crystals were cooled under helium (g) and used directly for loading experiments.

2.6.2 Guest loading studies

Guests were loaded in the empty host by two methods. A) The crystalline host was soaked in solution of the guest in a suitable solvent (CH_3CN or hexanes) for 0-24 h. B) The host was immersed directly in the liquid guest. For method A typical loading experiments were carried out on samples of host 1 (5-50 mg) by soaking in guest solutions (0.1 mM in CH_3CN for most guests or 0.5 mM in hexanes at 35 °C for 7-methoxy coumarin. As these guests all contain UV chromophores, their depletion from solution was followed by absorption spectroscopy until the absorbance reached a plateau, suggesting that equilibrium had been obtained. The loading ratios were then calculated through comparison to Lambert-Beer plots of known concentrations of the guest. Loading experiments were carried out on different batches and sizes of host **1** crystals and gave similar binding ratios. For method B host **1** (30 mg) was added to the pure liquid guest (10 mL) in a scintillation vial and kept undisturbed for equilibration (12 h). After filtration, the complexes were air dried (6 h) and analyzed by TGA. Two guests *cis*-stilbene and *trans*-β-methyl styrene were loaded by this method as they showed no loading by method A. Photoreactions. Each host **1**•guest complex (30 mg) was placed in a Norell S-5-500-7 NMR tubes (with 100% transmittance up to 400 nm). Samples of the pure guests (30 mg) were also used as controls. The samples were UV-irradiated at room temperature under argon atmosphere using a Hanovia 450 W medium pressure mercury arc lamp for between 0-96 h. Products were extracted into deuterated solvent for analysis. Additionally, the solid-complexes (2-3 mg) were also directly dissolved in DMSO-d_6 and analyzed by ^{1}H NMR spectroscopy to confirm that the products could be fully removed from the crystals. The powder X-ray diffraction (PXRD) data were

57

collected on a Rigaku Dmax-2100 & 2200 powder X-ray diffractometers using a Bragg-Brentano geometry with CuKα radiation. The step scans covered the angular range 2-40° 2θ in steps of 0.05°. Solid-state cross-polarized magic angle spinning $^{13}C\{^1H\}$CP-MAS NMR spectra. Solid state ^{13}C CP-MAS spectra were collected on a Bruker Avance III-HD 500 MHz spectrometer fitted with a 1.9 mm MAS probe. The spectra were collected at ambient temperature with sample rotation rate of 20 kHz. 1.5 ms contact time with linear ramping on the ^1H channel and 62.5 kHz field on the ^{13}C channel were used for cross polarization. ^1H dipolar decoupling was performed with SPINAL64 modulation and 145 kHz field strength. Free induction decays were collected with a 27 ms acquisition time over a 300 ppm spectra width with a relaxation delay of 1.5 s. In comparison, spectra from prior reports were acquired using double resonant Doty Scientific XC 4 mm MAS probe. TPPM modulated dipolar decoupling with 61 kHz field strength was applied during data acquisition. One second equilibration delay was used between each transient. Spinning speed of 8 kHz and TOSS side-band suppression was used for all measurements. Ramped cross polarization was used. Thermogravimetric analysis (TGA). TGA guest desorption studies were carried out on 5-10 mg of absorbed sample using TA Instruments SDT-Q600 simultaneous DTA-TGA at a heating rate of 4ºC/min from 25 to 170 ºC under helium.

2.6.3 Computational studies.

Computational studies were performed using the Monte Carlo for Complex Chemical Systems (MCCCS) Towhee[66] plug-in built into Scienomics Materials Processes and Simulations (MAPS) platform. First, amorphous guest systems were built using the Amorphous Builder plug-in within MAPS, and the chemical potentials of guests were

calculated *via* a 1 x 10^4 step canonical MC simulation with MCCCS Towhee for systems contain 100 guest molecules. The Dreiding force field[67] was applied to all our simulated systems. Next, we generated a simulation cell by importing the atomic coordinates from the X-ray structure of host **1**•nitrobenzene. The coordinates of the guests were removed to create a periodic simulation cell. The calculations of host **1**•guest complexes were performed using previously obtained guest chemical potential values. All calculations were conducted via GCMC simulations for 1x10^6 steps where the chemical potential (μ) of the corresponding guest was kept constant and the system was maintained at standard ambient constant temperature (t, 298.15K) and constant volume (V).

2.6.3 Guest loading studies
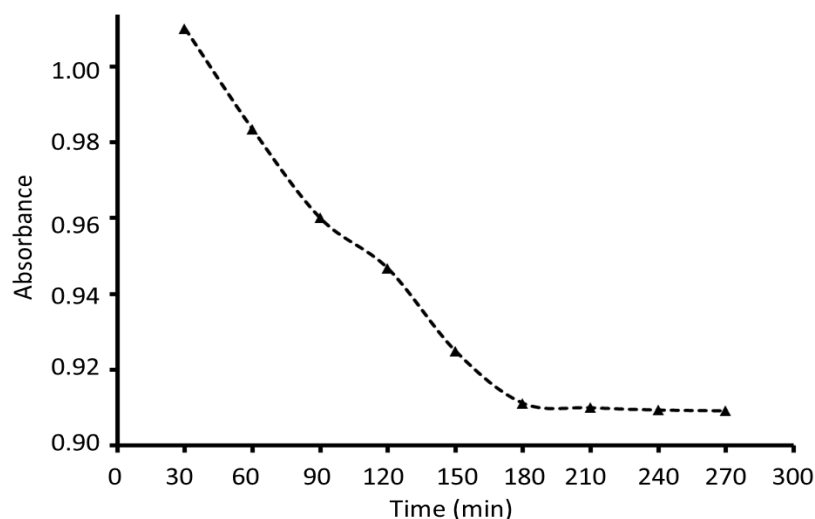
Figure 2.13. Depletion of 6-methyl coumarin concentration during introduction of this guest into the host **1** crystals with respect to time. Monitored by UV-vis spectroscopy at 273 nm.
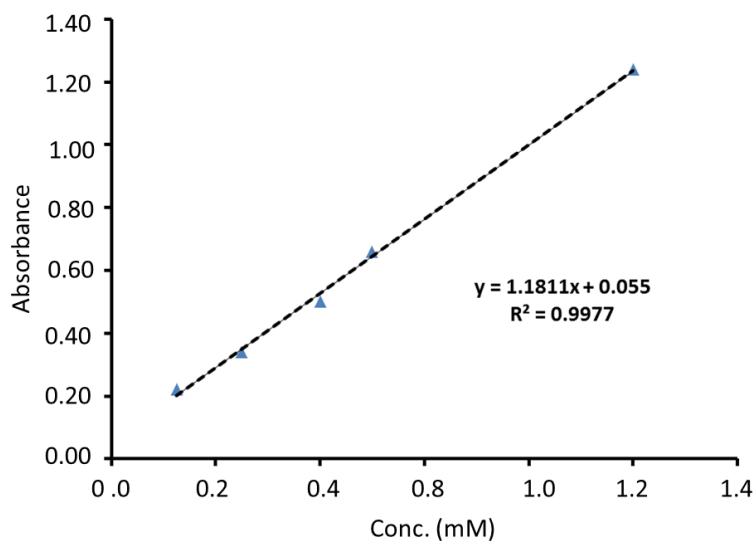
Figure 2.14. The Lambert-Beer analysis of 6-methyl coumarin solution in acetonitrile at increasing concentration monitored by UV-vis spectroscopy.

Table 2.3. Comparison of loading of 6-methyl coumarin from acetonitrile solution.

Guest Name	Trial #	H:G loading Ratio	Average H:G loading
6-methyl coumarin from acetonitrile solution	1	1:1.01	1: 1
	2	1: 1.03	
	3	1: 1.1	
	4	1: 0.95	
	5	1: 0.89	
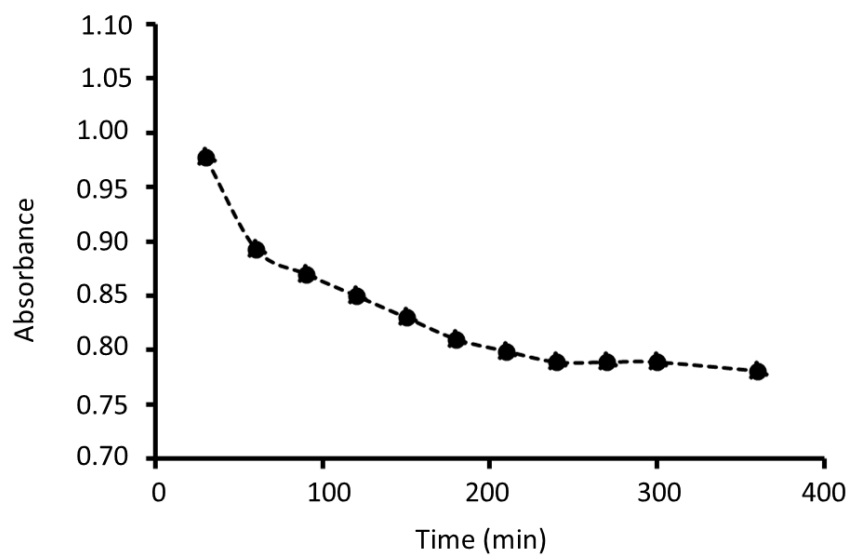
Figure 2.15. Depletion of 7-methyl coumarin concentration during introduction of this guest into the host **1** crystals with respect to time as monitored by UV-vis spectroscopy at 276 nm.
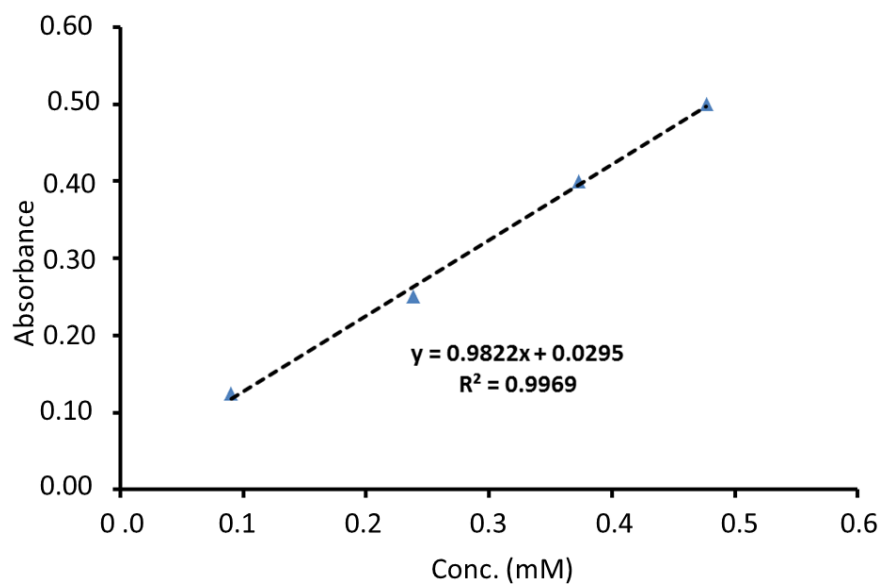
Figure 2.16. The Lambert-Beer analysis of 7-methyl coumarin solution in acetonitrile at increasing concentration monitored by UV-vis spectroscopy.

61

Table 2.4. Comparison of loading of 7-methyl coumarin from acetonitrile solution.

Guest Name	Trial #	H:G loading Ratio	Average H:G loading
7-methyl coumarin from acetonitrile solution	1	1:1.16	1: 1.1
	2	1: 1.03	
	3	1: 1.21	
	4	1: 0.95	
	5	1: 1.14	
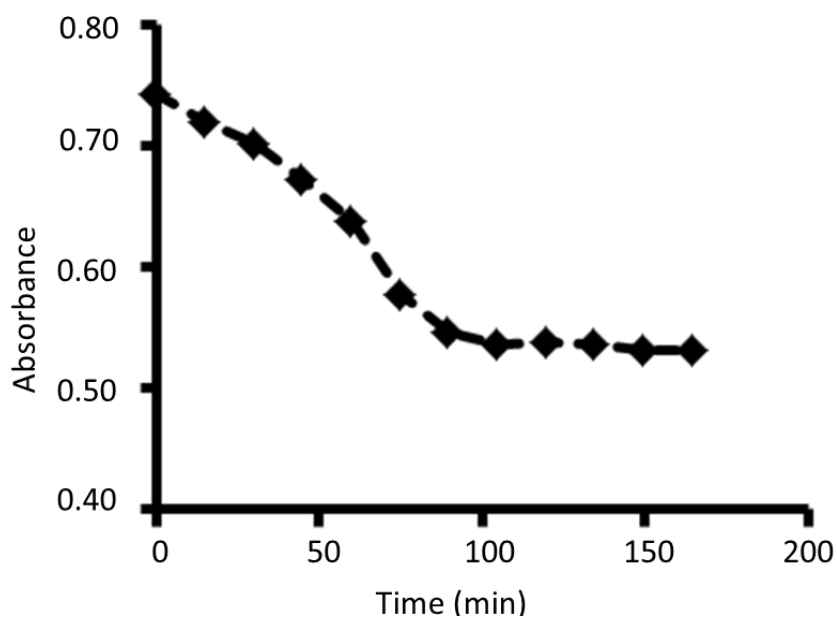
Figure 2.17. Depletion of acenaphthylene concentration during introduction of this guest into the host **1** crystals with respect to time as monitored by UV-vis spectroscopy at 322 nm.

62
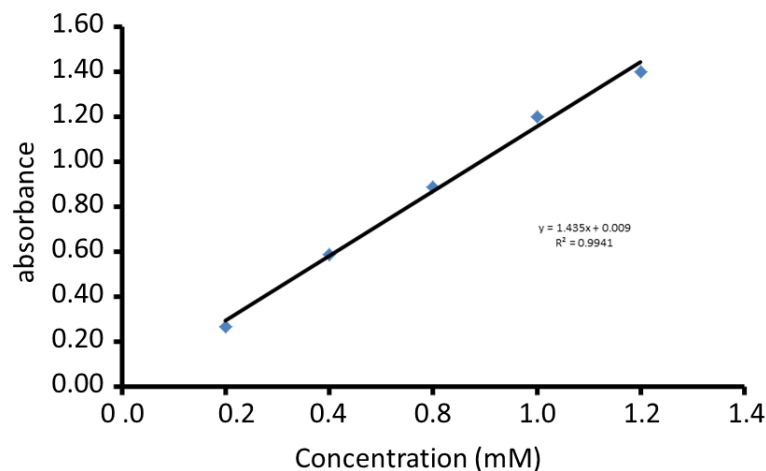
Figure 2.18. The Lambert-Beer analysis of acenaphthylene solution in acetonitrile at increasing concentration monitored by UV-vis spectroscopy.

Table 2.5. Comparison of loading of acenaphthylene from acetonitrile solution.

Guest Name	Trial #	H:G loading Ratio	Average H:G loading
acenaphthylene from acetonitrile solution	1	1:0.89	1: 0.8
	2	1: 0.76	
	3	1: 0.74	
	4	1: 0.86	
	5	1: 0.71	
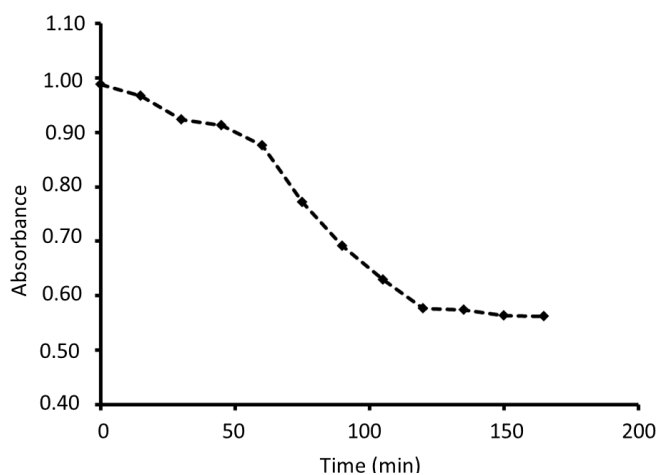
Figure 2.19. Depletion of *trans*-stilbene concentration during introduction of this guest into the host **1** crystals with respect to time as monitored by UV-vis spectroscopy at 294 nm.

63
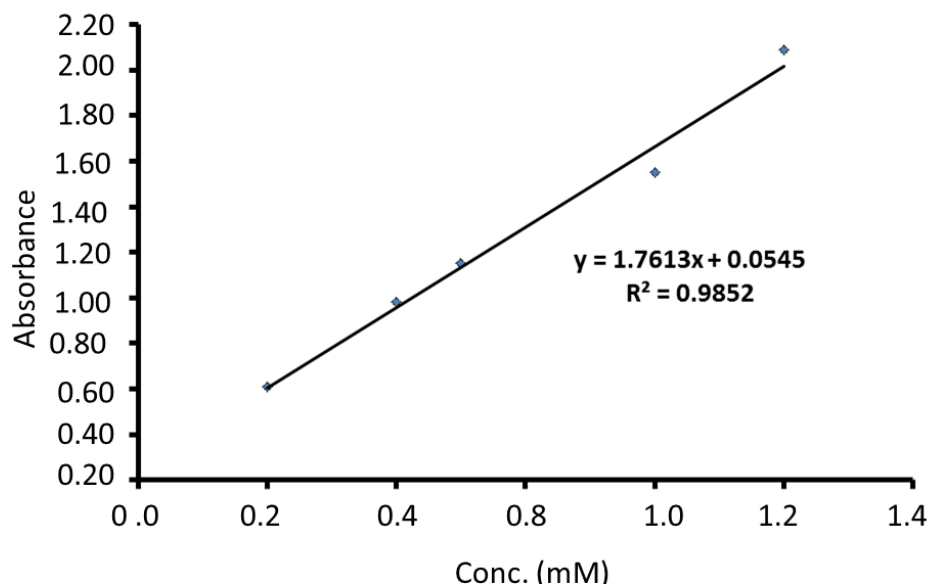
Figure 2.20. The Lambert-Beer analysis of *trans*-stilbene solution in acetonitrile at increasing concentration monitored by UV-vis spectroscopy.

Table 2.6. Comparison of loading of *trans*-stilbene from acetonitrile solution.

Guest Name	Trial #	H:G loading Ratio	Average H:G loading
trans- stilbene from acetonitrile solution	1	1:0.49	1: 0.45
	2	1: 0.41	
	3	1: 0.38	
	4	1: 0.51	
	5	1: 0.45	
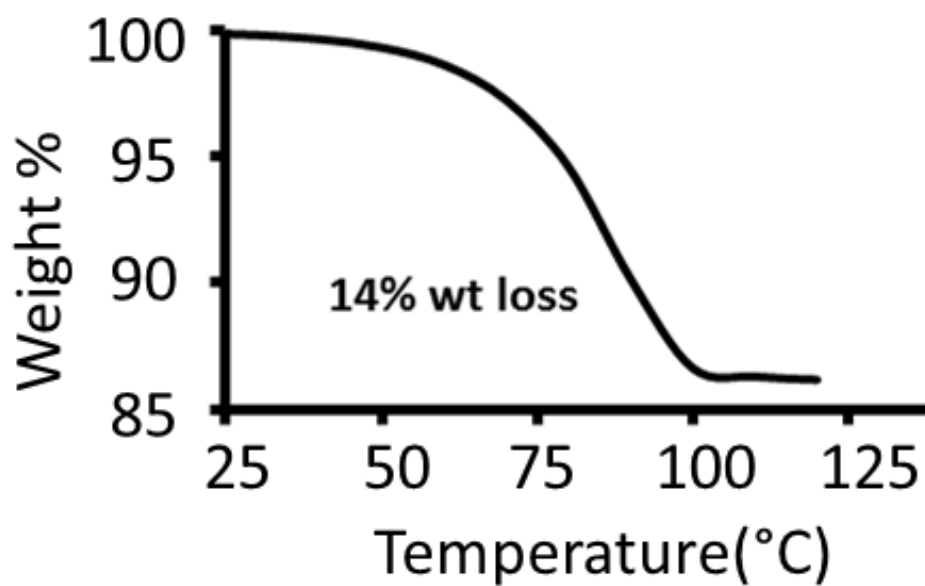
Figure 2.21. Desorption of *cis*-stilbene from host **1** as observed by TGA
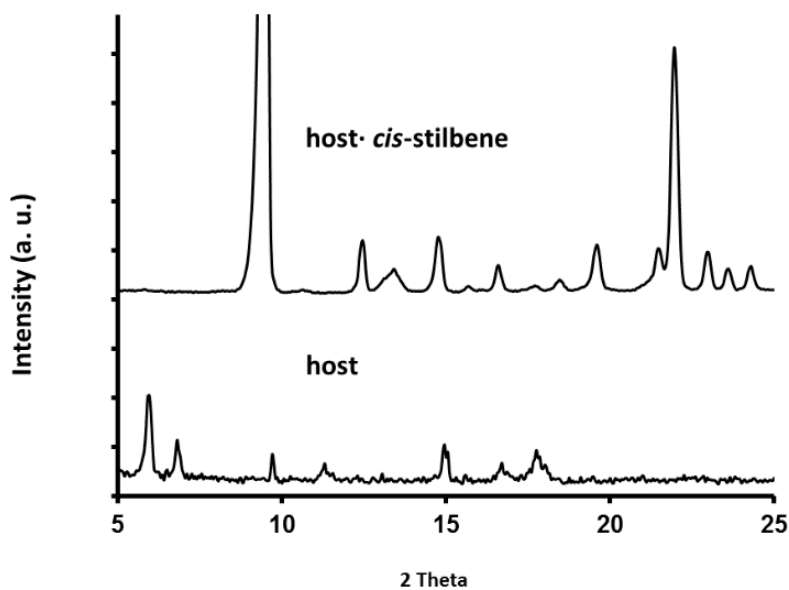
Figure 2.22. The PXRD analysis of host **1** *cis*-stilbene complex compared with empty host crystals.
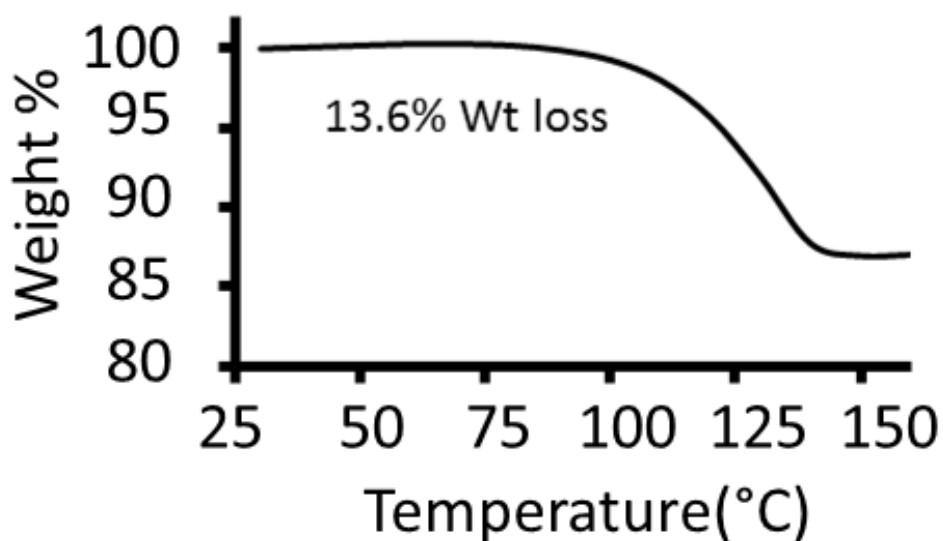
Figure 2.23. Desorption of *trans*-β-methyl styrene from host **1** as observed by TGA experiment.
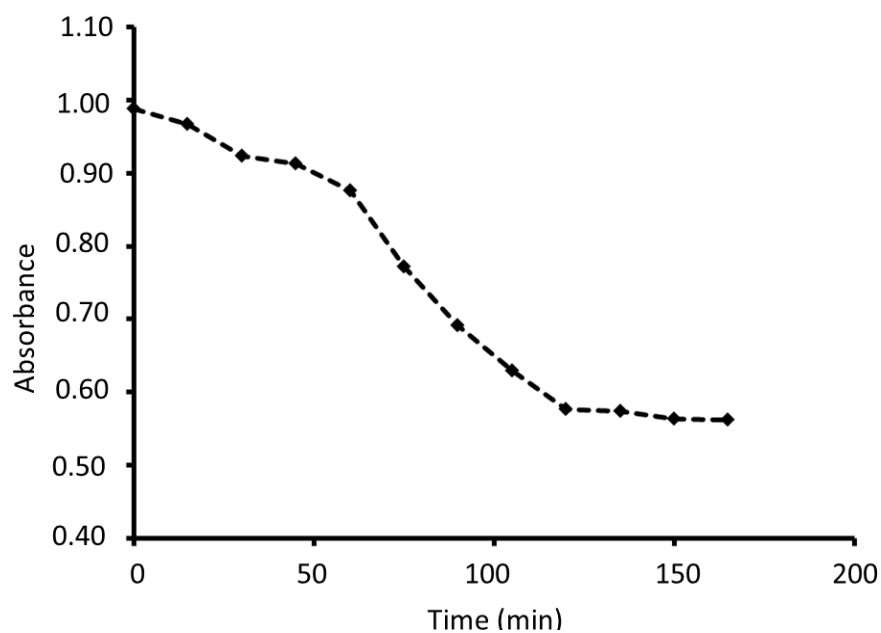
Figure 2.24. Depletion of *trans*-stilbene concentration during introduction of this guest into the host **1** crystals with respect to time as monitored by UV-vis spectroscopy at 294 nm.
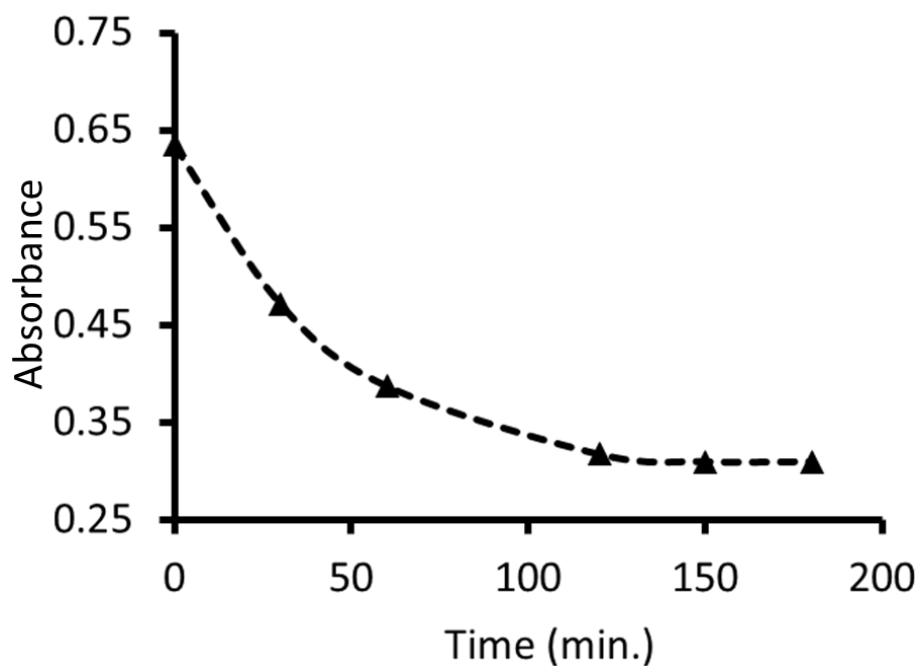
Figure 2.25. Depletion of 7-methoxy coumarin concentration during introduction of this guest into the host **1** crystals with respect to time as monitored by UV-vis spectroscopy at 315 nm.
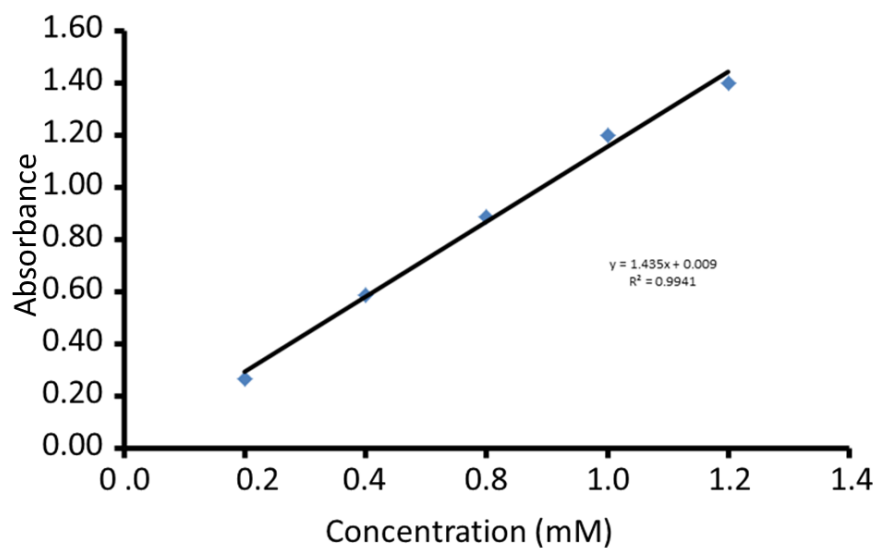
Figure 2.26. The Lambert-Beer analysis of 7-methoxy coumarin solution in acetonitrile at increasing concentration monitored by UV-vis spectroscopy.

2.6.4 Solid state NMR studies
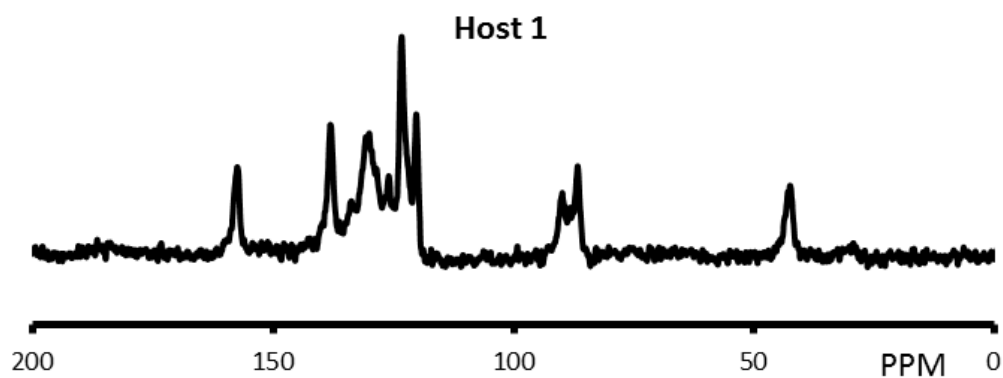
Figure 2.27. Solid-state $^{13}C\{1H\}$CP-MAS NMR spectra for host **1**.
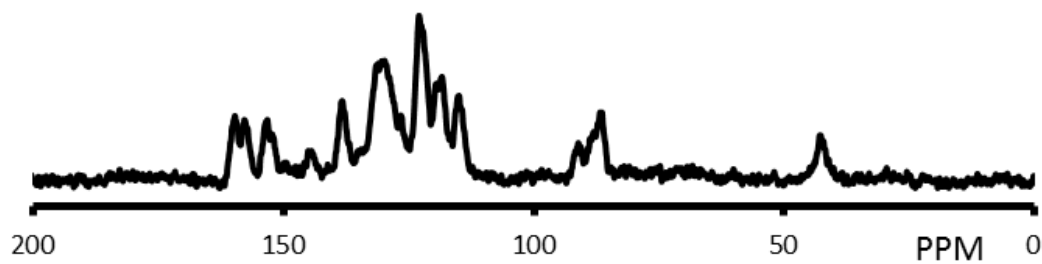
Figure 2.28. Solid-state $^{13}C\{1H\}$CP-MAS NMR for host **1**•coumarin complex.
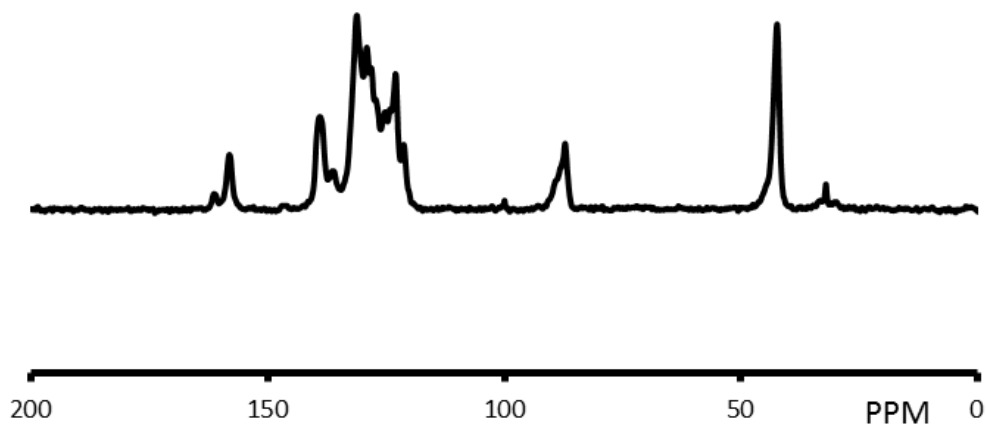
Figure 2.29. Solid-state $^{13}C\{1H\}$CP-MAS NMR for host **1**•6-methyl coumarin complex.
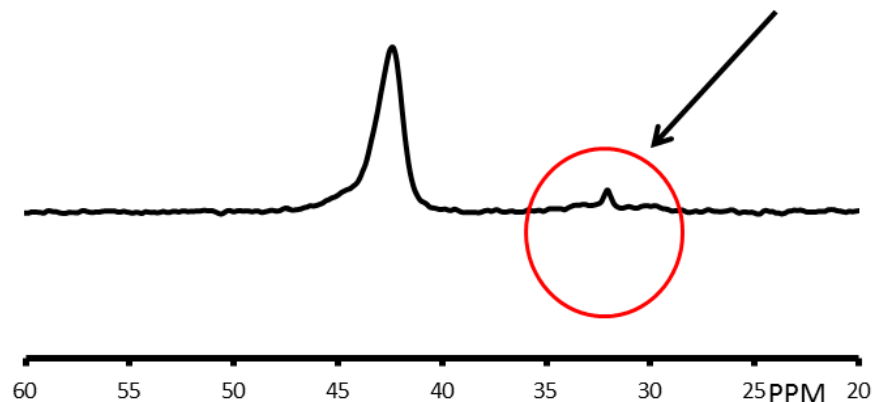
Figure 2.30. Solid-state $^{13}C\{1H\}$CP-MAS NMR for host **1**•6-methyl coumarin complex expanded to show the 20-60 ppm range. The arrow indicates a resonance with a reasonable shift for the 6-methyl group on coumarin.
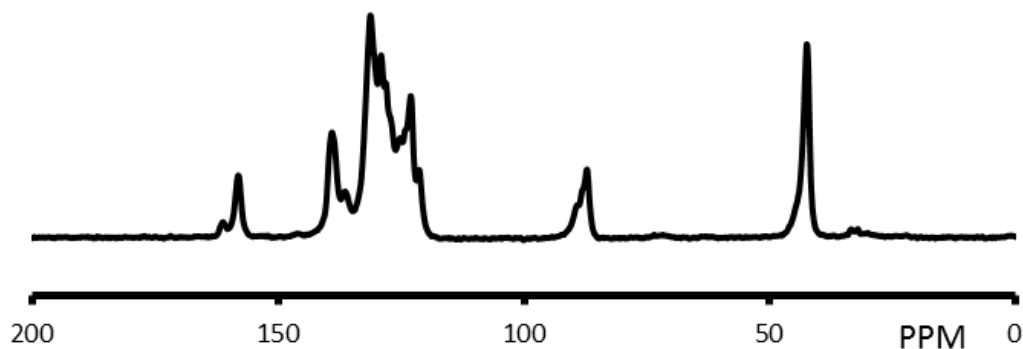
Figure 2.31. Solid-state $^{13}C\{1H\}$CP-MAS NMR for host **1**• 7-methyl coumarin complex.
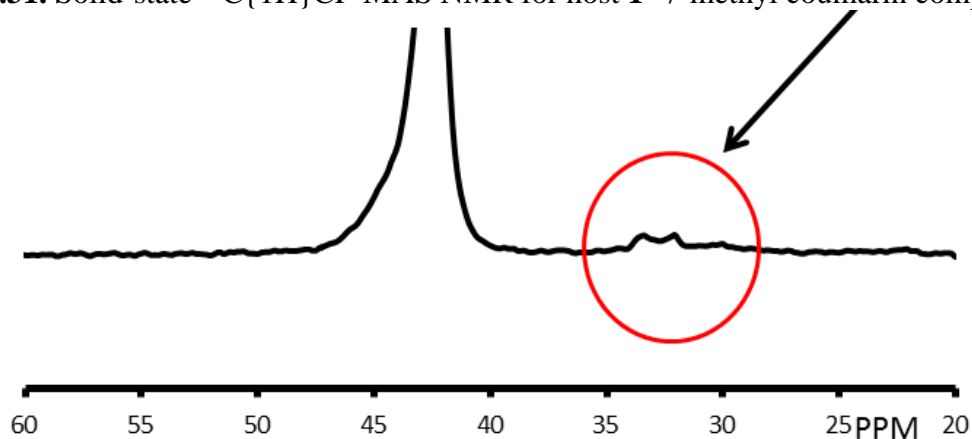
Figure 2.32. Solid-state $^{13}C\{1H\}$CP-MAS NMR for host **1**•7-methyl coumarin complex expanded to show the 20-60 ppm range. The arrow indicates a resonance with a reasonable shift for the 7-methyl group on coumarin.

69
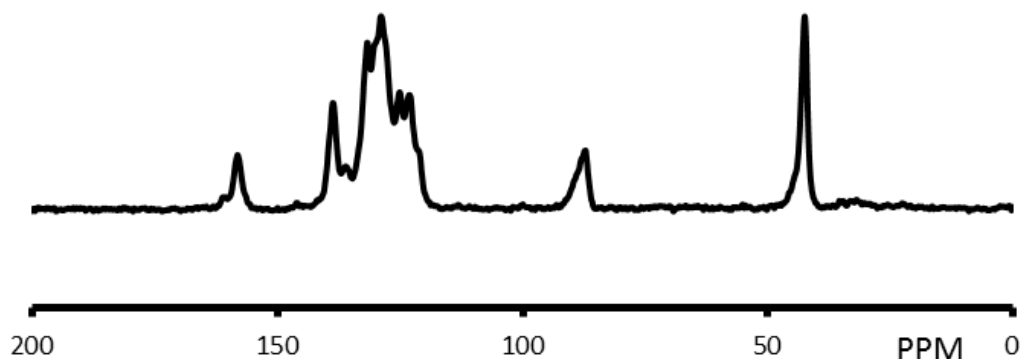
Figure 2.33. Solid-state $^{13}C\{1H\}$CP-MAS NMR for host **1•** 7-methoxy coumarin complex.

2.6.5 Comparison to literature reported PXRD patterns

Table 2.7. Literature reported and experimentally obtain PXRD data for host 1 • guest complexes and guest molecules.

Sample	PXRD Peaks (2θ values)	References
Host 1• DMSO	5.8, 6.1, 14.9, 16.6, 17.4, 19.8, 21.3, 22.3, 23.1, 24.2, 25.5, 27.2	Experimental
Host 1 empty	5.9, 7.1, 9.8, 11.1, 15.1, 16.9, 18.1	Experimental
Neat 6-Methyl Coumarin	6.2, 12.2, 24.9	Experimental
Host 1•6-Methyl Coumarin	16.1, 18.2, 20.1, 23.9, 27.3	Experimental
7-Methyl Coumarin	9.9, 13.2, 15.1, 16.9, 19.9, 24.9, 27.2	J.Org.Chem,1985, 50, 2337
Host 1•7-Methyl Coumarin	17.1, 17.6, 19.9, 20.2, 22.9, 25.1, 27.3	Experimental
Acenaphthylene (Literature)	Structure I: 10.1, 11.7, 17.8, 21.0, 24.9, 25.3	Acta Crystallogr. , 1957, 10, 699
	Structure II:10.1, 11.7, 17.8, 21.0, 24.9, 25.3	Acta Crystallogr.,Sect.C: Cryst.Struct.Commun. , 1986, 42, 690
Host 1• acenaphthylene	7.7, 7.9, 14.2, 14.7, 14.9, 16.9, 18.2, 18.8, 20.3	Experimental
trans-stilbene	Structure I: 12.1, 15.5, 15.6, 17.5, 18.5, 19.1, 19.5, 19.8, 21.2, 22.0, 22.9, 23.09, 23.59, 27.4, 27.6, 28.4	Proc.R.Soc.London,Ser.A, 1937, 162, 568
	Structure II: 1.8, 14.1, 15.1, 16.8, 19.4, 19.7, 22.6, 22.9, 27.3	J.Am.Chem.Soc., 2004, 126, 3539
Host 1• trans stilbene	6.1, 10.2, 11.1, 12.6, 15.1, 17.2, 17.9, 22.4, 24.9	Experimental

70
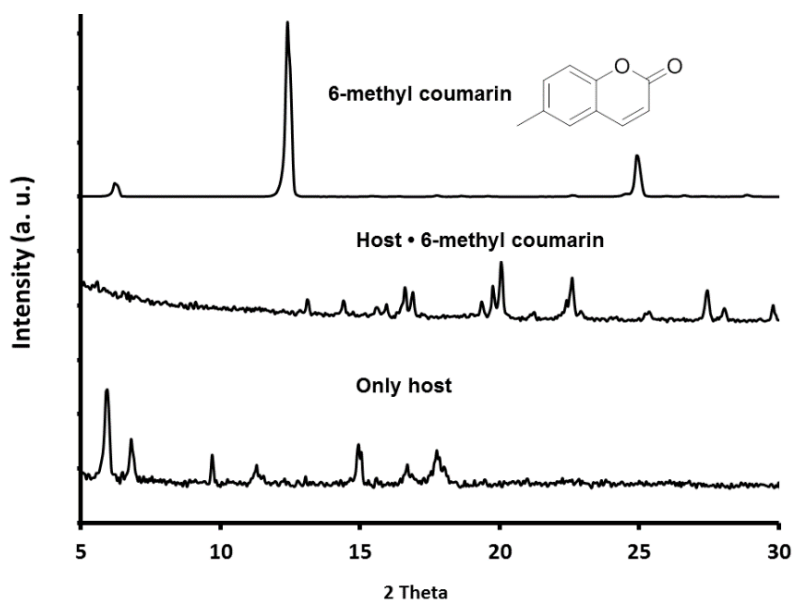
Figure 2.34. PXRD analysis of host **1**• 6-methyl coumarin. i) PXRD pattern of empty crystals (bottom); ii) Host **1**• 6-methyl coumarin complex; (middle) iii) Powdered 6-methyl coumarin (top).
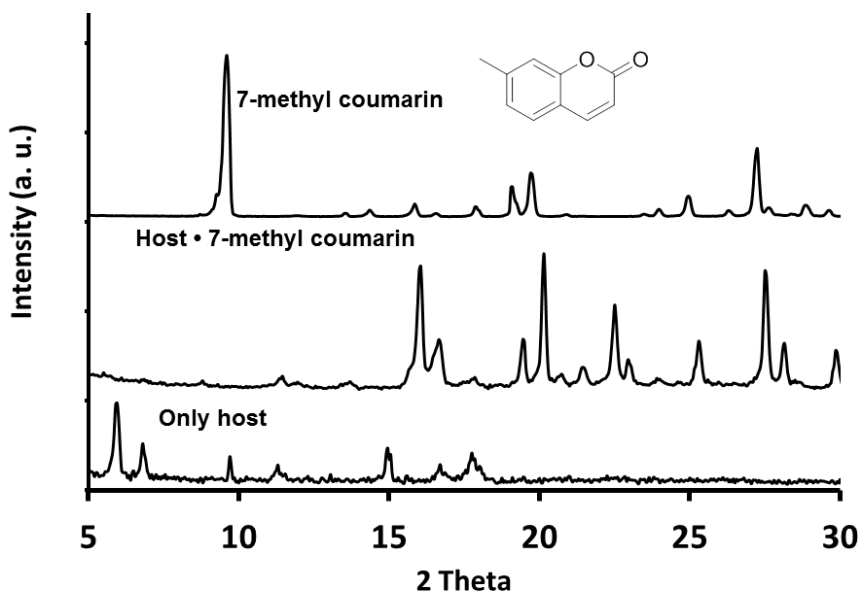
Figure 2.35. PXRD analysis of host **1**• 7-methyl coumarin complex. i) PXRD pattern of empty crystals (bottom); ii) Host **1**• 7-methyl coumarin complex (middle); iii) Powdered 7-methyl coumarin (top).

71
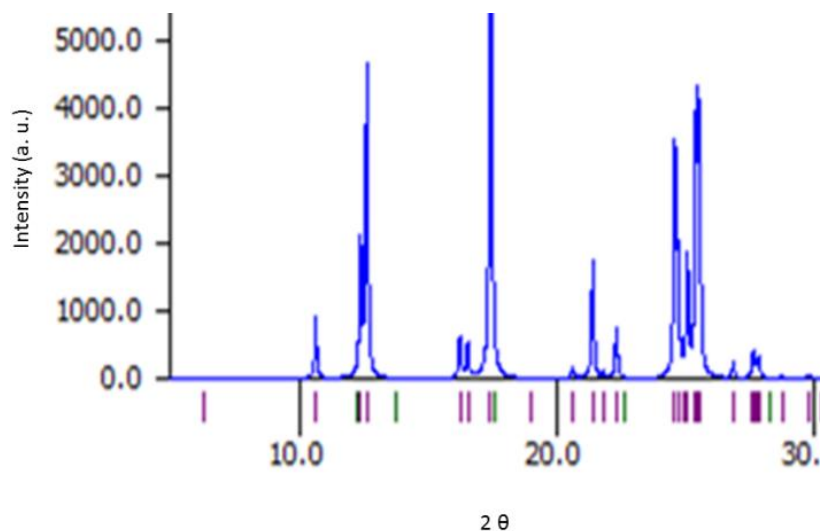
Figure 2.36. Predicted PXRD analysis of acenaphthylene crystals. The pattern was generated using the X-ray crystal data from reference 68.
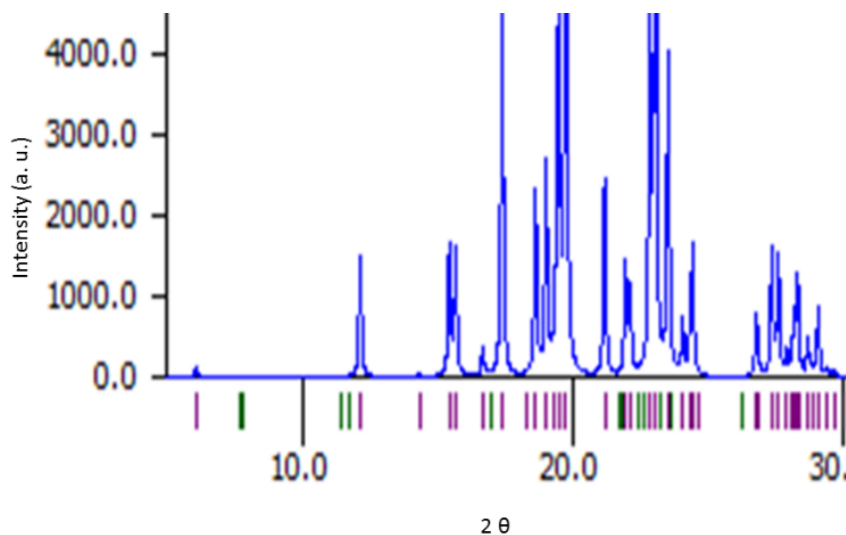
Figure 2.37. Predicted PXRD analysis of only guest crystals *trans-* stilbene. The pattern was generated using the X-ray crystal data from reference 69.

72

www.manaraa.com
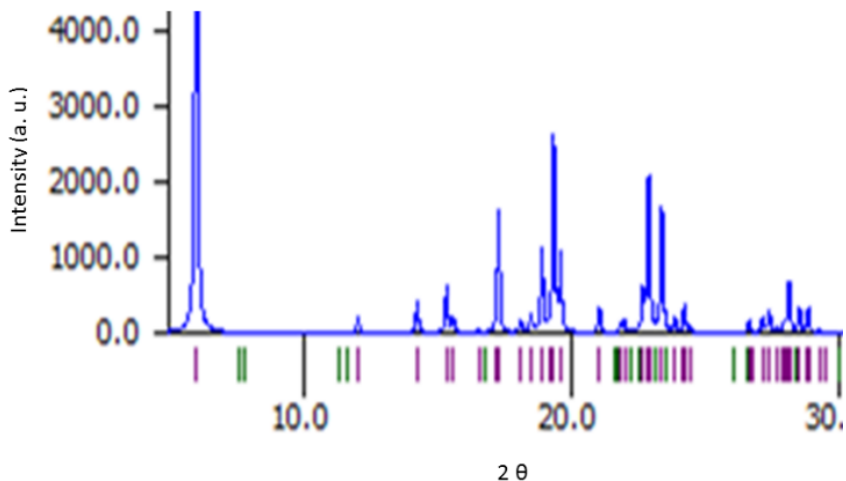
Figure 2.38. Predicted PXRD analysis of only guest crystals, another polymorph of 7-methyl coumarin. The pattern was generated using the X-ray crystal data from reference 70.
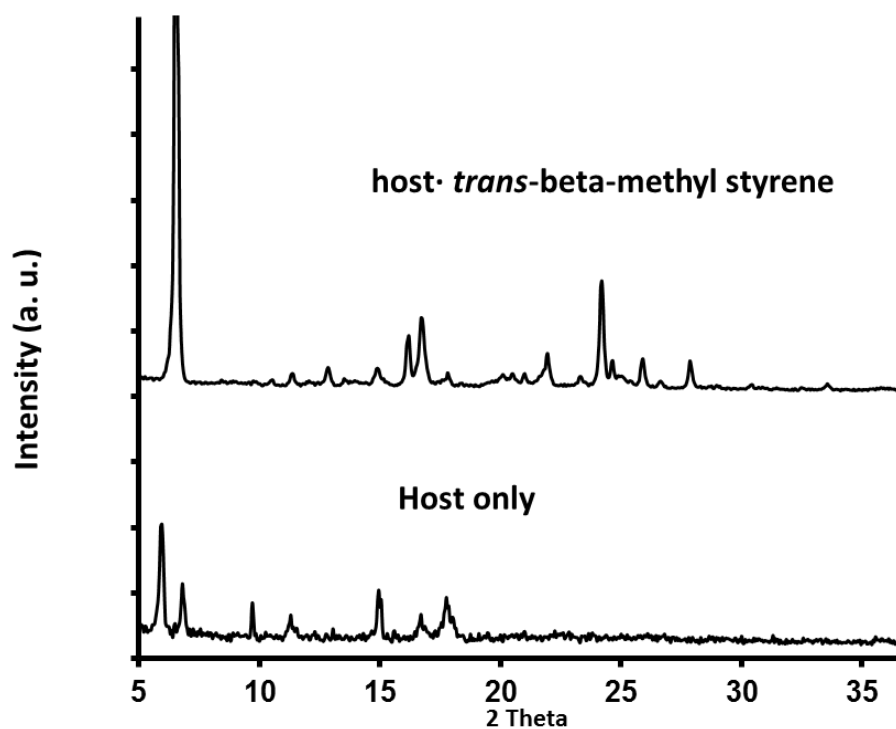
Figure 2.39. The PXRD analysis of host **1** *trans*-β-methyl styrene complex compared with empty host **1** crystals.
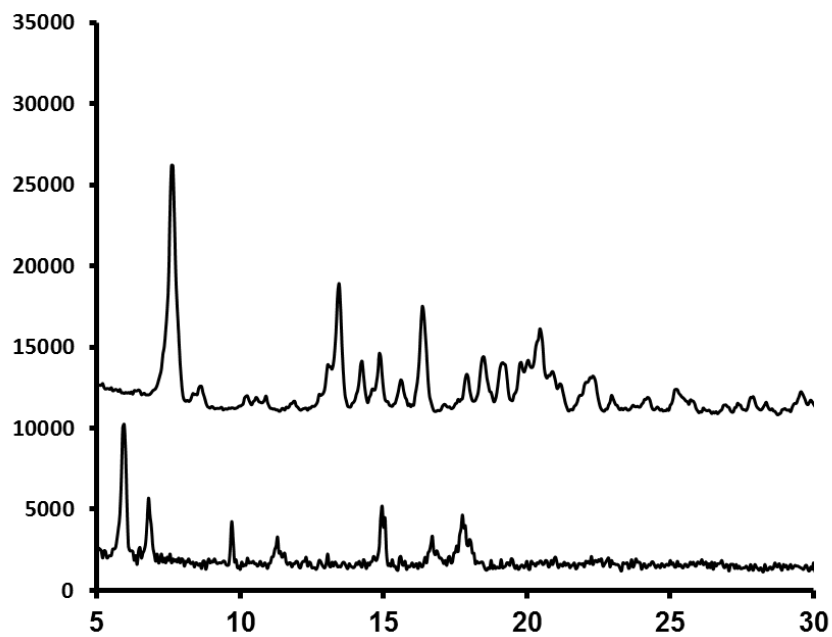
Figure 2.40. The PXRD analysis of host **1**• acenaphthylene complex (top) and empty crystals of host **1** (bottom).
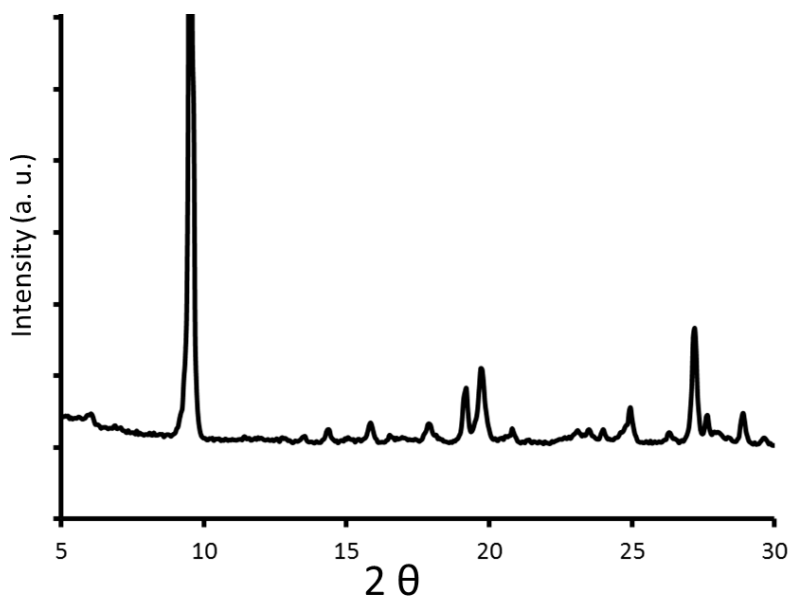
Figure 2.41. The PXRD analysis of host **1**• *trans*-stilbene complex.
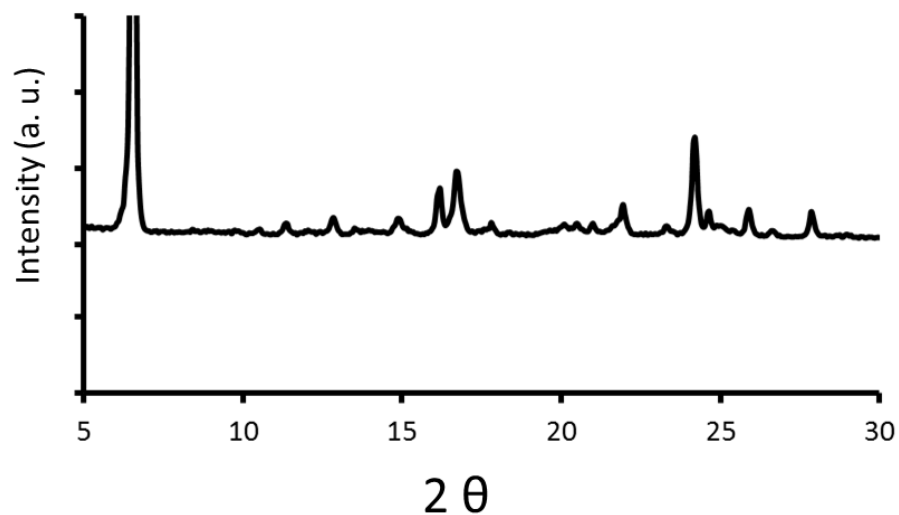
Figure 2.42. The PXRD analysis of host **1**•*cis* stilbene complex
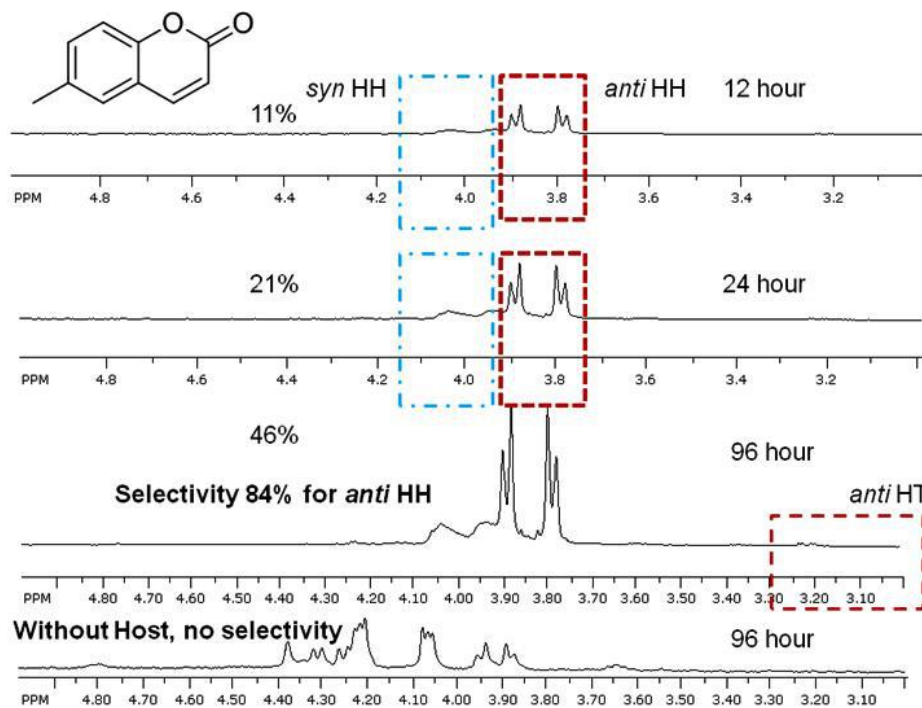
Figure 2.43. ¹H-NMR analysis of the product obtained from photoreaction of host **1**•6-methyl coumarin. The peaks correspond to the cyclobutyl region of the photodimers are shown.
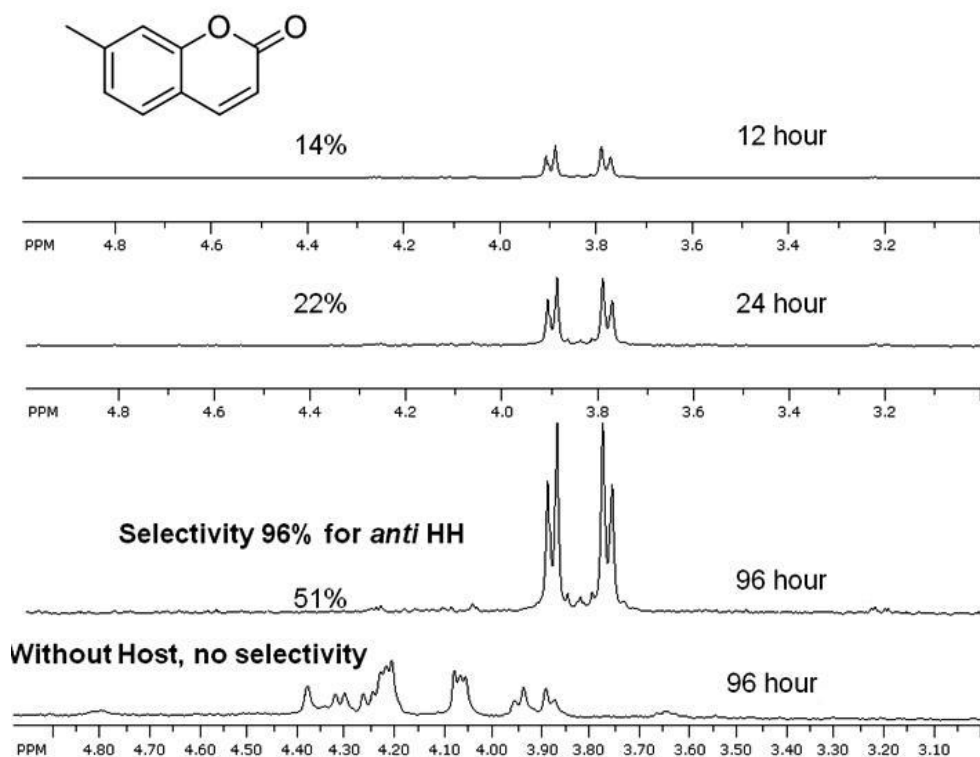
Figure 2.44. ^{1}H-NMR analysis of the product obtained from photoreaction of host **1**•7-methyl coumarin. The peaks correspond to the cyclobutyl region of the photodimers are shown.
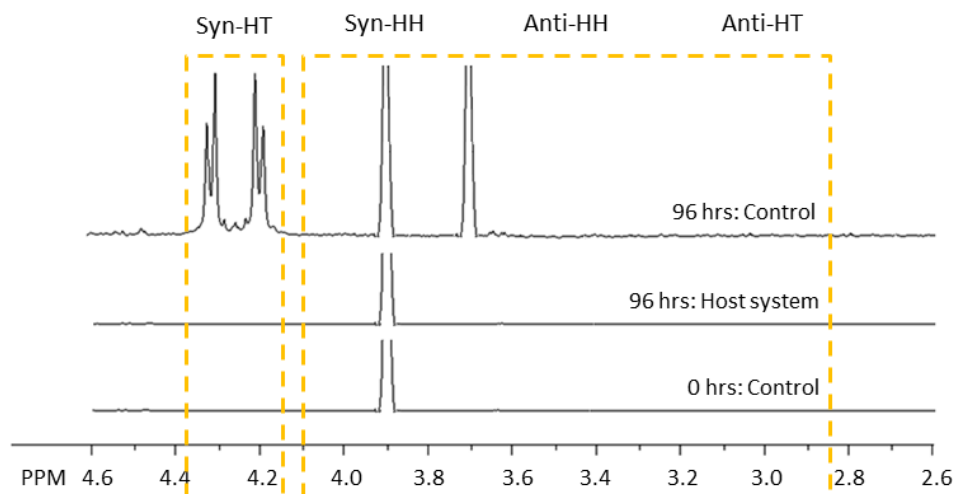
Figure 2.45. ^{1}H-NMR analysis of the product obtained from photoreaction of host **1**•7-methoxy coumarin.
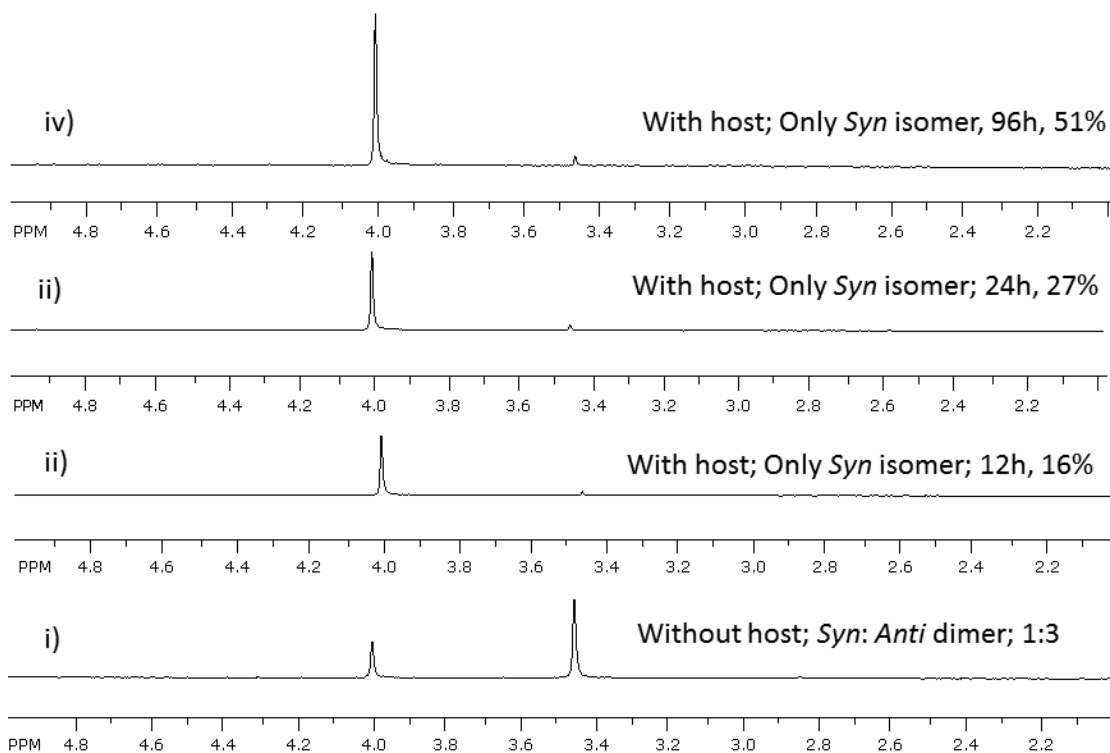
Figure 2.46. ^{1}H NMR analysis of the reaction of the solid host **1**•acenaphthylene complex under UV-irradiation for 12-96 h in an argon atmosphere.
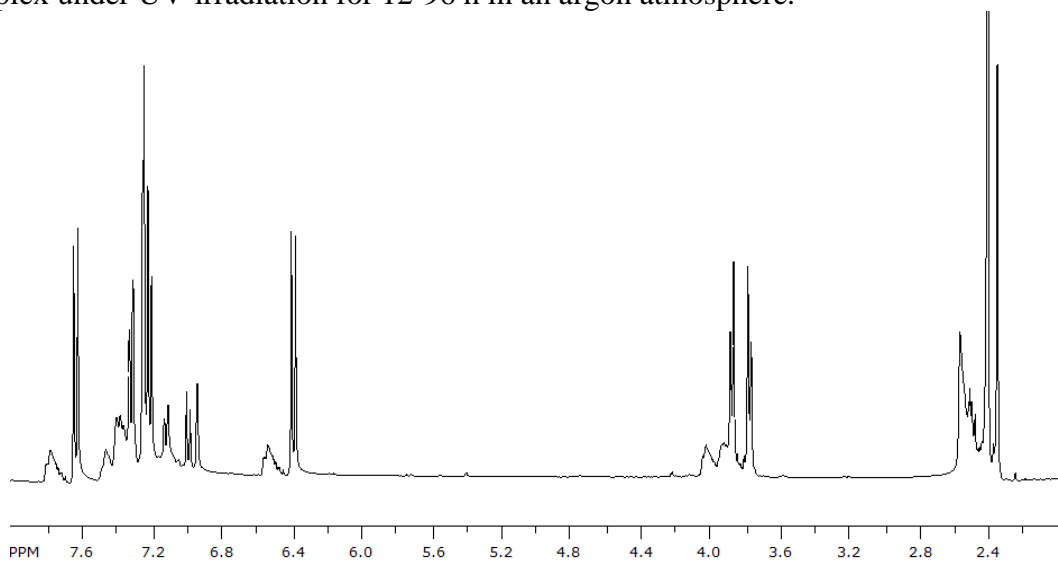
Figure 2.47. ^{1}H NMR spectra of *anti*-HH photodimer of 6-methyl coumarin (84%) and *syn*-HH (~16%) dimer of 6-methyl coumarin.

77
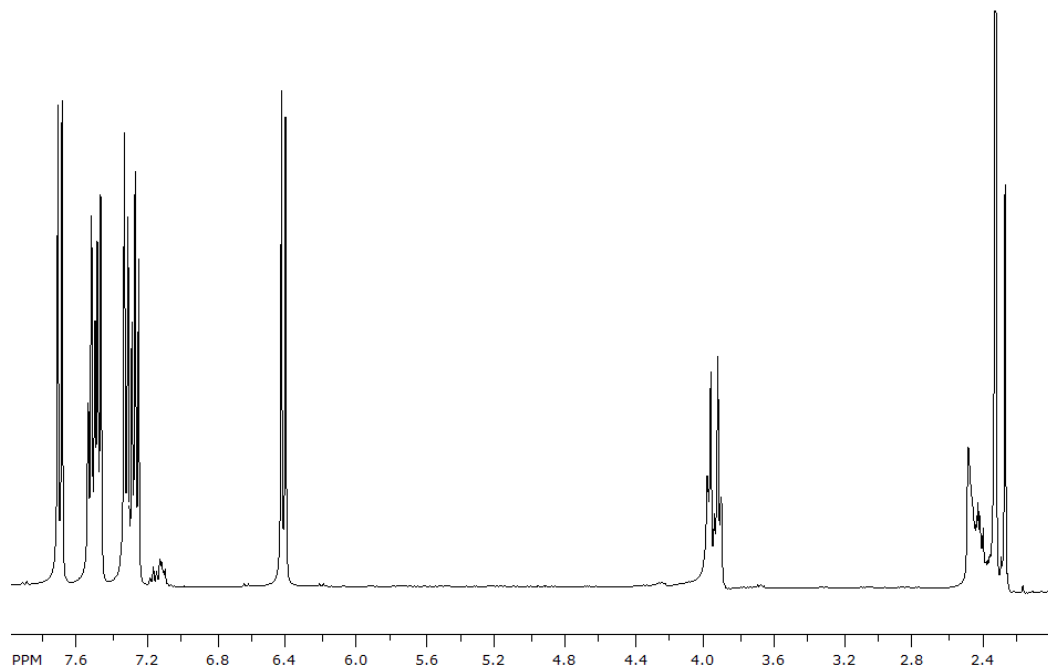
Figure 2.48. ^{1}H NMR spectra of *anti*-HH photodimer of 7-methyl coumarin.
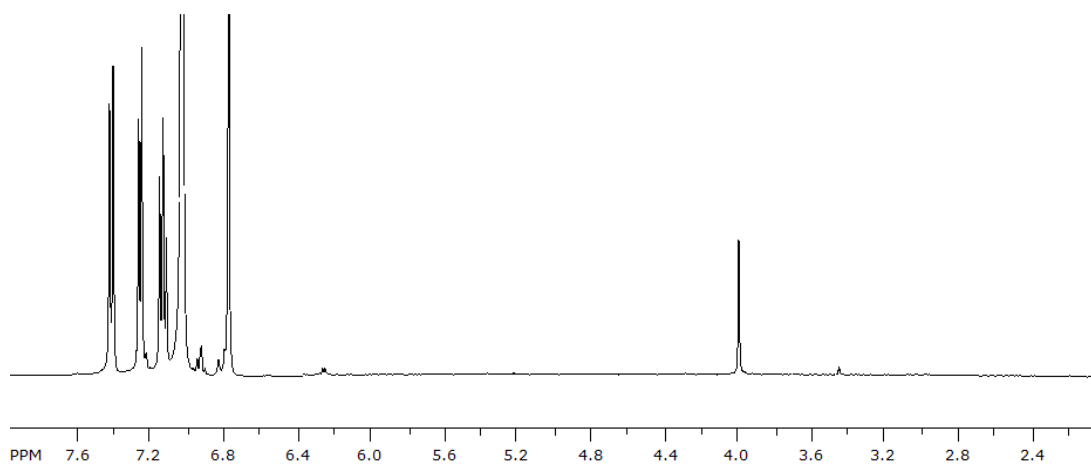
Figure 2.49. ^{1}H NMR spectra of *syn* photodimer of acenaphthylene.
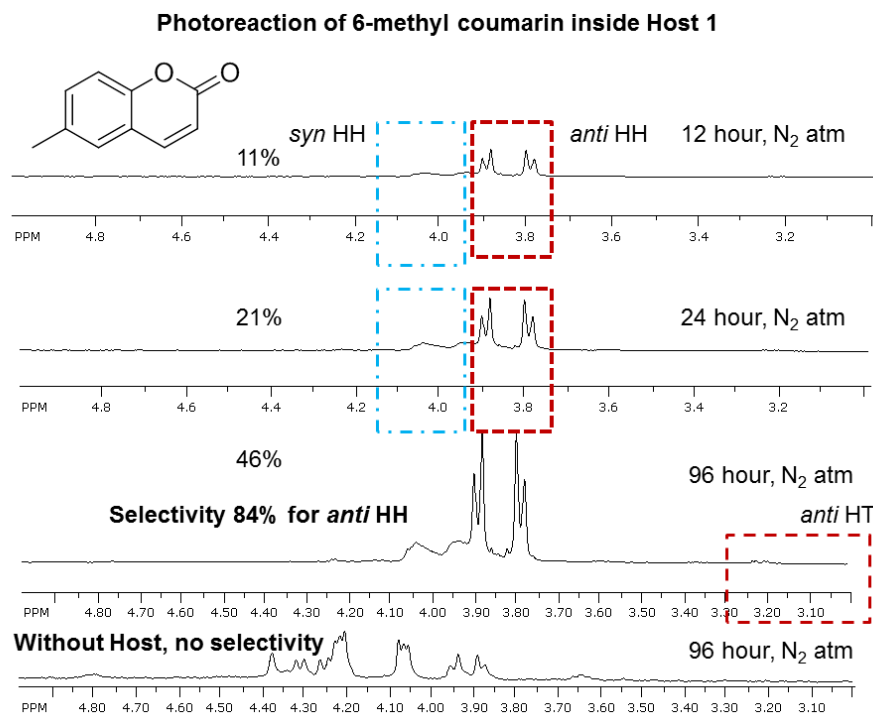
Figure 2.50. ^{1}H-NMR analysis of the product obtained from photoreaction of host **1**•6-methyl coumarin. The peaks correspond to the cyclobutyl region of the photodimers are shown.
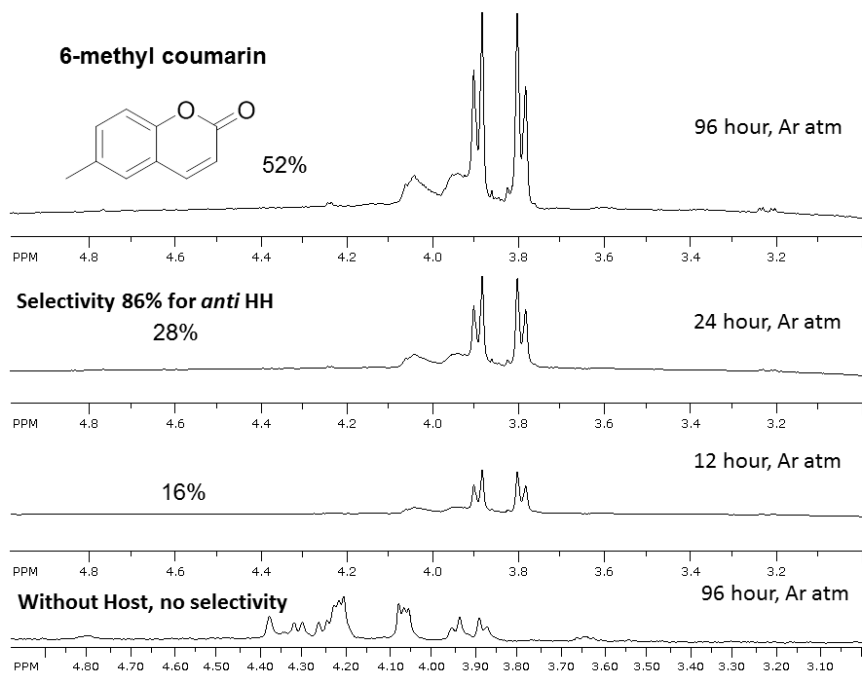
Figure 2.51. ^{1}H-NMR analysis of the product obtained from photoreaction of host **1**•6-methyl coumarin (Ar atmosphere). The peaks correspond to the cyclobutyl region of the photodimers are shown.
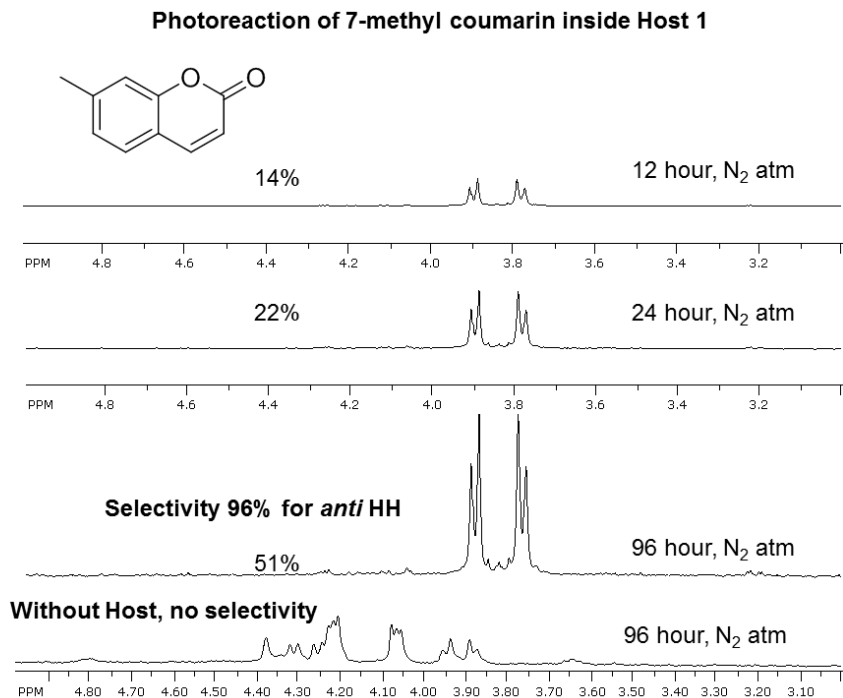
Figure 2.52. ¹H-NMR analysis of the product obtained from photoreaction of host **1**•7-methyl coumarin. The peaks correspond to the cyclobutyl region of the photodimers are shown.
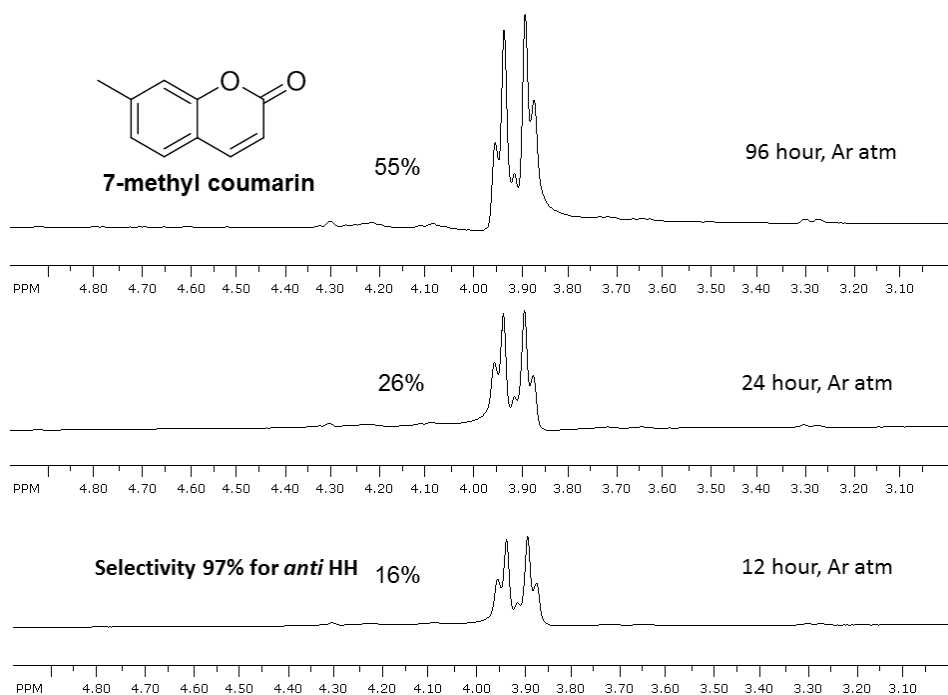
Figure 2.53. ¹H-NMR analysis of the product obtained from photoreaction of host **1**•7-methyl coumarin (Ar atmosphere). The peaks correspond to the cyclobutyl region of the photodimers are shown.

Table 2.8. Photoreaction of 7-methyl coumarin inside host.

Condition	Atmosphere	Time (h)	Product	% Conversion
Without Host	Ar or N_2	12-96 h	All four	>5
With Host	Ar	12	97% anti HH	16
With Host	Ar	24	98% anti HH	26
With Host	Ar	96	98% anti HH	55
With Host	N_2	12	97% anti HH	14
With Host	N_2	24	97% anti HH	22
With Host	N_2	96	97% anti HH	51
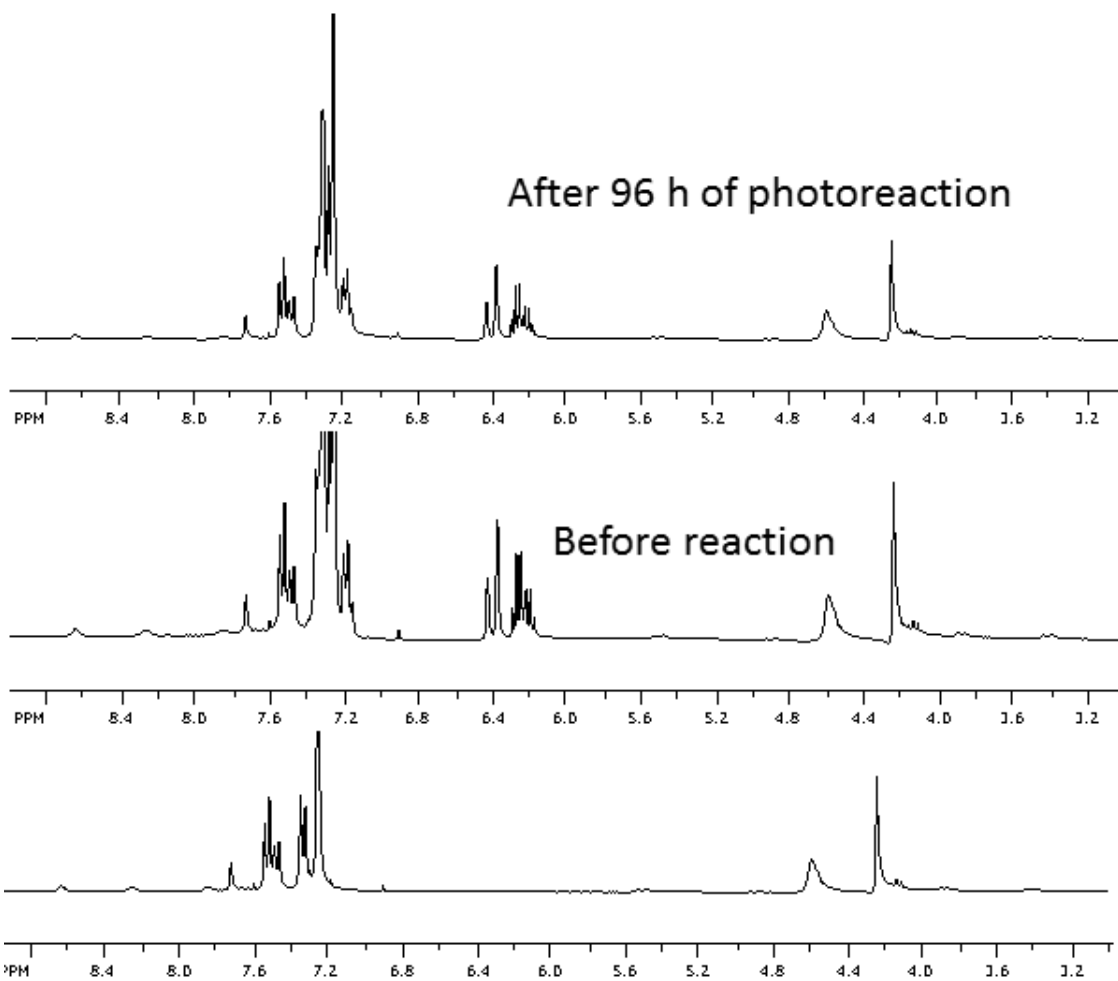
Figure 2.54. ^{1}H-NMR analysis of the product obtained from photoreaction of host **1**•β-methyl styrene.

2.6.6 Monte Carlo Simulation

Table 2.9. Moves and associated probability of Canonical Monte Carlo simulations for chemical potential calculations.

Move	Probability of move	Guest		
Configurational bias single box molecule reinsertion move	0.2	1.0		
Move	Probability of move	Guest	Guest	
Configurational bias partial molecule regrowth	0.4	1.0	1.0	
Move	Probability of move	Guest	Maximum displacement	Acceptance rate
Intramolecular single atom translation	0.6	1.0	0.5	0.5
Move	Probability of move	Guest	Maximum displacement	Acceptance rate
Center of mass molecule translation	0.8	1.0	0.5	0.5
Move	Probability of move	Guest	Maximum rotation	Acceptance rate
Rotation about the center of mass	1.0	1.0	0.05	0.5

Table 2.10. Moves and associated probability of Grand Canonical Monte Carlo simulations

Move	Probability of move	Host 1	Guest		
Configurational bias grand canonical insertion/deletion move	0.4	0	1.0		
Move	Probability of move	Host 1	Guest		
Configurational bias two box molecule transfer move	0.01	0	1.0		
Move	Probability of move	Host 1	Guest	Host 1	Guest
Configurational bias partial molecule regrowth	0.7	0	1.0	0.5	1.0
Move	Probability of move	Host 1	Guest	Maximum displacement	Acceptance rate
Intramolecular single atom translation	0.8	0.3	1.0	0.5	0.5
Move	Probability of move	Host 1	Guest	Maximum displacement	Acceptance rate
Center of mass molecule translation	0.9	0	1.0	0.5	0.5
Move	Probability of move	Host 1	Guest	Maximum rotation	Acceptance rate
Rotation about the center of mass	1.0	0	1.0	0.05	0.5

Figure 2.55. GCMC simulation outcome of host **1•** coumarin complex. a) Top view of the simulation cell along the y axis. b) Arrangement of coumarin pair in *anti*-HH orientation. c) Energy minimization profile during the simulation.
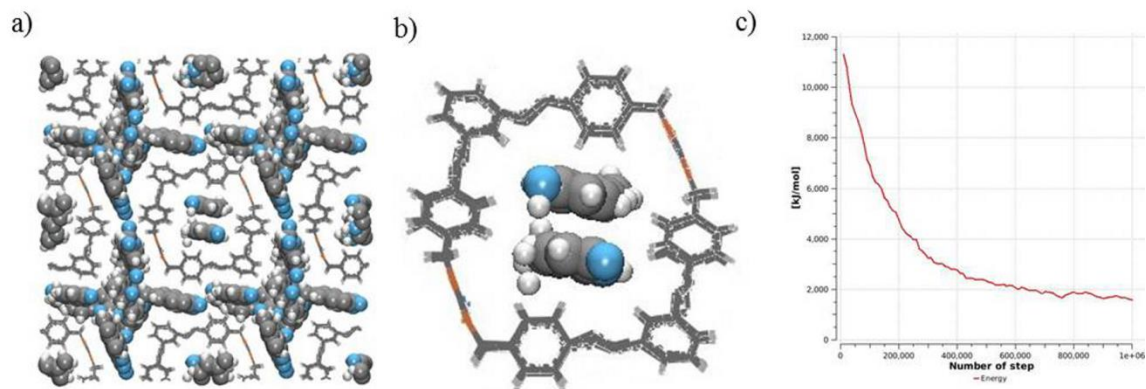
Figure 2.56. GCMC simulation outcome of host **1**• 6-methycoumarin complex. a) Top view of the simulation cell along the y axis. b) Arrangement of coumarin pair in *anti*-HH orientation. c) Energy minimization profile during the simulation.
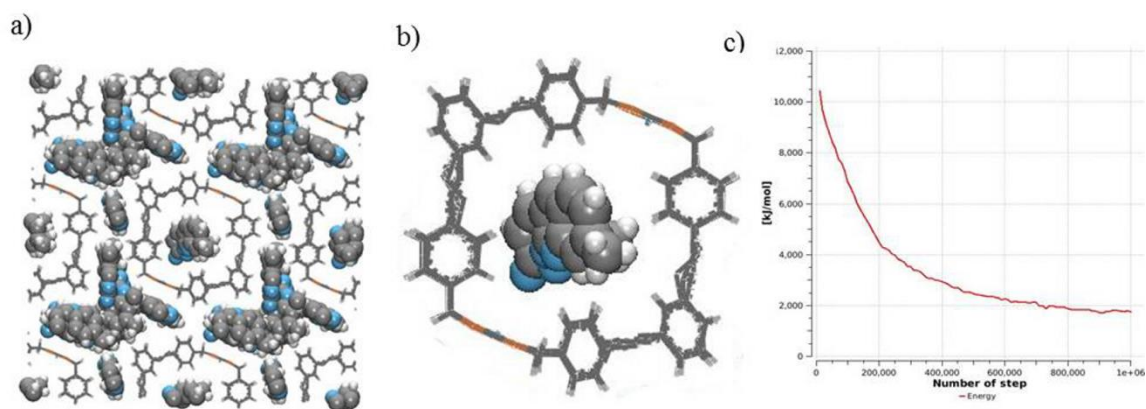
Figure 2.57. GCMC simulation outcome of host **1**• 7-methycoumarin complex. a) Top view of the simulation cell along the y axis. b) Arrangement of coumarin pair in *anti*-HH orientation. c) Energy minimization profile during the simulation.

85
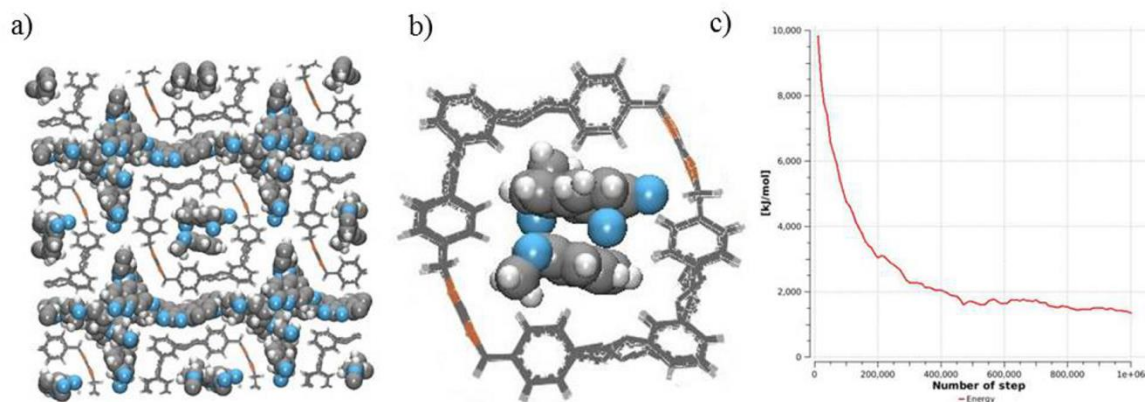
Figure 2.58. GCMC simulation outcome of host **1**• 7- methoxy coumarin complex. a) Top view of the simulation cell along the y axis. b) Arrangement of 7- methoxy coumarin complex inside the host **1** channel. c) Energy minimization profile during the simulation.
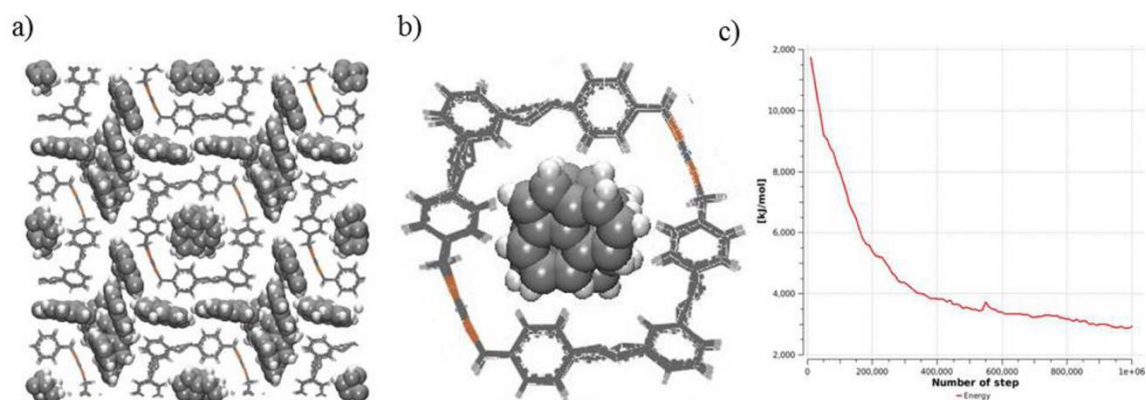
Figure 2.59. GCMC simulation outcome of host **1**• Acenaphthylene complex. a) Top view of the simulation cell along the y axis. b) Arrangement of acenaphthylene pair in *syn* orientation. c) Energy minimization profile during the simulation.

2.7 References

(1) Yoshizawa, M.; Klosterman, J. K.; Fujita, M. Functional Molecular Flasks: New Properties and Reactions within Discrete, Self-Assembled Hosts. *Angewandte Chemie International Edition* **2009**, *48*, 3418-3438.

(2) Breiner, B.; Clegg, J. K.; Nitschke, J. R. Reactivity modulation in container molecules. *Chemical Science* **2011**, *2*, 51-56.

(3) Vriezema, D. M.; Comellas Aragonès, M.; Elemans, J. A. A. W.; Cornelissen, J. J. L. M.; Rowan, A. E.; Nolte, R. J. M. Self-Assembled Nanoreactors. *Chemical Reviews* **2005**, *105*, 1445-1490.

(4) Pluth, M. D.; Bergman, R. G.; Raymond, K. N. Acid Catalysis in Basic Solution: A Supramolecular Host Promotes Orthoformate Hydrolysis. *Science* **2007**, *316*, 85-88.

(5) Fiedler, D.; Bergman, R. G.; Raymond, K. N. Supramolecular Catalysis of a Unimolecular Transformation: Aza-Cope Rearrangement within a Self-Assembled Host. *Angewandte Chemie* **2004**, *116*, 6916-6919.

(6) Murase, T.; Horiuchi, S.; Fujita, M. Naphthalene Diels−Alder in a Self-Assembled Molecular Flask. *Journal of the American Chemical Society* **2010**, *132*, 2866-2867.

(7) Yoshizawa, M.; Tamura, M.; Fujita, M. Diels-Alder in Aqueous Molecular Hosts: Unusual Regioselectivity and Efficient Catalysis. *Science* **2006**, *312*, 251-254.

(8) Yumura, T.; Takeuchi, M.; Kobayashi, H.; Kuroda, Y. Effects of ZSM-5 Zeolite Confinement on Reaction Intermediates during Dioxygen Activation by Enclosed Dicopper Cations. *Inorganic Chemistry* **2009**, *48*, 508-517.

(9) Frei, H. Selective Hydrocarbon Oxidation in Zeolites. *Science* **2006**, *313*, 309-310.

(10) Yoshizawa, M.; Takeyama, Y.; Kusukawa, T.; Fujita, M. Cavity-Directed, Highly Stereoselective [2+2] Photodimerization of Olefins within Self-Assembled Coordination Cages. *Angewandte Chemie International Edition* **2002**, *41*, 1347-1349.

(11) Yang, J.; Dewal, M. B.; Profeta, S.; Smith, M. D.; Li, Y.; Shimizu, L. S. Origins of Selectivity for the [2+2] Cycloaddition of α,β-unsaturated Ketones within a Porous Self-assembled Organic Framework. *Journal of the American Chemical Society* **2008**, *130*, 612-621.

(12) Raymond, K. N. Supramolecular chemistry: Phosphorus caged. *Nature* **2009**, *460*, 585-586.

(13) Caspar, J. V.; Ramamurthy, V.; Corbin, D. R. Modification of photochemical reactivity by zeolites. Preparation and spectroscopic characterization of polarons and bipolarons of thiophene oligomers within the channels of pentasil zeolites: the evolution of organic radical ions into conducting polymers. *Journal of the American Chemical Society* **1991**, *113*, 600-610.

(14) Iwasawa, T.; Hooley, R. J.; Rebek, J. Stabilization of Labile Carbonyl Addition Intermediates by a Synthetic Receptor. *Science* **2007**, *317*, 493-496.

(15) Jayathirtha Rao, V.; Prevost, N.; Ramamurthy, V.; Jayathirtha Rao, V.; Kojima, M.; J. Johnston, L. Generation of stable and persistent carbocations from 4-vinylanisole within zeolites. *Chemical Communications* **1997**, 2209-2210.

(16) Ziegler, M.; Brumaghim, J. L.; Raymond, K. N. Stabilization of a Reactive Cationic Species by Supramolecular Encapsulation. *Angewandte Chemie International Edition* **2000**, *39*, 4119-4121.

(17) Lambert, J. B. A Tamed Reactive Intermediate. *Science* **2008**, *322*, 1333-1334.

(18) Koblenz, T. S.; Wassenaar, J.; Reek, J. N. H. Reactivity within a confined self-assembled nanospace. *Chemical Society Reviews* **2008**, *37*, 247-262.

(19) Dawn, S.; Dewal, M. B.; Sobransingh, D.; Paderes, M. C.; Wibowo, A. C.; Smith, M. D.; Krause, J. A.; Pellechia, P. J.; Shimizu, L. S. Self-Assembled Phenylethynylene Bis-urea Macrocycles Facilitate the Selective Photodimerization of Coumarin. *Journal of the American Chemical Society* **2011**, *133*, 7025-7032.

(20) Ramamurthy, V.; Parthasarathy, A. Chemistry in Restricted Spaces: Select Photodimerizations in Cages, Cavities, and Capsules. *Israel Journal of Chemistry* **2011**, *51*, 817-829.

(21) Cohen, M. D. The Photochemistry of Organic Solids. *Angewandte Chemie International Edition in English* **1975**, *14*, 386-393.

(22) Weiss, R. G.; Ramamurthy, V.; Hammond, G. S. Photochemistry in organized and confining media: a model. *Accounts of Chemical Research* **1993**, *26*, 530-536.

(23) Ginsberg, D. S., G. M. J. Solid State Photochemistry; Verlag Chemie, New York, 1976.

(24) Qiu, Y.; Kaifer, A. E. Reactivity of Redox-Active Guests Trapped Inside Molecular Capsules. *Israel Journal of Chemistry* **2011**, *51*, 830-839.

(25) Purse, B. W.; Rebek, J. Functional cavitands: Chemical reactivity in structured environments. *Proceedings of the National Academy of Sciences of the United States of America* **2005**, *102*, 10777-10782.

(26) Kim, K.; Selvapalam, N.; Ko, Y. H.; Park, K. M.; Kim, D.; Kim, J. Functionalized cucurbiturils and their applications. *Chemical Society Reviews* **2007**, *36*, 267-279.

(27) Ajami, D.; Rebek, J. More Chemistry in Small Spaces. *Accounts of Chemical Research* **2013**, *46*, 990-999.

(28) Gibb, C. L. D.; Gibb, B. C. Well-Defined, Organic Nanoenvironments in Water: The Hydrophobic Effect Drives a Capsular Assembly. *Journal of the American Chemical Society* **2004**, *126*, 11408-11409.

(29) Zhang, Y.; Riduan, S. N. Functional porous organic polymers for heterogeneous catalysis. *Chemical Society Reviews* **2012**, *41*, 2083-2094.

(30) Organic Solid State Reactions, T. i. C. C. T., F., Ed.; Springer-Verlag: Berlin, 2005; Vol. 254.

(31) MacGillivray, L. R.; Papaefstathiou, G. S.; Friščić, T.; Hamilton, T. D.; Bučar, D.-K.; Chu, Q.; Varshney, D. B.; Georgiev, I. G. Supramolecular Control of Reactivity in the Solid State: From Templates to Ladderanes to Metal−Organic Frameworks. *Accounts of Chemical Research* **2008**, *41*, 280-291.

(32) Materials and Processes Simulations (MAPS), C. S. S., Paris, France, 2004–2013.

(33) Arai, T.; Sakuragi, H.; Tokumaru, K. Photosensitized <I>cis</I>-<I>trans</I> Isomerization of β-Alkylstyrenes. *Bulletin of the Chemical Society of Japan* **1982**, *55*, 2204-2207.

(34) Kamlet, M. J.; Abboud, J. L.; Taft, R. W. The solvatochromic comparison method. 6. The .pi.* scale of solvent polarities. *Journal of the American Chemical Society* **1977**, *99*, 6027-6038.

(35) Pandey, N.; Gahlaut, R.; Arora, P.; Joshi, N. K.; Joshi, H. C.; Pant, S. Study of dipole moments of some coumarin derivatives. *Journal of Molecular Structure* **2014**, *1061*, 175-180.

(36) Everard, K. B.; Kumar, L.; Sutton, L. E. 622. Polarisation in conjugated systems. Part I. The refractions and electric dipole moments of some derivatives of benzene, styrene, diphenyl, stilbene, and 1 : 4-diphenylbutadiene. *Journal of the Chemical Society (Resumed)* **1951**, 2807-2815.

(37) Krauch, C. H.; Farid, S.; Schenck, G. O. Photo-C4-Cyclodimerisation von Cumarin. *Chemische Berichte* **1966**, *99*, 625-633.

(38) Hoffman, R.; Wells, P.; Morrison, H. Organic photochemistry. XII. Further studies on the mechanism of coumarin photodimerization, observation of an unusual "heavy atom" effect. *The Journal of Organic Chemistry* **1971**, *36*, 102-108.

(39) Tanaka, K.; Toda, F. Solvent-Free Organic Synthesis. *Chemical Reviews* **2000**, *100*, 1025-1074.

(40) Pemberton, B. C.; Barooah, N.; Srivatsava, D. K.; Sivaguru, J. Supramolecular photocatalysis by confinement-photodimerization of coumarins within cucurbit[8]urils. *Chemical Communications* **2010**, *46*, 225-227.

(41) Pemberton, B. C.; Singh, R. K.; Johnson, A. C.; Jockusch, S.; Da Silva, J. P.; Ugrinov, A.; Turro, N. J.; Srivastava, D. K.; Sivaguru, J. Supramolecular photocatalysis: insights into cucurbit[8]uril catalyzed photodimerization of 6-methylcoumarin. *Chemical Communications* **2011**, *47*, 6323-6325.

(42) Barooah, N.; Pemberton, B. C.; Johnson, A. C.; Sivaguru, J. Photodimerization and complexation dynamics of coumarins in the presence of cucurbit[8]urils. *Photochemical & Photobiological Sciences* **2008**, *7*, 1473-1479.

(43) Moorthy, J. N.; Venkatesan, K.; Weiss, R. G. Photodimerization of coumarins in solid cyclodextrin inclusion complexes. *The Journal of Organic Chemistry* **1992**, *57*, 3292-3297.

(44) Yu, X.; Scheller, D.; Rademacher, O.; Wolff, T. Selectivity in the Photodimerization of 6-Alkylcoumarins. *The Journal of Organic Chemistry* **2003**, *68*, 7386-7399.

(45) Muthuramu, K.; Murthy, V. R. Photodimerization of coumarin in aqueous and micellar media. *The Journal of Organic Chemistry* **1982**, *47*, 3976-3979.

(46) Tanaka, K.; Fujiwara, T. Enantioselective [2 + 2]Photodimerization Reactions of Coumarins in Solution. *Organic Letters* **2005**, *7*, 1501-1503.

(47) Wolff, T.; Gorner, H. Photodimerization of coumarin revisited: Effects of solvent polarity on the triplet reactivity and product pattern. *Physical Chemistry Chemical Physics* **2004**, *6*, 368-376.

(48) Karthikeyan, S.; Ramamurthy, V. Templating Photodimerization of Coumarins within a Water-Soluble Nano Reaction Vessel. *The Journal of Organic Chemistry* **2006**, *71*, 6409-6413.

(49) Turro, N. J., Cycloaddition reactions; Modern Molecular Photochemistry, University Science books: Sausalito, CA, 1991; 462– 464.

(50) Cowan, D. O.; Drisko, R. L. E. Photochemical reactions. IV. Photodimerization of acenaphthylene. Mechanistic studies. *Journal of the American Chemical Society* **1970**, *92*, 6286-6291.

(51) Nerbonne, J. M.; Weiss, R. G. Liquid crystalline solvents as mechanistic probes. 3. The influence of ordered media on the efficiency of the photodimerization of acenaphthylene. *Journal of the American Chemical Society* **1979**, *101*, 402-407.

(52) Kaanumalle, L. S.; Ramamurthy, V. Photodimerization of acenaphthylene within a nanocapsule: excited state lifetime dependent dimer selectivity. *Chemical Communications* **2007**, 1062-1064.

(53) Rao, K. S. S. P.; Hubig, S. M.; Moorthy, J. N.; Kochi, J. K. Stereoselective Photodimerization of (E)-Stilbenes in Crystalline γ-Cyclodextrin Inclusion Complexes. *The Journal of Organic Chemistry* **1999**, *64*, 8098-8104.

(54) Ohara, K.; Inokuma, Y.; Fujita, M. The Catalytic Z to E Isomerization of Stilbenes in a Photosensitizing Porous Coordination Network. *Angewandte Chemie International Edition* **2010**, *49*, 5507-5509.

(55) Parthasarathy, A.; Ramamurthy, V. Role of free space and weak interactions on geometric isomerization of stilbenes held in a molecular container. *Photochemical & Photobiological Sciences* **2011**, *10*, 1455-1462.

(56) Dube, H.; Ams, M. R.; Rebek, J. Supramolecular Control of Fluorescence through Reversible Encapsulation. *Journal of the American Chemical Society* **2010**, *132*, 9984-9985.

(57) Choi, S.; Park, S. H.; Ziganshina, A. Y.; Ko, Y. H.; Lee, J. W.; Kim, K. A stable cis-stilbene derivative encapsulated in cucurbit[7]uril. *Chemical Communications* **2003**, 2176-2177.

(58) Duveneck, G. L.; Sitzmann, E. V.; Eisenthal, K. B.; Turro, N. J. Picosecond laser studies on photochemical reactions in restricted environments: the photoisomerization of trans-stilbene complexed to cyclodextrins. *The Journal of Physical Chemistry* **1989**, *93*, 7166-7170.

(59) Whitten, D. G. Photochemistry and photophysics of trans-stilbene and related alkenes in surfactant assemblies. *Accounts of Chemical Research* **1993**, *26*, 502-509.

(60) Madhavan, D.; Pitchumani, K. Photodimerisation of acenaphthylene in a clay microenvironment. *Photochemical & Photobiological Sciences* **2003**, *2*, 95-97.

(61) Dewal, M. B.; Xu, Y.; Yang, J.; Mohammed, F.; Smith, M. D.; Shimizu, L. S. Manipulating the cavity of a porous material changes the photoreactivity of included guests. *Chemical Communications* **2008**, 3909-3911.

(62) Spartan 04 for Macintosh, V. W., Inc.: Irvine, CA, 2007.

(63) Roy, K.; Wang, C.; Smith, M. D.; Dewal, M. B.; Wibowo, A. C.; Brown, J. C.; Ma, S.; Shimizu, L. S. Guest induced transformations of assembled pyridyl bis-urea macrocycles. *Chemical Communications* **2011**, *47*, 277-279.

(64) Murthy, G. S.; Arjunan, P.; Venkatesan, K.; Ramamurthy, V. Consequences of lattice relaxability in solid state photodimerizations. *Tetrahedron* **1987**, *43*, 1225-1240.

(65) Bhadbhade, M. M.; Murthy, G. S.; Venkatesan, K.; Ramamurthy, V. Topochemical dimerization of non-parallel double bonds: 7-methoxycoumarin. *Chemical Physics Letters* **1984**, *109*, 259-263.

(68) Bowers, C. R.; Dvoyashkin, M.; Salpage, S. R.; Akel, C.; Bhase, H.; Geer, M. F.; Shimizu, L. S. Crystalline Bis-urea Nanochannel Architectures Tailored for Single-File Diffusion Studies. *ACS Nano* **2015**, *9*, 6343-6353.

(69) Bowers, C. R.; Dvoyashkin, M.; Salpage, S. R.; Akel, C.; Bhase, H.; Geer, M. F.; Shimizu, L. S. Squeezing xenon into phenylether bis-urea nanochannels. *Canadian Journal of Chemistry* **2015**, *93*, 1031-1034.

(66) Martin, M. G. MCCCS Towhee: a tool for Monte Carlo molecular simulation. *Molecular Simulation* **2013**, *39*, 1212-1222.

(67) Mayo, S. L.; Olafson, B. D.; Goddard, W. A. DREIDING: a generic force field for molecular simulations. *The Journal of Physical Chemistry* **1990**, *94*, 8897-8909.

(70) Ehrlice, W. W. A refinement of the crystal and molecular structure of acenaphthene *Acta Crystallogrn.* 1957, 10, 699-705.

(71) Harada, J.; Ogawa, K. Invisible but common motion in organic crystals: a pedal motion in stilbenes and azobenzenes. *J. Am. Chem. Soc.* 2001, 123, 10884-10888.

(72) Gnanaguru, K.; Ramasubbu, N.; Venkatesan, K.; Ramamurthy, V. A study on the photochemical dimerization of coumarins in the solid state. *J. Org. Chem.* 1985, 50, 2337-2346.

CHAPTER III

MODULATING THE REACTIVITY OF CHROMONE AND ITS DERIVATIVES
THROUGH ENCAPSULATION IN A SELF-ASSEMBLED PHENYLETHYNYLENE
BIS-UREA HOST*

3.1 Abstract

This chapter reports on the modulation of the photoreactivity of a series of chromones, also known as benzo-γ-pyrones, by absorption into a porous self-assembled host formed from phenylethynylene *bis*-urea macrocycles. Chromone and four derivatives namely 6-fluorochromone, 6-bromochromone, 7-hydroxy-4-chromone, and 3-cyanochromone are unreactive in the solid-state. Each of these derivatives was loaded into the nanochannels of self-assembled phenylethynylene *bis*-urea macrocycles to form solid host•guest complexes, which were subsequently UV-irradiated at room temperature under argon atmosphere. We observed that chromone and 6-fluorochromone underwent selective [2+2] photodimerization reactions to produce *anti*-HT dimers in high selectivity and conversion. The 6-bromochromone also reacted in high selectivity and conversion to afford an aryl coupling adduct. In comparison, 7-hydroxy-4-chromone, and 3-cyanochromone were unreactive within the complex. Simple GCMC simulation studies suggest that chromone, 6-fluorochromone, and 6-bromochromone were loaded in orientations that facilitate photoreaction, and correctly predicted that the *anti*-HT dimer would be favored in the chromone case. In contrast, *syn*-HH dimers were predicted by GCMC simulations for the halogen containing derivatives but were not observed. The simulations with 7-hydroxy-4-chromone were in agreement with the observed reactivity. We compare these computational and experimental findings and suggest future methods for optimizing simulation parameters. Our goal is to expand the scope and accuracy our simulations to be able to predict the reactivity of guests encapsulated within columnar nanotubes.

97

3.2 Introduction

Inspired by Nature's exquisite control over reactivity within the defined spaces of enzyme active sites, chemists have designed and investigated many molecular and supramolecular hosts as well as examined the use of porous materials to facilitate the reaction of encapsulated guests.[1-7] These 'nanoreactors' provide confined environments to induce selectivity, modulate the reaction pathway, and potentially catalyze the reaction.[8] Our group studies how the photolysis of small organic molecules is altered and influenced by the encapsulation within the cylindrical channels of stable, porous, crystalline hosts.[9] These hosts are formed through the supramolecular assembly of *bis*-urea macrocycles, such as the phenylethynylene *bis*-urea **1**, which self-assembles into columns that contain guest accessible channels of ∼0.9 nm diameter (Figure 3.1). Here, we investigate the application of this host to uptake chromone and its derivatives and study the effects of this encapsulation on the subsequent photoreactions versus the reactions of these derivatives in their solid-state form. Specifically, this manuscript applies systematic experimental and computational methods to evaluate: 1) the reactivity of chromone and four of its derivatives in the solid-state; 2) the use of GCMC simulations to investigate the organization of guests within the confined channel of a self-assembled phenylethynylene *bis*-urea host and to analyze if neighboring guests are aligned for facile photoreaction; and to evaluate experimentally 3) the uptake of chromones and their subsequent reactivity upon UV-irradiation.

Chromone (4H-1-benzopyran-4-one) belongs to the flavonoid family. Flavonoids play a vital role in plants as secondary metabolites.[10] Chromone serves as a key scaffold in synthetic organic chemistry,[11] medicinal chemistry,[12] and drug discovery.[13] In solution,

98

simple chromones may undergo photodimerizations and photoaddition reactions[14] with olefins and acetylenes. For example, benzene solution UV-irradiation of chromone produced *anti*-HT and *trans-fused* HT dimers in ~1:1 ratio and 99% yield.[15] The dimerization efficiency greatly depended upon the concentration of chromone.[16] Indeed, UV-irradiation of chromone-2-carboxylic esters (methyl, ethyl, or *iso*-propyl) in acetonitrile solutions produced *anti*-HH dimers from the triplet excited state while solid state reactions of methyl and *iso*-propyl chromone-2-carboxylic ester yielded the *anti*-HT dimers, and no solid state reaction was observed in ethyl derivative or for the parent chromone. Cohen et al. reported the photoreactions of chromone with tetramethylethylene, 1-dimethoxyethylene, cyclopentene, and 2-butyne to obtain a variety of cycloadducts.[17,18] Venkateswaran et al. employed the photocycloaddition reaction of 2, 3, 7-trimethylchromone with ethylene as a key reaction in the synthesis of two marine natural products.[19] Studies from Kutateladze et al. showed that the Diels−Alder adducts of chromones could undergo an intramolecular [2л+ 2л] alkene–arene photocyclization reaction.[20]
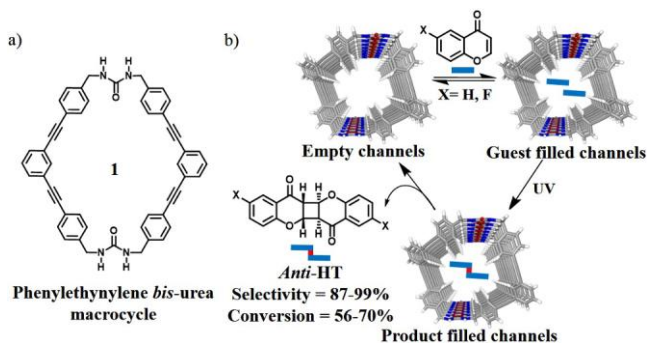
Figure 3.1. Self-assembled phenylethynylene *bis*-urea macrocycles used as a confinement for conducting selective photodimerization of chromones. (a) Structure of the phenylethynylene *bis*-urea macrocycle.[21] (b) Loading of chromone and 6-fluorochromone affords host **1**•guest complexes that facilitated the selective formation of the respective *anti*-HT photodimers upon UV-irradiation.

Herein, we examine the utility of host **1** to bind, organize and facilitate the photoreactions of a series of simple chromones in the solid-state. Host **1** is formed by the columnar self-assembly of a phenylethynylene *bis*-urea macrocycle (Figure 3.1a).[21] This assembly process is driven by the urea hydrogen-bonding motif as the compound crystallized from DMSO. Heating drives off the DMSO solvent leaving open columnar channels, which are accessible to new guests. Our study into the utility of this host proceeded through both experimental investigation of what guests can be loaded into this confined channel as well as through GCMC simulations to predict not only guest absorption but also subsequent effects of this confinement on guest reactivity. The GCMC simulations were carried out using Monte Carlo for Complex Chemical Systems (MCCCS) Towhee[22] plug-in built into Scienomics' Materials Processes and Simulations (MAPS) platform[23] and suggested that the chromone, 6-fluorochromone, 6-bromochromone, and 7-hydroxy-4-chromone would load into the channels of host **1**; however, simulations predict that only the first three compounds would be favorably positioned for photoreactions. Simulations were not carried out on 3-cyanochromone due to incompatibility of the configurational bias settings with the cyano functional group and consistency of the bias settings with previous simulations.

The simulations suggest that the orientation of chromone inside the channel should favor formation of *anti*-HH photodimers. In comparison, the *syn*-HH dimers were predicted for 6-fluorochromone, and 6-bromochromone. Experimentally, we confirmed that the crystalline chromones were stable to prolonged UV-irradiation. Host **1** absorbed each of these guests from solution to form solid-state host•guest complexes with the host:guest binding ratios dependent on the size and polarity of the guests (Figure 3.1b).

100

We tested if the solid-state photochemistry of chromones was modulated by incarceration within the crystalline host.   Upon UV-irradiation of the respective host **1**•guest complexes, both chromone and 6-fluorochromone underwent [2+2] photodimerization reactions within the host in high conversion and selectivity. We observed 55% of chromone and 70% of 6-fluorochromone converted into photodimers. The *anti*-HT dimers were afforded as the major products in these host•guest complexes with 87% selectivity for chromone and >99% for 6-fluorochromone.

The 6-bromochromone also reacted within the host complex forming a coupling adduct in high selectivity (>99%) and 70 % conversion. In this case, no [2+2] photocycloaddition was observed. In comparison, 7-hydroxy-4-chromone, and 3-cyanochromone proved to be unreactive within the host•guest complexes. The GCMC simulations predicted the reactivity of chromone, 6-fluorochromone, 6-bromochromone, and 7-hydroxy-4-chromone when encapsulated within the host. However, calculations predicted the observed product selectivity only in the case of chromone, which contains no additional polar functional groups. Our future goals are to synergistically evaluate the reactivity of encapsulated guets while concurrently optimizing GCMC simulations.

We are currently addressing the computational simulations by evaluating new force fields, probing the effects of configurational bias settings, and testing variety of MC moves as well as probabilities.

3.3 Results and discussion

Macrocycle **1** self-assembled from DMSO to afford crystals with columnar channels. Initially, these channels are filled with disordered solvent but heating (120 °C)

101

removes the DMSO to afford accessible channels, which can be filled with new guests (Fig. 3.3a). Previous work demonstrated that the ~0.9 nm diameter nanochannels of the self-assembled phenylethynylene *bis*-urea host are accessible to gases including Xe and CO_2.[24,25] The channels can also accommodate a range of organic guests including coumarins, acenaphthylene and stilbenes.[21,24] Confinement of guests within the nanochannels of host **1** facilitated the selective [2+2] photodimerization reactions of coumarin, 6-methyl coumarin, 7-methyl coumarin and acenaphthylene in good conversion. In comparison, stilbenes and 7-methoxy coumarin were unreactive. We turned to GCMC simulations to probe the origin of these changes in reactivity and selectivity, which afforded good predictions for these simple aromatic guests.[24]

Here, we test utility and scope of the previously employed GCMC simulation protocol to predict if chromone and its derivatives (1) will be absorbed by this host and (2) will be reactive inside the confined space of the host. These chromones provide a challenging test of our methodology because they are relatively less reactive than the simple coumarins.

They also present a range of polar substituents (hydroxyl, fluoro, bromo, or cyano), which introduce additional intermolecular interactions between neighboring guests as well as between the guests and the channel walls. Thus, these chromones serve as challenging targets to assess the scope and utility of the computational simulations.

102
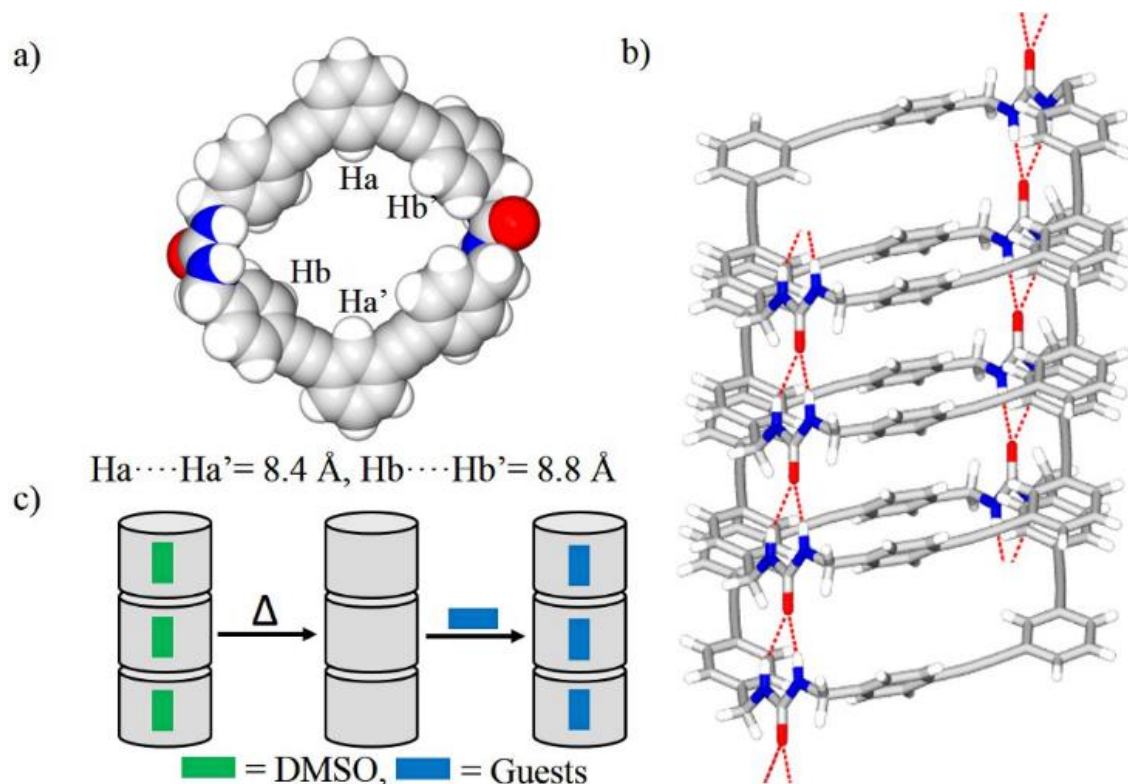
Figure 3.2. Host **1** structure and schematic of guest exchange. (a) Space filling model of host from X-ray structure of host **1**•nitrobenzene emphasizes its almost round channel with the dimensions Ha...Ha' = 8.4 Å and Hb…Hb' = 8.8 Å. (b) View down a single column organized through the urea hydrogen bonding motif. (c) Schematic representation of crystals used for this study, which are readily obtained by recrystallization from DMSO. The solvent was removed by heating to obtain porous nanochannels that can be loaded with new guests.

As our goal is to compare the effects of encapsulation on the solid-state reactivity of the chromone guests, we first set out to analyze the structures of chromone and its derivatives in the solid state and investigate their reactivity. Pioneering work from Schmidt and co-workers on crystalline cinnamic acid derivatives elucidated the effects of molecular packing and orientation of the reactants in the crystalline lattice and led to the 'topochemical postulates'.[26-28] These postulates enable prediction of the product conformation by analysis of the crystalline structures of the reactants. Photocycloadditions are generally favorable when the double bonds of the reacting

monomers are within 4.2 Å and aligned in parallel.[29] Although relatively simple in structure, only 6-bromochromone had previously been reported in the Cambridge Crystallographic Database.[30] Thus, we sought to grow single crystals of these compounds suitable for X-ray diffraction studies. Crystals of chromone were obtained from a mixture of chloroform/hexanes[15,31] while crystals of 6-fluorochromone,[31] 7-hydroxy-4-chromone and 3-cyanochromone were obtained by the cooling of hot acetonitrile solutions (25 mg/mL). Two new structures are reported here. Pale red plates of 7-hydroxy-4-chromone crystallized in monoclinic space group *P2₁/c*. Colorless parallelogram-shaped plate crystals of 3-cyanochromone crystallized triclinic space group *P-1*.
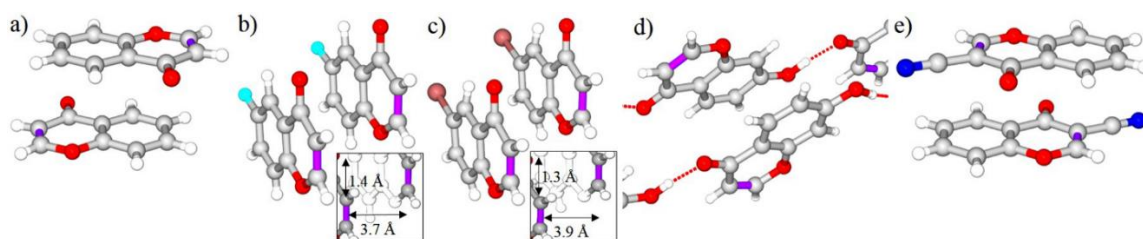
Figure 3.3. Analysis of chromone solid-state structures highlights the closest contact between potentially reactive alkenes (purple bonds). (a) Pairing of chromones via aryl stacking interactions.[31] (b) View of close pairs of 6-fluorochromone (Inset shows distance between reactive olefins).[31] (c) Relative positioning of 6-bromochromone (Inset shows distance between reactive olefins). (d) Hydrogen bonded chains of 7-hydroxy-4-chromone. (e) Relative positioning of 3-cyanochromone.

Figure 3.2 shows the arrangement of the reactive alkenes in chromone and in each of the four derivatives. Comparison of these structures shows that they exhibit markedly different relative orientations and distances between the potentially reactive alkenes. In the structure of chromone itself, the neighboring chromone molecules are paired through face-to-face aryl stacking interactions (3.63 Å ring centroid to centroid) with the electron rich portion of one chromone situated over the electron poor portion of its neighbor,

which minimizes dipole interactions (Figure 3.2a). This places the reactive olefins far apart from each other (closest C---C distance = 6.7 Å) disfavoring subsequent [2+2] cycloaddition in the solid state.

Similar pairing is observed for 3-cyanochromone (Fig. 3.2e), which are stabilized by aryl stacking interactions (ring centroid-centroid distance = 3.5 Å) and by CH---N and CH---O hydrogen bonding. Here, the electron withdrawing cyano group is positioned under the electron rich aryl group of the neighboring molecule. This positions the reactive alkenes on opposite sides, disfavoring subsequent reaction (closest C---C distance = 6.6 Å).

In the 7-hydroxy-4-chromone structure, strong OH---O hydrogen bonding dominates the crystal packing. Individual molecules are organized into one-dimensional chains through hydrogen bonds between the hydroxyl group on one molecule and the carbonyl oxygen of the neighboring molecule (Figure 3.2d, O---O = 2.6 Å, <OHO = 168.5°). The chains stack into layers with offset aryl stacking interactions (3.3 Å) stabilizing the layers. (Fig. 3.2d and Figure 3.12). The reactive alkenes are preorganized far apart (closest C---C distance = 5.4 Å) again disfavoring photoreaction. In summary, analysis of the crystal structures led to the hypothesis that chromone, 7-hydroxy-4-chromone and 3-cyanochromone are poor substrates for solid-state photolysis reactions.

The halogen derivatives show a different orientation for their aryl stacking interactions, which appears to be strongly influenced by the presence of the halides. The neighboring 6-fluorochromones interact through off-set aryl stacking interactions with a ring centroid-centroid distance of 3.7 Å (Figure 3.2b). However, the enone sides of

neighboring chromones are aligned on the same side and their halides are oriented in similar directions. The potentially reactive alkenes are close (bond centroid-centroid distance = 3.7 Å) and slightly offset by 1.6 Å. Similar molecular arrangement was observed in 6-bromochromone with offset л- stacking interactions (3.9 Å) placing the reactive olefins close in space 3.9 Å and offset by 1.3 Å (Figure 3.2c). Potentially, a favorable [2+2] photoreaction would favor *syn*-HH dimers.

Survey of the solid-state structures predicted that only 6-fluorochromone and 6-bromochromone are aligned for potentially [2+2] photodimerization reaction. Thus, we next tested the reactivity of the crystalline chromones. Samples of the each of the five recrystallized solids (10 mg) were UV-irradiated under argon for 96 h. Then the solids were dissolved and analyzed by ^{1}H NMR. Only resonances corresponding to the starting materials were observed (Figure 3.13), demonstrating that the photoreactions of these chromones are indeed unfavorable in the reported crystal forms.

Next, we sought to computationally predict if host **1** could be used to modulate the reactivity of these molecules. Figure 3.3 illustrates the columnar structure of the assembled phenylethynylene *bis*-urea macrocycle, which is organized through the urea hydrogen bonding motif with (N)H…O hydrogen bond distances ranging from 2.06 to 2.20 Å.[21] The interior cross-section of the channel is almost round with dimensions of ~8.4 Å x ~8.8 Å. In addition to the bifurcated urea-urea hydrogen bonding, the columnar structure is further stabilized by edge to face aryl stacking and alkyne-л interactions.

These crystal structure parameters were imported into the MAPS program and the coordinates for the nitrobenzene guests were removed. The chemical potentials (μ) of the

guests were calculated as previously described.[24] Next, 1 x 10^6 step Grand Canonical (μVT) Monte Carlo simulations were conducted for each guest using the Dreiding force field with pre-determined guest chemical potentials (μ). We then analyzed the significant configurations of these GCMC simulations to investigate the fit of chromones within the nanochannels and to analyze if their relative orientation with respect to neighboring guests would be favorable for a photoreaction. Four of the five chromones were amenable to this simulation protocol. The cyano-derivative gave an error with the Martin and Frischknecht configurational bias setting.[32] We are currently examining the simulations of this molecule using different bias settings including Martin and Thompson.[33]

During the simulation, two chromone molecules entered the channel and paired in the center of the host **1** (Figure 3.4a). The primary stabilizing interactions are edge to face aryl stacking interactions. The distance between the aryl H of the channel wall and the benzene of the chromone molecules is ~2.6 Å. Of particular interest is the distance and orientation of the two potentially reactive alkenes. Here, the distances range between 4.2 and 4.4 Å, likely favorable for reaction. The two molecules are oriented to place the reactive olefins in an *anti*-fashion (figure 3.4a), suggesting a high probability to afford *anti*-HT photodimer upon UV-irradiation.
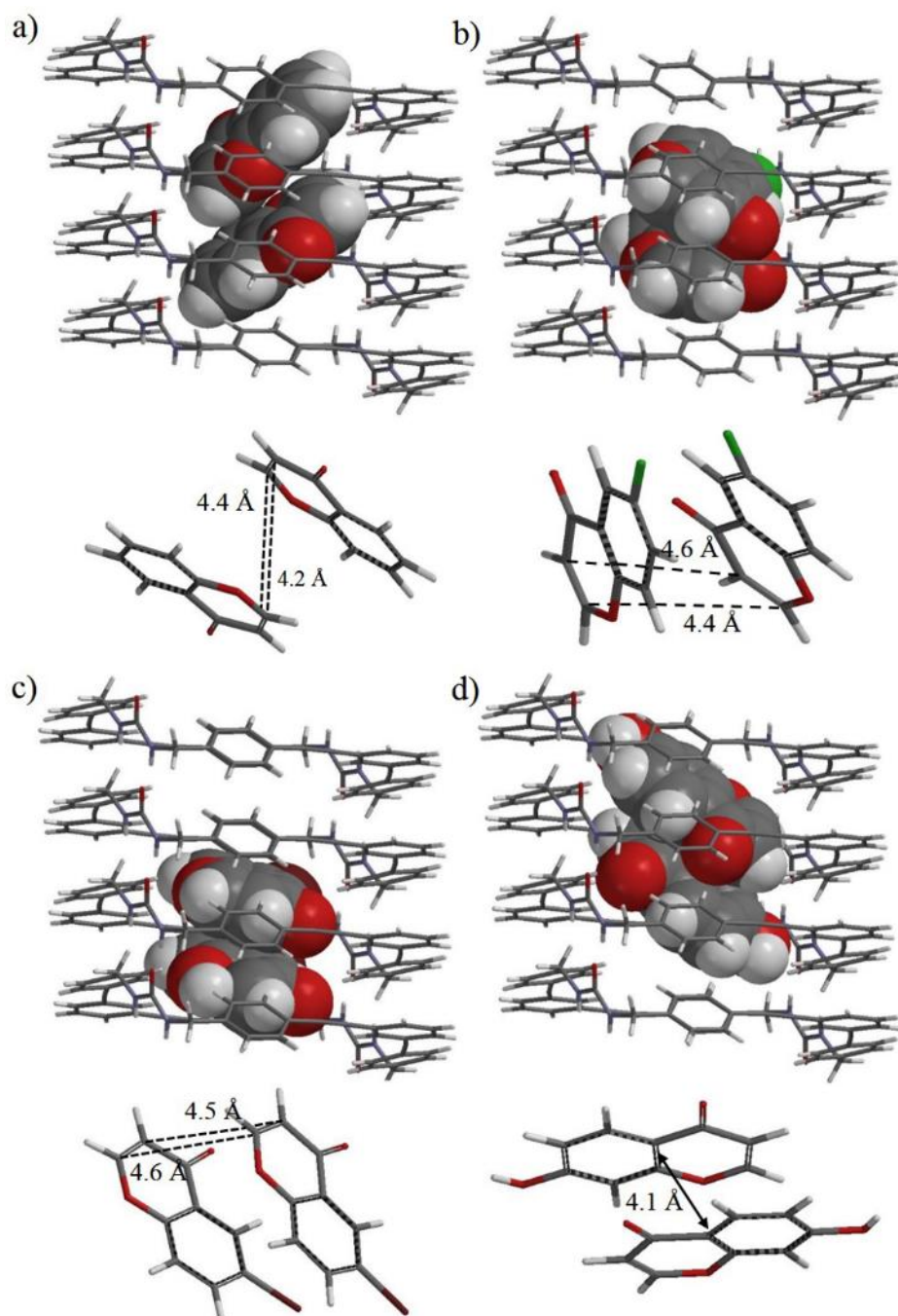
Figure 3.4. Results of GCMC modeling of host **1**•guest complexes and analysis of the relative orientation of neighboring reactants. (a) Orientation and distance of neighboring chromones encapsulated in host **1** suggests *anti*-HT dimer will be favored. (b) Orientation and distance of neighboring 6-fluorochromones suggests *syn*-HH photodimer formation. (c) Orientation and distance of neighboring 6-bromochromones within host **1** suggests *syn*-HH dimer formation. (d) Orientation and distance of neighboring 7-hydroxy-4-chromones within host **1** appears to be unfavorable for [2+2] cycloadditions. (Centroid to centroid distance highlighted)

The structure of host **1**•6-fluorochromone was modeled using the same GCMC simulation procedure. The minimized structure is illustrated in Figure 2.4b. The simulation suggests that the four molecules are arrange in pairs within the channels. Only the central pair is depicted in the figure for clarity. The molecules are stabilized by the edge to face pi interactions between aryl C-H from the channel wall and pi surface of the benzene moiety in 6-fluorochromone with a distance of 3.2 Å. The reactive olefins are aligned and separated by 4.4 to 4.6 Å, slightly longer than the 4.2 Å predicted for optimal reaction.

We observed a similar packing and orientation of the molecules in the host **1**•6-bromochromone GCMC simulation (figure 3.4c). The molecules were arranged in pairs in the channels and show stabilizing edge to face interactions between the aryl C-H from the channel wall and the pi surface of the chromones. We observed a distances ranging from 4.4 to 4.6 Å between reactive olefins. Should a [2+2] cycloaddition reaction occur in these complexes upon UV-irradiation, we predict that both **1**•6-fluorochromone and host **1**•6-bromochromone would favor the formation of their respective *syn*-HH dimers.

A different relative orientation was observed for the guests within the simulated host **1**•7-hydroxy-4-chromone structure (figure 3.4d). Here, molecules are paired through offset aryl stacking interactions with the distance of 4.1 Å. There are no hydrogen bonding interactions apparent, suggesting that our force field and/or our protocol needs further optimization. The reactive olefins are far apart and unfavorably oriented for photoreaction. In summary, our GCMC simulations suggest that three of the four chromones tested may potentially undergo photochemical reactions and predicts that

chromone should favor *anti*-HT products while the 6-fluorochromone and 6-bromochromone favor the formation of *syn*-HH photoproducts.

Next, the series of chromone derivatives were loaded into host **1**. First, the solvent was removed from freshly recrystallized host **1**•DMSO by heating and the empty crystals were equilibrated with 1 mM solutions of the guest (Fig. 3.4a). A UV-vis spectrophotometer was used to monitor the depletion of the guest from solution, and the host:guest binding ratios were calculated through comparison to standard Lambert-Beer plots with known concentrations of guests (see SI). For example, host **1** (15 mg) was soaked in a solution of chromone (1 mM in hexanes) at 45 °C for 0-3 h. The depletion of chromone from solution was monitored by absorbance spectroscopy at 290 nm (Figure 3.4b). The absorbance reached a plateau by 2 h, suggesting that an equilibrium had been reached.

Assuming that the loss of guest from solution is due to the absorption of the guest by host **1**, we calculated a host guest ratio of 1:0.68 by comparison of the final absorbance to a Lambert-Beer plot of known concentration of chromone in (hexanes). The binding ratios reported in Table 2.1 are the average ratio of three separate loading experiments.
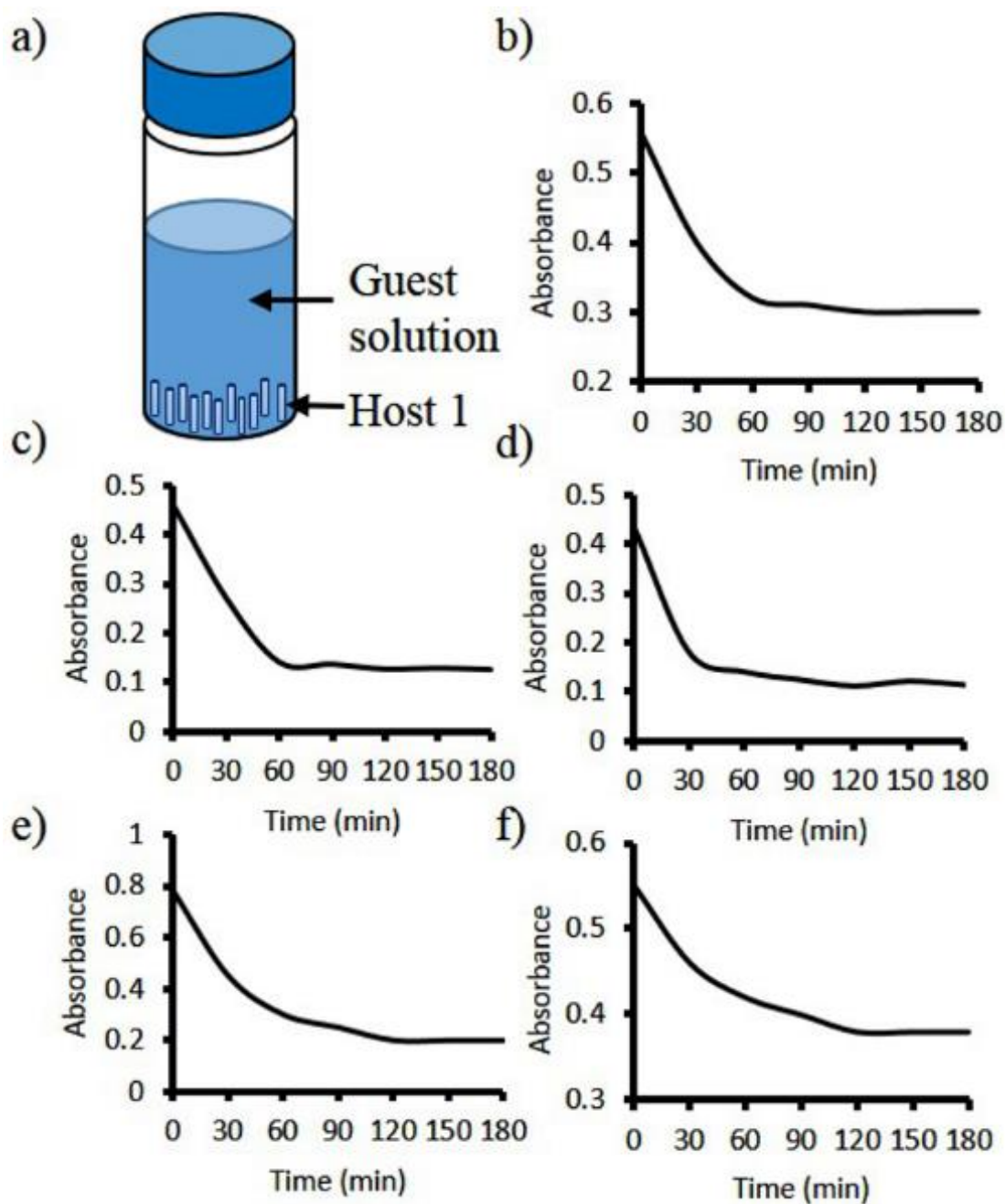
Figure 3.5. Loading of the guests and the depletion of each guest from the solution monitored by UV/Vis spectrophotometry. (a) Soaking of host **1** crystals in guest solutions. (b) Depletion of chromone from the solution (1 mM in hexanes at 45 °C) monitored at 290 nm, (c) Depletion of 6-fluorochromone (1 mM in hexanes at 45 °C) monitored at 300 nm, (d) Depletion of 6-bromochromone (1 mM in hexanes at 45 °C) monitored at 300 nm, (e) Depletion of 7-hydroxy-4-chromone (1 mM in acetonitrile at rt) monitored at 295 nm, and (f) Depletion of 3-cyanochromone (1 mM in acetonitrile at rt) monitored at 295 nm.

111

From Table 3.1, it is apparent that all the derivatives tested could be loaded into host **1**; however, the loading ratio was not simply based on size. Indeed chromone (volume = 127.84 Å^3, polarity = 3.5 D), the smallest compound tested, showed a slightly lower binding ratio with 1:0.68 host **1**:chromone versus the larger and slightly more polar halide containing derivatives (polarity ~ 4.1 D), which loaded at 1:0.97. The more polar 7-hydroxy-4-chromone (4.5 D) showed a slightly higher ratio of 1:1.07. A relatively low binding ratio (1:0.48) was observed for the most polar 3-cyanochromone (7.16 D), which is similar in volume to 6-bromochromone, suggesting that shape likely also influences the binding ratio in addition to size and polarity.

Table 3.1. Guests absorbed by host **1**.

Guest	Volume[a] (Å^3)	Polarity (D)	H:G
chromone	127.84	3.54[b]	1 : 0.68
6-fluoro chromone	133.28	4.23[a]	1 : 0.97
6-bromo chromone	147.15	4.14[a]	1 : 0.97
7-hydroxy-4-chromone	135.87	4.53[a]	1 : 1.07
3-cyano chromone	144.97	7.16[a]	1 : 0.48

[a]Calculated in Spartan[34] using DFT (B3LYP) with 6-311++G** basis set. [b]Ref[35]

To test the photoreactivity of these host•guest complexes samples (15 mg) were UV-irradiated at room temperature (26 ℃) under an argon atmosphere using a Hanovia 450 W medium pressure mercury arc lamp. Samples (15 mg) were removed periodically (0, 3, 12, 24, and 96 h), extracted into CDCl₃ (0.6 mL). The photoproducts were monitored by ¹H NMR. Samples were also completely dissolved in DMSO-d6 to confirm that the guests could be completely removed from the crystals.

Table 3.2 summarizes these photochemical studies and shows that three of the five encapsulated guests underwent photolysis reactions. After UV-irradiation of host **1**•chromone for 3 h, we observed 19% conversion of chromone to afford two photodimers (Table 3.2, entry 2). The ¹H NMR resonances for the major product, matched those reported for the *anti*-HT photodimer.[15] GC/MS was used to further monitor the selectivity and showed an *anti*-HT selectivity of 87.4% with the minor photodimer formed in 12.6% selectivity (Figure 3.20).

Increasing the UV-irradiation time (12 h, entry 3; 24 h, entry 4, and 96 h, entry 5) gave an increase in conversion of chromone from 46% at 12 h to 70% at 96 h with similar selectivity for two photodimers (Figure 3.6a). We were able to isolate the photoproducts using preparative TLC and single crystals suitable for XRD analysis of both photodimers were obtained from the slow evaporation of CDCl₃ solution.

The two photodimers formed crystals with distinct morphology of the crystals, allowing ready separation of both dimer products. Indeed, the structure of the major product, which formed as large colorless blocky crystals, was confirmed as the *anti*-HT (Figure 3.6b). The minor photodimer, which formed thin colorless plates, was identified

113

as the *anti*-HH dimer (Figure 3.6c) and is the first report of the synthesis and characterization of this photodimer.

In solution, chromone photodimerization was reported to yield two products, the *anti*-HT and the *trans*-fused HT photodimers, and XRD data for these dimers have been reported.[15] In contrast in the host **1**•chromone complex no *trans*-fused HT dimers were observed.

Table 3.2. Summary of photoreactions.

Guest	Entry	Host	Time (h)	Conv. (%)	Selectivity (%)				
					syn-HH	*syn*-HT	*anti*-HH	*anti*-HT	Coupling adduct
chromone	1	-	96	0	-	-	-	-	-
	2	1	3	19	0	0	13	87	0
	3	1	12	46	0	0	13	87	0
	4	1	24	55	0	0	13	87	0
	5	1	96	70	0	0	13	87	0
6-fluorochromone	6	-	96	0	-	-	-	-	-
	7	1	6	22	0	0	0	>99	0
	8	1	12	34	0	0	0	>99	0
	9	1	96	56	0	0	0	>99	0
6-bromochromone	10	-	96	0	-	-	-	-	-
	11	1	3	25	0	0	0	0	>99
	12	1	6	52	0	0	0	0	>99
	13	1	24	70	0	0	0	0	>99
7-hydroxy-4-chromone	14	-	96	0	-	-	-	-	-
	15	1	96	0	-	-	-	-	-
3-cyanochromone	16	-	96	0	-	-	-	-	-
	17	1	96	0	-	-	-	-	-
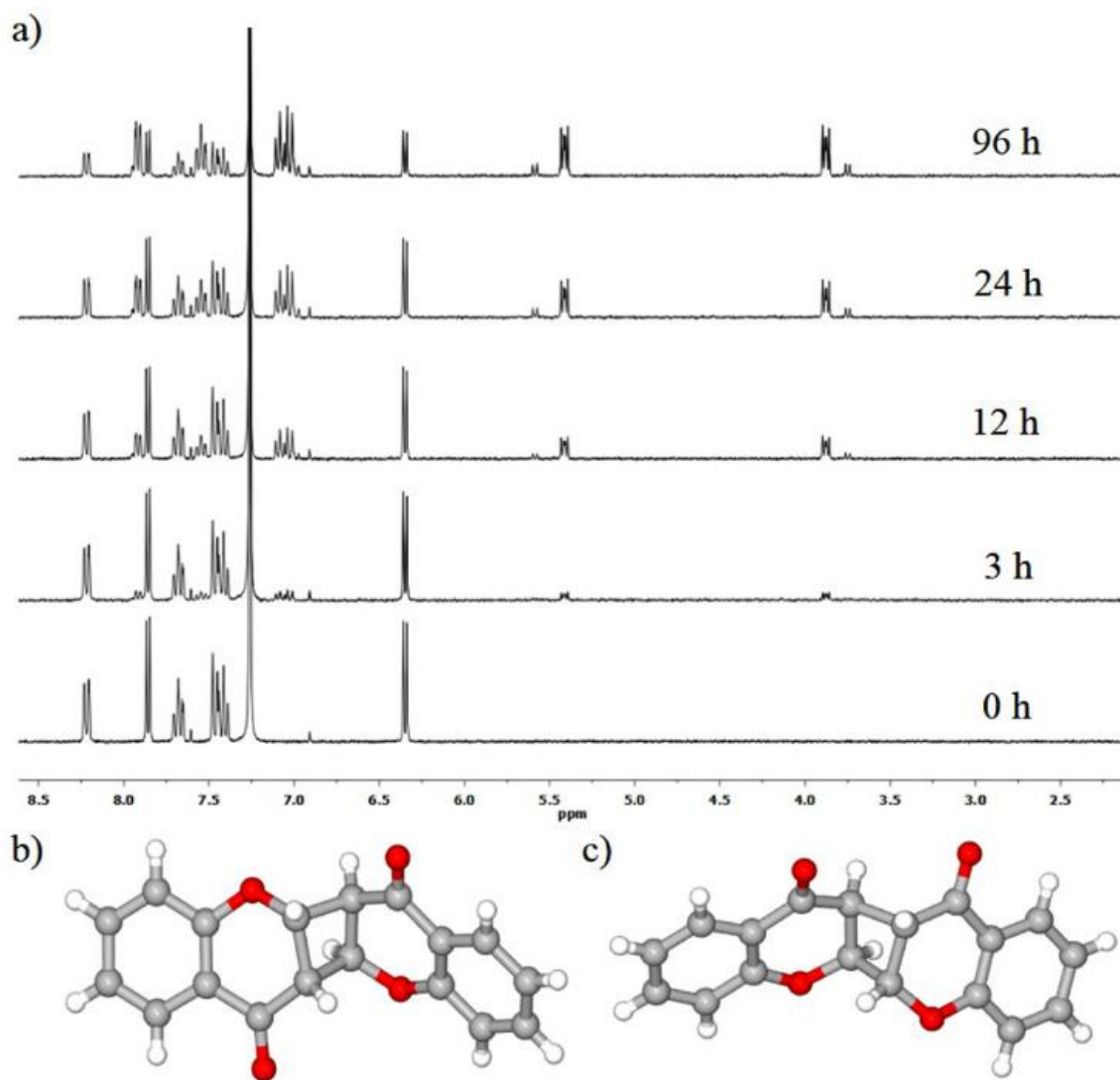
Figure 3.6. Monitoring the photoreaction of host **1**•chromone and observed photoproducts. a) ^{1}H NMR analysis of the photoreaction of host **1**•chromone in different time intervals. b) Crystal structure of the *anti*-HT dimer, which was the major product. c) Crystal structure of the *anti*-HH dimer.

Similar UV-irradiation of the host **1**•6-fluorochromone crystals facilitated a remarkably selective photodimerization, yielding the *anti*-HT dimer with >99% selectivity in 22% conversion after 6 h (Table 3.2, entry 7). Figure 2.7a shows new resonance for the *anti*-HT photodimer. Again, increasing the UV-irradiation time to 12 h or 96 h afforded increased conversion to 34% and 56% respectively with similarly high

selectivity (entries 8 and 9). This is the first report of a [2+2]-photocycloaddition of 6-fluorochromone, and its structure was confirmed by X-ray diffraction.
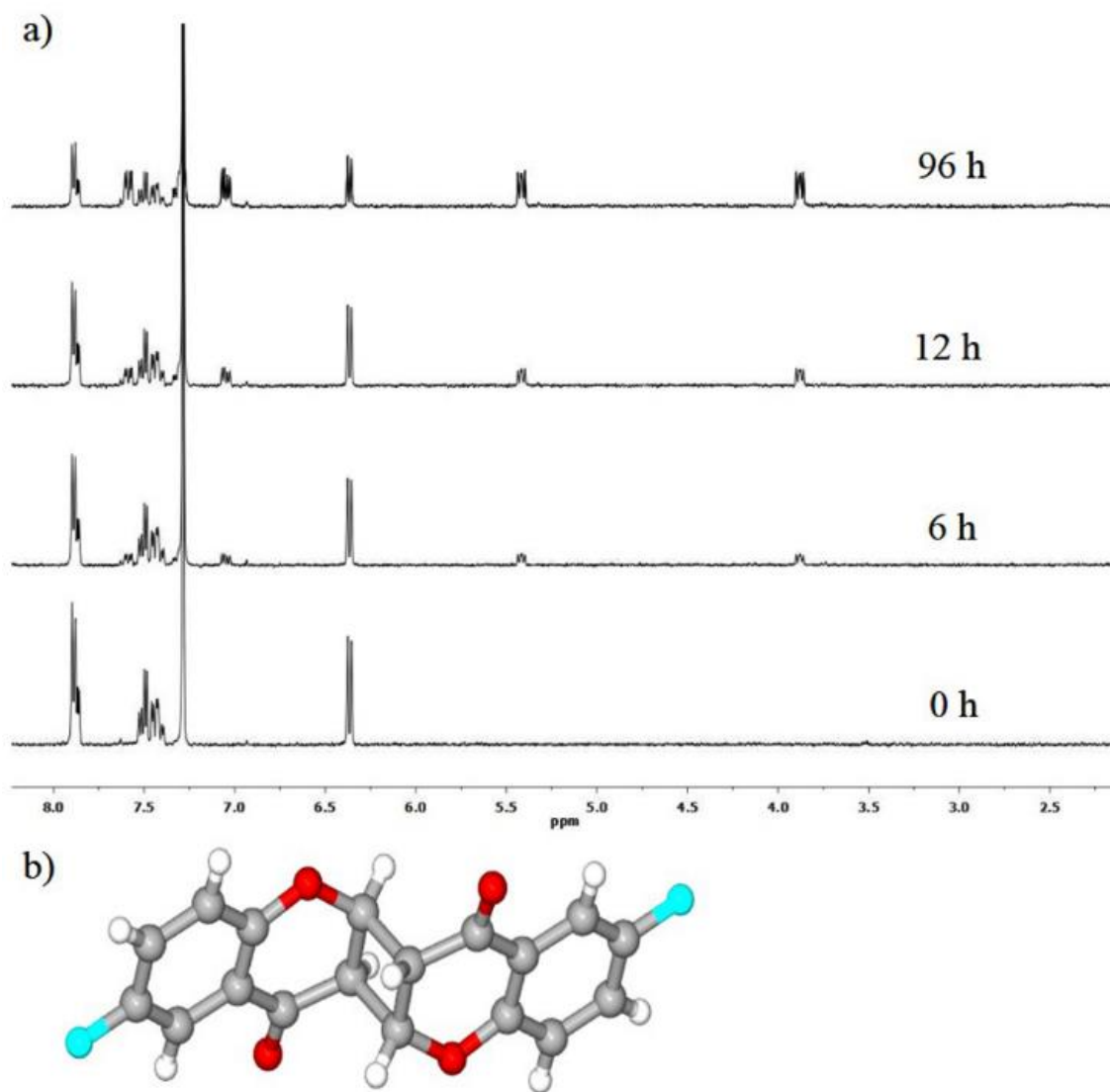
Figure 3.7. Monitoring the photoreaction of host **1**•6-fluorochromone. a) ^{1}H NMR analysis of the photoreaction of host **1**•6-fluorochromone in different time intervals. b) Crystal structure of the *anti*-HT photodimer.

We found that host **1**•6-bromochromone showed distinctly different reactivity inside host **1**. UV-irradiation of host **1**•6-bromochromone facilitated 25% conversion of the bromochromone to a single new product after 3 h (Table 3.2, entry 11). Inspection of the ^{1}H NMR showed alkenes resonances at 6.16 ppm (Figure 3.8a) and that surprisingly

no resonances were observed in the cyclobutane region (5.75-2.75 ppm) typical for [2+2] cycloadditions. Increasing the UV-irradiation time to 6 h or 24 h resulted in increased production of this product in 52% and 70% conversion respectively (entries 12 and 13). Longer irradiation times (> 24 h) did not show any additional conversion. The products were extracted with chloroform and the residual 6-bromochromone was removed by preparative TLC. The product was characterized by NMR (^{1}H, ^{13}C, 2D COSY) and HRMS. The formation of this aryl coupling product suggests a radical mechanism due to the labile Br atom at the 6 position. Halogenated chromones including 6-bromo and 6-flouro derivatives have been used to synthesize a variety of isoflavone structural motifs through metal catalyzed cross coupling reactions. A palladium catalyzed direct cross coupling of 6-bromo and 6-flourochromones with quinones[36] and a rhodium catalyzed direct oxidative cross coupling of 6-bromochromone with alkenes have been reported.[37]
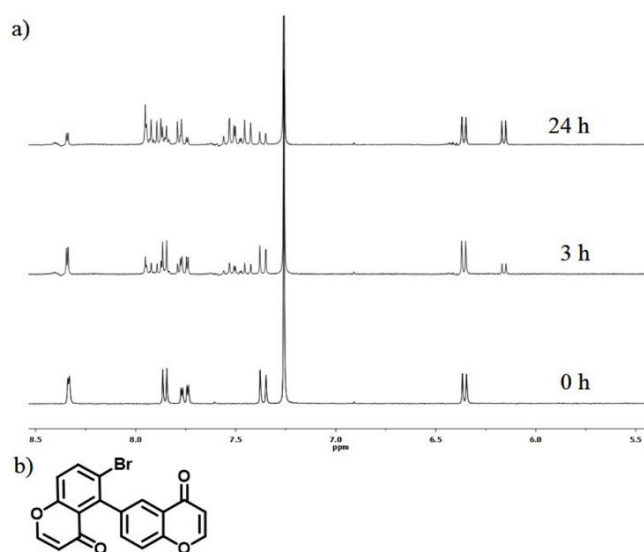
Figure 3.8. Photoreaction of host **1**· 6-bromochromone and observed photoproduct. a) ^{1}H NMR analysis of the photoreaction of host **1**· 6-bromochromone in different time intervals. b) Structure of the coupling product.

117

We found that the host **1**•7-hydroxy-4-chromone was stable to prolonged UV-irradiation (96 h, entry 15).   This was the same as what was observed for solid 7-hydroxy-4 chromone. The host **1**•3-cyanochromone complex was also photostable and was reisolated after 96 h of UV-irradiation (entry 17).   Again, solid 3-cyanochromone crystals were also unreactive under similar conditions.

We next compared our experimental findings with the GCMC predictions. As predicted each of our compounds were able to be loaded into the nanochannels of host **1**. The simulations further suggested that chromone, 6-fluorochromone and 6-bromochromone would be reactive while the 7-hydroxy-4-chromone would likely be unreactive within their respective host **1** complexes, although the host **1**•3-cyanochromone complex was not amenable to our simulation protocol. The selectivity of the host **1**•chromone reaction was successfully predicted by our GCMC simulations for chromone, which indeed formed the *anti*-HT photodimer as its major product. Unfortunately, our current GCMC protocol did not accurately predict the selectivity of the halogen containing derivatives. Future work will focus on the optimization of the force field parameters, GCMC bias settings, type of the Monte Carlo moves, and probabilities to enable more accurate simulations of guest reactivity and selectivity within our host complexes. For example, more detailed force fields Amber_Cornell or CHARMM may increase the accuracy of the simulations. Our goal is to expand the scope and accuracy of our simulations in order to predict the reactivity of guests with different functionality.

118

3.4 Conclusions

In summary, a porous columnar host from self-assembled phenylethynylene *bis*-urea macrocycles was successfully employed to modulate the reactivity of chromone, 6-fluorochromone and 6-bromochromone, which were otherwise unreactive in the solid state. Encapsulated chromone and 6-fluorochromone underwent [2+2] photodimerization reactions to afford their respected *anti*-HT dimers in moderate to good yields with high selectivity. We observed 55-70% of reactants converted into photodimers and *anti*-HT dimers afforded in 87%-99% selectivity. For 6-fluorochromone, our studies gave the first reported formation of its *anti*-HT photodimer. In comparison, the photoreaction of encapsulated 6-bromochromone produced an unusual aryl coupling product in 70% conversion and >99% selectivity. Although bound by our host, hydroxy-4-chromone and 3-cyanochromone were unreactive under UV-irradiation.

Our long term goal is to develop computational simulations to understand and to accurately predict the photoreactivity of a wide range of small organic reactants within the nanochannels of assembled hosts. Thus far, our GCMC simulation gave mixed results with the compounds tested. The simulations correctly predicted that all these compounds could be loaded into the nanochannels of host **1**, but had only a 50% success rate of determining the product selectivity of the subsequent photoreactions. In particular, the reaction selectivity for encapsulated halogen containing derivatives (6-fluorochromone and 6-bromochromone) was incorrect. Current work focuses on exploring force fields that more accurately describe the non-bonded interactions and on the optimization of the GCMC bias settings.

3.5 Experimental

3.5.1 Materials and methods

All chemicals were purchased from Aldrich or VWR. Chromone and all its derivatives were further purified by recrystallization prior to loading. The phenylethynylene *bis*-urea macrocycle was prepared and recrystallized from DMSO to obtain host 1•DMSO according to previous procedures.[21] Thermogravimetric analysis (TGA) was carried out in TA instrument SDT-Q600 to evacuate DMSO solvent from the channels of host 1•DMSO prior to loading studies. UV-Vis data was collected on SoftMax M2e spectrophotometer. ^{1}H NMR and ^{13}C NMR spectra were recorded on Varian Mercury/VX 300 and VX 400 NMR. GC/MS data was recorded on VG70S magnetic sector mass spectrometer with EI+. All photoreactions were carried out using a Hanovia medium-pressure 450 W mercury arc lamp cooled in a borosilicate immersion well. The entire apparatus was placed in a UV shielded chamber. The temperature of the chamber was kept between 24 to 26 ºC. The X-ray intensity data were collected at 100(2) K using a Bruker SMART APEX diffractometer (Mo Kα radiation, λ = 0.71073 Å).[38] The raw area detector data frames were reduced and corrected for absorption effects using the SAINT+ and SADABS programs.[38] Final unit cell parameters were determined by least-squares refinement of 5081 reflections from the data set. The structure was solved by direct methods with SHELXS.[39] Subsequent difference fourier calculations and full-matrix least-squares refinement against F^2 were performed with SHELXL-2014[39] using OLEX2.[40] All non-hydrogen atoms were refined with anisotropic displacement

parameters. Hydrogen atoms were located in difference maps before being included as riding atoms with refined isotropic displacement parameters.

3.5.2 Crystallization of 7-hydroxy-4-chromone, and 3-cyanochromone

Each compound (50 mg) was added to a scintillation vial with 2 mL of acetonitrile and heated. Single crystals suitable for X-ray analysis were obtained upon cooling.

3.5.3 Loading of guest molecules and calculating the binding ratios

The solvent was removed from freshly recrystallized host **1**•DMSO by TGA or by heating samples (~50 mg) at 120 °C 1 h. Next empty host **1** crystals (15 mg) were soaked in solutions containing the guest (1 mM). Loading studies of chromone, 6-fluorochromone, and 6-bromochromone were carried out in hexane at 45 ℃, while 7-hydroxy-4-chromone and 3-cyanochromone were carried out at rt in acetonitrile. The uptake of the guests into the host **1** was monitored through the change in the absorbance of the solution over time (from 0 to 3 h). A standard Beer-Lambert curve was generated for each guest and used to calculate the binding ratios (see Figures 3.14-3.18).

3.5.4 UV-irradiation of chromones

Recrystallized samples of chromones (10 mg) were placed in Norell S-5-500-7 NMR tubes (with 100% transmittance up to 400 nm) and purged with argon. Each sample was UV-irradiated for 96 h at 26 °C. Samples were dissolved in $CDCl_3$ (0.6 mL) or CD_3CN (0.6 mL) and analyzed by ^1H NMR.

3.5.5 UV-irradiation of host **1**•guest complexes

All photoreactions were performed in Norell S-5-500-7 NMR tubes using 15 mg of each complex under argon atmosphere. Each sample was UV-irradiated using a Hanovia 450 W medium pressure mercury arc lamp cooled in a quartz immersion well. The irradiation chamber temperature was kept at 26 ºC. Samples (15 mg) were removed periodically (0, 3, 12, 24, and 96 h), extracted into $CDCl_3$ (0.6 mL) via ultrasonic sonication (15 min), and monitored by ^{1}H NMR. Conversion of the starting materials to products was calculated using the ratio of integrals between starting material and corresponding product.

3.5.6 Crystallization of chromone and 6-fluorochromone photolysis products

At the end of the photoreactions, the encapsulated guests were removed from the host by extraction with $CHCl_3$. Products were separated from residual starting materials by preparative TLC. The crystals of chromone photodimers, both *anti*-HT and *anti*-HH, were obtained through slow evaporation of the dimer mixture in $CDCl_3$ (~ 10 mg/mL). Crystals of 6-fluorochromone *anti*-HT photodimer were obtained by slow evaporation of dimer solution in $CDCl_3$ (~ 10 mg/mL).

3.5.7 Grand Canonical Monte Carlo (GCMC) simulations

All GCMC simulations were performed using the Monte Carlo for Complex Chemical Systems (MCCCS) Towhee plug-in built into Scienomics' Materials Processes and Simulations (MAPS) platform[23] as previously reported.[24] Each guest was built using the amorphous builder within MAPS and their chemical potentials were calculated on a systems containing 100 guest molecules via a 5×10^4 step canonical MC simulation with MCCS Towhee and using the Widom insertion method and the Dreiding force field.[41]

122

Next, a periodic simulation cell was constructed by importing the atomic coordinates from the X-ray structure of host **1**•nitrobenzene into MAPS. The nitrobenzene guests were removed from this structure. New host **1**•guest complexes were generated using the calculated guest chemical potential values. Finally, GCMC simulations were performed using Martin and Frischknecht configurational bias setting[32] for 1 x 10^6 steps, where the chemical potential (μ) of the corresponding guest was kept constant and the system was maintained at standard ambient constant temperature (T, 298.15 K) and constant volume (V). The Martin and Frischknecht configurational bias setting was used in the GCMC simulations for all chromone derivatives, however that scheme was incapable of setting up the simulations for the cyano derivative. Therefore, no simulations were performed for the cyano derivative.

3.5.8 Characterization data for the phenylethynylene *bis*-urea macrocycle
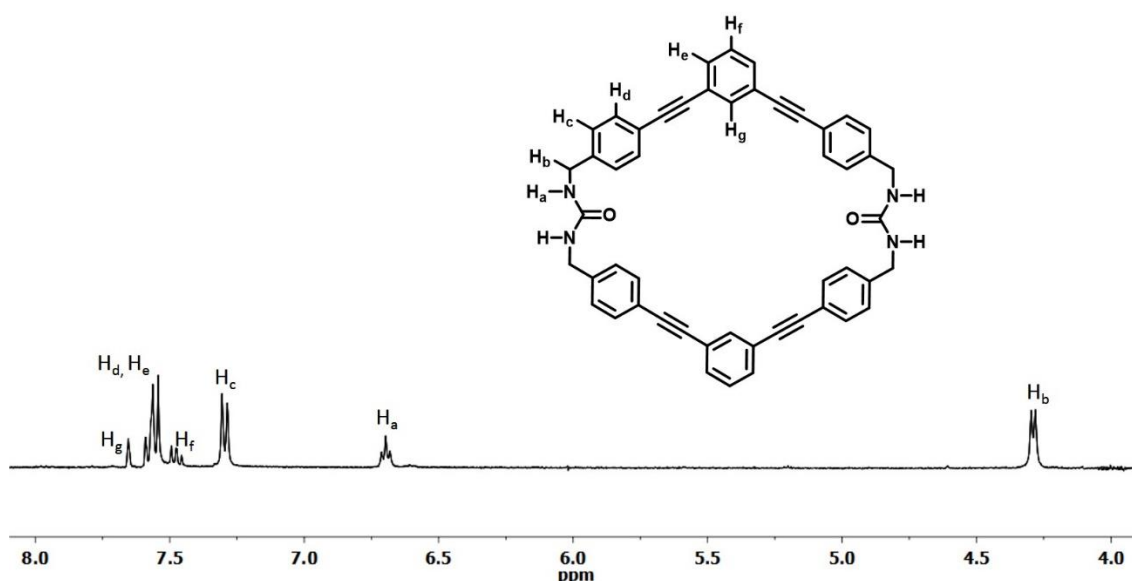
Figure 3.9. ^{1}H NMR (DMSO-d$_6$, 400 MHz) of **1**.
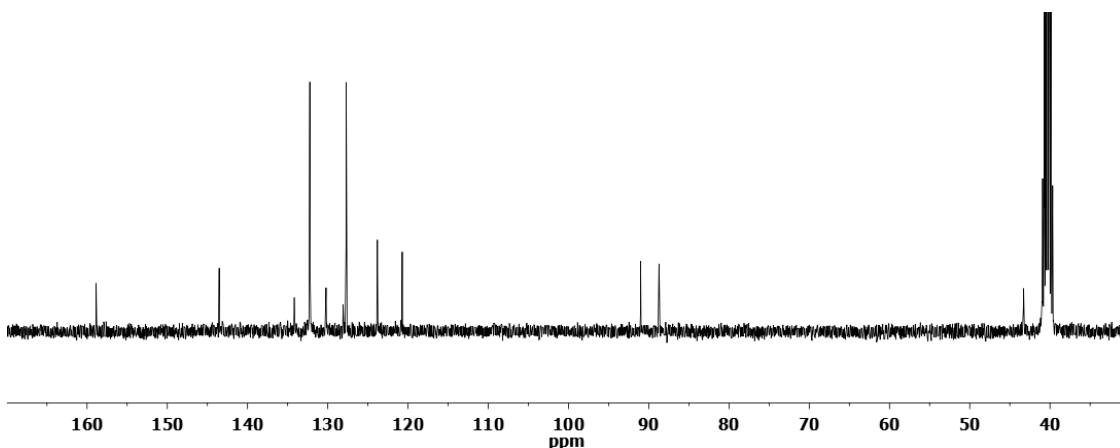
Figure 3.10. ^{13}C NMR spectra (DMSO-d$_6$, 100 MHz) of **1**.

^{1}H-NMR: (400 MHz, DMSO δ): 7.64 (s, 2H, Ar-H), 7.55(m, J=20.0 Hz, 12H, Ar-H), 7.47 (t, J=16.0 Hz, 2H, Ar-H), 7.28 (d, J=8.0 Hz, 8H, Ar-H), 6.69 (t, J=12.0 Hz, 4H, -NH), 4.28 (d, J=8.0 Hz, 8H, -CH2)^{13}C-NMR: (100 MHz, DMSO δ): 158.9, 134.5, 134.2, 132.3, 130.2, 128.1, 127.7, 123.8, 120.7, 91.0, 88.7, 43.3; IR (cm^{-1}): 3269, 1665, 1508, 1412, 817, 704, 684; HRMS (ES$^+$): [M+H]$^+$ Calculated formula for C$_{50}$H$_{36}$N$_4$O$_2$:724.2838 Found: 724.2845.

3.5.9 Recrystallization of macrocycle:

Phenylethynylene *bis*-urea macrocycle **1** (150 mg) was dissolved in hot DMSO (~30 mL) at 130 °C in a pressure tube. The solution was slowly cooled to room at 1 ºC/h. Host **1**•DMSO microcrystals were obtained after 5 days.

3.5.10 TGA Analysis:

Freshly crystallized Host **1**•DMSO microcrystals (15 mg) were heated at a rate of 4ºC/min from 25 to 170 ºC under helium and held isothermal for 10 min. The samples were slowly cooled to room temperature.[1]

124
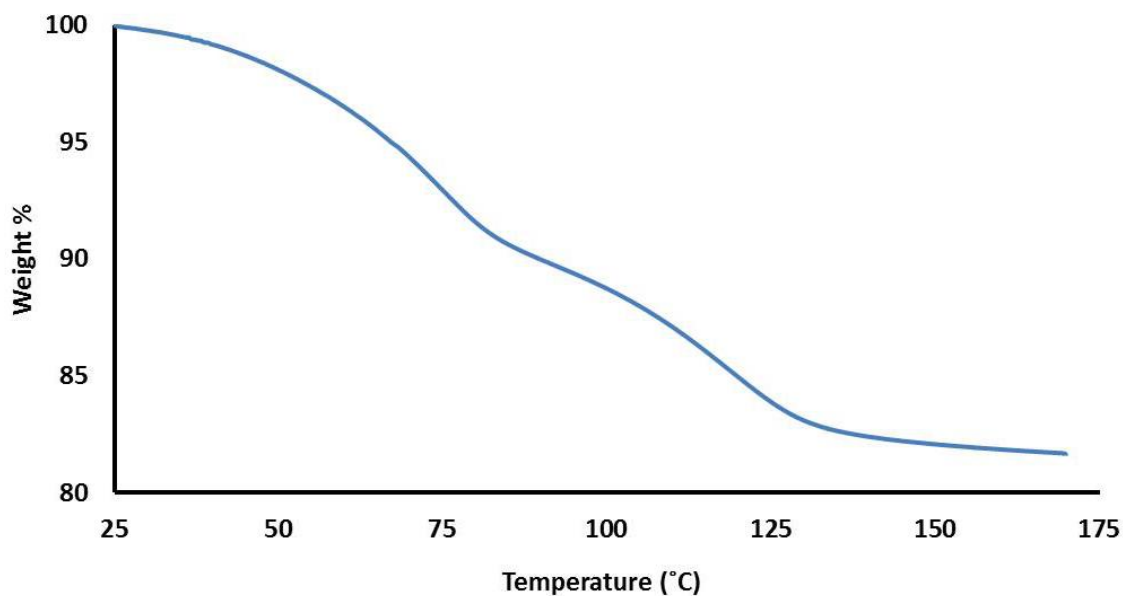
Figure 3.11. TGA profile of freshly crystallized host **1**•DMSO.
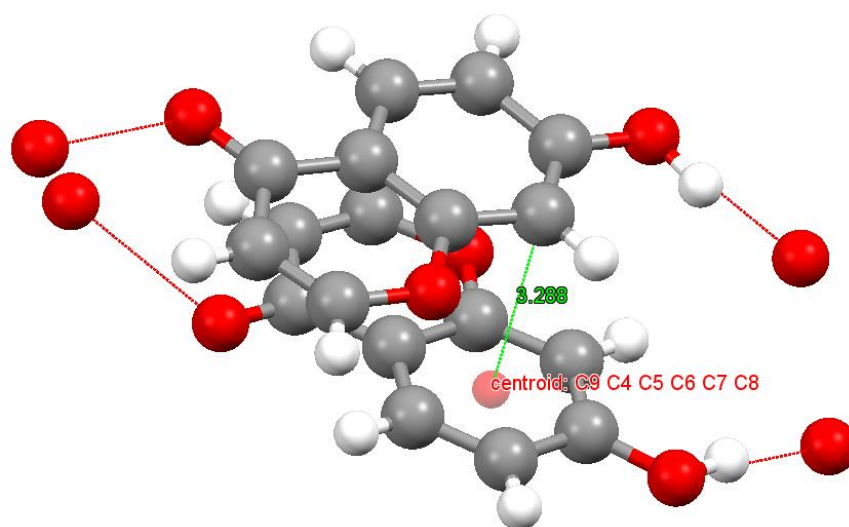
Figure 3.12. One-dimensional chains of 7-hydroxy-4-chromone stack into layers with offset aryl stacking interactions.
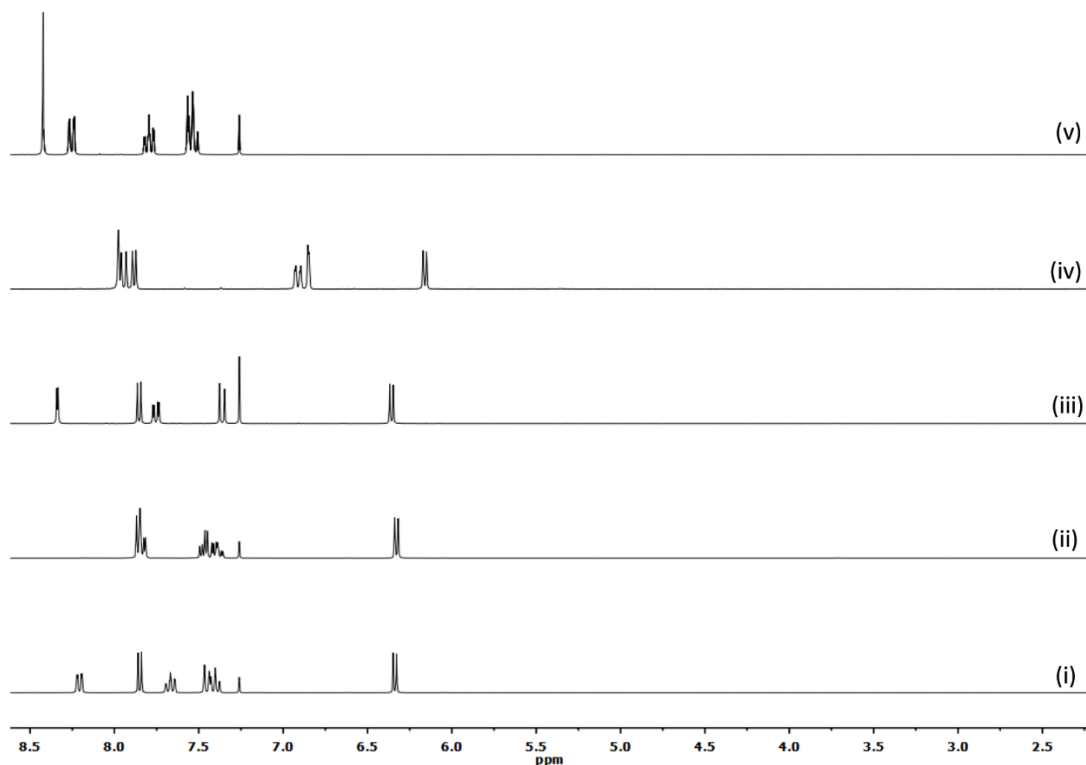
Figure 3.13. ^{1}H NMR (300 MHz) of control photoreactions after 96 h under Ar (g) (i) Chromone in CDCl$_3$, (ii) 6-flourochromone in CDCl$_3$, (iii) 6-bromochromone in CDCl$_3$, (iv) 7-hydroxy-4-chromone in CD$_3$CN, and (v) 3-cyanochromone in CDCl$_3$.
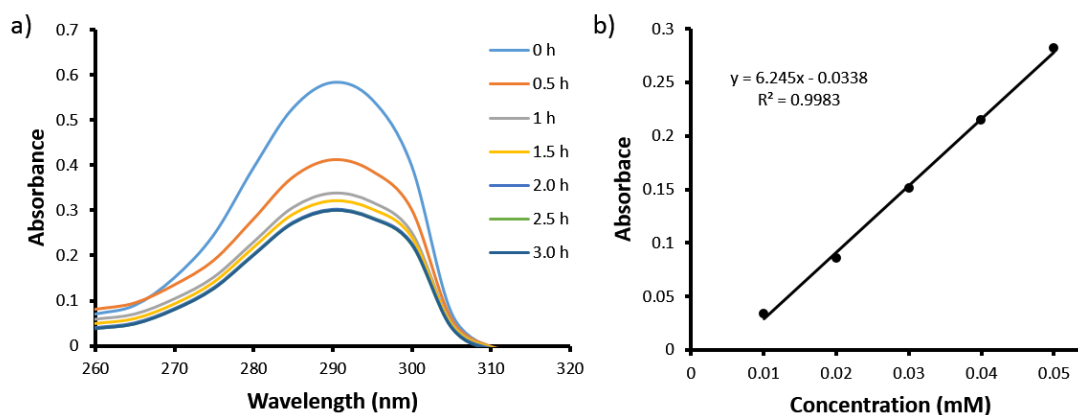
Figure 3.14. Loading of chromone into host **1** to form host **1**•chromone complex. (a) Absorption of chromone by host **1** monitored by UV-visible absorption spectroscopy at 290 nm. (b) Standard Beer-Lambert's plot of chromone in hexanes monitored at 290 nm.

126
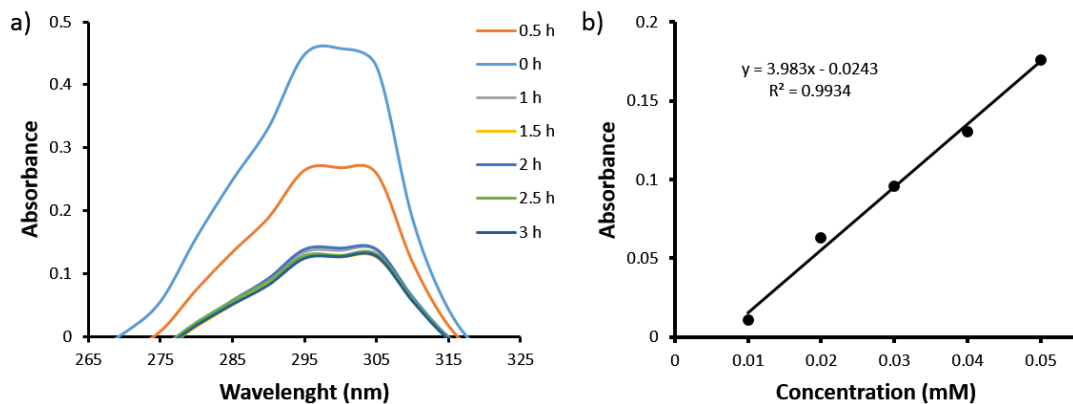
Figure 3.15. Loading of 6-flourochromone into host **1** to form host **1**•6-fluorochromone complex. (a) Absorption of 6-flourochromone by host **1**, monitored by UV-visible absorption spectroscopy at 300 nm. (b) Standard Beer-Lambert's plot of 6-flourochromone in hexanes at 300 nm.
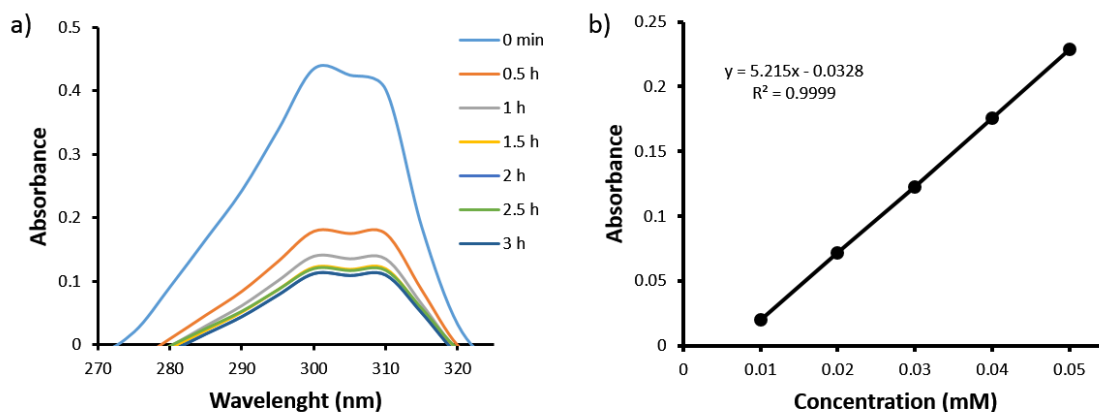
Figure 3.16. Loading of 6-bromochromone into host **1** to form host **1**•6-bromochromone complex. (a) Absorption of 6-bromochromone by host **1** monitored by UV-visible absorption spectroscopy at 300 nm. (b) Standard Beer-Lambert's plot of 6-bromochromone in hexanes at 300 nm.

127
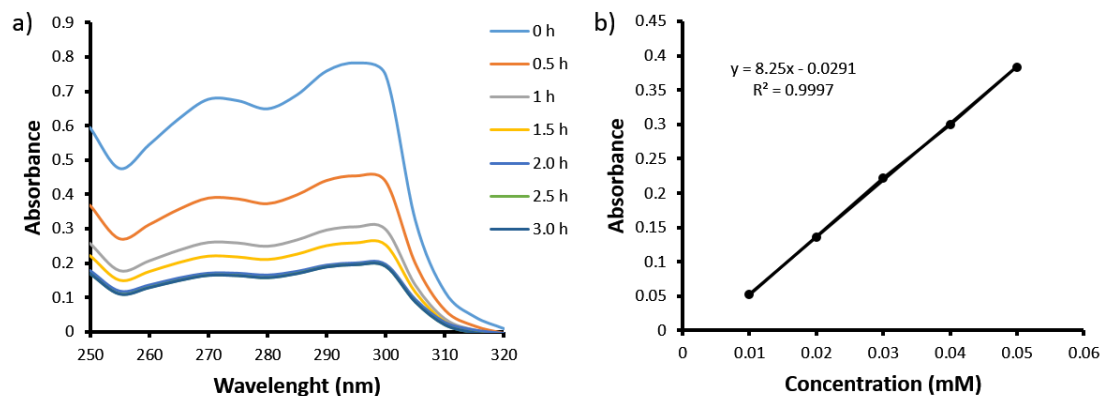
Figure 3.17. Loading of 7-hydroxy-4-chromone into host **1** to form host **1**•7-hydroxy-4-chromone complex. (a) Absorption of 7-hydroxy-4-chromone by host **1** monitored by UV-visible absorption spectroscopy at 295 nm. (b) Standard Beer-Lambert's plot of 7-hydroxy-4-chromone in acetonitrile at 295 nm.
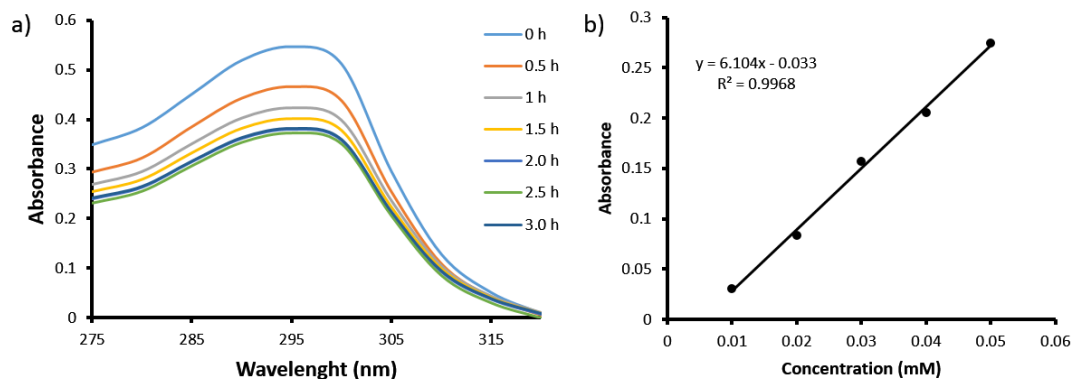
Figure 3.18. Loading of 3-cyanochromone into host **1**. (a) Absorption of 3-cyanochromone by host **1** monitored by UV-visible absorption spectroscopy at 295 nm. (b) Standard Beer-Lambert's plot of 3-cyanochromone in acetonitrile at 295 nm.

After the photoreaction, the guests were extracted from host **1** with CHCl$_3$, the solvent was reduced *in vacuo* and crude product purified by preparative TLC (1:4 ethyl acetate: hexane).

128
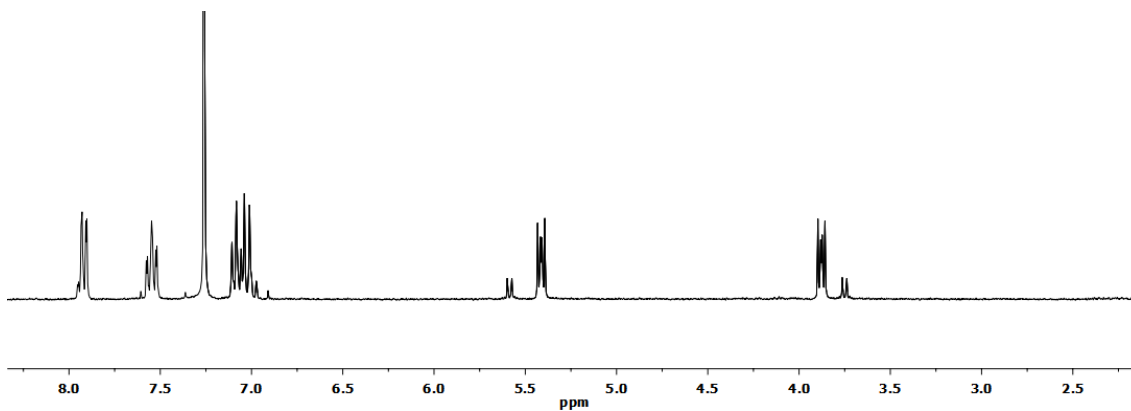
Figure 3.19. ^{1}H NMR (CDCl$_3$, 300 MHz) of the chromone photodimer mixture in CDCl$_3$ (*anti*-HT and *anti*-HH) after removal of the residual starting material.
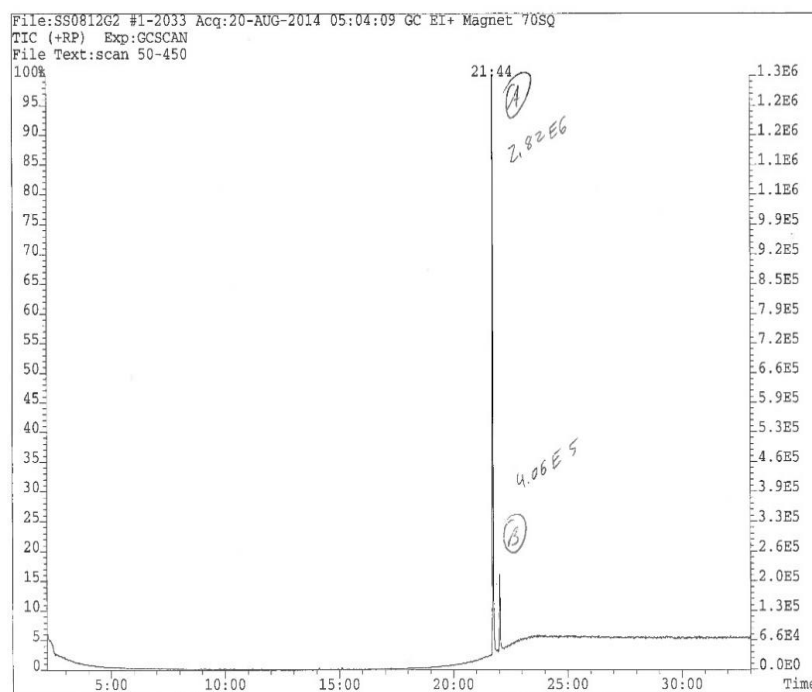
Figure 3.20. GC trace of the chromone photodimer mixture (*anti*-HT and *anti*-HH) after 96 h UV-irradiation of host **1**•chromone complex. Residual chromone was removed prior to GC by preparative TLC.

129

3.5.11 Photolysis of host1• 6-flourochromone:

At the end of the photoreaction, the guests were extracted from host **1** with CHCl₃. The solvent was evaporated *in vacuo* and the crude reaction mixture was purified by
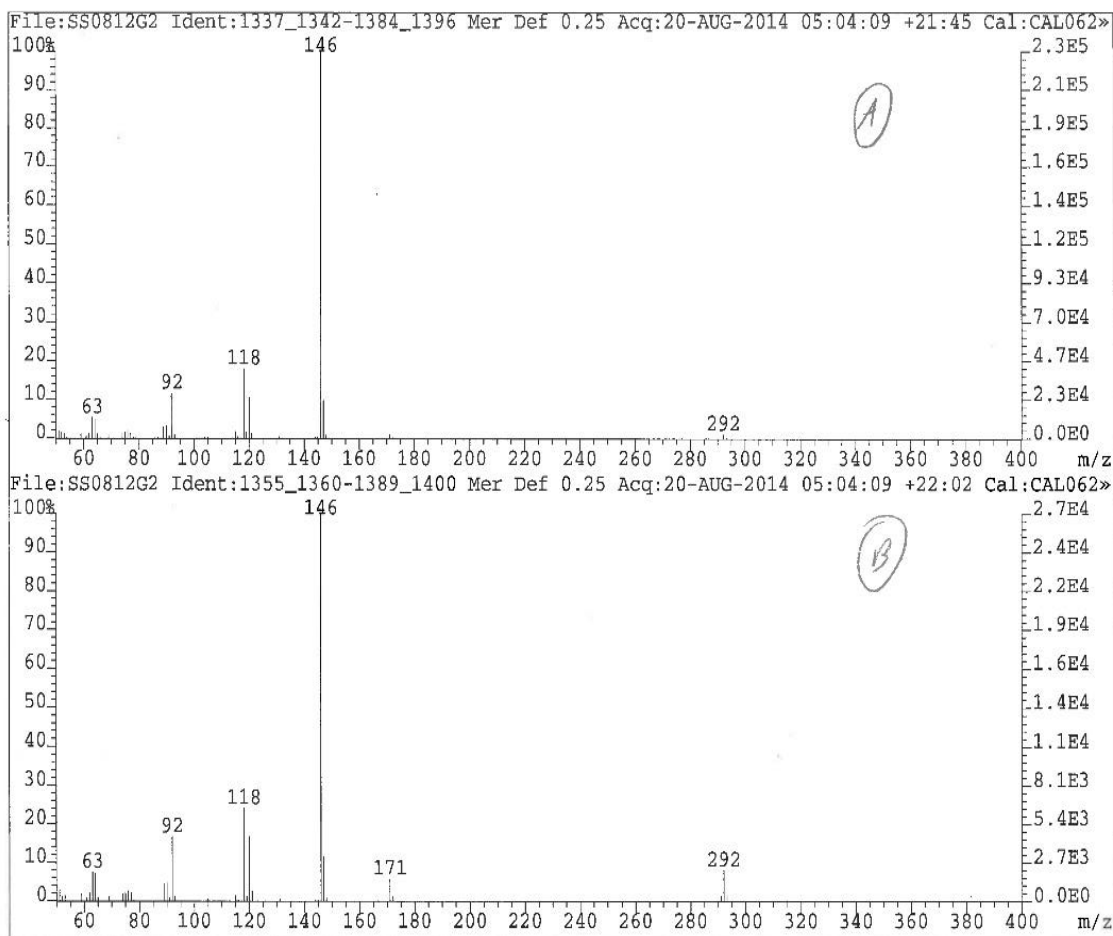
preparative TLC in ethyl acetate: hexane (1:3) to obtain *anti*-HH photo dimer.

Figure 3.21. MS of the GC purified chromone photodimers *anti*-HT (top) and *anti*-HH (bottom) after 96 h UV-irradiation of host **1**•chromone complex.
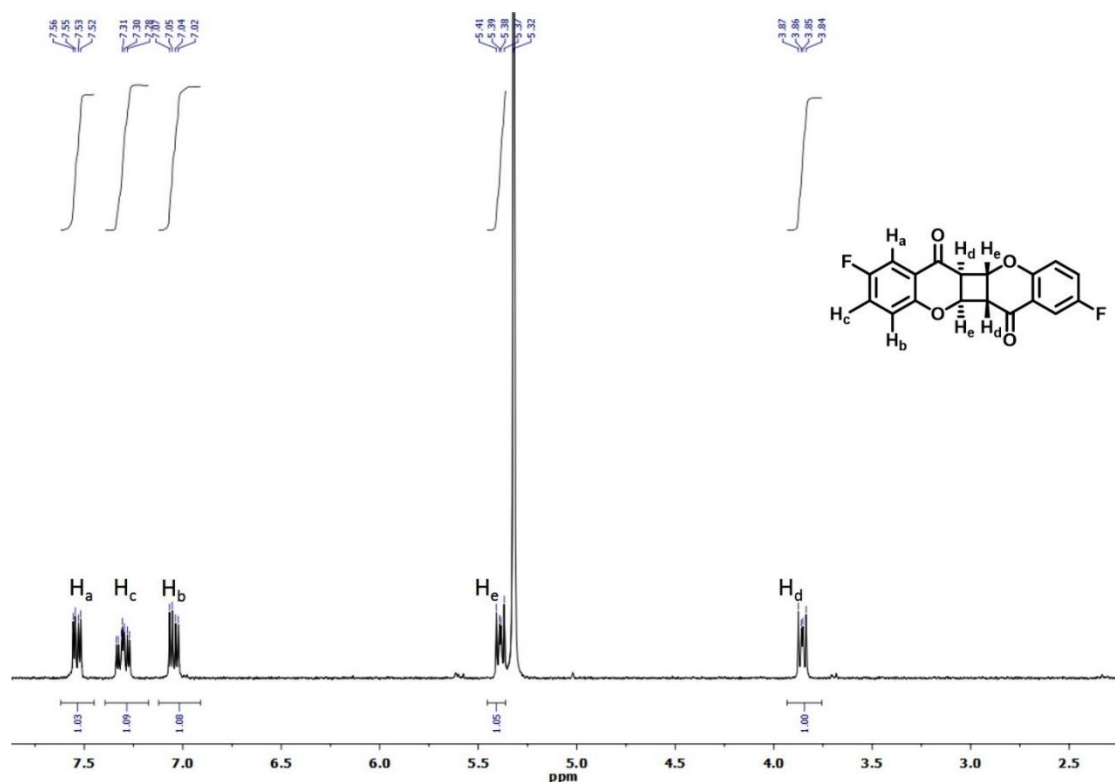
Figure 3.22. ^{1}H NMR (CD$_2$Cl$_2$, 300 MHz) of the 6-fluorochromone *anti*-HH photodimer.

^{1}H-NMR: (300 MHz, CD$_2$Cl$_2$ δ): 7.56-7.52 (m, 2H, Ar-H), 7.31-7.28 (m, 2H, Ar-H), 7.07-7.02 (m, 2H, Ar-H), 5.39 (dd, *J*=4.7 and *J*=7.1 Hz, 2H), 3.86 (dd, *J*=4.7 and *J*=7.1 Hz, 2H); HRMS (ES$^+$): [M+H]$^+$ Calculated formula for C$_{18}$H$_{10}$F$_2$O$_4$: 328.0543 Found: 328.0547.

3.5.12 Photolysis of host 1•6-bromochromone:

At the end of the photoreaction, the guests were extracted from host **1** with CHCl$_3$. The solvent was evaporated *in vacuo* and the crude reaction mixture was purified by preparative TLC in dichloromethane: ethyl acetate: methanol (64:35:1) to obtain the coupling product.

131

www.manaraa.com
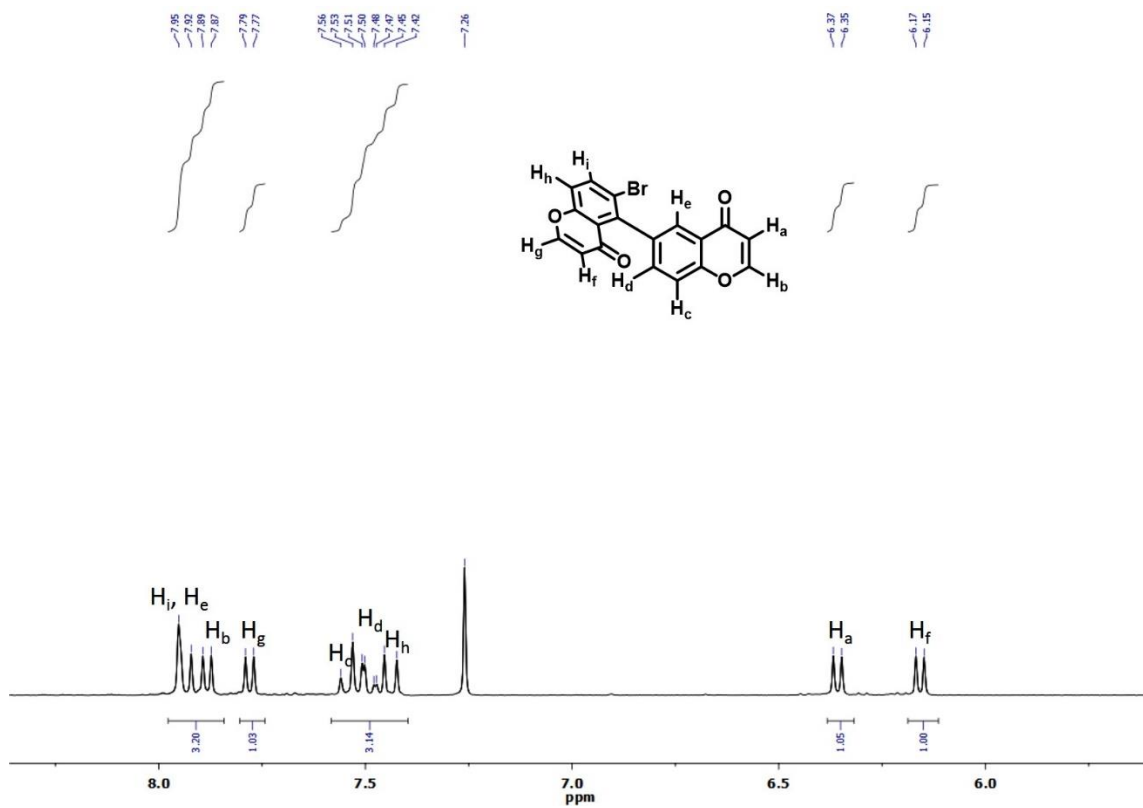
Figure 3.23. ^{1}H NMR (CDCl$_3$, 300 MHz) of the 6-bromochromone aryl coupling adduct.
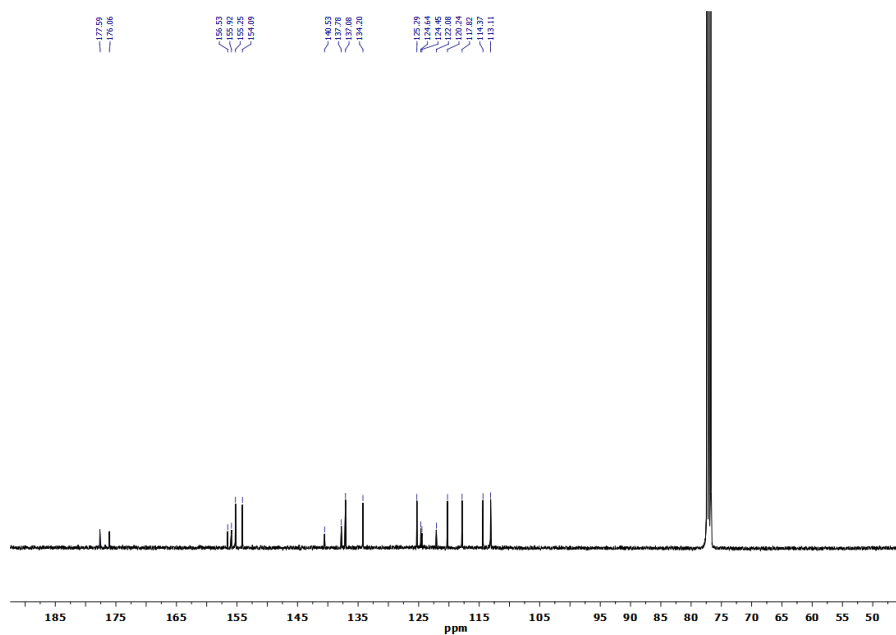
Figure 3.24. ^{13}C NMR (CDCl$_3$, 300 MHz) of 6-bromochromone aryl coupling adduct.

132

^{1}H-NMR: (300 MHz, CDCl$_3$ δ): 7.95-7.92 (m, 2H, Ar-H), 7.88 (d, J=6.0 Hz, 1H, Ar-H), 7.78 (d, J=6.0 Hz, 1H, Ar-H), 7.56-7.47 (m, 2H, Ar-H), 7.44 (d, J=9.0 Hz, 1H), 6.36 (d, J=6.0 Hz, 1H), 6.16 (d, J=6.0 Hz, 1H); ^{13}C-NMR: (100 MHz, CDCl$_3$ δ): 177.6, 176.1, 156.5, 155.9, 155.3, 154.1, 140.5, 137.8, 137.1, 134.2, 125.3, 124.6, 124.5, 122.1, 120.2, 117.8, 114.4, 113.1; HRMS (ES$^+$): [M+H]$^+$ Calculated formula for C$_{18}$H$_9$BrO$_4$: 367.9676 Found: 367.9684.
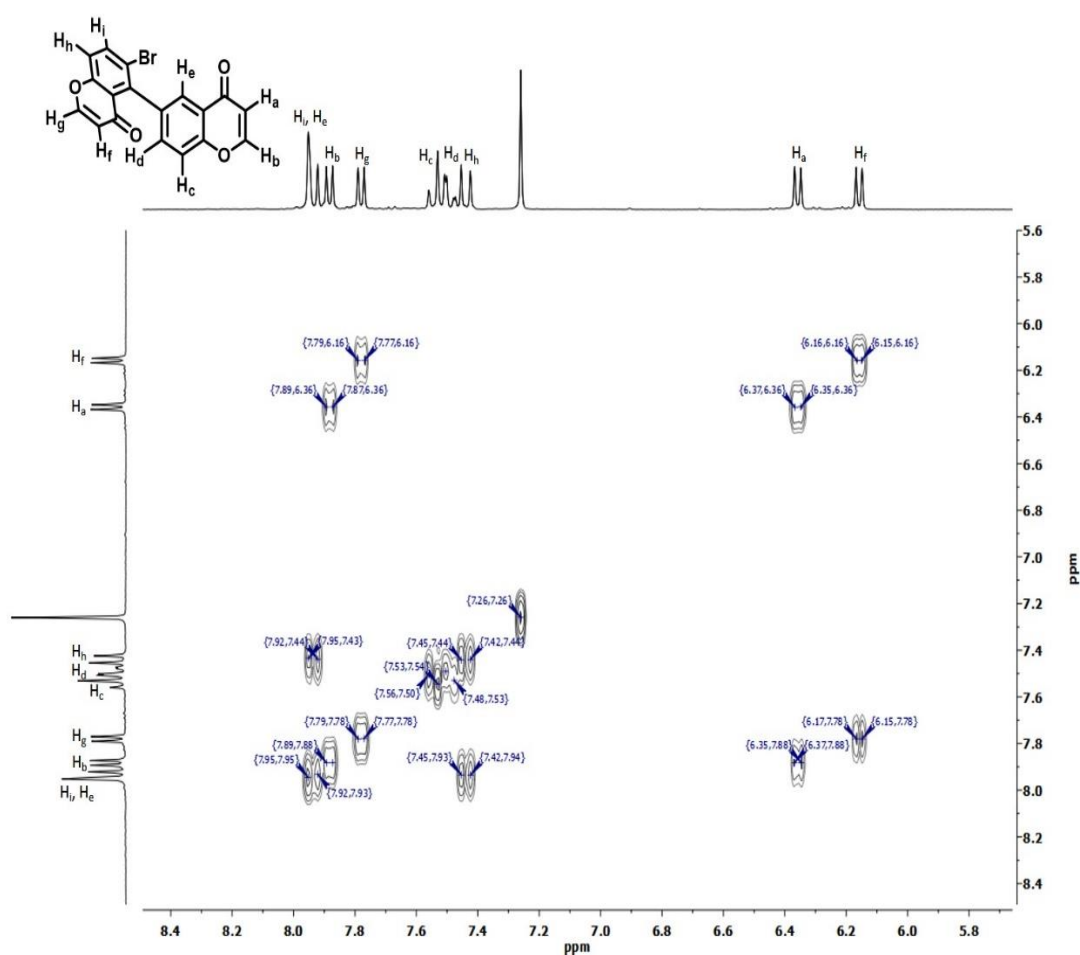
Figure 3.25. 2D COSY NMR (CDCl$_3$, 300 MHz) of 6-bromochromone aryl coupling adduct.

3.5.13. Grand Canonical Monte Carlo Simulations

Table 3.3. Moves and associated probabilities of Grand Canonical Monte Carlo simulations.

Move	Probability of move	Host 1	Guest		
Configurational bias grand canonical insertion/deletion move	0.4	0	1.0		
Move	**Probability of move**	**Host 1**	**Guest**	**Host 1**	**Guest**
Configurational bias partial molecule regrowth	0.7	0	1.0	0.5	1.0
Move	**Probability of move**	**Host 1**	**Guest**	**Maximum displacement**	**Acceptance rate**
Intramolecular single atom translation	0.8	0.3	1.0	0.5	0.5
Move	**Probability of move**	**Host 1**	**Guest**	**Maximum displacement**	**Acceptance rate**
Center of mass molecule translation	0.9	0	1.0	0.5	0.5
Move	**Probability of move**	**Host 1**	**Guest**	**Maximum displacement**	**Acceptance rate**
Rotation about the center of mass	1.0	0	1.0	0.05	0.5

Figure 3.26. GCMC simulation outcome of host **1**•chromone complex. a) Top view of the simulation cell. b) Energy minimization profile during the simulation.
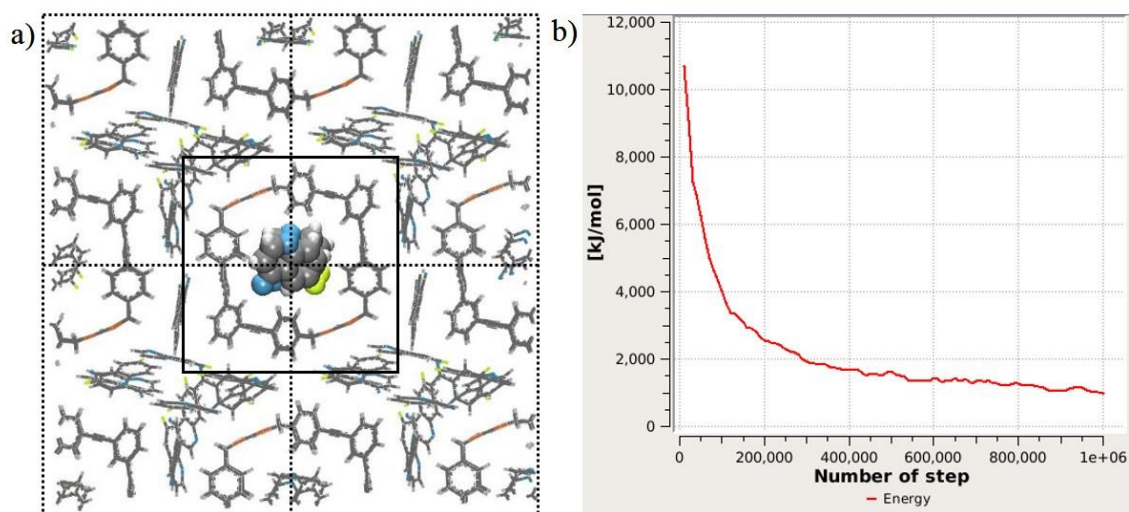
Figure 3.27. GCMC simulation outcome of host **1**• 6-fluorochromone complex. a) Top view of the simulation cell. b) Energy minimization profile during the simulation.

135
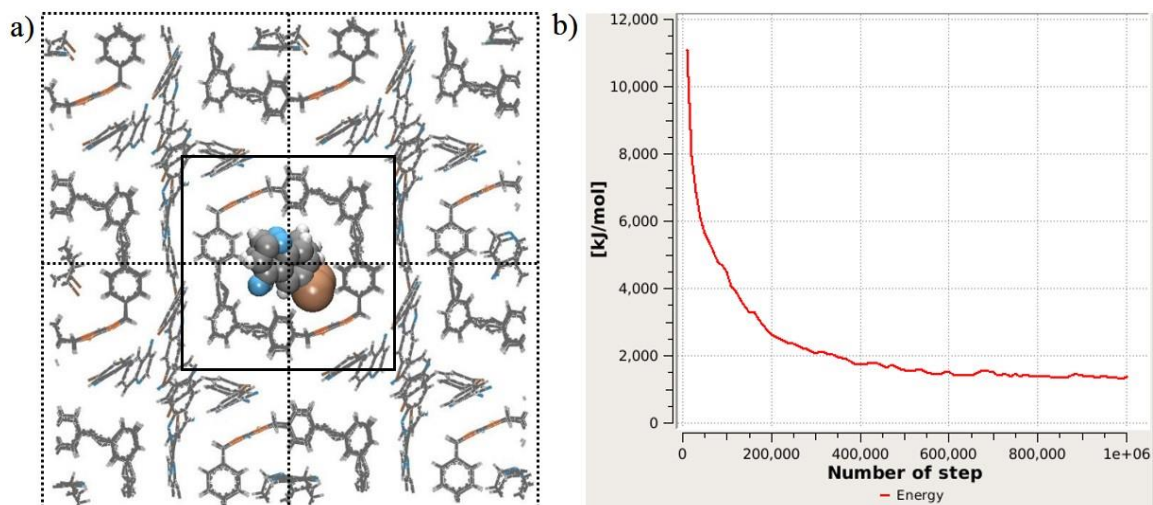
Figure 3.28. GCMC simulation outcome of host **1•** 6-bromochromone complex. a) Top view of the simulation cell. b) Energy minimization profile during the simulation.
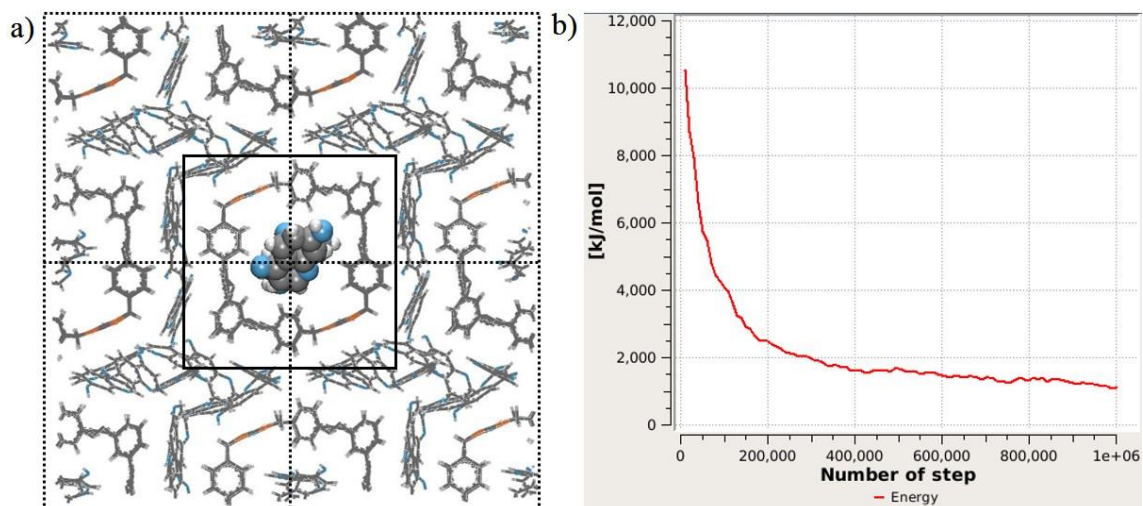
Figure 3.29. GCMC simulation outcome of host **1•**7-hydroxy-4-chromone complex. a) Top view of the simulation cell. b) Energy minimization profile during the simulation.

3.6 References

(1) Ramamurthy, V.; Gupta, S. Supramolecular photochemistry: from molecular crystals to water-soluble capsules. *Chemical Society Reviews* **2015**, *44*, 119-135.

136

(2) Ballester, P.; Fujita, M.; Rebek, J. Molecular containers. *Chemical Society Reviews* **2015**, *44*, 392-393.

(3)Ajami, D.; Rebek, J. More Chemistry in Small Spaces. *Accounts of Chemical Research* **2013**, *46*, 990-999.

(4) Ramamurthy, V.; Sivaguru, J.: Controlling Photoreactions Through Noncovalent Interactions Within Zeolite Nanocages. In *Supramolecular Photochemistry*; John Wiley & Sons, Inc., 2011; pp 389-442.

(5) Ramamurthy, V.; Parthasarathy, A. Chemistry in Restricted Spaces: Select Photodimerizations in Cages, Cavities, and Capsules. *Israel Journal of Chemistry* **2011**, *51*, 817-829.

(6) Inokuma, Y.; Kawano, M.; Fujita, M. Crystalline molecular flasks. *Nature Chemistry* **2011**, *3*, 349-358.

(7) Berryman, O. B.; Dube, H.; Rebek, J. Photophysics Applied to Cavitands and Capsules. *Israel Journal of Chemistry* **2011**, *51*, 700-709.

(8) Ramamurthy, V.; Mondal, B. Supramolecular Photochemistry Concepts Highlighted with Select Examples. *Journal of Photochemistry and Photobiology C: Photochemistry Reviews*.

(9) Shimizu, L. S.; Salpage, S. R.; Korous, A. A. Functional Materials from Self-Assembled Bis-urea Macrocycles. *Accounts of Chemical Research* **2014**, *47*, 2116-2127.

(10) Verpoorte, R.; Memelink, J. Engineering secondary metabolite production in plants. *Current Opinion in Biotechnology* **2002**, *13*, 181-187.

137

(11) Zhao, J.; Zhao, Y.; Fu, H. Transition-Metal-Free Intramolecular Ullmann-Type O-Arylation: Synthesis of Chromone Derivatives. *Angewandte Chemie International Edition* **2011**, *50*, 3769-3773.

(12) Gaspar, A.; Matos, M. J.; Garrido, J.; Uriarte, E.; Borges, F. Chromone: A Valid Scaffold in Medicinal Chemistry. *Chemical Reviews* **2014**, *114*, 4960-4992.

(13) Keri, R. S.; Budagumpi, S.; Pai, R. K.; Balakrishna, R. G. Chromones as a privileged scaffold in drug discovery: A review. *European Journal of Medicinal Chemistry* **2014**, *78*, 340-374.

(14) Yusuf, M.; Solanki, I.; Jain, P.; Kumar, R. Photochemical studies: Chromones, bischromones and anthraquinone derivatives. *Arabian Journal of Chemistry*.

(15) Sakamoto, M.; Kanehiro, M.; Mino, T.; Fujita, T. Photodimerization of chromone. *Chemical Communications* **2009**, 2379-2380.

(16) Sakamoto, M.; Yagishita, F.; Kanehiro, M.; Kasashima, Y.; Mino, T.; Fujita, T. Exclusive Photodimerization Reactions of Chromone-2-carboxylic Esters Depending on Reaction Media. *Organic Letters* **2010**, *12*, 4435-4437.

(17) Hanifin, J. W.; Cohen, E. Photoaddition reactions of chromone. *Journal of the American Chemical Society* **1969**, *91*, 4494-4499.

(18) Hanifin, J. W.; Cohen, E. Photoaddition reactions of chromome. *Tetrahedron Letters* **1966**, *7*, 5421-5426.

(19) Nath, A.; Ghosh, A.; Venkateswaran, R. V. Rapid, high-yield synthesis of the marine sesquiterpenes debromoaplysin and aplysin via the acid-catalyzed rearrangement of a cyclobutachromanol. *The Journal of Organic Chemistry* **1992**, *57*, 1467-1472.

(20) Valiulin, R. A.; Kutateladze, A. G. First example of intramolecular [] alkene–arene photocyclization in the chromone series and its synthetic utility. *Tetrahedron Letters* **2010**, *51*, 3803-3806.

(21) Dawn, S.; Dewal, M. B.; Sobransingh, D.; Paderes, M. C.; Wibowo, A. C.; Smith, M. D.; Krause, J. A.; Pellechia, P. J.; Shimizu, L. S. Self-Assembled Phenylethynylene Bis-urea Macrocycles Facilitate the Selective Photodimerization of Coumarin. *Journal of the American Chemical Society* **2011**, *133*, 7025-7032.

(22) Martin, M. G. MCCCS Towhee: a tool for Monte Carlo molecular simulation. *Molecular Simulation* **2013**, *39*, 1212-1222.

(23) Materials and Processes Simulations (MAPS), Copyright Scienomics SARL. Paris, France, 2004-2013.

(24) Dawn, S.; Salpage, S. R.; Koscher, B. A.; Bick, A.; Wibowo, A. C.; Pellechia, P. J.; Shimizu, L. S. Applications of a Bis-Urea Phenylethynylene Self-Assembled Nanoreactor for [2 + 2] Photodimerizations. *The Journal of Physical Chemistry A* **2014**, *118*, 10563-10574.

(25) C. R. Bowers, M. D., S. R. Salpage, C. Akel, H. Bhase, M. F. Geer, L. S. Shimizu Crystalline bis-Urea Nanochannel Architectures Tailored for Single-File Diffusion Studies. . *ACS Nano submitted Manuscript ID:nn-2015-018952.*

(26) Schmidt, G. M. J.: Photodimerization in the solid state. In *Pure and Applied Chemistry*, 1971; Vol. 27; pp 647.

(27) Cohen, M. D.; Schmidt, G. M. J.; Sonntag, F. I. 384. Topochemistry. Part II. The photochemistry of trans-cinnamic acids. *Journal of the Chemical Society (Resumed)* **1964**, 2000-2013.

(28) Cohen, M. D.; Schmidt, G. M. J. 383. Topochemistry. Part I. A survey. *Journal of the Chemical Society (Resumed)* **1964**, 1996-2000.

(29) Biradha, K.; Santra, R. Crystal engineering of topochemical solid state reactions. *Chemical Society Reviews* **2013**, *42*, 950-967.

(30) Staples, R. J.; Lea, W.: Crystal structure of 6-bromochromone, C9H5BrO2. In *Zeitschrift für Kristallographie - New Crystal Structures*, 2005; Vol. 220; pp 371.

(31) Salpage, S. R. S., M. D.; Shimizu, L. S., in preparation.

(32) Martin, M. G.; Frischknecht, A. L. Using arbitrary trial distributions to improve intramolecular sampling in configurational-bias Monte Carlo. *Molecular Physics* **2006**, *104*, 2439-2456.

(33) Martin, M. G.; Thompson, A. P. Industrial property prediction using Towhee and LAMMPS. *Fluid Phase Equilibria* **2004**, *217*, 105-110.

(34) Spartan 10, P. f. C. o. M. P.; Wavefunction Inc.: Irvine, C., USA.

(35) Orlov, V. D.; Borovoi, I. A.; Tishchenko, V. N.; Lavrushin, V. F. Polarity of chromone and flavone molecules. *Theor Exp Chem* **1975**, *10*, 73-75.

(36) Moon, Y.; Hong, S. A facile route to isoflavone quinones via the direct cross-coupling of chromones and quinones. *Chemical Communications* **2012**, *48*, 7191-7193.

(37) Samanta, R.; Narayan, R.; Antonchick, A. P. Rhodium(III)-Catalyzed Direct Oxidative Cross Coupling at the C5 Position of Chromones with Alkenes. *Organic Letters* **2012**, *14*, 6108-6111.

(38) SMART Version 5.631, SAINT+ Version 6.45a.; Bruker Analytical X-ray Systems, Inc.: Madison, Wisconsin, USA., 2003.

(39) Sheldrick, G. A short history of SHELX. *Acta Crystallographica Section A* **2008**, *64*, 112-122.

(40) Dolomanov, O. V.; Bourhis, L. J.; Gildea, R. J.; Howard, J. A. K.; Puschmann, H. OLEX2: a complete structure solution, refinement and analysis program. *Journal of Applied Crystallography* **2009**, *42*, 339-341.

(41) Mayo, S. L.; Olafson, B. D.; Goddard, W. A. DREIDING: a generic force field for molecular simulations. *The Journal of Physical Chemistry* **1990**, *94*, 8897-8909.

CHAPTER IV

PHOTOPOLYMERIZATION OF ISOPRENE IN A SELF-ASSEMBLED *BIS*-UREA NANOREACTOR*

4.1 Abstract

Porous organic crystalline materials with one dimensional channels of ~4.5 Å were obtained by the assembly of pyridine-phenylethynylene *bis*-urea macrocycle. These organic nanoreactors were applied to absorb isoprene and to facilitate the stereoselective polymerization to exclusively produce *trans*-1, 4- polyisoprene with low PDI under mild conditions.

4.2 Introduction

Isoprene is widely used in industry to synthesize block copolymers,[1-3] as compatibilizers for natural rubber and acrylic polymer blends,[4,5] as nanocomposites,[6,7] and to produce macromolecular core shell nano architectures.[8,9] These materials can have low glass transition temperatures, degradability, and unsaturated backbone or side chains that allow further functionalization at later stages.[10] Isoprene has a conjugated diene moiety, and its conventional polymerization can provide various isomeric polymers through different addition modes (cis-1,4-; trans-1,4-, 1,2- or 3,4) depending upon how the C-C double bonds react (Figure 4.1a).[11] The *trans*-1,4 (Balata), which is produced by plants using enzymatic synthesis, is considered the most important variant and exhibits thermoplastic characteristics, high tensile strength, abrasion resistance, and is free from odor and taste.[12,13] However, stereoselective synthesis of *trans*-1,4-polyisoprene remains a challenge. Confined environments have been applied for the selective radical polymerization of isoprene trapped within the controlled pores; however, typically gamma irradiation is required necessitating careful handling and specialized reactors.[14] Here, we report the synthesis and self-assembly of a pyridyl phenylethynylene *bis*-urea

macrocycle 1 to afford a new functional porous organic crystal with regular 1-dimensional channels of ~ 4.5 Å. This new material is applied for the polymerization of isoprene with high selectivity and afforded *trans*-1,4-polyisoprene upon mild UV-irradiation (Figure 4.1b).
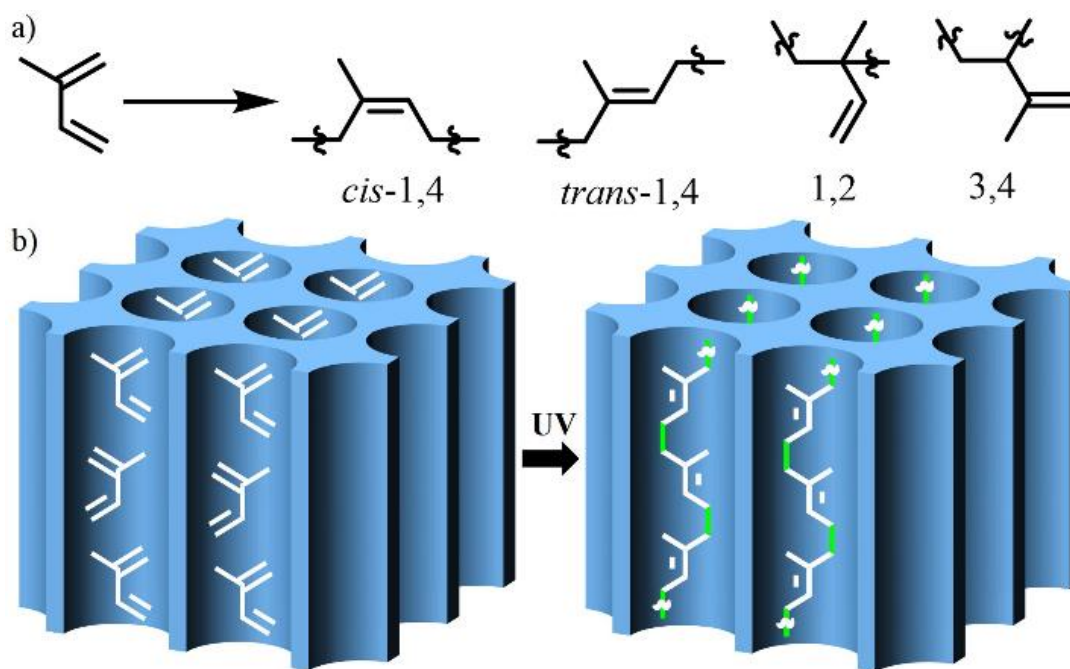
Figure 4.1. Conventional synthesis compared to stereoselective polymerization of isoprene in the pyridyl phenylethynylene *bis*-urea. (a) Addition modes of isoprene during conventional polymerization leads to multiple isomers. (b) Photo irradiation of isoprene in host 1 produce *trans*-1,4-polyisoprene in high selectivity.

Porous materials have demonstrated utility in catalysis, storage, and molecular separations as well as emerging uses in new technology for energy and medicine.[15] Such confined functional materials offer as the potential to carry out reactions in high selectivity under relatively mild conditions.[16-19] Confined media including crystals, inclusion complexes, microporous zeolites, coordination polymers and mesoporous

materials have been investigated as media to perform topochemically driven inclusion polymerization reactions[20-25] For example narrow channels of urea, thiourea, deoxycholic acid (DCA), and perhydrotriphenylene (PHTP), have been used to polymerize variety of diene monomers to obtain stereoregular polymers.[14] Stereoregular polymers are typically high-strength materials due to the enhanced packing of the more uniform polymer chains. Stereocontrolled polymerization of isoprene within tunnels of clathrates formed by tris(*o*-phenylenedioxy)cyclotriphosphazene and porous dipeptide crystals have been reported to yield *trans*-1,4-polyisoprene in high selectivity.[26,27] High energy gamma rays were used to generate initial radicals needed for polymerization and resultant polymers were separated by either using $CHCl_3/H_2O$ or refluxing the host·isoprene conjugate for 48 h in benzene

Our group investigates the use of porous well-defined materials from self-assembled utilizes *bis*-urea macrocycles building blocks that consist of two urea groups and two C-shaped spacers. When the urea groups are preorganized approximately perpendicular to the plane of the macrocycle and in the absence of competing hydrogen bond acceptors, these macrocycles assemble into columnar structures.[28] For example, phenylethynylene *bis*-urea 2 assembled into columns of ~ 9 Å in diameter (Figure 4.2c), affording functional crystals that were applied to the photodimerizations of coumarins, chromones and acenaphthylene.[29-31] Here, we replace the central aryl group of that C-spacer with pyridine to test the effects of the pyridyl group on the subsequent assembly (Figure 4.2a) into a porous crystal. We then demonstrate the utility of this porous organic crystal for the polymerization of isoprene.

4.3 Results and discussion

The *bis*-urea macrocycle was synthesized in four steps from commercially available 2, 6-dibromopyridine using a protected urea, triazinanone strategy employed previously (Scheme 4.1). The protected macrocycle crystallized by slow evaporation as the CH_2Cl_2 solvate and shows the urea groups preorganized approximately perpendicular and pointing to the same side of the macrocycle (Figure 4.14). Following deprotection, the host (20 mg / 4 mL DMSO) was crystallized by vapour diffusion of methanol affording pale yellow needle crystals suitable for single crystal X-ray diffraction. The crystal structure revealed the expected *bis*-urea macrocycle as a solvate; however, macrocycle 1 was not planar but folded into a bowl or saddle conformation with C2 point symmetry (Figure 4.2b). Here, the two urea groups point in the same direction. This folded architecture assembles through typical bifurcated urea hydrogen bonds (N(H)•••O distances of 2.81-2.87 Å) with four neighbouring macrocycles to afford 2D assemblies of interdigitated cycles (Figure 4.2d). The packing of the layers creates tubular channels of ~4.5 Å in diameter along the crystallographic *b* axis (Figure 4.2e). The channels are occupied by disordered solvent molecules (DMSO and/ or MeOH). Adjacent layers alternate ureas in an *anti*-parallel fashion resulting in a cancellation of the dipoles. The assembly is further stabilized by aryl stacking and CH-pi interactions. The crystalline structures have regular and aligned 1-dimensional pores with diameters of ~ 4.5 Å (Figure 4.13).
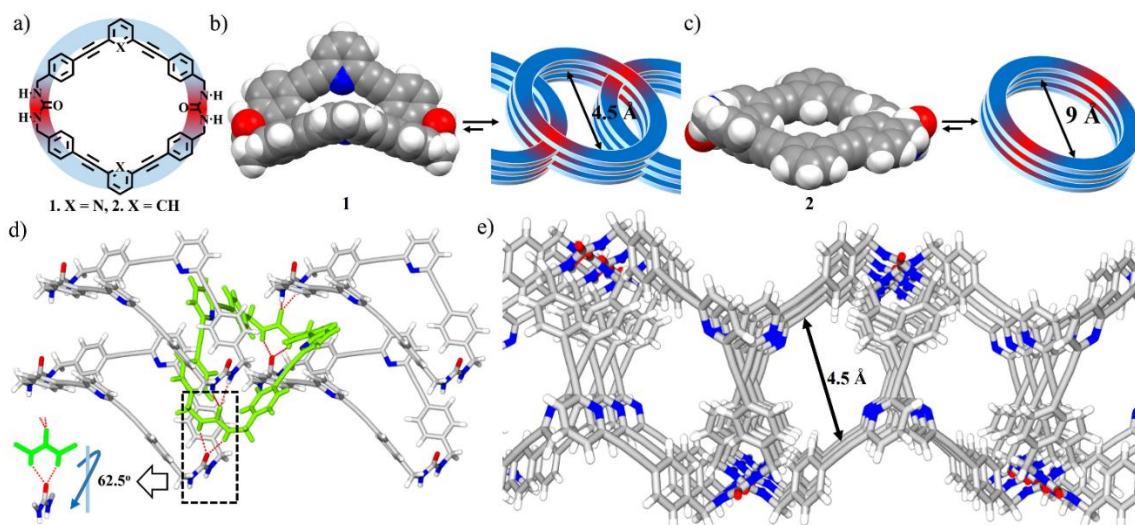
Figure 4.2. Assembly of 1 and comparison with 2. (a) Chem draw structure of hosts 1 (X = N) and 2 (X= CH). (b) Macrocycle 1 adopts a saddle structure that self assembles into interdigitated layers shown schematically. (c) Macrocycle 2 is relatively planar and affords columnar structures with much larger diameters ~ 9 Å.[29] (d) A single macrocycle forms bifurcated urea hydrogen bonds with four neighbouring cycles with N(H)•••O distances of 2.81-2.87 Å. This interdigitated assembly twists the urea groups 62.5°. (e) 2D zigzag layers form parallel to the *ab* plane with adjacent layers packing in an *anti*-parallel fashion to afford 1D channels along the *b*-axis.

The conformational difference between the saddle structure of 1 (X = N) with the relatively planar conformation of the previously reported 2 (X = CH) is striking and appears to drive the interdigitated assembly of 1 over the columnar assembly of 2. The calculated density of 1 is 1.028 mg/mm^3 (orthorhombic, space group *Pbcn*) and a solvent accessible volume of unit cell estimated as 1341.4 Å^3 (28.6% of the total unit cell volume). In comparison columnar assembled 2 (monoclinic, space group P2$_{1/n}$) has a density of 1.230 mg/mm^3 and a solvent-accessible volume of the unit cell estimated as 491.1 Å^3 (21.6% of the total unit cell volume).

We further compared the assemblies using Hirshfeld analysis.[32-34] Interestingly, the two assembly motifs show similar contributions of key interactions including hydrogen bonding (1: 5.5% vs. 2: 6.1% O…H), and CH-aryl interactions (1: 26.5% vs 2:

147

26.4% C…H contacts) but showed small differences in aryl stacking interactions (1: 7% vs. 2: 11.7% C…C) as well as contacts to nitrogen (1: 4.3% vs. 2: 1.4% N…H) (Figure 4.15 and 4.16). A screen of crystallization conditions has not yet yielded other crystal forms.

The smaller diameter channels of 1 versus 2 (4.5 vs. 9 Å) are comparable to channels in inclusion complexes of isoprene with dipeptides and cyclotriphosphazenes, which have been previously reported to facilitate isoprene polymerization.[26,27] Thus, our next goal was to test the ability of 1 to absorb isoprene. Initially, the channels of 1 are filled with solvent, which was removed prior to the introduction of isoprene.

Thermogravimetric Analysis (TGA) showed two step desorption from rt to 250 °C with a 9.98% weight loss. The crystals were also heated at 120 °C for 3 h resulting in a similar weight loss (Figure 4.17). Removal of the disordered solvent did not change the morphology of the crystals. Powder X-ray diffraction (PXRD) was used to compare the solvated and activated structures before and after solvent removal (Figure 4.3b). Comparison of the two PXRD patterns show they are nearly identical suggesting that the material still maintains its crystallinity after solvent evaculation.

Freshly recrystallized 1 (20 mg) was heated at 120°C to remove the disordered solvent and further evacuated under high vacuum before exposure to isoprene under reduced pressure at room temperature for 3 h. A custom made loading apparatus was used to absorb Isoprene from its vapor phase under reduce pressure at room temperature for 24 h, conditions which likely lead to an equilibrium for diffusion (Figure 4.3a).
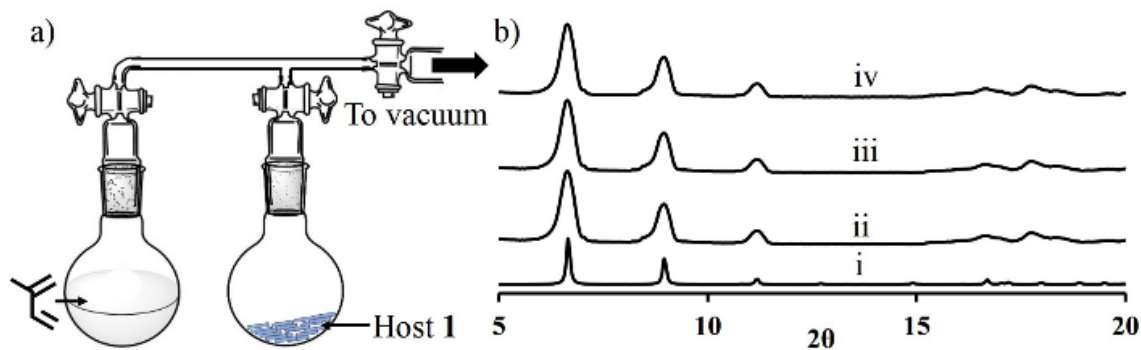
Figure 4.3. Vapor loading of isoprene into the host 1 and PXRD analysis. (a) Schematic of the loading apparatus was used to load isoprene form its vapor phase under reduced pressure. (b) PXRD analysis of the host 1 and host 1·polymer conjugate. (i) Calculated PXRD pattern of empty host 1. (ii) Powder pattern of host 1 with trapped solvents. (iii) Powder pattern of host 1 after heated at 120 °C. (iv) Powder pattern of host 1·polymer conjugate.

The host 1·isoprene complex frozen in liquid N_2, vacuum sealed and UV-irradiated in a Rayonet RPR-200 UV reactor equipped with 350 nm for 24 h at rt. The irradiated complex showed similar PXRD pattern suggesting that the crystal form was not altered during the loading process and the subsequent reaction (Figure 4.3b, patterns iii and iv). The polymer was then extracted from the complex by sonication with $CHCl_3$ (10 mL). The suspension of host 1 and polymer was filtered to recover the host and the filtrate concentrated *in vacuo*. Polyisoprene was precipitated by the dropwise addition of ice-cold methanol.

The products displayed the simple 1H NMR spectra shown in Figure 4.4a. The polymer microstructure consists mainly of *trans*-1, 4-isoprene in 96.7% with 3.3% *cis*-1, 4-isomer. The absence of signals at ~5.9 ppm and ~4.7 ppm indicated that no significant amount of the branched 1,2-or 3,4-structures had been formed. Gel Permeation Chromatography (GPC) was used to analyze the molar mass of the resulting polymer. The polymer shows a Mw = 6129 g mol^{-1} with a dispersity (*Đ*) of 1.39 (Figure 4.4b). The

149

average length of the channels in the bulk material was estimated from dark field microscope images as ~212.8 μm. Assuming isoprene is fully absorbed in channels of **1**, the rough maximum Mw is ~3.02 x 107 g mol^{-1}.

Studies are underway to probe conditions that may enhance the degree of polymerization including lower temperatures and shorter UV-irradiation times. Evacuated host **2** (20 mg) was exposed to isoprene and similarly UV-irradiated; however, no oligomers or polymers were formed, suggesting that isoprene has a low affinity for the larger channels of **2** or is not reactive within these channels.

Isoprene, which has a low boiling point, desorbs from these hosts at room temperature as the sample warms over the 24 h irradiation period. Thus, the reasonably high molecular weight polymer obtained by UV-irradiation of isoprene in the confined environment of 1 suggests that either isoprene is bound and unusually stable within the pores of 1 or that the reaction proceeds relatively quickly before isoprene has a chance to desorb.

Recent work from Kitagawa and coworkers on the radical polymerization of 2,3,-dimethyl-1,3-butadiene in a porous coordination polymer suggests that the confined environment stabilizes the propagating radicals and inhibits radical termination.[35] Studies are currently underway to examine the isoprene polymerization in host 1 at lower temperatures and shorter UV-irradiation times as well as probing this presumably radical mediated process by electron spin resonance (ESR), to see if similar stabilization is observed in 1.

150
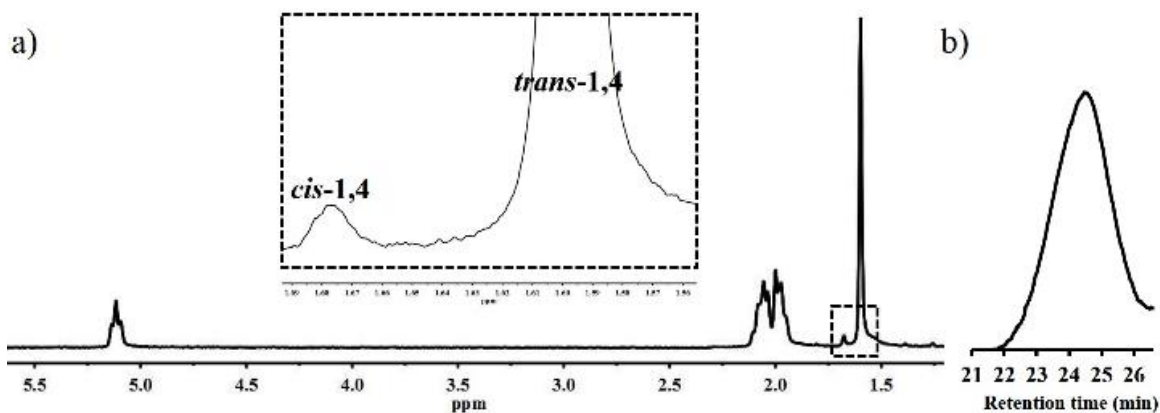
Figure 4.4. Characterization of the isolated polyisoprene. (a) ^{1}H NMR (CDCl$_3$, 400 MHz) of the polyisoprene. (b) GPC trace of polyisoprene.

4.4 Conclusions

In conclusion, we have designed, synthesized, and applied a new porous crystalline material for the selective polymerization of isoprene. The pyridine-phenylethynylene *bis*-urea host's 1D channels were used to absorb isoprene and initiated its polymerization by mild UV-irradiation. Within the confined channels of 1, we observed the selective formation of *trans*-1, 4 polyisoprene. The resulting polymer was be easily released from the host by sonication in CHCl$_3$, and host 1 was recovered by filtration and reused. The structure of the host 1 was remarkably robust and stable throughout the process of removing solvents, isoprene loading, polymerization and recovery. The NMR and GPC analysis of the polymer indicates a 96.7% *trans* content and low PDI for a radical polymerization. We are currently studying alternative methods for extruding the polyisoprene from the crystalline nanoreactor. Future studies will be focused on the use pyridine-phenylethynylene *bis*-urea host as confined media to control the tacticity of polymers of other vinyl monomers.

151

4.5 Experimental

4.5.1 Materials and Methods

All chemicals were purchased from Sigma-Aldrich or VWR and used without further purification. Triazinanone was prepared as previously described.[36] ^{1}H-NMR and ^{13}C-NMR spectra were recorded on Varian Mercury/VX300 or VX400. PXRD data was collected on Rigaku Dmax 2200 powder X-ray diffractometer using Cu Kα radiation. The step-scans were collected at +0.05° steps at an angular range of 2−20° 2θ at ambient conditions. TGA data were collected on TA SDT Q600. UV-irradiations were performed in a Rayonet reactor equipped with 16 × 120 W lamps (350 nm). GPC data were collected using Varian 290-Lc using polystyrenes as the standard.

4.5.2. Synthesis of the *bis*-urea macrocycle 1
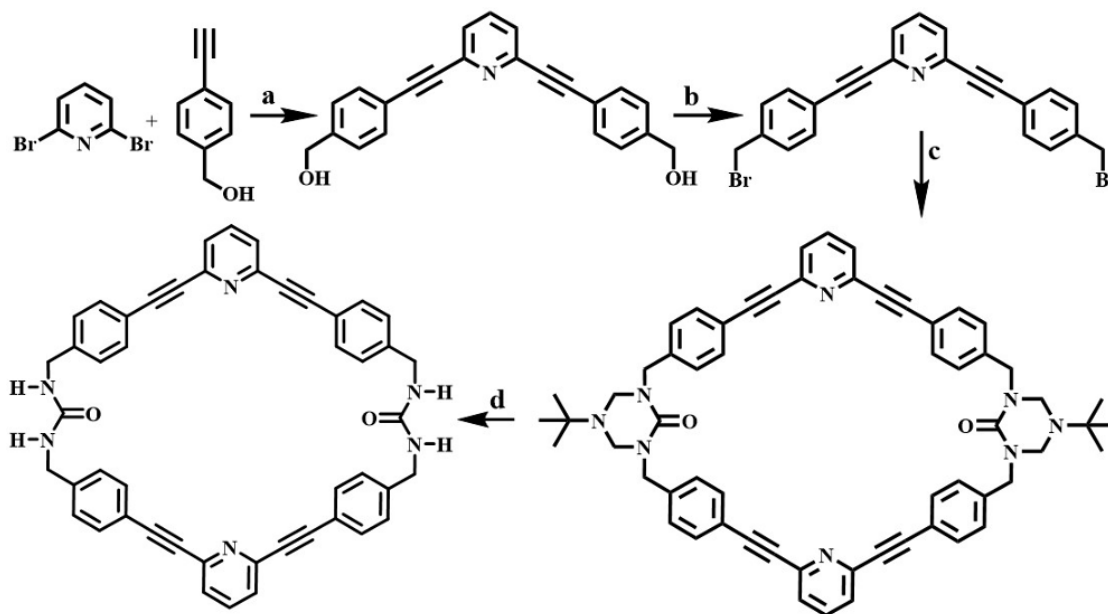
Scheme 4.1. Synthesis of the macrocycle. (a) Pd(PPh₃)₂Cl₂, TBAF•3H₂O, 80 ºC (b) NBS/ PPh₃, THF, -10 °C to rt (c) Triazinanone, NaH, THF, reflux (d) 1:1 of 20% [NH(CH₂CH₂OH)₂/H₂O, adjusted with HCl to pH~2] : MeOH, reflux.

Synthesis of the diol compound.[37]
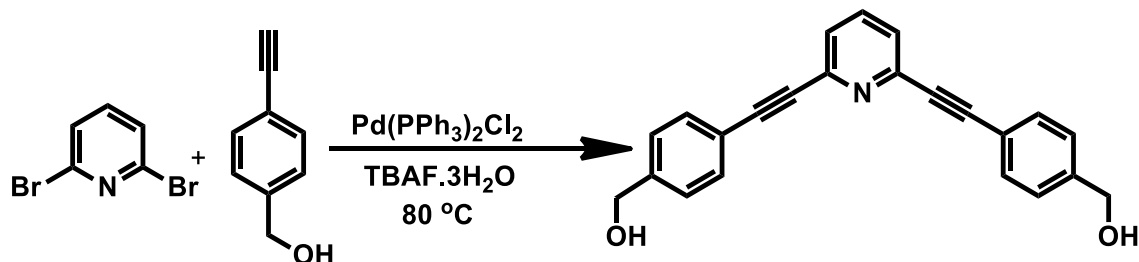
Scheme 4.2. Synthesis of the diol compound.

To an oven dried flask, 2, 6-dibromopyridine (1.0 g, 4.22 mmol), 4-ethynylbenzyl alcohol (1.23 g, 12.7 mmol) and bis(triphenylphosphine)palladium(II) dichloride (0.18 g, 2.53 x 10^{-1} mmol) were added under nitrogen. Next, TBAF. $3H_2O$ (6.6 g, 25.3 mmol) was added, and the mixture was heated to 110 °C in an oil bath for 10 minutes. The reaction mixture was then stirred at 80 °C for 48 h. The reaction mixture was dissolved in acetonitrile (100 mL) and dried *in vacuo*. The crude product was purified by flash chromatography in dichloromethane : methanol (95 : 5). Product was further washed with water followed by hexane to remove excess TBAF. 3 H_2O and dried *in vacuo* to obtain the diol as pale yellow solid 1.3 g, (91%); mp. 221 °C; ^{1}H-NMR: (400 MHz, DMSO δ): 7.93-7.89 (t, 1H, *J*=8.1 Hz, Ar-H), 7.65 (d, *J*=7.8 Hz, 4H, Ar-H), 7.60 (d, 4H, *J*=8.1 Hz, Ar-H), 7.41 (d, *J*=8.1 Hz, 2H, Ar-H), 5.35 (t, *J*=5.8 Hz, 2H, -OH), 4.55 (d, *J*=5.7 Hz, 4H, -CH$_2$); ^{13}C-NMR: (100 MHz, DMSO): δ 145.16, 143.48, 138.45, 132.30, 127.39, 127.33, 119.89, 89.82, 88.59, 63.13; IR (cm^{-1}): 3340, 3315, 2214, 1440, 1244, 1163, 804; HRMS (EI+): [M+] Calculated: 339.1259 Found: 339.1260.
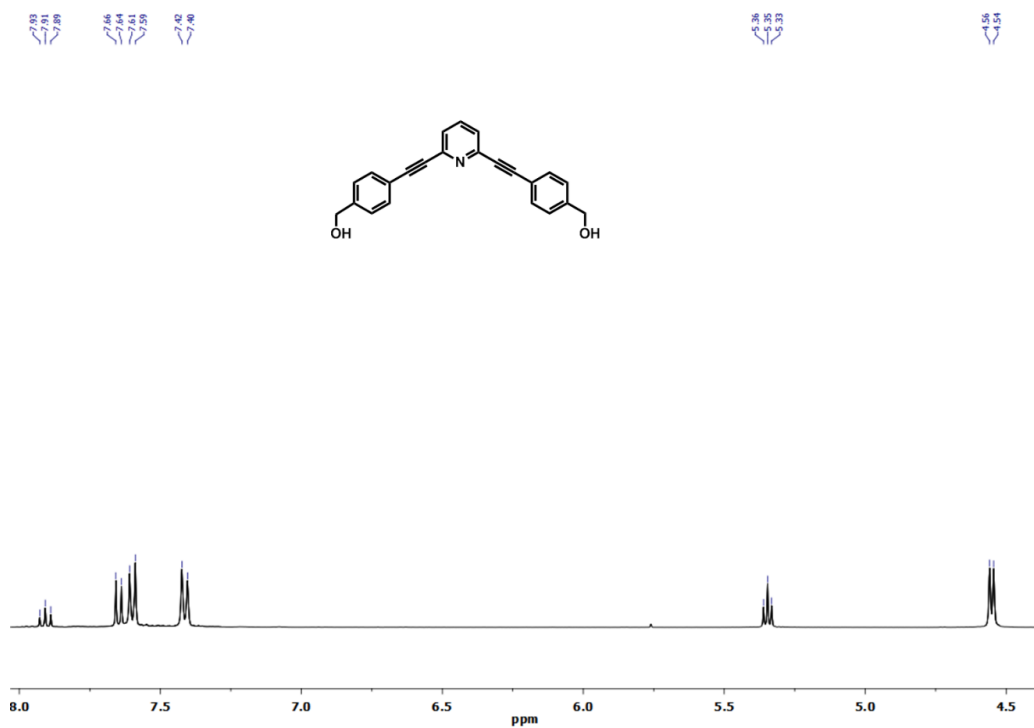
Figure 4.5. ^{1}H-NMR (CDCl$_3$, 400 MHz) of the diol compound.
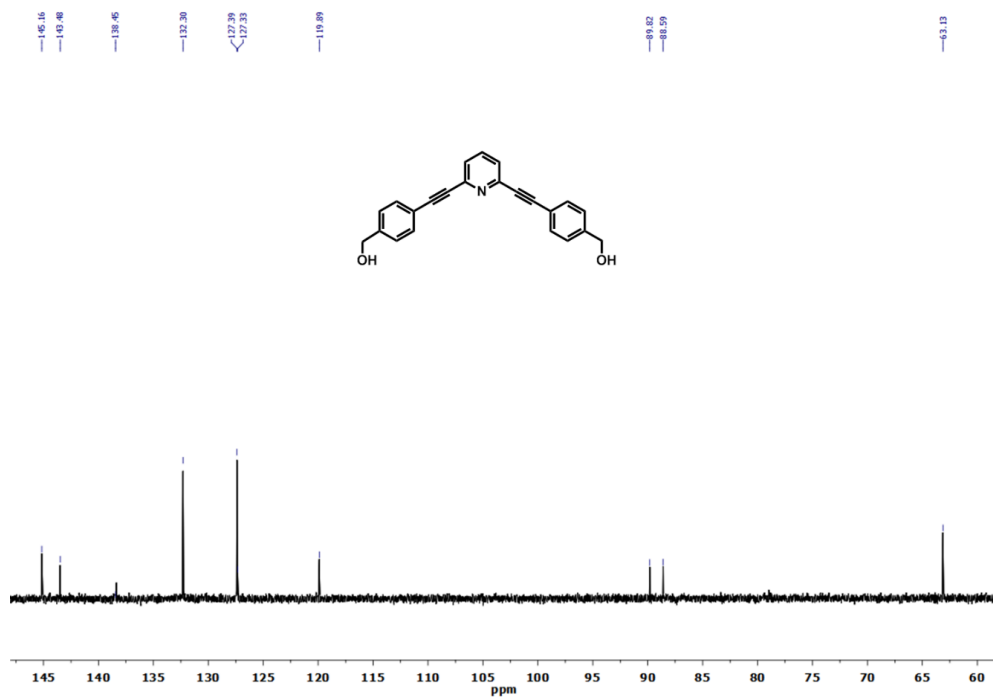
Figure 4.6. ^{13}C-NMR (CDCl$_3$, 100 MHz) of the diol compound.

Synthesis of the dibromide compound:
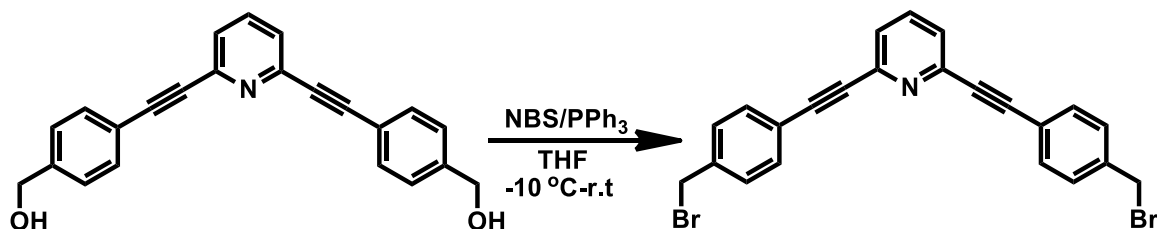
Scheme 4.3. Synthesis of the dibromo compound.

The diol (1.0 g, 2.94 mmol) was dissolved in dry THF (150 mL), and the solution was cooled in ice/acetone bath to -10 °C. Next, N-bromosuccinimide (1.26 g, 7.07 mmol) and triphenylphosphine (1.70 g, 6.48 mmol) were added simultaneously to the reaction mixture. The reaction was warmed to room temperature. After 12 h, the reaction was quenched with saturated aqueous $NaHCO_3$ and extracted with CH_2Cl_2 (100 mL x 2). Then the solvent was evaporated *in vacuo* and the crude reaction mixture was purified by flash chromatography in dichloromethane : hexanes (1 : 1) eluent to obtain the dibromide as pale yellow solid 0.9 g, (66%); mp. 183 °C; ^{1}H-NMR: (400 MHz, CD_3Cl δ): 7.75-7.64 (t, J=8.2 Hz, 1H, Ar-H), 7.58 (d, J=7.2 Hz, 4H, Ar-H), 7.48 (d, 4H, J=7.8 Hz, Ar-H), 7.39 (d, J=8.2 Hz, 2H, Ar-H), 4.49 (s, 4H, -CH_2); ^{13}C-NMR: (100 MHz, CD_3Cl) δ: 143.88, 138.91, 136.75, 132.72, 129.36, 126.66, 122.42, 89.32, 89.20, 33.04 ; IR (cm^{-1}): 3315, 2214, 1440, 1244, 1163, 804; HRMS (EI+): [M+] Calculated: 462.9571 Found: 462.9590.
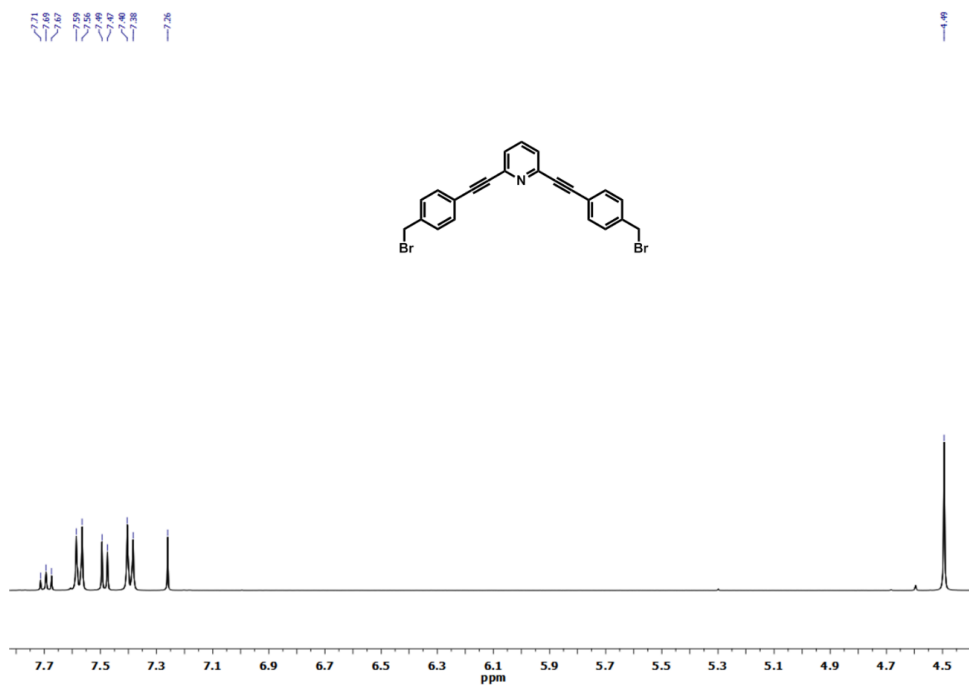
Figure 4.7. ^{1}H-NMR (CDCl$_3$, 400 MHz) of the dibromo compound.
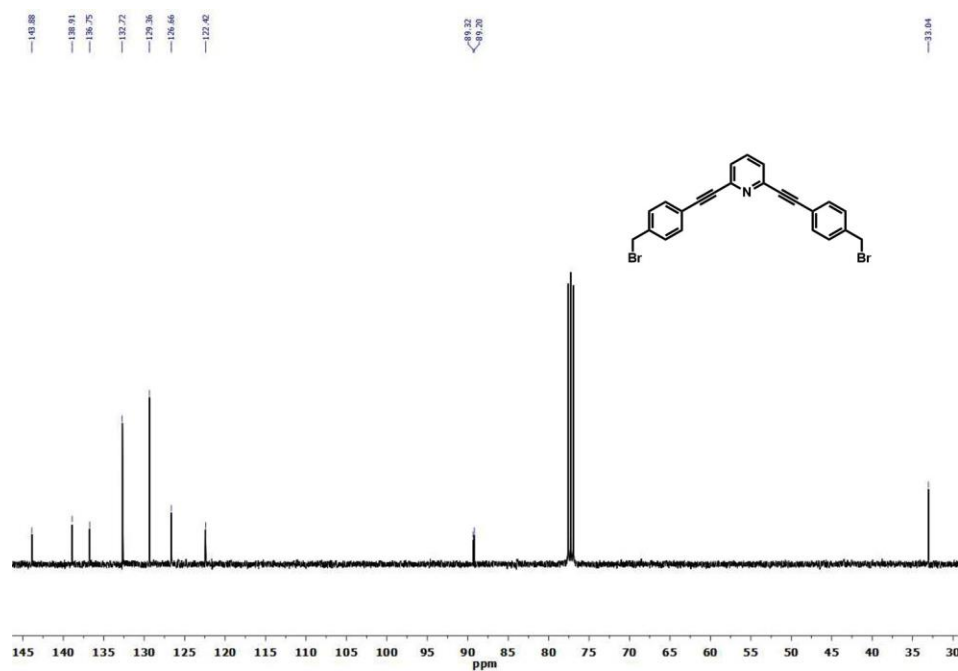
Figure 4.8. ^{13}C-NMR (CDCl$_3$, 100 MHz) of the dibromo compound.

156

Synthesis of the protected macrocycle:

Scheme 4.4. Synthesis of the protected macrocycle.

Triazinanone (0.326 g, 2.15 mmol) and NaH (0.345 g, 8.62 mmol) were heated to reflux for 1 h in dry THF (150 mL). The solution was cooled to room temperature and dibromide spacer (1.00 g, 2.15 mmol) in dry THF (100 mL) was added. Next, the reaction mixture was heated at reflux for 48 h. The reaction was quenched with H_2O (10 mL) and THF removed *in vacuo*. The solution was then extracted with dichloromethane (100 mL x 3). Combined organic layers were washed with brine and crude reaction mixture was purified by flash chromatography in silica with dichloromethane : ethyl ether : methanol (4 : 4 : 0.5) eluent to obtain the product as pale yellow solid 0.19 g (19%). ; ^{1}H-NMR: (300 MHz, CDCl$_3$ δ): 7.70-7.61 (m, 2H, Ar-H), 7.63-7.57 (m, 8H, Ar-H), 7.47-7.45 (m, 8H, Ar-H), 7.36-7.34 (m, 4H, Ar-H), 4.59 (s, 8H, -CH$_2$-), 4.25 (s, 8H, -CH$_2$-), 0.96 (s, 18H, -CH$_3$); ^{13}C-NMR: (100 MHz, CDCl$_3$ δ): 155.87, 143.87, 139.46, 136.40, 132.50, 128.15, 125.96, 121.16, 89.45, 88.49, 61.82, 54.38, 48.59, 28.24; IR (cm^{-1}): 3315, 2214, 1630, 1440, 1244, 1163, 804; HRMS (ES+): [M+H]$^+$ Calculated: 921.4604 Found: 921.4582.

157

www.manaraa.com
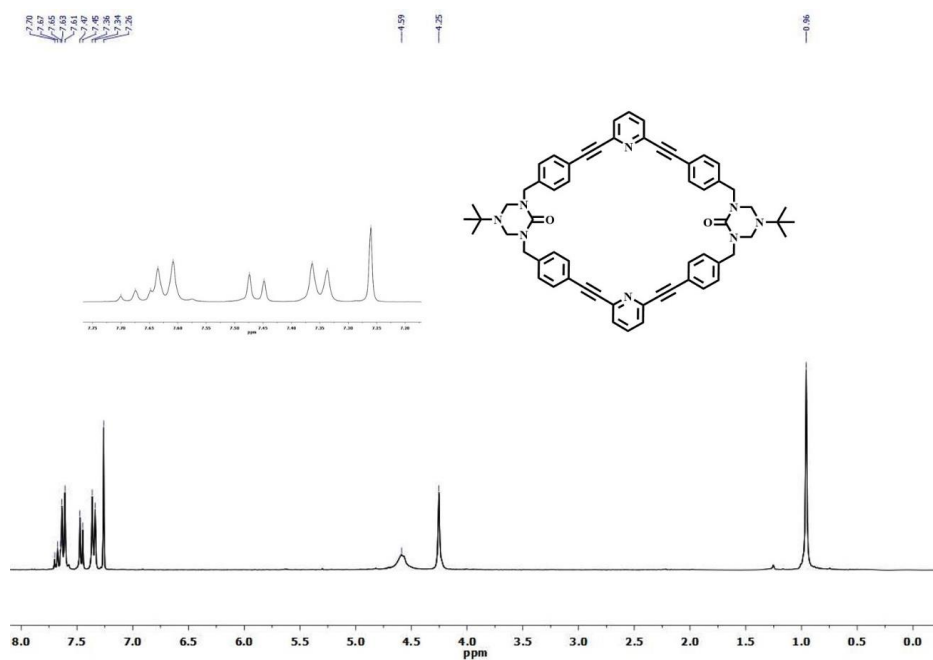
Figure 4.9. ^{1}H-NMR (CDCl$_3$, 300 MHz) of the protected macrocycle.
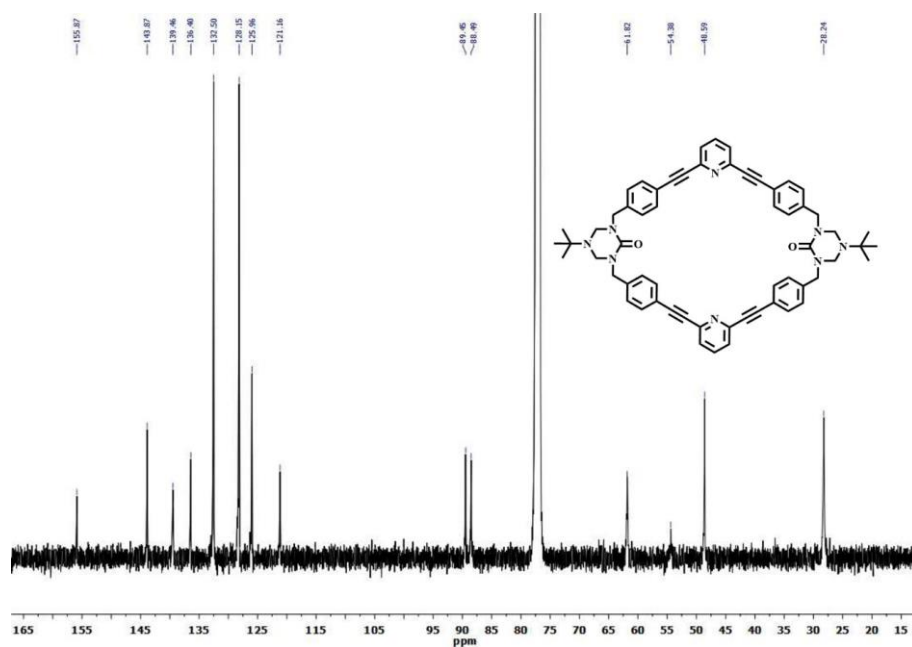
Figure 4.10. ^{13}C-NMR (CDCl$_3$, 100 MHz) of the protected macrocycle.

158

Deprotection to afford the *bis*-urea macrocycle:
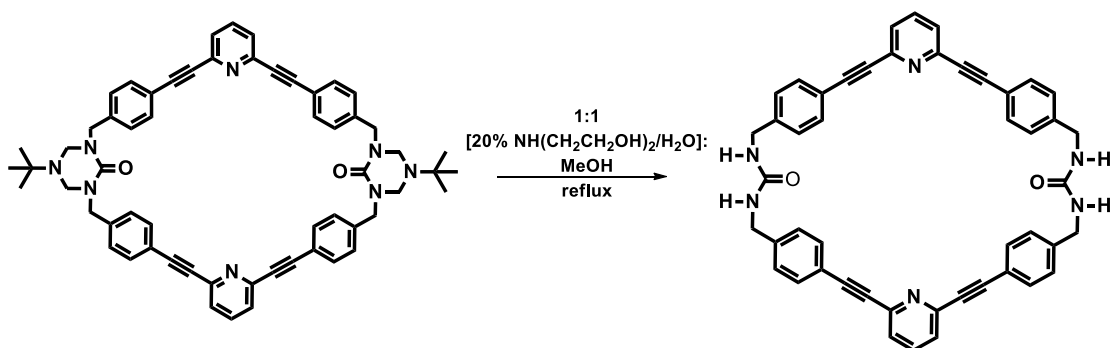
Scheme 4.5. Deprotection to afford the target *bis*-urea macrocycle.

Triazinanone protected macrocycle (0.2 g, 2.17 X 10^{-1} mmol) was added to 80 mL of a 1:1 mixture of 20% [NH(CH$_2$CH$_2$OH)$_2$/H$_2$O, adjusted with HCl to pH~2] : MeOH and heated to reflux for 48 h. A pale yellow precipitate formed after 24 h. The solution was cooled to room temperature and placed in an ice bath for 30 min. The product was suction filtered and washed with H$_2$O (30 mL) and methanol (30 mL). The residue was dried *in vacuo* to obtain the final product as pale yellow powder 0.14 g (90%). ^{1}H-NMR: (400 MHz, DMSO δ): 7.91-7.87 (m, 2H, Ar-H), 7.64-7.60(m, 12H, Ar-H), 7.33-7.31 (m, 8H, Ar-H), 6.69 (t, *J*=6.2 Hz, 4H, -NH), 4.30 (d, *J*=6.1 Hz, 8H, -CH$_2$); ^{13}C-NMR: (100 MHz, DMSO δ): 158.54, 143.84, 143.29, 138.07, 132.28, 127.53, 127.09, 119.60, 89.48, 88.50, 43.01; IR (cm^{-1}): 3315, 2214, 1630, 1554, 1440, 1244, 1163, 804; HRMS (ES+): [M+H]$^+$ Calculated: 727.2821 Found: 727.2795.
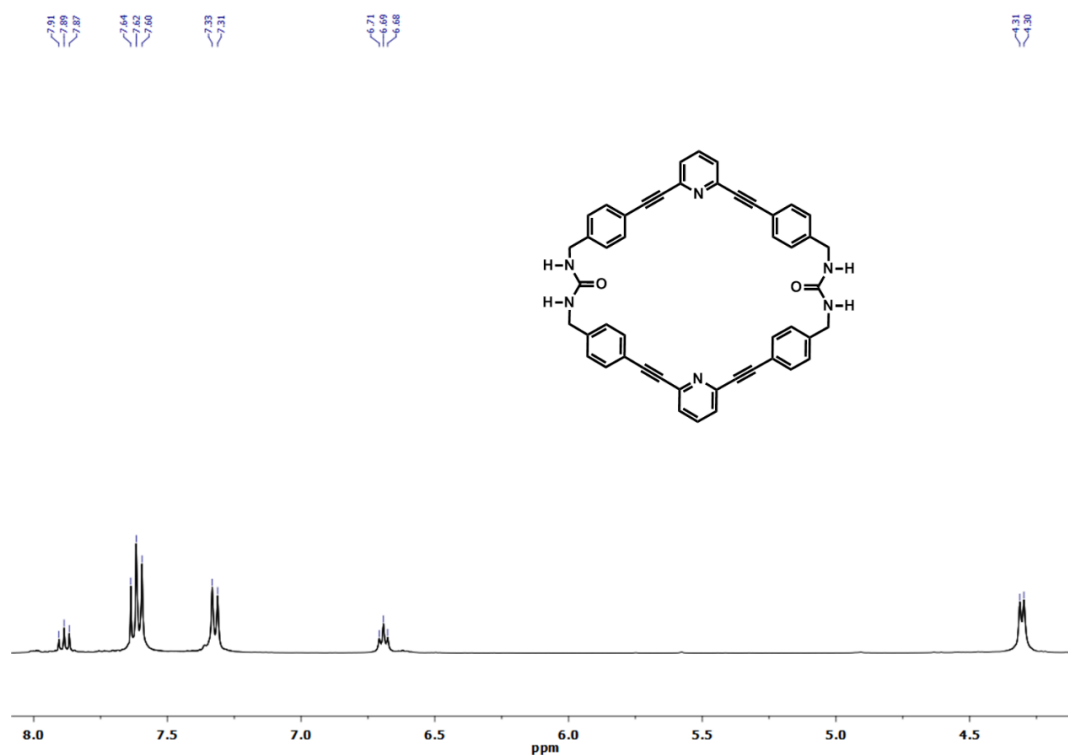
Figure 4.11. ^{1}H-NMR (CDCl$_3$, 400 MHz) of the *bis*-urea macrocycle.
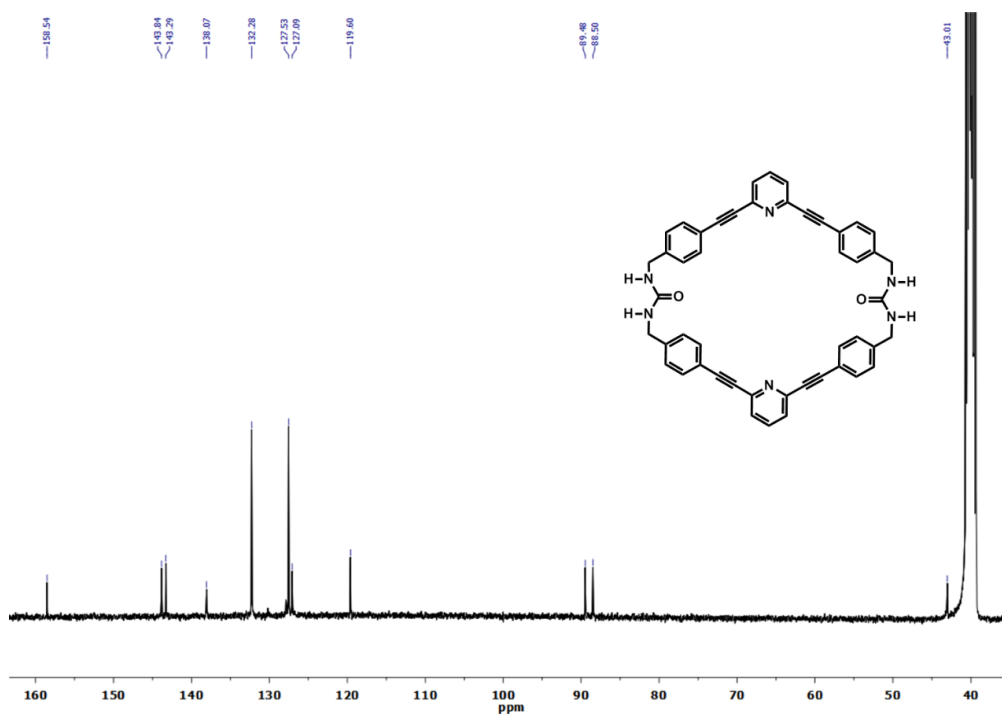
Figure 4.12. ^{13}C-NMR (CDCl$_3$, 100 MHz) of the *bis*-urea macrocycle.

4.5.3. Self-assembly of the *bis*-urea macrocycle to afford host 1

Self-assembly was carried out using following methods:

Method 1

The macrocycle (50 mg) was placed in a small scintillation vial and heated in ~ 10 mL DMSO to obtain a clear pale yellow solution. The small vial was placed inside a larger vial containing MeOH and sealed. Needle shaped pale yellow crystals were obtained after a week.

Method 2

The macrocycle (10 mg) was placed in a small scintillation vial and heated in ~ 2 mL DMSO to obtain a clear pale yellow solution. The small vial was placed inside a larger vial containing H_2O and sealed. Needle shaped pale yellow crystals were obtained after a few days.

Method 3

A small scintillation vial was charged with macrocycle (10 mg) and ~ 1 mL DMSO. The vial was placed in temperature controlled crystallization bath at 90 °C for 20 min to obtain a clear pale yellow color solution. Sample was slowly cooled (1 °C/h) to rt over few days to yield needle shaped pale yellow crystals.

Crystals obtained from all three methods were subjected to XRD analysis and yielded the same assembled structure with disordered solvent molecules. All studies were carried out using crystals obtained from method 1.

161

4.5.4. Additional single crystal X-ray diffraction details for 1 and urea protected macrocycle

Single crystal X-ray diffraction details for **1**.

X-ray intensity data from a pale yellow needle crystal were collected at 100(2) K using a Bruker SMART APEX diffractometer (Mo Ka radiation, l = 0.71073 Å).[38] The crystals diffracted weakly because of size, needle morphology and disorder. No diffraction was observed above a 2θ value of ca. 45°, and the data were truncated at that value. The raw area detector data frames were reduced using the SAINT+ program.[38]

Final unit cell parameters were determined by least-squares refinement of 2962 reflections from the data set. The structure was solved by direct methods with SHELXS.[39] Subsequent difference Fourier calculations and full-matrix least-squares refinement against F2 were performed with SHELXL-2013/42[39] using OLEX2[40] Corrections to the structure factors for the contribution of disordered species were performed with the Squeeze program in PLATON.[41,42]

The compound crystallizes in the orthorhombic space group Pbcn as determined uniquely by the pattern of systematic absences in the intensity data. The asymmetric unit consists of half of one molecule, which is located on a crystallographic two-fold axis of rotation, and a tubular volume of disordered solvent species running along the crystallographic b axis.

No reasonable disorder model could be achieved for the disordered guests after many trials. Their contribution to the scattering factors was accounted for with the

Squeeze program.[41,42] The solvent-accessible volume of the unit cell was calculated to be 1341.4 Å^3 (28.6% of the total unit cell volume), corresponding to 342 electrons per unit cell. The reported F.W, dcalc and F(000) reflect only the known unit cell contents.

Non-hydrogen atoms were refined with anisotropic displacement parameters. Hydrogen atoms bonded to carbon were placed in geometrically idealized positions and included as riding atoms. The two unique urea hydrogen atoms were located in difference maps and refined isotropically with their N-H distances restrained to be similar (SHELX SADI). The largest residual electron density peak in the final difference map is 0.20 e-/Å^3, located 1.1 Å from C21.

The crystal structure revealed the expected *bis*-urea macrocycle as a solvate; however, macrocycle 1 was not planar but folded into a bowl or saddle conformation with C2 point symmetry. Here, the two urea groups point in the same direction. This folded architecture assembles through typical bifurcated urea hydrogen bonds (N(H)•••O distances of 2.81-2.87 Å) with four neighboring macrocycles to afford 2D assemblies of interdigitated cycles.

The packing of the layers creates tubular channels of ~4.5 Å in diameter along the crystallographic *b* axis. The channels are occupied by disordered solvent molecules (DMSO and/ or MeOH). Adjacent layers alternate ureas in an *anti*-parallel fashion resulting in a cancellation of the dipoles. The assembly is further stabilized by aryl stacking and CH-pi interactions. The crystalline structures have regular and aligned 1-dimensional pores with diameters of ~ 4.5 Å.

Crystal data and structure refinement for 1 (srs33mqz_sq_s)

Identification code	srs33mqz_sq_s
Empirical formula	$C_{48}H_{34}N_6O_2$
Formula weight	726.81
Temperature/K	100(2)
Crystal system	orthorhombic
Space group	Pbcn
a/Å	19.711(5)
b/Å	8.983(2)
c/Å	26.520(6)
α/°	90
β/°	90
γ/°	90
Volume/Å^3	4695.7(18)
Z	4
ρ_{calc}mg/mm^3	1.028
μ/mm^{-1}	0.064

164

F(000)	1520.0
Crystal size/mm^3	0.48 × 0.20 × 0.08
Radiation	MoKα (λ = 0.71073)
2Θ range for data collection	3.072 to 45.078°
Index ranges	-21 ≤ h ≤ 21, -9 ≤ k ≤ 9, -28 ≤ l ≤ 28
Reflections collected	45741
Independent reflections	3087[R(int) = 0.1417]
Data/restraints/parameters	3087/1/261
Goodness-of-fit on F^2	1.080
Final R indexes [I>=2σ (I)]	R_1 = 0.0596, wR_2 = 0.1732
Final R indexes [all data]	R_1 = 0.0909, wR_2 = 0.1868
Largest diff. peak/hole / e Å^{-3}	0.20/-0.15
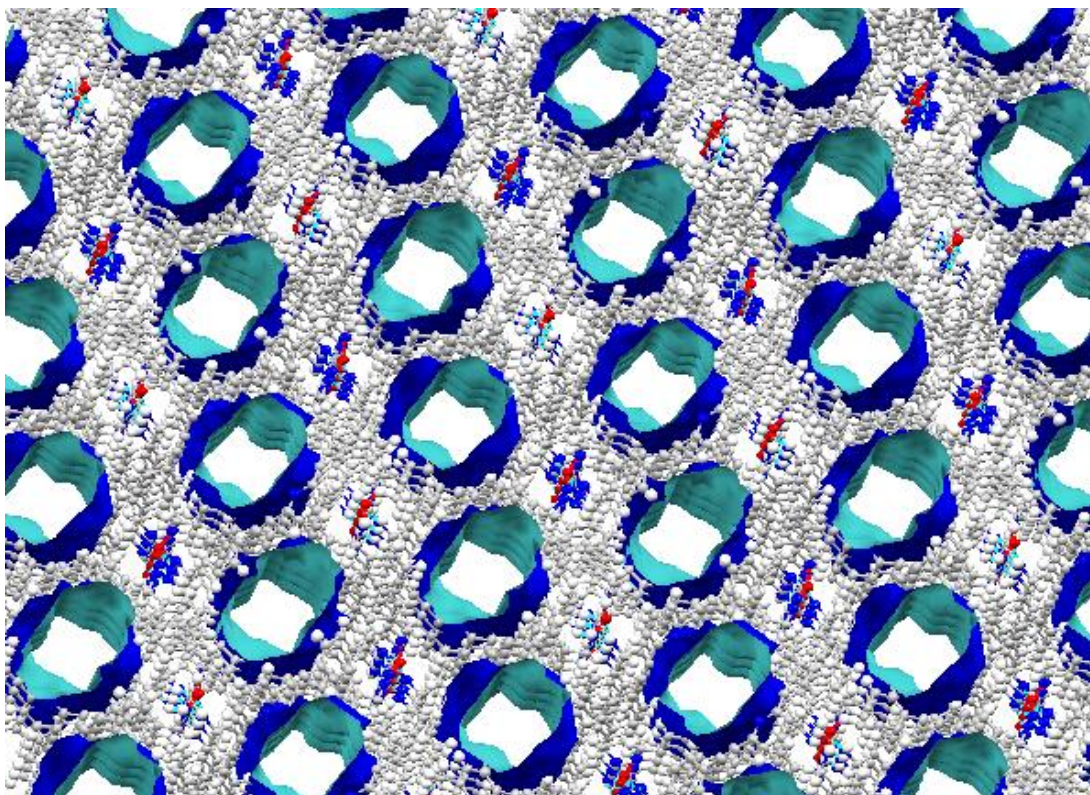
Figure 4.13. 1D channels extended along the crystallographic *b* axis.

Single crystal X-ray diffraction details for urea protected macrocycle.

X-ray intensity data from a pale yellow pale crystal were measured at 150(2) K on a Bruker SMART APEX diffractometer (Mo Kα radiation, λ = 0.71073 Å).[43] Raw area detector data frame integration was performed with SAINT+.[43] Final unit cell parameters were determined by least-squares refinement of 3774 reflections from the data set. Direct methods structure solution, difference Fourier calculations and full-matrix least-squares refinement against F^2 were performed with SHELXTL.[44] The compound crystallizes in the space group $P2_1/m$ as determined by the pattern of systematic absences in the intensity data and by achieving a reasonable solution and refinement of the structure. The asymmetric unit consists of half of one $C_{60}H_{56}N_8O_2$ molecule located on a

166

crystallographic mirror plane, and half of one methylene chloride molecule also located on a mirror plane. The *tert*-butyl group C31-C34 is disordered across the mirror plane. The displacement ellipsoids of *tert*-butyl group C3-C5 also indicate slight disorder but this could not be modeled successfully. The methylene chloride molecule is disordered over multiple positions across the mirror plane. To account for this electron density, a disorder model involving one carbon atom position and five chlorine atom positions was refined. Occupancies for the carbon atom C1S and for Cl1 were fixed at 0.5. Occupancies for the remaining four chlorine sites were fixed manually such that they summed to 0.5 and gave reasonable displacement parameters. The reported methylene chloride hydrogen atom positions correspond to the major disorder fraction of this group, and some short C-Cl distances reflect the limitations of the disorder model. All non-hydrogen atoms were refined with anisotropic displacement parameters except for Cl3, Cl4 and Cl5 (isotropic). Hydrogen atoms were placed in geometrically idealized positions and included as riding atoms. The high R-factors are because of the *t*-butyl and solvent disorder in the crystal.
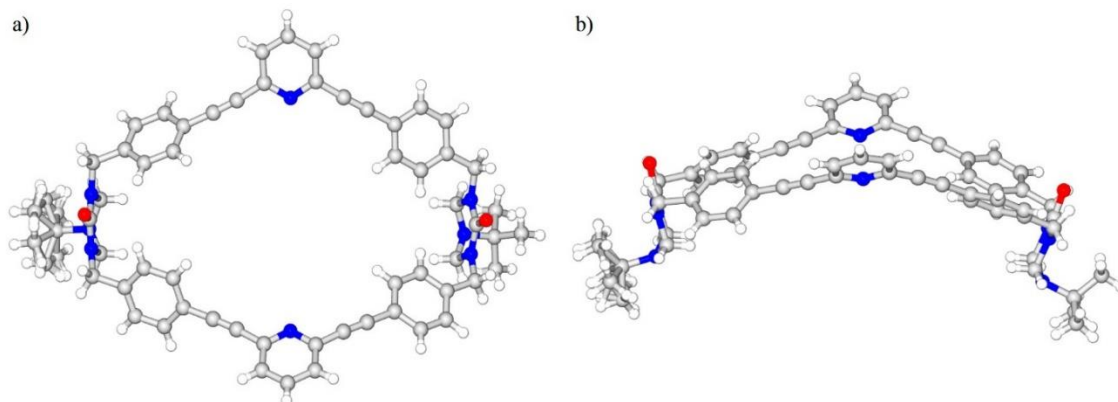
Figure 4.14. X-ray crystal structure of urea protected **1**. (solvent CH_2Cl_2 omitted for clarity) (a) Top view of the macrocycle (b) View through the crystallographic *b* axis.

167

Crystal data and structure refinement for urea protected macrocycle (yx031_3m).

Identification code	yx031_3m
Empirical formula	C61 H58 Cl2 N8 O2
Formula weight	1006.05
Temperature	150(2) K
Wavelength	0.71073 Å
Crystal system	Monoclinic
Space group	$P2_1/m$
Unit cell dimensions	a = 9.6662(4) Å $\alpha = 90°$.
	b = 18.8900(8) Å $\beta = 91.464(1)°$.
	c = 14.4567(6) Å $\gamma = 90°$.
Volume	2638.85(19) Å^3
Z	2
Density (calculated)	1.266 Mg/m^3
Absorption coefficient	0.175 mm^{-1}
F(000)	1060

168

Crystal size	$0.28 \times 0.20 \times 0.08$ mm^3
Theta range for data collection	1.41 to 23.26°.
Index ranges	-10<=h<=10, -20<=k<=20, -16<=l<=16
Reflections collected	28637
Independent reflections	3930 [R(int) = 0.0615]
Completeness to theta = 23.26°	100.0 %
Absorption correction	None
Refinement method	Full-matrix least-squares on F^2
Data / restraints / parameters	3930 / 10 / 379
Goodness-of-fit on F^2	1.017
Final R indices [I>2sigma(I)]	R1 = 0.0750, wR2 = 0.2161
R indices (all data)	R1 = 0.1066, wR2 = 0.2410
Largest diff. peak and hole	0.822 and -0.321 e.Å^{-3}

4.5.5. Hirshfeld surface analysis of 1 and comparison with phenylethynylene *bis*-urea macrocycle (**2**)

Molecular Hirshfeld surface for **1** and **2** were constructed using Crystal Explorer 3.0.[45] The Crystallographic Information File (.cif) of host **1** was imported into Crystal

169

Explorer and a high resolution Hirshfeld surface was mapped with the function d_{norm}. Two dimensional (2D) fingerprints maps were obtained by calculating the distances from the Hirshfeld surface to the nearest nucleus inside the surface (d_i) to the outside surface (d_e) to analyze the molecular interactions around the nearest neighbor molecules. In 2D maps, green regions shows closer contacts and longer contacts indicated in blue color. The Hirshfeld surfaces of **1** and **2** were generated over a d_{norm} range -0.5 to 1.5. All surfaces constructed using d_{norn} function were illustrated as transparent hollow maps in order to clearly visualize the pyridine-phenylethynylene macrocycle inside the surface. The red spots on the surfaces represent the distances shorter than sum of vdW radii and blue regions correspond to the distances longer than sum of vdW radii.
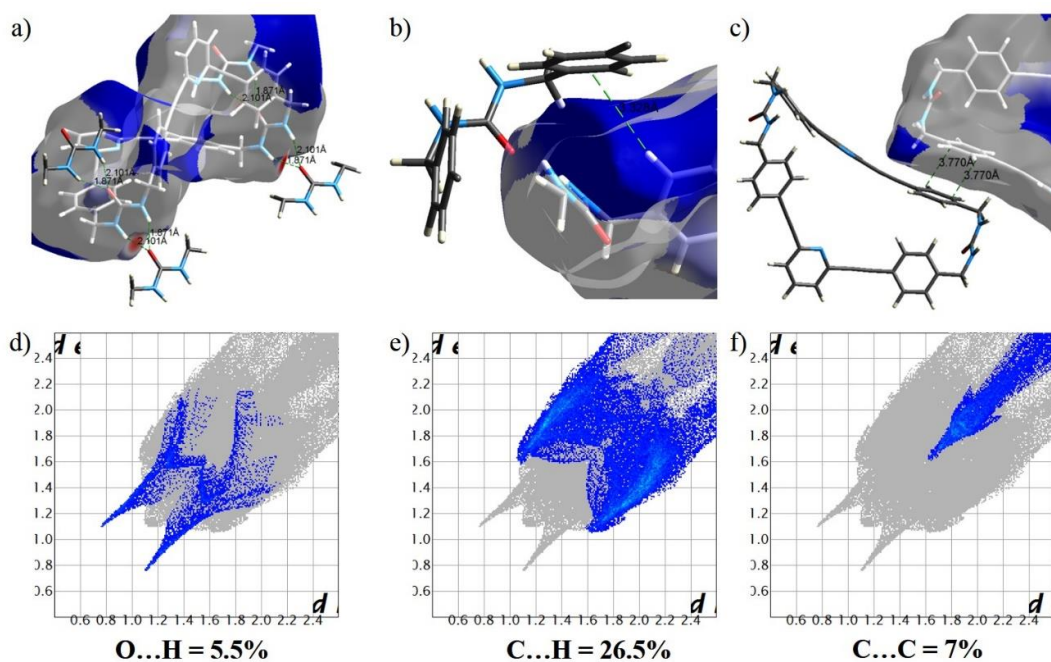
Figure 4.15. Hirshfeld surface analysis of the macrocycle **1**. a) Bifurcated H bonding between macrocycles. b) CH-л interactions between neighboring macrocycle. c) Offset л-stacking interactions between neighboring macrocycle. d) Two dimensional map resolved into O...H/H...O contacts. e) Two dimensional map resolved to show C...H/H...C contacts. f) Two dimensional map highlighting the C...C contacts.

170
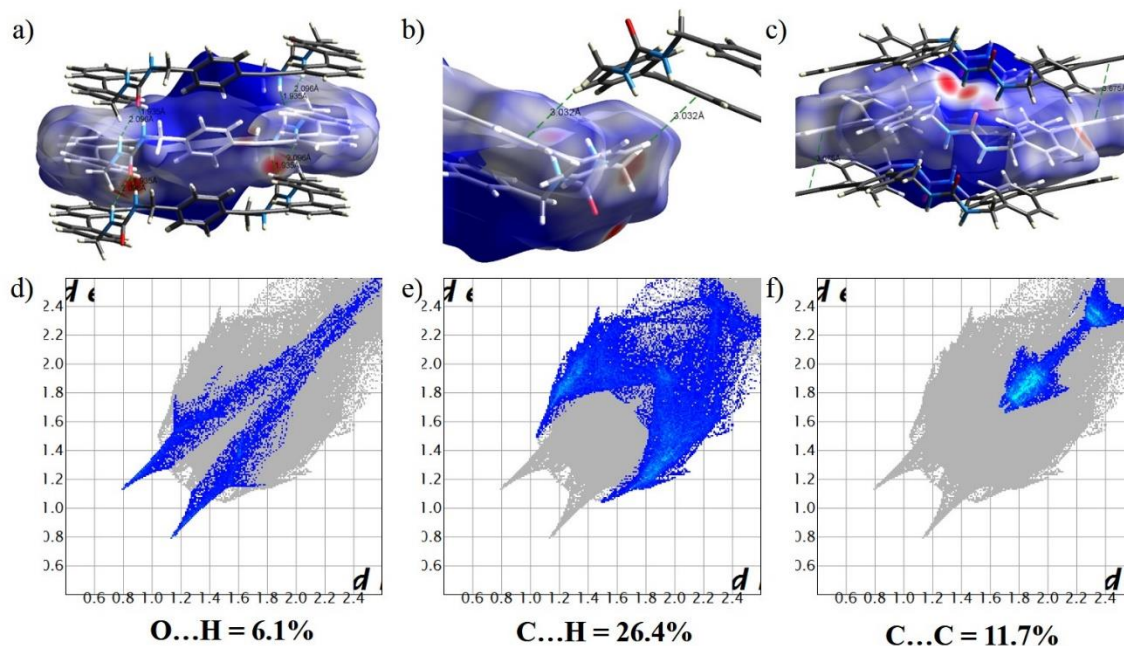
Figure 4.16. Hirshfeld surface analysis of the macrocycle **2**. a) Bifurcated H bonding between macrocycles. b) CH-л interactions between neighboring macrocycle. c) Offset л-stacking interactions between macrocycles. d) Two dimensional map resolved into O...H/H...O contacts. e) Two dimensional map resolved to show C...H/H...C contacts. f) Two dimensional map highlighting the C...C contacts.

4.5.6. TGA analysis of host **1**.

TGA analysis of host 1 was carried out using two methods:

Method 1:

Freshly crystalized host **1** (~ 15 mg) was heated at 2 °C/min from rt to 120 °C under He atmosphere and kept isothermally for 2 h.

Method 2:

Freshly crystalized host **1** (~ 15 mg) was heated at 2 °C/min from rt to 170 °C under He atmosphere and kept isothermally for 1 h.
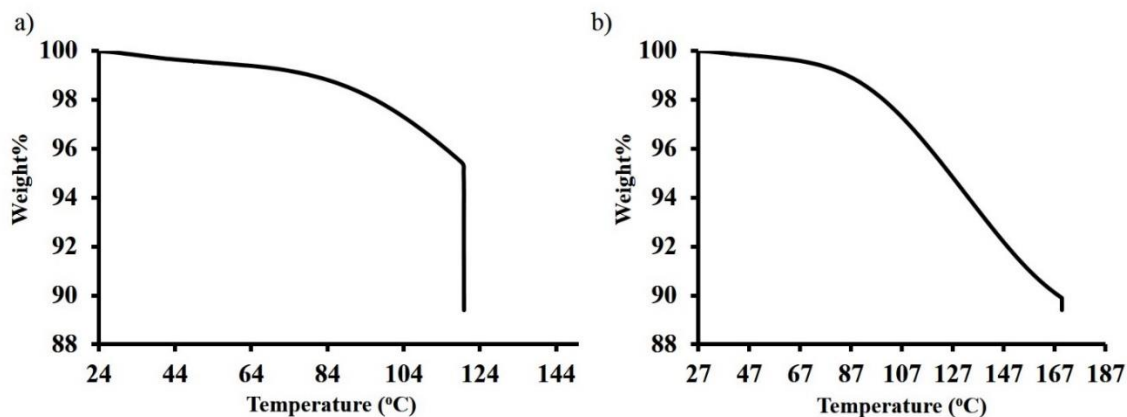
Figure 4.17. Thermogravimetric analysis of host **1**. (a) Using method 1. (b) Using method 2.

All studies were carried out using host material obtained from method 1.

4.5.7. Isoprene loading studies, photo irradiation and polymer isolation.

Isoprene monomer was purified using an alumina plug prior to loading studies. Monomer loading experiments were performed under high vacuum using a loading apparatus.
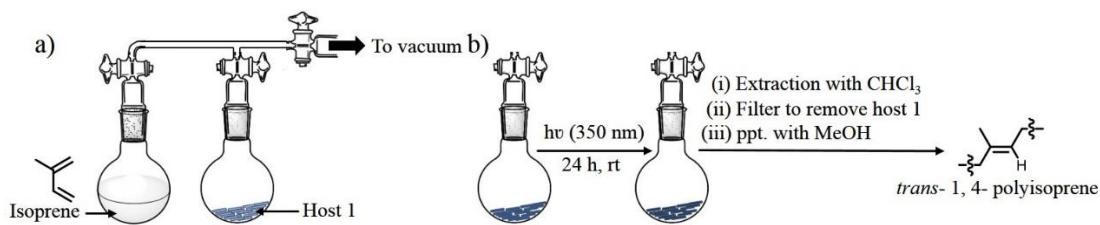
Figure 4.18. Loading of isoprene, photo irradiation and polymer isolation. a) Loading apparatus used in the study. b) Photoreaction and isolation of *trans*-1,4-polyisoprene.

Host **1** (20 mg) was place in a 10 mL flask and evacuated under high vacuum for 3 h. Isoprene 5 mL was placed in the second flask and degassed using at least 4 freeze

172

pump thaw cycles. Isoprene absorbed from its vapor phase under reduce pressure at room temperature for 24 h, conditions which likely lead to an equilibrium for diffusion. Next, the isoprene loaded host **1** (host **1•** isoprene) was frozen and vacuum sealed. The sealed vial was transferred into Rayonet reactor for UV-irradiation. Sample was irradiated at 350 nm for 24 h at room temperature. The polymer was extracted with CHCl$_3$ using an ultra sound sonicator for 30 min. The suspension of the host and polymer was filtered and host **1** recovered. The filtrate was concentrated in *vacuo,* and polyisoprene was precipitated by adding ice-cold methanol drop wise.

4.5.8. Characterization of the polymer
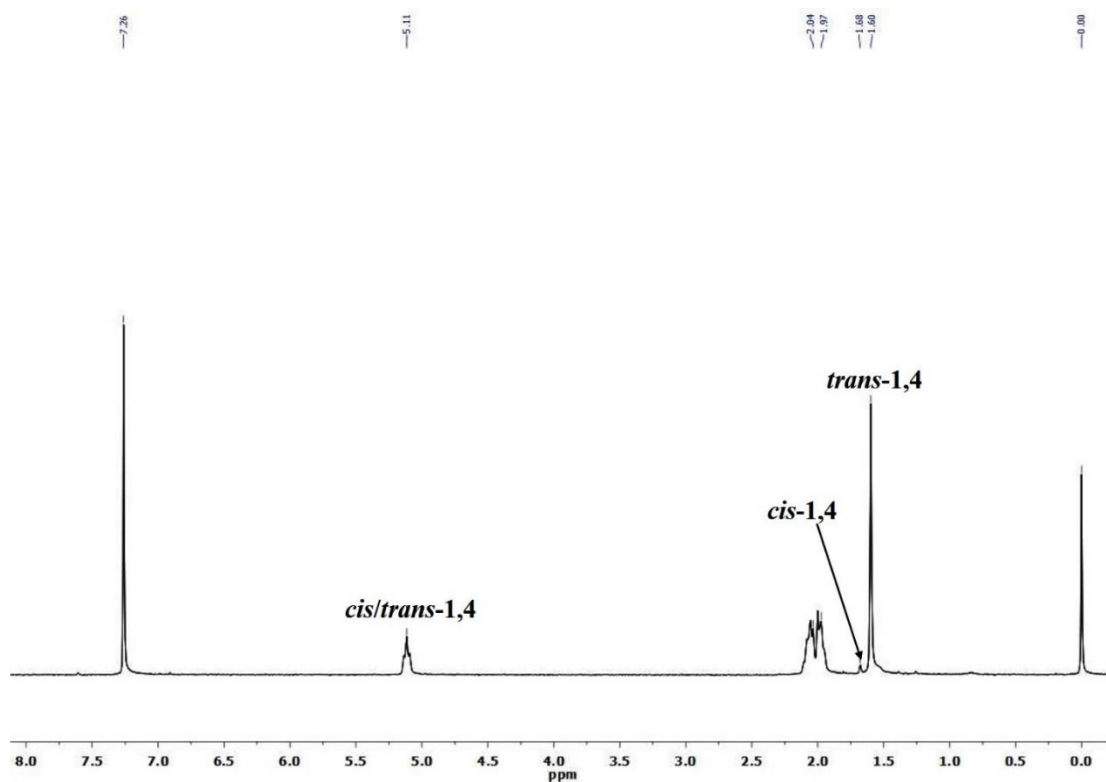
Figure 4.19. ^{1}H-NMR (CDCl$_3$, 400 MHz) of *trans*-1, 4-polyisoprene.
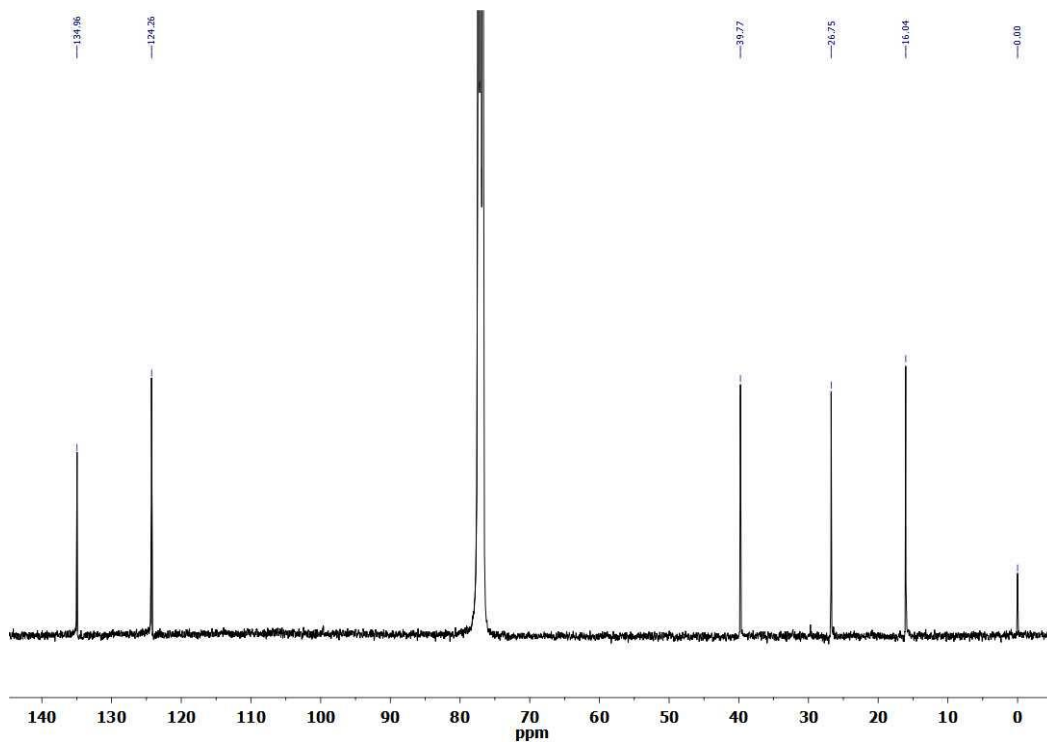
Figure 4.20. ^{13}C-NMR (CDCl$_3$, 125 MHz) of *trans*-1,4-polyisoprene.
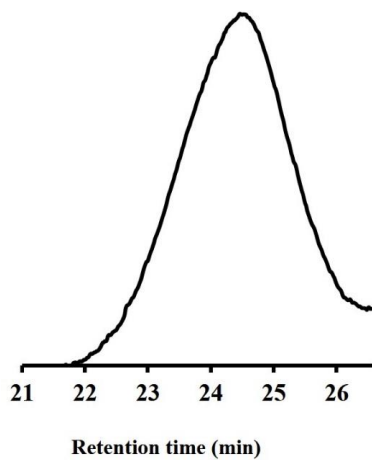
Figure 4.21. GPC trace of *trans*-1,4-polyisoprene. (Eluent: THF, calibrated to polystyrene standards)

174

^{1}H-NMR: (300 MHz, CD$_3$Cl δ): olefinic H atoms for 1,4-motif: 5.11 (s, *br*, 1H); aliphatic H atoms for 1,4-motif: 2.06 (m, 2H), 1.97 (m, 2H), 1.68 (s, 3H), 1.60 (s, 3H); ^{13}C-NMR: (125 MHz, CD$_3$Cl δ): olefinic H atoms for 1,4-motif: 134.96, 124.26, 39.77, 26.75, 16.04; SEC chromatography (eluent: THF, Polystyrene standards): *Mw* = 6129 g/mol, Đ = 1.39. Selectivity[46] *trans*-1,4 = 96.7%, *cis*-1,4 = 3.3%.

4.6. References

(1) Hayakawa, T.; Horiuchi, S.; Shimizu, H.; Kawazoe, T.; Ohtsu, M. Synthesis and characterization of polystyrene-b-poly (1,2-isoprene-ran-3,4-isoprene) block copolymers with azobenzene side groups. *Journal of Polymer Science Part A: Polymer Chemistry* **2002**, *40*, 2406-2414.

(2) Liu, G.; Li, Z.; Yan, X. Synthesis and characterization of polystyrene-block-polyisoprene nanofibers with different crosslinking densities. *Polymer* **2003**, *44*, 7721-7727.

(3) Schmidt, S. C.; Hillmyer, M. A. Synthesis and Characterization of Model Polyisoprene−Polylactide Diblock Copolymers. *Macromolecules* **1999**, *32*, 4794-4801.

(4) Batis, C.; Karanikolopoulos, G.; Pitsikalis, M.; Hadjichristidis, N. Metallocene-Catalyzed Copolymerization of MMA with Anionically Synthesized Methacryloyl Macromonomers. *Macromolecules* **2000**, *33*, 8925-8930.

(5) Wootthikanokkhan, J.; Tongrubbai, B. Compatibilization efficacy of poly(isoprene–butyl acrylate) block copolymers in natural/acrylic rubber blends. *Journal of Applied Polymer Science* **2003**, *88*, 921-927.

(6) Knite, M.; Teteris, V.; Kiploka, A.; Kaupuzs, J. Polyisoprene-carbon black nanocomposites as tensile strain and pressure sensor materials. *Sensors and Actuators A: Physical* **2004**, *110*, 142-149.

(7) Ren, J.; Silva, A. S.; Krishnamoorti, R. Linear Viscoelasticity of Disordered Polystyrene−Polyisoprene Block Copolymer Based Layered-Silicate Nanocomposites. *Macromolecules* **2000**, *33*, 3739-3746.

(8) Cheng, C.; Qi, K.; Khoshdel, E.; Wooley, K. L. Tandem Synthesis of Core−Shell Brush Copolymers and Their Transformation to Peripherally Cross-Linked and Hollowed Nanostructures. *Journal of the American Chemical Society* **2006**, *128*, 6808-6809.

(9) Murthy, K. S.; Ma, Q.; Remsen, E. E.; Kowalewski, T.; Wooley, K. L. Thermal shaping of shell-crosslinked (SCK) nanoparticles, facilitated by nanoconfinement of fluid-like cores. *Journal of Materials Chemistry* **2003**, *13*, 2785-2795.

(10) Germack, D. S.; Wooley, K. L. Isoprene polymerization via reversible addition fragmentation chain transfer polymerization. *Journal of Polymer Science Part A: Polymer Chemistry* **2007**, *45*, 4100-4108.

(11) Jitchum, V.; Perrier, S. Living Radical Polymerization of Isoprene via the RAFT Process. *Macromolecules* **2007**, *40*, 1408-1412.

(12) Kent, E. G.; Swinney, F. B. Properties and Applications of trans-1,4-Polyisoprene. *I&EC Product Research and Development* **1966**, *5*, 134-138.

(13) Song, J.-S.; Huang, B.-C.; Yu, D.-S. Progress of synthesis and application of trans-1,4-polyisoprene. *Journal of Applied Polymer Science* **2001**, *82*, 81-89.

(14) Gale, P. A. S., J. W. Supramolecular chemistry; from molecules to nanomaterials. Reactions in Solid-State Inclusion Compounds; Harris, K. D. M.; Palmer, B. A.; Edwards-Gau, G. R. Eds.; Wiley: West Sussex, 2012; Vol. 4, pp 1589–1612.

(15) Slater, A. G.; Cooper, A. I. Function-led design of new porous materials. *Science* **2015**, *348*.

(16) Inokuma, Y.; Kawano, M.; Fujita, M. Crystalline molecular flasks. *Nat Chem* **2011**, *3*, 349-358.

(17) Ramamurthy, V.; Gupta, S. Supramolecular photochemistry: from molecular crystals to water-soluble capsules. *Chemical Society Reviews* **2015**, *44*, 119-135.

(18) Ramamurthy, V.; Parthasarathy, A. Chemistry in Restricted Spaces: Select Photodimerizations in Cages, Cavities, and Capsules. *Israel Journal of Chemistry* **2011**, *51*, 817-829.

(19) Yoshizawa, M.; Klosterman, J. K.; Fujita, M. Functional Molecular Flasks: New Properties and Reactions within Discrete, Self-Assembled Hosts. *Angewandte Chemie International Edition* **2009**, *48*, 3418-3438.

(20) Comotti, A.; Bracco, S.; Mauri, M.; Mottadelli, S.; Ben, T.; Qiu, S.; Sozzani, P. Confined Polymerization in Porous Organic Frameworks with an Ultrahigh Surface Area. *Angewandte Chemie International Edition* **2012**, *51*, 10136-10140.

(21) Kageyama, K.; Tamazawa, J.-i.; Aida, T. Extrusion Polymerization: Catalyzed Synthesis of Crystalline Linear Polyethylene Nanofibers Within a Mesoporous Silica. *Science* **1999**, *285*, 2113-2115.

(22) Lu, Y.; Yang, Y.; Sellinger, A.; Lu, M.; Huang, J.; Fan, H.; Haddad, R.; Lopez, G.; Burns, A. R.; Sasaki, D. Y.; Shelnutt, J.; Brinker, C. J. Self-assembly of mesoscopically ordered chromatic polydiacetylene/silica nanocomposites. *Nature* **2001**, *410*, 913-917.

(23) Tajima, K.; Aida, T. Controlled polymerizations with constrained geometries. *Chemical Communications* **2000**, 2399-2412.

(24) Uemura, T.; Yanai, N.; Kitagawa, S. Polymerization reactions in porous coordination polymers. *Chemical Society Reviews* **2009**, *38*, 1228-1236.

(25) Wu, C.-G.; Bein, T. Conducting Carbon Wires in Ordered, Nanometer-Sized Channels. *Science* **1994**, *266*, 1013-1015.

(26) Allcock, H. R.; Silverberg, E. N.; Dudley, G. K.; Pucher, S. R. Inclusion Polymerization within a Tris(2,3-naphthylenedioxy)cyclotriphosphazene Clathrate. *Macromolecules* **1994**, *27*, 7550-7555.

(27) Distefano, G.; Comotti, A.; Bracco, S.; Beretta, M.; Sozzani, P. Porous Dipeptide Crystals as Polymerization Nanoreactors. *Angewandte Chemie International Edition* **2012**, *51*, 9258-9262.

(28) Shimizu, L. S.; Salpage, S. R.; Korous, A. A. Functional Materials from Self-Assembled Bis-urea Macrocycles. *Accounts of Chemical Research* **2014**, *47*, 2116-2127.

(29) Dawn, S.; Dewal, M. B.; Sobransingh, D.; Paderes, M. C.; Wibowo, A. C.; Smith, M. D.; Krause, J. A.; Pellechia, P. J.; Shimizu, L. S. Self-Assembled Phenylethynylene Bis-urea Macrocycles Facilitate the Selective Photodimerization of Coumarin. *Journal of the American Chemical Society* **2011**, *133*, 7025-7032.

(30) Dawn, S.; Salpage, S. R.; Koscher, B. A.; Bick, A.; Wibowo, A. C.; Pellechia, P. J.; Shimizu, L. S. Applications of a Bis-Urea Phenylethynylene Self-Assembled Nanoreactor

178

for [2 + 2] Photodimerizations. *The Journal of Physical Chemistry A* **2014**, *118*, 10563-10574.

(31) Salpage, S. R.; Donevant, L. S.; Smith, M. D.; Bick, A.; Shimizu, L. S. Modulating the reactivity of chromone and its derivatives through encapsulation in a self-assembled phenylethynylene bis-urea host. *Journal of Photochemistry and Photobiology A: Chemistry* **2016**, *315*, 14-24.

(32) McKinnon, J. J.; Jayatilaka, D.; Spackman, M. A. Towards quantitative analysis of intermolecular interactions with Hirshfeld surfaces. *Chemical Communications* **2007**, 3814-3816.

(33) Parkin, A.; Barr, G.; Dong, W.; Gilmore, C. J.; Jayatilaka, D.; McKinnon, J. J.; Spackman, M. A.; Wilson, C. C. Comparing entire crystal structures: structural genetic fingerprinting. *CrystEngComm* **2007**, *9*, 648-652.

(34) Spackman, M. A.; McKinnon, J. J.; Jayatilaka, D. Electrostatic potentials mapped on Hirshfeld surfaces provide direct insight into intermolecular interactions in crystals. *CrystEngComm* **2008**, *10*, 377-388.

(35) Uemura, T.; Nakanishi, R.; Mochizuki, S.; Murata, Y.; Kitagawa, S. Radical polymerization of 2,3-dimethyl-1,3-butadiene in coordination nanochannels. *Chemical Communications* **2015**, *51*, 9892-9895.

(36) Mitchell, A. R.; Pagoria, P. F.; Coon, C. L.; Jessop, E. S.; Poco, J. F.; Tarver, C. M.; Breithaupt, R. D.; Moody, G. L. Nitroureas 1. Synthesis, scale-up and characterization of K-6. *Propellants, Explosives, Pyrotechnics* **1994**, *19*, 232-239.

(37) Liang, Y.; Xie, Y.-X.; Li, J.-H. Modified Palladium-Catalyzed Sonogashira Cross-Coupling Reactions under Copper-, Amine-, and Solvent-Free Conditions. *The Journal of Organic Chemistry* **2006**, *71*, 379-381.

(38) SMART Version 5.631, S. V. a., Bruker analytical X-ray Systems, Inc., Madison, Wisconsin, USA., 2003.

(39) Sheldrick, G. M. *Acta Cryst.* **2008**, *A64*, 112-122.

(40) Dolomanov, O. V.; Gildea, R. J.; Howard J. A. K.; Puschmann, H. OLEX2: a complete structure solution, refinement and analysis program. *J. Appl. Cryst.* **2009**, *42*, 339-341.

(41) Sluis, P. V. D.; Spek, A. L. *Acta Crystallogr*., *Sect. A* **1990**, *46*, 194-201.

(42) PLATON: Spek, A. L. *J. Appl. Cryst.* **2003**, *36*, 7-13.

(43) SMART Version 5.630, SAINT+ Version 6.45; Bruker Analytical X-ray Systems, Inc., Madison, Wisconsin, USA, 2003.

(44) Sheldrick, G. M. SHELXTL Version 6.14; Bruker Analytical X-ray Systems, Inc., Madison, Wisconsin, USA, 2000.

(45) McKinnon, J. J. S., M. A.; Mitchell, A. S. *Acta Crystallogr., Sect. B* **2004**, *60*, 627-668.

(46) Tanaka, Y. T., Y.; Kobayashi, M.; Tadokoro, H. *J. Polym. Sci., Part A-2: Polym. Phys.* **1971**, *9*, 43-57.

CHAPTER V

STRUCTURE, ELECTROCHEMISTRY AND PHOTOPHYSICAL PROPERTIES OF AN *EXO*CYCLIC DI-RUTHENIUM COMPLEX AND ITS APPLICATION AS A PHOTOSENSITIZER*

5.1 Abstract

The reaction of *cis*-bis(2,2'-bipyridine)dichlororuthenium(II) hydrate with a conformationally mobile bipyridyl macrocycle afforded [(bpy)$_2$Ru(μ-L)Ru(bpy)$_2$]Cl$_4$•6H$_2$O, a bridged di-Ru complex. Single crystal X-ray diffraction showed the macrocyclic ligand adopting a bowl-like structure with the *exo*-coordinated Ru(II) centers separated by 7.29 Å. Photophysical characterization showed that the complex absorbs in the visible region (λ_{max}= 451 nm) with an emission maximum at 610 nm (τ = 706 ns, ϕ_{PL} = 0.021). Electrochemical studies indicate the di-Ru complex undergoes three one-electron reversible reductions and a reversible one-electron oxidation process. This reversibility is a key characteristic for photosensitizers and electron transfer agents. The complex was evaluated as a photocatalyst for the electronically mismatched Diels-Alder reaction of isoprene and *trans*-anethole using visible light. It afforded the expected product in good conversion (69%) and selectivity (dr: > 10:1) at low loadings (0.5 – 5.0 mol %) and the sensitizer/catalyst was readily recycled. These results suggest that the bipyridyl macrocycle could be widely applied as a bridging ligand for the assembly of chromophore linked catalysts.

5.2 Introduction

Coordination complexes that contain macrocyclic ligands, such as naturally occurring magnesium-porphyrins and iron-porphyrins, play a vital role in biological systems.[1,2] The chelation effects of a macrocyclic ligand, known as the macrocyclic effect, affords thermodynamically and kinetically stable complexes and offers an easily modulated ligand environment.[3,4] In addition, macrocycles that contain multiple N-donor binding sites, such as bipyridine, allow the macrocycle to act as a 'bridging ligand'

182

between multiple transition metal centers, as illustrated in Figure 5.1. The advantages of bridging multiple transition metal centers in the fields of photosensitizers and photocatalysis have been extensively studied.[5-8] The photosensitizing and electron transport properties of ruthenium complexes are of particular interest as functional materials for use in light harvesting,[9] solar conversion,[10] catalysis,[11] molecular recognition,[12] and in supramolecular devices.[13]
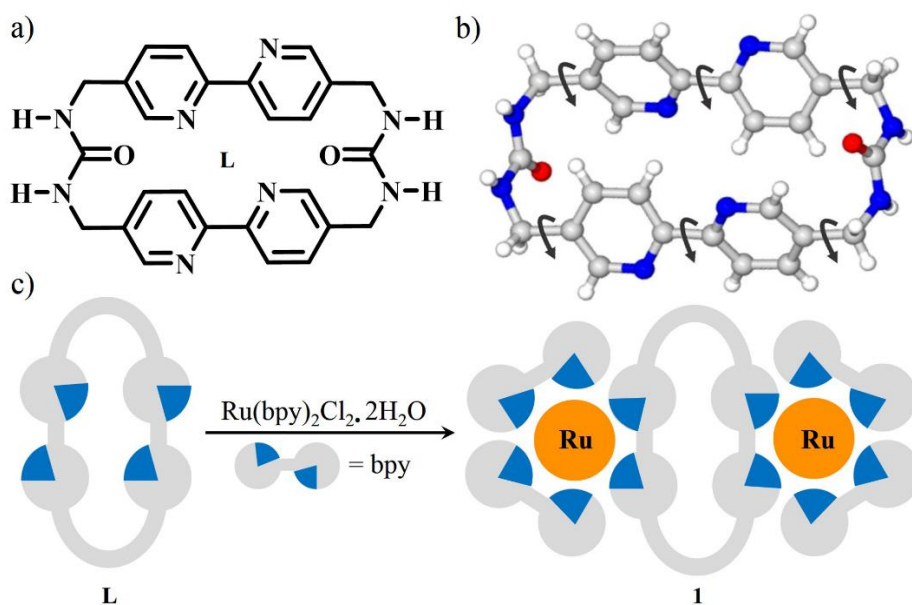
Figure 5.1. A conformationally mobile bipyridyl macrocycle was used as bridging ligand to complex two ruthenium bis(2,2'-bipyridine) units. a) The structure of the bipyridyl *bis*-urea macrocycle (**L**) used in the study as the bridging ligand. b) The crystal structure of the macrocyclic ligand (**L**) highlighting freely rotating bonds. c) The reaction of ligand (**L**) with $Ru(bpy)_2Cl_2.2H_2O$ generates the doubly *exo*-coordinated ruthenium complex shown schematically.

Studies have been conducted in order to investigate and understand the photophysical and electrochemical behavior of macrocyclic ruthenium complexes.[14-19] The photophysical and electrochemical studies on these systems concluded that the individual metal-macrocycle unit can be used as starting building blocks to construct photo and redox active supramolecular materials. In addition, these investigations on the

transition metal complexs of osmiunm and ruthenium assembled through macrocyclic brigding ligands showed that the chemical structure and nature of the macrocycle plays a significant role in a) determing the photophysical and electrochemical outcome of the bound metals, b) regulating the electrochemical communication between multiple metal centers, and c) determining the overall structure and properties of the final assembly.

Our group has reported a bipyridyl *bis*-urea macrocycle (**L**) (Figure 5.1a), which displays conformational mobility and can be used as a ligand to chelate metals in its interior *endo,* or through rotation position the binding sites on the exterior *exo,* which allows for the bridging of two metal centers (Figure 5.1).[20,21] This manuscript reports the use of this macrocycle as a bridging ligand (**μ-L**) to synthesize a diruthenium complex for use as a photosensitizer. The complex was characterized by NMR, HRMS, X-ray diffraction, DFT calculations, and photophysical and electrochemical methods. To test the ability of this complex to act as a photosensitizer, we investigated the electronically mismatched Diels-Alder reaction of isoprene and *trans*-anethole in the presence of complex and visible light.

5.3 Results and discussion

The bipyridyl *bis*-urea macrocycle, **L**, offers the advantage of conformational mobility and can rotate to afford either an interior or exterior metal binding site. We chose a ruthenium salt with two additional bipyridine units to provide the steric bulk to force **L** into the *exo* conformation that is capable of bridging two metals (**μ-L**). The resulting complex is the di-nuclear ruthenium complex **1**, Figure 5.2. A solvothermal method was used to synthesize complex **1**. The bipyridyl ligand (**L**, 10.0 mg, 0.021 mmol) and the ruthenium source $Ru(bpy)_2Cl_2\cdot2H_2O$ (21.85 mg, 0.042 mmol) were placed

184

in ethanol (12.5 mL). A 1:2 **L**: metal salt ratio was used to ensure the saturation of the two bipyridine binding sites of **L**. The reagents and the solvent were added to a pressure tube (~25 mL) and sonicated for 10 minutes. The pressure tube was secured in a steel tube and the sample temperature/time was control according to the ramp cycle illustrated in the Figure 5.2a in a programmable crystallization oven. At the end of the reaction orange block like crystals were obtained with the molecular formula of $[(Ru(C_{10}H_8N_2)_2)_2C_{26}H_{24}N_8O_2)](Cl)_4(H_2O)_6$ as confirmed by NMR, HRMS, and single crystal XRD analysis.
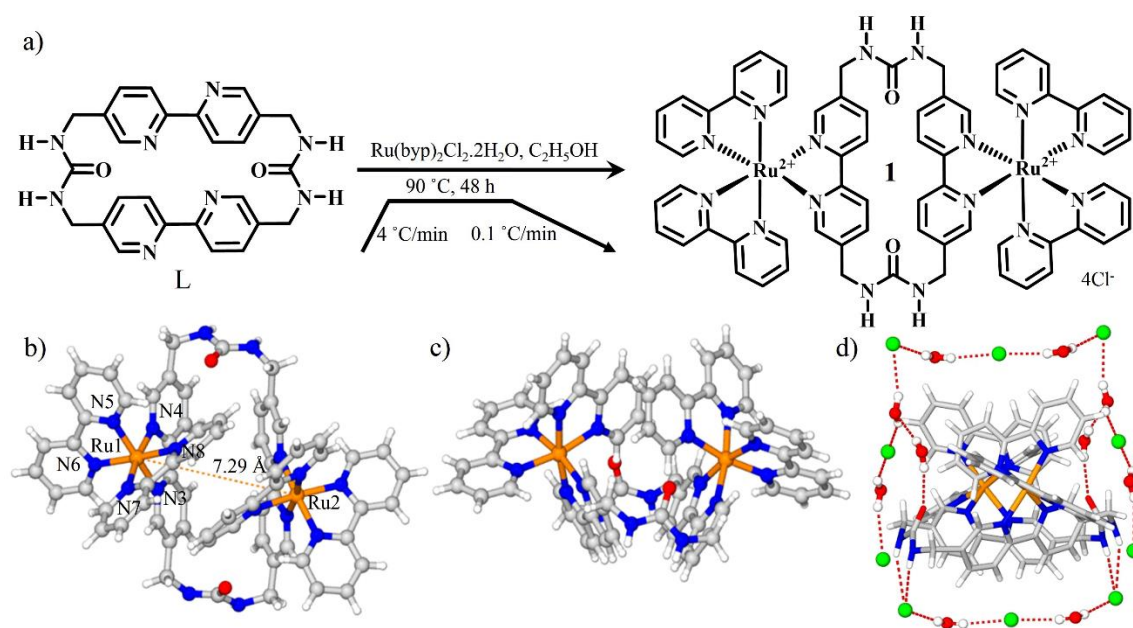
Figure 5.2. Synthesis and the structure of $[(bpy)_2Ru(\mu\text{-L})Ru(bpy)_2]Cl_4 \cdot 6H_2O$ (**1**). a) Ligand **L** (0.021 mmol) and $Ru(bpy)_2Cl_2 \cdot 2H_2O$ (0.042 mmol) were heated in ethanol (12.5 mL) as indicated to afford orange block crystals. b) Top view of the bowl-like structure of complex **1** cation with the ruthenium centers 7.29 Å apart. c) Side view of complex **1** cation comparing the Ru coordination geometry. d) Part of the hydrogen bonding network formed from the urea groups and water molecules and the chloride anions (red dashed lines) is shown.

185

5.3.1 Solid state structure of $[(bpy)_2Ru(\mu-L)Ru(bpy)_2]Cl_4\cdot 6H_2O$ (1).

The compound crystallizes in the space group C2/c and obtained in the homochiral form (Figure 5.2b) with the unit cell containing one $\Delta\Delta$ and one $\Lambda\Lambda$ isomer. The asymmetric unit consists of half of one $[(Ru(C_{10}H_8N_2)_2)_2C_{26}H_{24}N_8O_2)]^{4+}$ complex, which is situated about a two-fold axis of rotation, three independent chloride anions, and three independent water molecules. The coordination of the Ru to the macrocycle resulted in the formation of a bowl-like structure. As can be seen from Figure 5.2b, the ruthenium centers are 7.29 Å apart and the macrocyclic carbonyl oxygen atoms are directed inward of the macrocycle whilst the $[Ru(bpy)_2]^{2+}$ units are directed toward the outside of the macrocycle. The macrocyclic ligand (**L**) as depicted in Figure 5.2c has a wide top and narrow base. This conformation helps alleviate repulsion between the bipyridine units of the octahedral coordinated Ru centers (Figure 5.2c). The Ru-N bond lengths range from 2.05 to 2.08 Å, which are comparable to those reported for di-*exo*-Ru complexes.[17] However, the Ru-N interatomic distances were different for each bipyridine unit, which is probably due to steric interactions. One of the free bipyridine units has the shortest Ru-N interatomic distances (Ru1-N5 and Ru1-N6). The macrocyclic N3-Ru1-N4 bite angle (78.96°) is almost identical with that of the free bipyridine units (79.31°), which is less than the ideal octahedral angle of 90°. On the other hand, N-Ru-N angles between bipyridine units are higher averaging 93.86° indicating a response to congestion around the Ru center. Figure 5.2d shows a hydrogen bonding network surrounding complex **1** cation formed by the urea group hydrogens, water molecules and the chloride ions (see Figure 5.17 for more details).

5.3.2 Photophysical measurements

The photophysical properties of **1** measured in N_2 deaerated acetonitrile are presented in Figure 5.3 and Table 5.3. The absorption spectrum of **1** exhibits strong ligand centered π-π* transitions from 260-320 nm and $d_{Ru(II)} \rightarrow π^*$ MLCT transition from 370-550 nm that are typical for ruthenium polypyridyl complexes.[22] Upon excitation at 450 nm **1** exhibits broad ^{3}MLCT emission with a peak maximum at 610 nm, an excited state lifetime of 706 ns and an emission quantum yield of 0.021 (Table 5.3) At sufficiently high excitation intensities one might expect to observe significant excited state quenching in **1** due to triplet-triplet annihilation between adjacent $Ru(bpy)_2^{2+}$ moieties of the dimer but this was not observed under the relatively weak excitation intensities used here (<1 mW/cm^2).
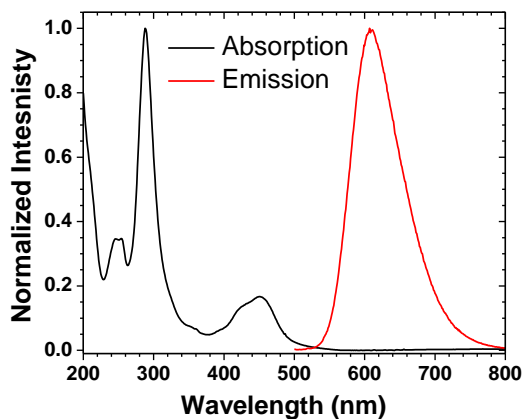
Figure 5.3. Normalized absorption and emission spectra of **1** in N_2 deaerated acetonitrile at room temperature ($λ_{ex} = 450$ nm).

5.3.3 Electrochemical Measurements.

The electrochemical properties of **1** were measured and the in Table 5.1 and Figure 5.4. Cyclic voltammetry data in DMF indicates all redox couples of **1** are quasi-

reversible (ΔE= 80-100 mV and peak currents vary linearly with the square root of scan rate from 10 to 500 mVs^{-1} (Figure 5.10). The anodic wave at $E_{1/2}$ = 1.52 V vs. NHE is attributed to the Ru(II)Ru(III)/Ru(II)Ru(II) redox couple and is similar to the Ru(III)/Ru(II) couple for the related [Ru(bpy)$_3$](PF$_6$)$_2$ compound. Three cathodic waves are also observed for **1** as shown in Figure 5.4. These cathodic waves are assigned to ligand-based reductions as is observed in analogous compounds.[22] In acetonitrile, the third reduction of the complex during CV measurements at $E_p \approx -1.6$ V vs. NHE became irreversible, possibly indicating bpy ligand dissociation and coordination of acetonitrile solvent.

All observed redox couples are characteristic for one electron processes. This one-electron assignment is supported by differential pulse voltammetry (DPV) in Figure 5.4, and by a comparison to the one-electron oxidation couple of ferrocene (Figure 5.11). Each redox peak in the DPV assigned to **1** is nearly identical and comparable in charge passed to the one-electron oxidation of ferrocene. Since peak currents in DPVs are directly proportional to the number of electrons transferred, each redox event has an equivalent amount of electrons transferred. Therefore, a second oxidation of **1** was not observed within the potential window of DMF despite the two Ru centers of **1**. The second oxidation is assumed to be higher in energy due to electrostatic interactions. Compound **1** in the ground state is a cation with +4 charge, and an one-electron oxidation generates a cation with +5 charge. Further oxidation to a cation with +6 charge is a large buildup of positive charge and is likely accompanied by a large solvent reorganization energy, which results in an increase in the oxidation potential beyond the solvent window.

188

Spectroelectrochemistry of complex **1** was studied in MeCN with UV-Visible absorbance changes observed over time during a controlled potential electrolysis at 1.55 V vs. NHE. The difference in shape of absorption spectra between 0 minutes and 58 minutes is shown in Figure 5.5 and Figure 5.12. Decreases in the metal-to-ligand charge transfer (MLCT) absorption at 455 nm and the л-л* transition at 290 nm are accompanied by increases in the abs. at 257 nm, 305 nm and 315 nm upon one electron oxidation. A slight increase in absorptivity was observed at 690 nm (inset Figure 5.5). These spectral changes indicate formation of a Ru(III)Ru(II) **1**$^+$ species. The analogous [Ru(II)(bpy)$_3$](PF$_6$)$_2$ molecule, upon oxidation to Ru(III), also exhibits a decrease in absorptivity near 290 and 450 nm and an increase in absorptivity near 680 nm.[23] After electrolysis, the complex returns to its UV-Vis spectra with original shape and identical intensity in just one minute. The CVs of the complex after and before electrolysis also remain almost identical with no such decrease in peak current intensity (Figures 5.13 and 5.14). These results demonstrate that complex **1** is electrochemically reversible and chemically stable during the one-electron oxidation process in acetonitrile, which is an important characteristic for photosensitizers and electron transfer agents.

Table 5.1. Electrochemical data for **1** in 0.1 M TBAPF$_6$/DMF, GC as working electrode, Pt as counter electrode and scan rate of 100 mVs^{-1}. Potentials reported versus the normal hydrogen electrode.

	1st Oxidation ($E_{1/2}$)/ΔE(mV)	1st Reduction ($E_{1/2}$)/ΔE(mV)	2nd Reduction ($E_{1/2}$)/ΔE(mV)	3rd Reduction ($E_{1/2}$)/ΔE(mV)
1	1.52 / 90	-1.02 / 80	-1.26 / 90	-1.50 / 80
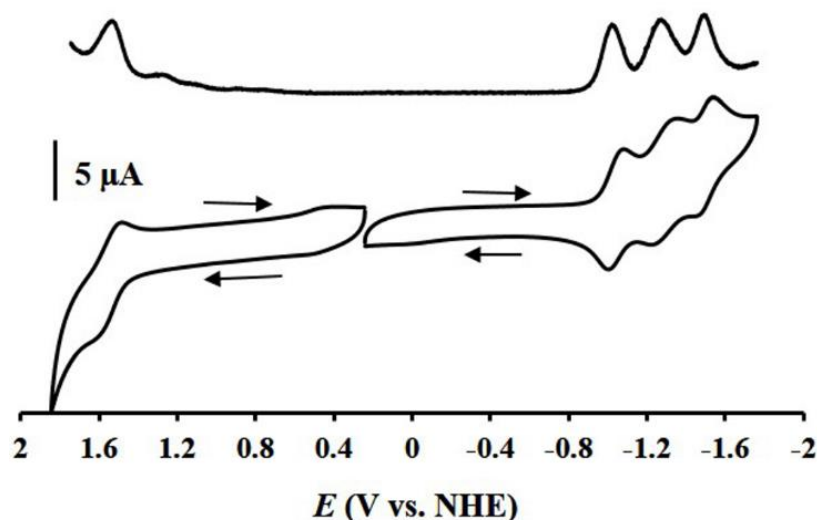
Figure 5.4. DPV (top) and CV (below) of **1** complex in 0.1 M TBAPF$_6$ in DMF. GC as working electrode; Pt as counter electrode; scan rate = 100 mV/s. DPV parameters are as follows; pulse amplitude = 10 mV, pulse width = 100 ms, pulse period = 1000 ms and step increment = 1.5 mV, sample period = 3 ms.
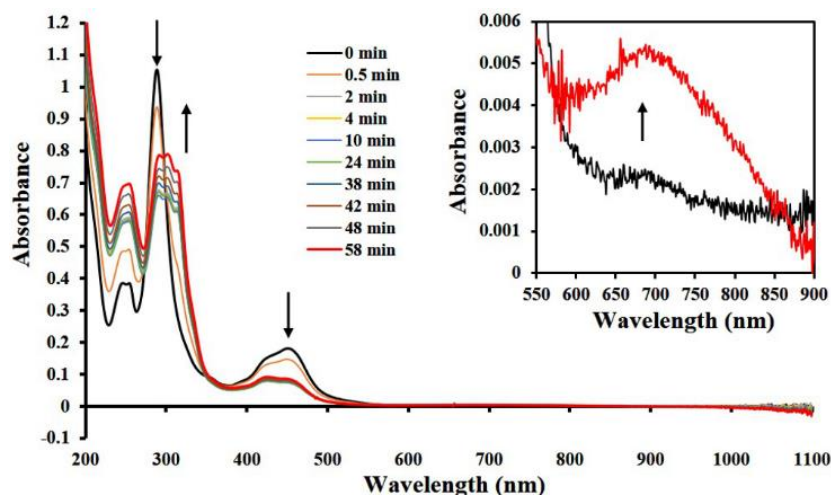
Figure 5.5. Absorption spectral changes of complex **1** during controlled potential (1.55 V vs. NHE) electrolysis over the period of 58 minutes. Inset: magnification of spectral changes that occur between 550 and 900 nm.

5.3.4 Photocatalytic Experiments.

To evaluate the photoinduced electron transfer of complex **1**, we sought to test it as a photosensitizer in organophotocatalysis. Ruthenium based photosensitizers have

been widely used in visible light organocatalysis.[24-28] The concept relies on the ability of a photosensitizer to enable single electron transfers (SETs) upon visible light excitation. Inverse-demand Diels-Alder reactions between either two electron rich or two electron poor substrates requires SETs to generate organic radicals for the reaction to efficiently take place.[29-31] Such radical cation mediated pathways have been investigated for both homo- and hetero Diels-Alder reactions with the radical cations generated by photoinitiated electron transfer using photosensitizers.[29,32]

As reported by Yoon and coworkers the Diels-Alder reaction between isoprene and *trans*-anethole was expected to proceed under mild conditions using an efficient SET catalysts and a co-oxidant under visible light irradiation.[33] The Diels Alder reactions were carried out in dram vials in which the dienophile *trans*-anethole, the diene isoprene, complex **1,** and the co-oxidant methyl viologen were stirred in CH_3NO_2 at room temperature. The reaction was subjected to visible light irradiation for 1 h using a commercial 13 W CFL bulb, compared to a 23 W CFL bulb in previous studies.[33] Upon excitation with visible light the photosensitizer **1** undergoes metal to ligand charge transfer (MLCT) to form photoexited **1*** (Figure 5.6), which is oxidatively quenched by methyl viologen, generating **1**$^+$. The determined oxidation potential for the **1**$^+$/**1** couple of 1.52 V vs. NHE (Table 5.1) is sufficient to generate the *trans*-anethole radical cation (2$^{\bullet+}$) as illustrated in Figure 5.6. The *trans*-anethole radical cation then undergoes a facile reaction with the electron rich isoprene to produce [4+2] cycloadduct (4) via radical cation intermediate 3$^{\bullet+}$.

191
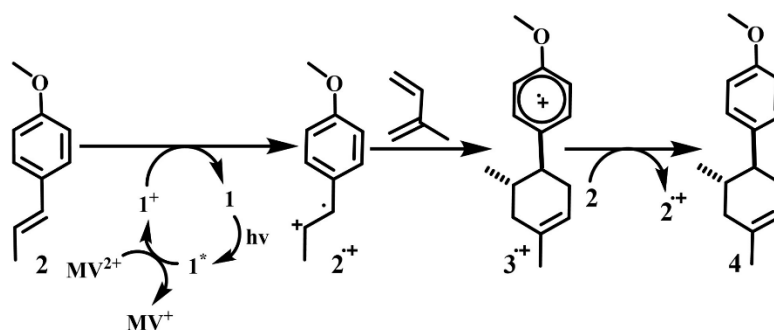
Figure 5.6. Overview of the Diels-Alder reaction between *trans*-anethole and isoprene.

Table 5.2. Summary of Photocatalytic Studies.[a]

Entry	Catalyst	Loading (mol%)	Co-oxidant $MV(PF_6)$(mol%)	% Yield[b]
1	No Catalyst	0	15	0
2	Complex **1**	5	15	69
3	Complex **1**	reused from entry 2[c]	reused from entry 2[c]	61
4	Complex **1**	2.5	7.5	66
5	Complex **1**	1	3	51
6	Complex **1**	0.5	2.5	40
7	$Ru(bpy)_3(PF_6)_2$	1	3	31

[a]trans-anethole, (0.11 mmol), isoprene, (1 mmol). [b]Crude mixtures were passed through a silica column (EtOAc eluent) to remove the catalyst, co-oxidant, and excess trans-anethole. The product was isolated as a clear oil and characterized by NMR and GC/MS. [c]The catalyst and co-oxidants were collected off the silica together and directly reused (see SI).

Table 5.2 summarizes the photocatalytic studies. In the absence of **1** no production of the cycloadduct was observed (entry 1). In the presence of **1** at 5 mol% loading (10 mol% with respect to Ru) a 69% yield of the cycloadduct product was obtained (entry 2). Complex 1 and the co-oxidant were then recovered from this reaction mixture and used for a second consecutive reaction in the presence of fresh diene and dienophile. The recycled catalyst afforded the Diels-Alder product in similar conversion (61%) suggesting that the catalyst is robust (entry 3). In separate reactions the loading the complex **1** was decreased down to just 0.5 mol% loading (1 mol% Ru) which still

192

resulted in reasonable product formation (entries $4-6$). For comparison, a reaction was performed using 1 mol% loading of $Ru(bpy)_3(PF_6)_2$ as the photosensitizer instead of **1** (entry 7). The yield of isolated product for $Ru(bpy)_3(PF_6)_2$ was slightly lower (31%) than obtained for an equivalent mol% Ru from **1** (40%). These results indicate that **1** is not only robust, but exhibits equal to slightly greater reactivity for this Diels-Alder reaction compared to $Ru(bpy)_3(PF_6)_2$.

5.4 Conclusions

These results demonstrate that complex **1** can facilitate the radical cation mediated Diels-Alder reaction upon visible light excitation. The bimetallic complex **1** could be used at low catalyst loading and was recyclable. Photophysical investigations show that **1** strongly absorbs light in the visible spectrum and has a relatively long-lived excited state. Electrochemically reversible one-electron oxidation and three reversible one-electron reductions were also observed.

As reversible redox behavior is important for electron transfer agents and photosensitizers, complex **1** was tested as a photocatalyst for the radical cation Diels-Alder reaction between *trans*-anethole and isoprene. The catalyst facilitated the reaction in good conversion and high selectivity. Following the reaction, the catalyst was recovered and reused, suggesting it has good stability. Strong visible light absorbtion, powerful reductive driving force and the exceptional stability of the complex will broaden its applicability as a photosensitizer for variety of organic transformations. In addition, the ability to bridge two distinct metal centers also makes this macrocycle a candidate as a bridging ligand in chromophore-catalyst assemblies.[34] Studies are

193

underway on the synthesis of mixed metal complexes containing μ-**L** for use in photoredox catalysis.

5.5 Experimental

5.5.1 General methods and materials.

Unless otherwise specified, reagents were used as received without further purification. The bipyridine *bis*-urea macrocycle (**L**) was synthesized according to previous procedures.[35]   All catalytic reactions were conducted in the presence of molecular sieves. ^{1}H NMR and ^{13}C NMR spectra were recorded on Varian Mercury/VX 300 NMR.
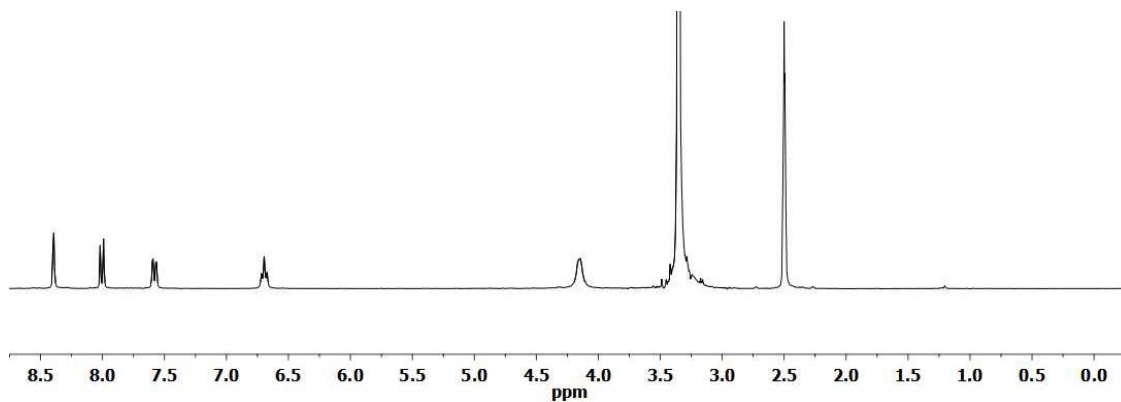
Figure 5.7. ^{1}H NMR spectrum of **L** in DMSO-*d6*.

^{1}H NMR (300 MHz, DMSO-*d6*): δ 8.39 (s, 4H, Ar-H), 8.01 (d, J = 8.1 Hz, 4H, Ar-H), 7.58 (dd, J = 8.1, 1.8 Hz, 4H, Ar-H), 6.70 (t, J = 6.6 Hz, 4H, N-H), 4.1 (s, 8H, -CH$_2$-).

194

5.5.2 Synthesis of [(bpy)$_2$Ru(μ-L)Ru(bpy)$_2$]Cl$_4$•6H$_2$O (1)

Single crystals of complex **1** were synthesized via the solvothermal reaction of bipyridine *bis*-urea macrocycle (10.0 mg, 0.021 mmol) and Ru(bpy)$_2$Cl$_2$.2H$_2$O (21.85 mg, 0.042 mmol) in ethanol (12.5 mL). The reagents and the solvent were added to a ~25 mL pressure tube and sonicated for 10 minutes. Then the tube was secured in a steel tube and placed in a programmable crystallization oven. The sample was heated (4 ˚C/h) to 90 ˚C for 48 h and cooled (0.1 ˚C/min) to room temperature. At the end of the reaction, orange block like crystals were obtained in 92.5 % yield with the molecular formula of [(Ru(C$_{10}$H$_8$N$_2$)$_2$)$_2$C$_{26}$H$_{24}$N$_8$O$_2$)](Cl)$_4$(H$_2$O)$_6$ as confirmed by single crystal XRD analysis.
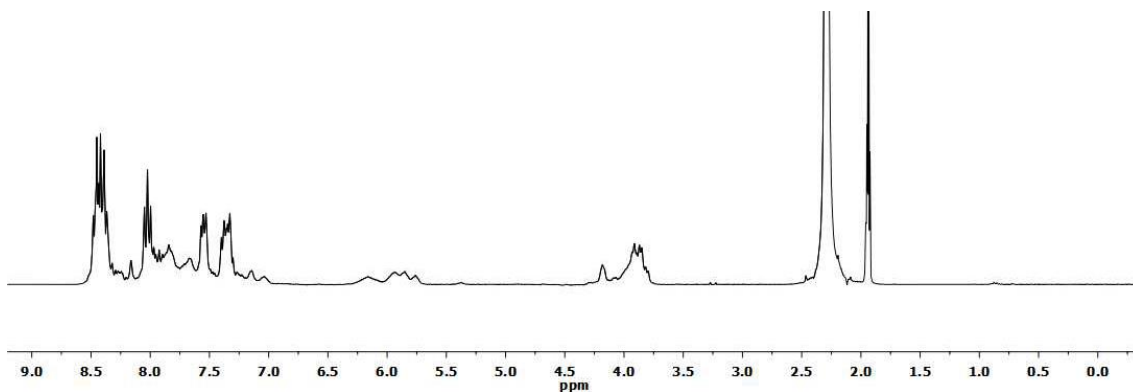
Figure 5.8. ^{1}H NMR (400 MHz, CD3CN) spectrum of **1**.
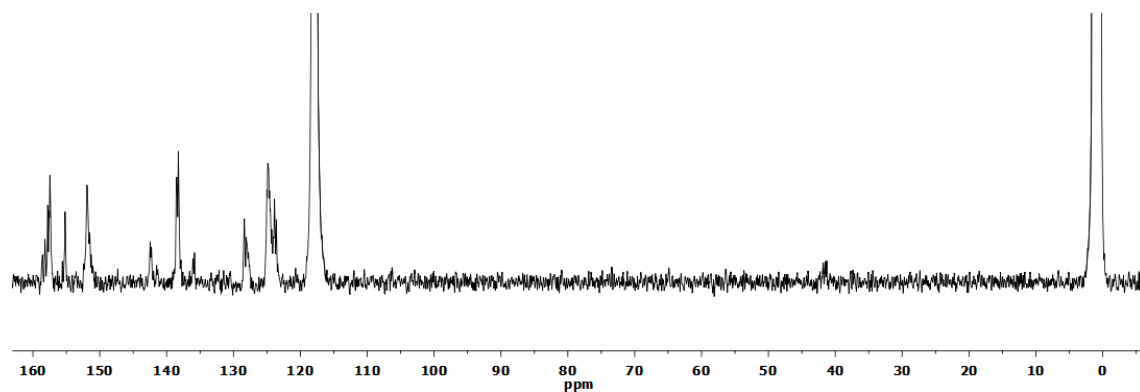
Figure 5.9. ^{13}C NMR (100 MHz, CD3CN) spectrum of **1**.

^{1}H-NMR: (400 MHz, CD3CN): δ 8.39-8.51 (m, 12H, Ar-H), 7.87-8.08 (m, 8H, Ar-H), 7.56-7.70 (m, 8H, Ar-H), 7.33-7.43 (m, 12H, Ar-H), 7.07-7.17 (m, 4H, Ar-H), 5.79-6.19 (m, 4H, -NH), 3.82-4.21 (m, 8H, -CH$_2$). ^{13}C-NMR: (100 MHz, CD3CN): δ 41.51, 123.58, 123.87, 124.88, 127.79, 128.09, 128.37, 135.83, 136.06, 138.25, 138.48, 142.28, 142.47, 151.49, 151.86, 155.19, 155.60, 157.47, 157.79, 158.29, 158.57 HRMS (TOF MS ES+): m/z: (C$_{66}$H$_{56}$N$_{16}$O$_2$Ru$_2$)$^{4+}$: Calculated 327.1, found 327.1.

5.5.3 X-ray crystallography

X-ray intensity data were collected at 100(2) K using a Bruker SMART APEX diffractometer (Mo Kα radiation, λ = 0.71073 Å).[36] The raw area detector data frames were reduced with the SAINT+ program.[36] Final unit cell parameters were determined by least-squares refinement of 3647 reflections from the data set. Direct methods structure solution, difference Fourier calculations and full-matrix least-squares refinement against F^2 were performed with SHELXS/L[37] as implemented in OLEX2.

The compound [(bpy)$_2$Ru(μ-L)Ru(bpy)$_2$]Cl$_4$•6H$_2$O (**1**) crystallizes in the space group C2/c as determined by the pattern of systematic absences in the intensity data and

196

by the successful solution and refinement of the structure. Two chloride anions are located on special positions: Cl2 is on an inversion center and Cl3 is on a two-fold axis of rotation. Non-hydrogen atoms were refined with anisotropic displacement parameters. Hydrogen atoms bonded to carbon were placed in geometrically idealized positions and included as riding atoms. The two urea group hydrogen atoms H1 and H2 were located in difference maps and refined freely. The water hydrogen atoms were also located in difference maps but could not be refined freely. Their located positions were adjusted to give $d(O-H) = 0.85$ Å and they were subsequently refined as riding atoms. The largest residual electron density peak in the final difference map is located 0.9 Å from the ruthenium atom.

5.5.4 Photophysical experiments

Steady-state and time-resolved emission data were collected at room temperature using an Edinburgh FLS980 spectrometer. For steady-state emission, samples were excited using light output from a housed 450 W Xe lamp passed through a single grating (1800 l/mm, 250 nm blaze) Czerny-Turner monochromator and finally a 1 nm bandwidth slit. Emission from the sample was passed through a single grating (1800 l/mm, 500 nm blaze) Czerny-Turner monochromator (1.5 nm bandwidth) and finally detected by a peltier-cooled Hamamatsu R928 photomultiplier tube. The dynamics of emission decay were monitored by using the FLS980's time-correlated single-photon counting capability (1024 channels; 10 μs window) with data collection for 5,000 counts. Excitation was provided by an Edinburgh EPL-445 picosecond pulsed diode laser (445 ± 10 nm, pulse width – 100.0 ps) operated at 0.1 MHz. Kinetics were fit with a single exponential function by using Edinburgh software package. Absolute Emission quantum yields were

197

acquired using an integrating sphere incorporated into a spectrofluorimeter (FLS980, Edinburgh Instruments). The samples were placed in the sphere and a movable mirror was used for direct or indirect excitation, making it possible to measure absolute emission quantum efficiency following the De Mello method.[38] No filters were used during quantum yield measurements.

Table 5.3. Photophysical properties of $Ru(bpy)_3^{2+}$ and **1** in N_2 deaerated acetonitrile at room temperature ($\lambda_{ex} = 450$ nm).

Compound	Absorbance λ (nm)	Emission at rt			k_r (× 10^7s^{-1})[a]	k_{nr} (× 10^8s^{-1})[b]
		λ_{max} (nm)	τ (ns)	ϕ_{PL}		
$Ru(bpy)_3^{2+}$	288, 451	610	824	0.0348	0.004	0.012
1	288, 451	610	706	0.0208	0.003	0.014

(a) $k_r = \Phi/\tau$. (b) $k_{nr} = (1-\Phi)/\tau$.

5.5.5 Electrochemical Experiments.

Cyclic voltammetry (CV) and differential pulse voltammetry (DPV) were carried out using a WaveDriver 20 Bipotentiostat/Galvanometer (Pine Research Instrumentation). The working electrode was a 3 mm diameter glassy-carbon electrode (CH Instruments). A Pt wire (99.99%) was used as the counter electrode. The reference electrode was a saturated calomel electrode (SCE) (CH Instruments). The potential of the reference electrode was adjusted by 0.24 V for the reported potentials versus the normal hydrogen electrode (NHE). The glassy-carbon electrode was prepared by manually polishing with 0.05 μm Alumina suspension (DE agglomerated, Allied High Tech Product, iNC).

All solutions used for electrochemical measurements contained 0.1 M tetrabutylammonium hexafluorophosphate (TBAPF$_6$, Acros Organics) further purified by recrystallization from ethanol and dried under vacuum at 80 ^{o}C for 24 hours. Solution of

dimethylformamide (DMF) (Acros, extra dry, water ≤ 50 ppm) and acetonitrile (EMD Chemicals DriSolv®, 99.8%, water ≤ 50 ppm) were used without further drying, but were purged with N_2 for five minutes before measurements were performed. Spectroelectrochemical experiments were performed using a platinum honeycomb spectroelectrochemical cell-kit (Pine Research Instrumentation) with an Agilent Technologies Cary 8454 UV-Vis instrument.
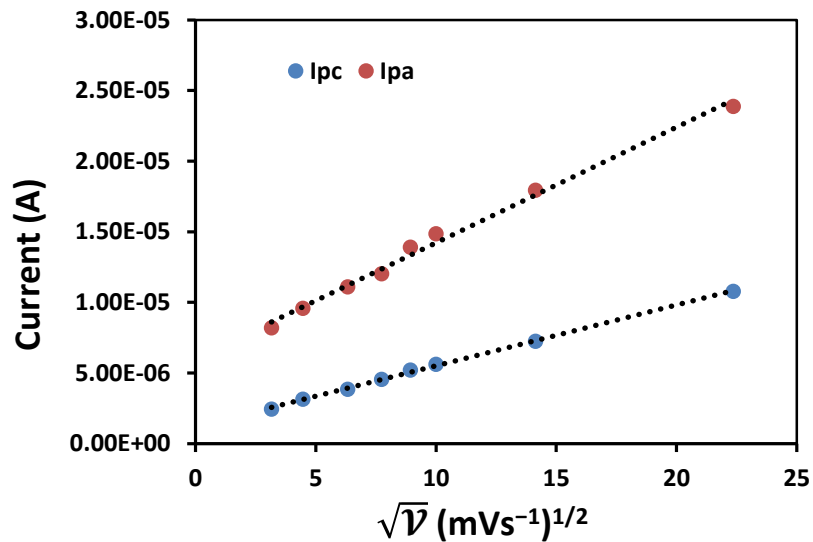
Figure 5.10. Graphical plot of Current vs. $\sqrt{v}$ for first oxidation

199
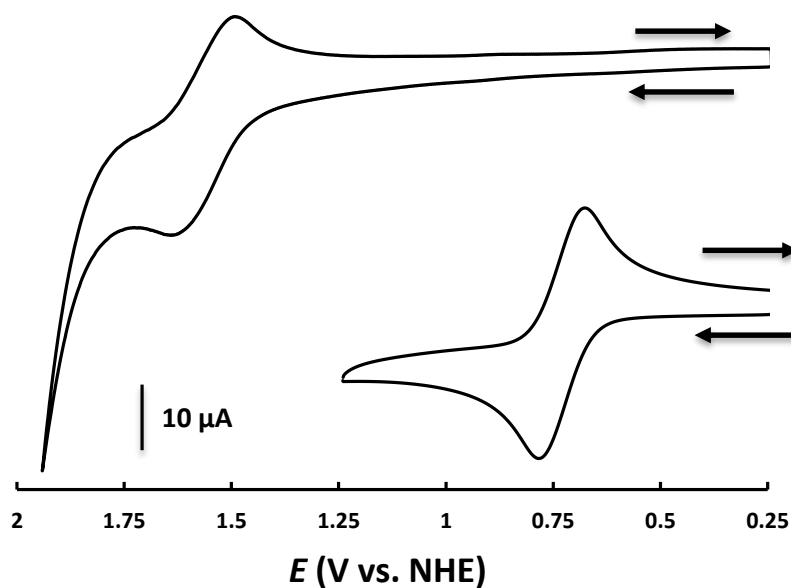
Figure 5.11. Comparison of oxidative currents of 10^{-3} M solution of **1**(top) and 10^{-3} M solution of Ferrocene (below). 0.1 M TBAPF$_6$ in DMF as electrolyte; GC as working electrode; Pt as counter electrode; scan rate = 100 mVs^{-1}
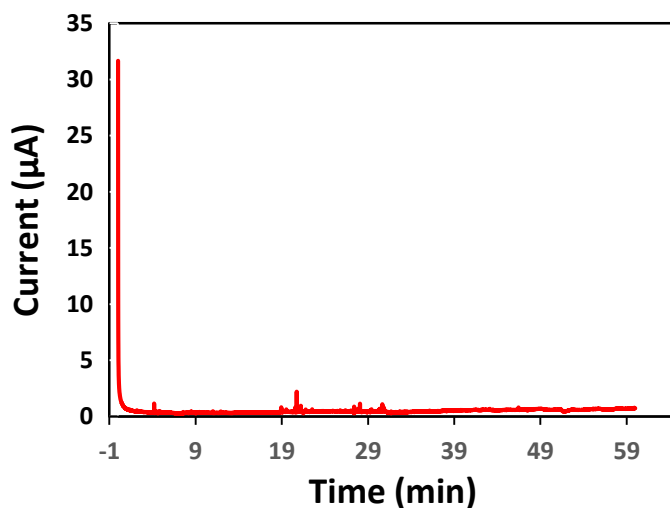
Figure 5.12. Controlled potential (at 1.55V vs. NHE) electrolysis in 0.1 M TBAPF$_6$/MeCN solution over the period of 60 minutes. Performed in 2 mm path length UV-vis cell and with honeycomb spectroelectrochemical set up.
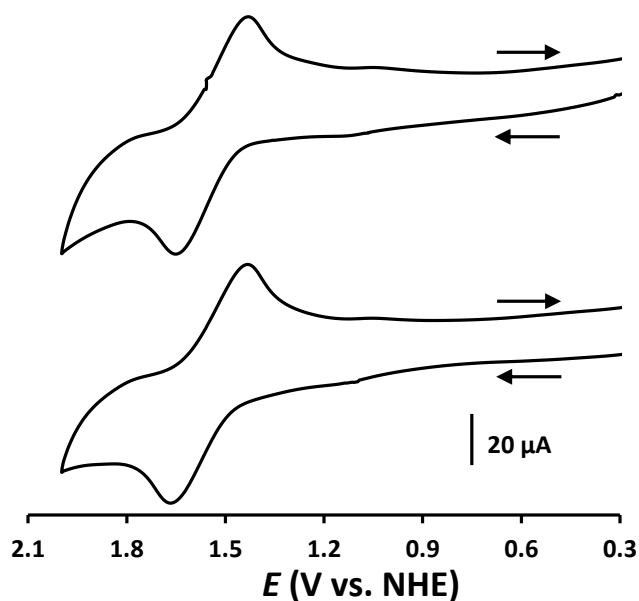
Figure 5.13. CVs of complex **1** before (below) and after (top) 61 minutes of electrolysis in 0.1 M TBAPF$_6$/MeCN solution. Performed in 2 mm path length UV-vis cell and with honeycomb spectroelectrochemical set up (Pt as counter and working electrodes). Scan rate = 100 mVs^{-1}
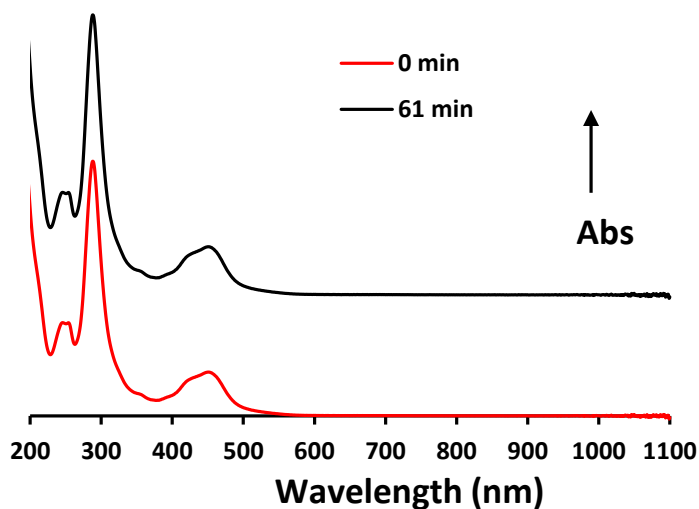
Figure 5.14. Absorption spectra of complex 1 in 0.1 M TBAPF$_6$/MeCN solution before (red) and after (black) 61 mins of electrolysis.

201

5.5.6 Photocatalytic experiments

Starting compounds *trans*-anethole, isoprene, and the solvent CH_3NO_2 were dried with molecular sieves prior to use. The reactions were carried out as follows. *Trans*-anethole, (14.82 mg, 0.11 mmol) and isoprene (68.12 mg, 1 mmol) were stirred in CH_3NO_2 (1 mL) and calculated amounts of complex **1** and the co-oxident methyl viologen were added (Table 5.4).The mixture was irradiated with a 13 W CFL for 1 h. The crude mixture was passed through a silica column (EtOAc eluent) to remove the catalyst, co-oxidant, and excess *trans*-anethole. The Diels-Alder product was isolated as a clear oil. The catalyst was recovered from silica-gel and reused. All the photocatalytic experiments are summarized in the Table 5.4. Stock solutions of either the catalysts or co-oxidant (5 mg/mL) were prepared for the experiments in entries 3, 6, and 7 and appropriate volumes were added. The total volume of CH_3NO_2 was kept at 1 mL. The conversions were calculated using ^1H NMR.

Table 5.4. Photocatalytic experiments in detail.

Entry	Catalyst	Loading (mol%)	Catalyst amount added	Co-oxidant $MV(PF_6)$(mol%)	Co-oxidant amount added	Trial 1 conv. (%)	Trial 2 conv. (%)	Trial 3 conv. (%)	Average conv. (%)
1	No catalyst	0	-	15	4.3 mg	0	0	0	0
2	Complex **1**	5	7.5 mg	15	4.3 mg	70	68	68	69
3	Complex **1**	reused from entry 2		reused from entry 2		61	-	-	-
4	Complex **1**	2.5	3.8 mg	7.5	2.15 mg (430 μL)	65	66	67	66
5	Complex **1**	1	1.5 mg (300 μL)	3	0.86 mg (172 μL)	55	50	47	51
6	Complex **1**	0.5	0.75 mg (150 μL)	2.5	0.43 mg (86 μL)	40	38	41	40
7	$Ru(bpy)_3(PF_6)_2$	1	0.86 mg (172 μL)	3	2.6 mg	28	32	33	31

5.5.7 Recovery of the catalyst

After the reaction in entry 2, the crude mixture was passed through a small silica plug using ethyl acetate. The catalyst and the remaining co-oxidant were retained on silica. The silica was recovered and sonicated with MeOH/MeCN (1:2) ~5 mL 3 times.[39] The mixture was filtered to remove the silica. The filtrate was reduced under vacuum and catalyst was recovered and used to perform the reaction in entry 3.

5.5.8 Characterization of the DA product
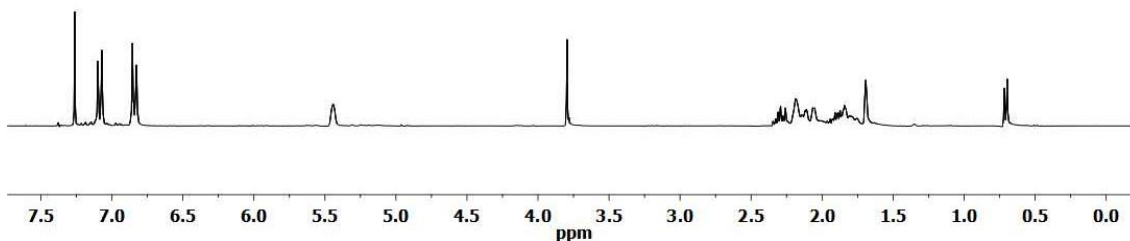
Figure 5.15. ^{1}H NMR (300 MHz, CDCl3) spectrum of **4**.
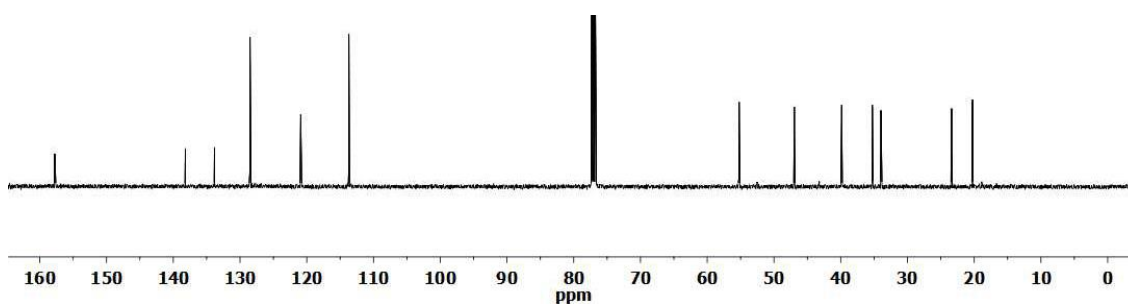
Figure 5.16. ^{13}C NMR (100 MHz, CDCl$_3$) spectrum of **4**.

^{1}H NMR: (300 MHz, CDCl3) δ 7.08 (d, J = 8.7 Hz, 2H), 6.84 (d, J = 8.7 Hz, 2H), 5.45 (s, 1H), 3.8 (s, 3H), 2.35-2.26 (m, 2H), 2.19-2.1 (m, 2H), 1.96-1.75 (m, 2H), 1.7 (s, 3H),

203

0.71 (d, J = 6.2 Hz, 3H); ^{13}C-NMR: (100 MHz, CDCl$_3$): δ 157.8, 138.2, 133.8, 128.4, 120.9, 113.7, 55.2, 46.9, 39.9, 35.3, 34, 23.4, 20.2 HRMS (TOF MS ES+): *m/z*: (C$_{15}$H$_{20}$O)$^+$: Calculated 216.1514, found 216.1516.
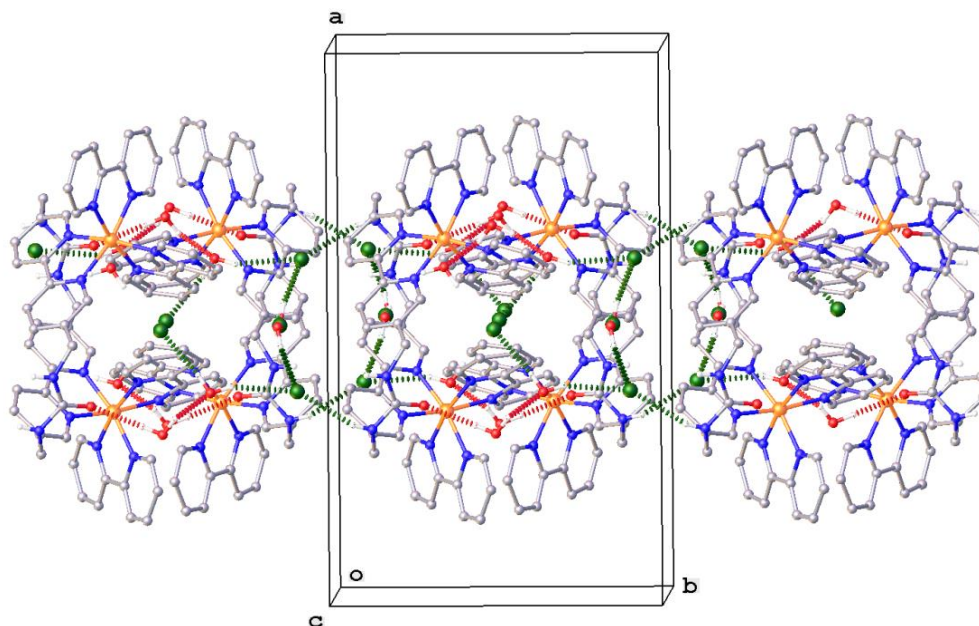
Figure 5.17. Hydrogen bonding network forms layers parallel to the crystallographic (bc) plane.

5.5.8. XRD data of complex 1-

Identification code	srs193m
Empirical formula	C$_{66}$H$_{68}$Cl$_4$N$_{16}$O$_8$Ru$_2$
Formula weight	1557.30
Temperature/K	100(2)
Crystal system	monoclinic
Space group	C2/c

204

a/Å	22.283(4)
b/Å	12.976(2)
c/Å	22.649(4)
α/°	90.00
β/°	102.976(4)
γ/°	90.00
Volume/Å^3	6381.5(19)
Z	4
ρ_{calc}mg/mm^3	1.621
m/mm^{-1}	0.712
F(000)	3184.0
Crystal size/mm^3	0.24 × 0.2 × 0.16
2Θ range for data collection	3.66 to 52.98°
Index ranges	-27 ≤ h ≤ 27, -16 ≤ k ≤ 15, -28 ≤ l ≤ 28
Reflections collected	31245
Independent reflections	6574[R(int) = 0.0787]
Data/restraints/parameters	6574/0/447
Goodness-of-fit on F^2	0.956
Final R indexes [I>=2σ (I)]	R_1 = 0.0472, wR_2 = 0.1102
Final R indexes [all data]	R_1 = 0.0700, wR_2 = 0.1182
Largest diff. peak/hole / e Å^{-3}	1.39/-0.62

5.6 References

(1) Kadish, K. M. S., K. M.; Guilard, R., editors. Synthesis and Coordination Chemistry
(Part 1).; Science., V. W. S. P. S. H. o. P. **2010**.

(2) Harvey, J. D.; Ziegler, C. J. Developments in the metal chemistry of N-confused
porphyrin. *Coordination Chemistry Reviews* **2003**, *247*, 1-19.

(3) Comba, P.; Schiek, W. Fit and misfit between ligands and metal ions. *Coordination Chemistry Reviews* **2003**, *238–239*, 21-29.

(4) Hancock, R. D.; Martell, A. E. The Chelate, Cryptate and Macrocyclic Effects. *Comments on Inorganic Chemistry* **1988**, *6*, 237-284.

(5) Medlycott, E. A.; Hanan, G. S. Synthesis and properties of mono- and oligo-nuclear Ru(II) complexes of tridentate ligands: The quest for long-lived excited states at room temperature. *Coordination Chemistry Reviews* **2006**, *250*, 1763-1782.

(6) Balzani, V.; Juris, A. Photochemistry and photophysics of Ru(II)□polypyridine complexes in the Bologna group. From early studies to recent developments. *Coordination Chemistry Reviews* **2001**, *211*, 97-115.

(7) De Cola, L.; Belser, P. Photoinduced energy and electron transfer processes in rigidly bridged dinuclear Ru/Os complexes. *Coordination Chemistry Reviews* **1998**, *177*, 301-346.

(8) Sauvage, J. P.; Collin, J. P.; Chambron, J. C.; Guillerez, S.; Coudret, C.; Balzani, V.; Barigelletti, F.; De Cola, L.; Flamigni, L. Ruthenium(II) and Osmium(II) Bis(terpyridine) Complexes in Covalently-Linked Multicomponent Systems: Synthesis, Electrochemical Behavior, Absorption Spectra, and Photochemical and Photophysical Properties. *Chemical Reviews* **1994**, *94*, 993-1019.

(9) Grätzel, M. Recent Advances in Sensitized Mesoscopic Solar Cells. *Accounts of Chemical Research* **2009**, *42*, 1788-1798.

(10) Yin, J.-F.; Velayudham, M.; Bhattacharya, D.; Lin, H.-C.; Lu, K.-L. Structure optimization of ruthenium photosensitizers for efficient dye-sensitized solar cells – A goal toward a "bright" future. *Coordination Chemistry Reviews* **2012**, *256*, 3008-3035.

206

(11) Blakemore, J. D.; Crabtree, R. H.; Brudvig, G. W. Molecular Catalysts for Water Oxidation. *Chemical Reviews* **2015**.

(12) Chang, K.-C.; Sun, S.-S.; Odago, M. O.; Lees, A. J. Anion recognition and sensing by transition-metal complexes with polarized NH recognition motifs. *Coordination Chemistry Reviews* **2015**, *284*, 111-123.

(13) Balzani, V.; Bergamini, G.; Ceroni, P. From the photochemistry of coordination compounds to light-powered nanoscale devices and machines. *Coordination Chemistry Reviews* **2008**, *252*, 2456-2469.

(14) Constable, E. C.; Housecroft, C. E.; Neuburger, M.; Rösel, P. J.; Schaffner, S.; Zampese, J. A. Metallomacrocycles with a Difference: Macrocyclic Complexes with Exocyclic Ruthenium(II)-Containing Domains. *Chemistry – A European Journal* **2009**, *15*, 11746-11757.

(15) Henze, O.; Lentz, D.; Schäfer, A.; Franke, P.; Schlüter, A. D. Phenylacetylene Macrocycles with Two Opposing Bipyridine Donor Sites: Syntheses, X-ray Structure Determinations, and Ru Complexation. *Chemistry – A European Journal* **2002**, *8*, 357-365.

(16) Kaes, C.; Wais Hosseini, M.; Kaes, C.; De Cian, A.; Fischer, J. Synthesis and structural analysis of a exo-ditopic macrocyclic ligand bearing 2,2[prime or minute]-bipyridine units interconnected by silane spacers and of its binuclear ruthenium complex. *Chemical Communications* **1997**, 2229-2230.

(17) Beer, P. D.; Szemes, F.; Balzani, V.; Salà, C. M.; Drew, M. G. B.; Dent, S. W.; Maestri, M. Anion Selective Recognition and Sensing by Novel Macrocyclic Transition

Metal Receptor Systems. 1H NMR, Electrochemical, and Photophysical Investigations. *Journal of the American Chemical Society* **1997**, *119*, 11864-11875.

(18) Venturi, M.; Marchioni, F.; Ferrer Ribera, B.; Balzani, V.; Opris, D. M.; Schlüter, A. D. Photoinduced Energy- and Electron-Transfer Processes in Dinuclear RuII–OsII, RuII–OsIII, and RuIII–OsII Trisbipyridine Complexes Containing a Shape-Persistent Macrocyclic Spacer. *ChemPhysChem* **2006**, *7*, 229-239.

(19) Venturi, M.; Marchioni, F.; Balzani, V.; Opris, Dorina M.; Henze, O.; Schlüter, A. D. A Photophysical and Electrochemical Investigation on a Phenylacetylene Macrocycle Containing Two 2,2′-Bipyridine Units, Its Protonated Forms, and RuII and OsII Complexes. *European Journal of Organic Chemistry* **2003**, *2003*, 4227-4233.

(20) Shimizu, L. S.; Salpage, S. R.; Korous, A. A. Functional Materials from Self-Assembled *Bis*-urea Macrocycles. *Accounts of Chemical Research* **2014**, *47*, 2116-2127.

(21) Dawn, S.; Salpage, S. R.; Smith, M. D.; Sharma, S. K.; Shimizu, L. S. A trinuclear silver coordination polymer from a bipyridine *bis*-urea macrocyclic ligand and silver triflate. *Inorganic Chemistry Communications* **2012**, *15*, 88-92.

(22) Juris, A.; Balzani, V.; Barigelletti, F.; Campagna, S.; Belser, P.; von Zelewsky, A. Ru(II) polypyridine complexes: photophysics, photochemistry, eletrochemistry, and chemiluminescence. *Coordination Chemistry Reviews* **1988**, *84*, 85-277.

(23) Kalyanasundaram, K. Photophysics, photochemistry and solar energy conversion with tris(bipyridyl)ruthenium(II) and its analogues. *Coordination Chemistry Reviews* **1982**, *46*, 159-244.

(24) Ravelli, D.; Fagnoni, M.; Albini, A. Photoorganocatalysis. What for? *Chemical Society Reviews* **2013**, *42*, 97-113.

(25) Beatty, J. W.; Stephenson, C. R. J. Amine Functionalization via Oxidative Photoredox Catalysis: Methodology Development and Complex Molecule Synthesis. *Accounts of Chemical Research* **2015**, *48*, 1474-1484.

(26) Schultz, D. M.; Yoon, T. P. Solar Synthesis: Prospects in Visible Light Photocatalysis. *Science* **2014**, *343*.

(27) Prier, C. K.; Rankic, D. A.; MacMillan, D. W. C. Visible Light Photoredox Catalysis with Transition Metal Complexes: Applications in Organic Synthesis. *Chemical Reviews* **2013**, *113*, 5322-5363.

(28) Yoon, T. P.; Ischay, M. A.; Du, J. Visible light photocatalysis as a greener approach to photochemical synthesis. *Nat. Chem.* **2010**, *2*, 527-532.

(29) Gieseler, A.; Steckhan, E.; Wiest, O.; Knoch, F. Photochemically induced radical-cation Diels-Alder reaction of indole and electron-rich dienes. *The Journal of Organic Chemistry* **1991**, *56*, 1405-1411.

(30) Valentine, D.; Turro, N. J.; Hammond, G. S. Thermal and Photosensitized Dimerizations of Cyclohexadiene. *Journal of the American Chemical Society* **1964**, *86*, 5202-5208.

(31) Sullivan, B. P.; Salmon, D. J.; Meyer, T. J. Mixed phosphine 2,2'-bipyridine complexes of ruthenium. *Inorganic Chemistry* **1978**, *17*, 3334-3341.

(32) Wosinska, Z. M.; Stump, F. L.; Ranjan, R.; Lorance, E. D.; Finley, G. N.; Patel, P. P.; Khawaja, M. A.; Odom, K. L.; Kramer, W. H.; Gould, I. R. N-Alkoxyheterocycles As Irreversible Photooxidants(). *Photochemistry and photobiology* **2014**, *90*, 313-328.

(33) Lin, S.; Ischay, M. A.; Fry, C. G.; Yoon, T. P. Radical Cation Diels–Alder Cycloadditions by Visible Light Photocatalysis. *Journal of the American Chemical Society* **2011**, *133*, 19350-19353.

(34) Jasimuddin, S.; Yamada, T.; Fukuju, K.; Otsuki, J.; Sakai, K. *Chemical Communications* **2010**, *46*, 8466-8468.

(35) Tian, L.-l.; Wang, C.; Dawn, S.; Smith, M. D.; Krause, J. A.; Shimizu, L. S. Macrocycles with Switchable exo/endo Metal Binding Sites. *Journal of the American Chemical Society* **2009**, *131*, 17620-17629.

(36) SMART Version 5.630, S. V. B. A. X.-r. S., Inc., Madison, Wisconsin, USA, 2003.

(37) Dolomanov, O. V., Bourhis, L. J., Gildea, R. J., Howard J. A. K. and Puschmann, H. . OLEX2: a complete structure solution, refinement and analysis program. . *J. Appl. Cryst.* **2009**, *42*, 339-341.

(38) de Mello, J. C.; Wittmann, H. F.; Friend, R. H. An improved experimental determination of external photoluminescence quantum efficiency. *Advanced Materials* **1997**, *9*, 230-232.

(39) Xia, J.-D.; Deng, G.-B.; Zhou, M.-B.; Liu, W.; Xie, P.; Li, J.-H. Reusable Visible Light Photoredox Catalysts; Catalyzed Benzylic C(sp3)–H Functionalization/Carbocyclization Reactions. *Synlett* **2012**, *23*, 2707-2713.

CHAPTER VI

CRYSTAL STRUCTURES AND HIRSHFELD SURFACE ANALYSES OF 6-SUBSTITUTED CHROMONES*

6.1 Abstract

In this chapter, we compare structures determined by single crystal X-ray (SCXRD) diffraction of chromone (4H-chromen-4-one) and simple chromone derivatives including 6-methylchromone, 6-methoxychromone, 6-fluorochromone, and 6-chlorochromone, which differ in their electronic characteristics, with the previously reported 6-bromochromone. Analysis showed four different molecular arrangements in the solid state: (1) chromone, (2) 6-methylchromone and 6-methoxychromone (3) 6-fluorochromone and (4) 6-chlorochromone and 6-bromochromone. We probe the effect of substituents at the 6-position on chromone on their crystal structures using an in-depth analysis of Hirshfeld surfaces and fingerprint analysis to identify and understand the non-covalent interactions between the molecules within the crystal lattice that guide these different molecular arrangements. In chromone, hydrogen bonds (O...H) and CH-л interactions predominate. In the second molecular arrangement observed for 6-methylchromone and 6-methoxychromone, hydrogen bonds (O...H) and aryl-stacking interactions serve as major packing interactions. Analysis of SCXRD data of halogen containing derivatives showed two distinctly different molecular packing patterns; however, each also involved significant hydrogen bonding interactions. In the 6-fluorochromone structure, Hirshfeld analysis showed two distinct types of hydrogen bonds with O…H hydrogen bonds having a greater contribution than F…H hydrogen bonds in stabilizing the lattice structure. In contrast, in lattice structures of 6-chlorochromone and 6-bromochromone, the halogen contributes the larger percentage of stabilizing hydrogen bonding interactions with Cl…H and Br…H hydrogen bonds

212

predominating over the O…H hydrogen bond motif. This subtle variation of non-covalent forces influences the molecular arrangement observed in the solid state. A greater understanding and control of these forces could help generate functional crystalline materials.

6.2 Introduction

Crystal engineering is a widely used tool that seeks to understand and control non-covalent intermolecular interactions to organize molecules on the molecular level with the goal of producing functional solid-state materials.[1-7] Elucidating the principles of crystal engineering could allow one to readily and reproducibly afford solids with predictable properties and reactivity that can be used in molecular recognition,[8,9] molecular and supramolecular devices,[10,11] storage,[12,13] and catalysis.[14,15] However, understanding the intricate molecular recognition process that takes place during crystallization to form highly ordered crystalline structures remains a challenge.[16,17] The information gathered from single crystal X-ray studies and subsequent analysis of the molecular surfaces by modelling techniques provides insight into this complex process. This paper investigates the substituent effect on molecular packing of 6-substituted chromones by employing a combination of single crystal X-ray diffraction (SCXRD) and Hirshfeld analysis. Herein, the 6-position of chromone is substituted with a series of electron donating or electron withdrawing substituents, which allows alteration of the electronic properties of the aryl ring as well as introduces additional intermolecular forces innate to the specific substituent. We analyzed the solid state structures of these compounds by SCXRD and observed different packing pattern of molecules in each crystal lattice. Hirshfeld based surface tools were then used to identify and quantify the

213

subtle change in the non-covalent interactions that contribute to the different assembly motifs.

Chromones are oxygen-containing heterocyclic compounds that have a benzoannelated γ-pyrone moiety as the core structure. The chromone scaffold can be found in plants as flavonoids and is employed in medicinal chemistry.[18-20] Studies by Ishar et al. showed that 6-chloro- and 6-fluorochromone-containing structures have promising *anti*-cancer activity both *in vitro* and *in vivo*.[21] Chromones undergo UV light induced reactions including [2+2] photodimerizations[22,23] as well as reactions with olefins and acetylenes.[24,25] Despite their significance, few structures of simple chromone derivatives have been reported in the Cambridge Structural Database (CSD). Our interest in chromones stems from the use nanochannels of self-assembled *bis*-urea macrocycles to modulate their photoreactivity in the solid-state.[26] In 1964, Schmidt set forth topochemical postulates, which correlated solid state structure and photochemical reactivity.[27-29] Specifically, non-covalent intermolecular interactions contribute to the molecular orientation of the crystal lattice and play important roles in determining the nature of the excited states of a molecule, exerting control over photochemical transformations in the solid-state and influence the structure of the final photoproducts. Therefore, we were interested in the structure and reactivity of these compounds in the absence of the host. Here, we investigate simple chromones to analyze a) the crystal structures and molecular packing of these chromones, and b) the interactions that govern lattice stability of a series of 6-substituted chromones to identify the major effects of the substituent on the assembled structure.

214

To compare and contrast the molecular arrangements within these structures, we turned to molecular surface mapping techniques. Models of molecular surfaces such as common fused sphere van der Waals and smoothed Connolly surfaces are defined only by the molecule itself. In contrast, the Hirshfeld method generates the molecular surface by combining single molecule information with the proximity of its nearest neighbors.[30-34] This model relies on the use of high resolution crystal structure data that includes positions of the hydrogen atoms and solvents. Disordered crystal structures typically yield poor and unrealistic surfaces.[35] Hirshfeld surfaces elucidate close contacts between molecules and offer a comprehensive picture by providing the distribution of the intermolecular contacts between the molecules in the lattice using 2D finger print maps. Further, they help identify and provide basic quantitative analysis of the major interactions that are responsible for packing in crystals.

This chapter systematically investigates the molecular packing behavior of chromone and a series of simple chromone derivatives which differ in their electronic characteristics. We have selected chromone (**1**) and five 6-substituted derivatives. Compounds 6-methylchromone (**2**), and 6-methoxychromone (**3**) contain electron donating methyl and methoxy groups at the 6 position respectively. In comparison, 6-fluorochromone (**4**), 6-chlorochromone (**5**), and 6-bromochromone (**6**) have electron withdrawing halogens F, Cl, and Br as the substituents. We have obtained single crystals of compounds **1**-**5** and determined their structures by SCXRD. X-ray data for compound **6** was reported previously.[36] Analysis showed four different molecular arrangements in the solid state within these **6** derivatives. The Hirshfeld surface analysis suggest that O…H hydrogen bonding, CH-л, and aryl-stacking interactions play major roles in

215

stabilizing the lattice structures containing electron donating substitutes, while derivatives

containing electron withdrawing substituents display O…H and X…H (X= F, Cl, or Br)

hydrogen bonding as the major packing interactions.

Table 6.1 Crystal data and refinement results for compounds **1**-**6.**

	1	2	3	4	5	6[d]
CCDC deposition numbers	1415399	1415400	1415401	1415402	1415403	293294
empirical formula	$C_9H_6O_2$	$C_{10}H_8O_2$	$C_{10}H_8O_3 \cdot H_2O$	$C_9H_5O_2F$	$C_9H_5O_2Cl$	$C_9H_5O_2Br$
M	146.14	160.16	194.18	164.13	180.58	225.04
crystal system	monoclinic	triclinic	monoclinic	triclinic	monoclinic	monoclinic
space group	$P2_1/n$	$P\text{-}1$	$P2_1/n$	$P1$	$P2_1$	$P2_1$
flack parameter	n.a.	n.a.	n.a.	opposites averaged	0.01(2)	not given
a (Å)	8.1546(8)	7.0461(3)	8.1923(4)	3.7059(2)	3.8220(2)	3.922(1)
b (Å)	7.8364(7)	10.2108(5)	7.0431(3)	6.1265(4)	5.6985(2)	5.723(2)
c (Å)	11.1424(11)	10.7083(5)	15.3943(8)	7.6161(5)	16.9107(7)	17.208(5)
α (deg)	90	89.884(2)	90	84.085(3)	90	90
β (deg)	108.506(2)	77.679(2)	92.819(2)	87.070(3)	95.8256(18)	95.447(6)
γ (deg)	90	87.367(2)	90	83.390(3)	90	90
V/Å³	675.21(11)	751.86(6)	887.16(7)	170.719(18)	366.41(3)	384.5
Z	4	4	4	1	2	2
D_c/g cm^{-3}	1.438	1.415	1.454	1.596	1.637	1.944
μ/ mm^{-1}	0.102	0.098	0.113	0.131	0.464	5.29
$2\theta_{max}$ (°)	55.460	52.734	56.620	56.562	56.652	55.7
h, k, l ranges	-10 to 10, -10 to 10, -14 to 14	-8 to 8, -12 to 12, -13 to 13	-10 to 10, -9 to 9, -20 to 20	-4 to 4, -8 to 8, -10 to 10	-5 to 5, -7 to 7, -22 to 22	not given
F(000)	304	336	408	84	184	220
R1,[a] wR2[b] [I > 2σ(I)]	0.0376, 0.1047	0.0380, 0.1066	0.0375, 0.1005	0.0332, 0.0868	0.0251, 0.0617	0.038, 0.106
GOF[c] on F²	1.042	1.089	1.044	1.060	1.153	not given

(a) $R1 = \Sigma\ ||F_o| - |F_c||\ /\ \Sigma|F_o|$ (b) $wR2 = \{\ \Sigma\ [\ w(F_o^2 - F_c^2)^2\ ]\ /\ \Sigma\ [\ w(F_o^2)^2\ ]\ \}^{1/2}$ (c) GOF = S

216

$= \{ \Sigma [w(F_o^2-F_c^2)^2] / (n-p) \}^{1/2}$, $w = 1 / [\sigma^2(F_o^2) + (aP)^2 + bP]$ where P is $[2F_c^2 + Max(F_o^2,0)] / 3$.(d) Ref. 36

6.3 Results and discussion

Six chromones were crystallized that differ only in the substituent at the 6-position. This substituent served to modulate the electronics of the fused benzene ring by changing hydrogen at C-6 (**1**) to either electron donating groups including methyl (**2**) or methoxy (**3**) or electron withdrawing groups including as fluoro (**4**), chloro (**5**), or bromo (**6**). We explored how the change of electronics of the ring affects the molecular packing in the crystalline state by analyzing single crystal X-ray diffraction data. Each molecular surface was then mapped by Hirshfeld analysis to (a) analyze the number and types of non-covalent interactions that are present and (b) evaluate percent contribution of each interaction on lattice structure stabilization. The electronic effects of changing the substituent at the 6-position on the ring were also compared with the *beta* value of the substituent, or its ability to act as a hydrogen bond acceptor.

6.3.1 Description of the crystal structures

Chromone, 6-methylchromone, and 6-methoxychromone were crystallized from a mixture of CHCl$_3$/hexane. Chromone crystalized in the monoclinic space group $P2_1/n$ as solvent-free, colorless plates. 6-methylchromone crystallized in the space group P-1 (No. 2) of the triclinic system as solvent-free blocky colorless crystals. Hydrated colorless flat needle crystals of 6-methoxychromone crystallized in the monoclinic space group $P2_1/n$. Solvent-free crystals of compounds 6-fluorochromone and 6-chlorochromone were obtained from acetonitrile solutions. Colorless needle-like crystals of 6-fluorochromone

217

crystallized in the triclinic system in the acentric space group *P*1 (No. 1) and 6-chlorochromone crystalized as colorless plates in the acentric monoclinic space group *P*2$_1$.

In simple aromatic scaffolds such as chromone, typical organization occurs through aryl stacking of electron rich part of a one molecule over an electron poor part of another molecule to minimize the overall dipole in the crystal lattice. As expected, we observed the aryl stacking of neighboring molecules in chromone **1** in an orientation that minimizes the overall dipoles (figure 6.1). Individual molecules associate in a pairwise fashion, with neighboring pairs arranged edge-to-face. The off-set aryl stacking interactions have a centroid-to-centroid distance of 3.614(1) Å, which was calculated using 10 ring atoms between two adjacent molecules. Although the polar ketone oxygen is a good hydrogen bond acceptor (β =5.8, estimate for simple ketone), apart from the hydrate structure of **3** these molecules contain only weak hydrogen bond donors of the type aryl-H (α ~1.0) or aryl-CH3. Additional stabilization is contributed by edge-to-face CH-pi interactions with a normalized H-centroid distance of 2.899(2) Å as shown in the figure 6.1a.

A simple substitution of a methyl group for the H at the 6-position gives compound **2**. The lone pairs of ketone oxygen of one molecule forms two hydrogen bonds with methyl (C-H) groups of two adjacent molecules with C=O1A---C10B distances of 3.504(2) and 3.541(2) Å. A hydrogen bond is also present between the ketone oxygen of one methyl chromone molecule and the H atom next to ring oxygen of a neighboring molecule with C=O1A---C3B distance of 3.226(2) Å. Here, methyl is a mild electron donating group (2.3 Pauling scale)[37] ability compared to hydrogen (2.28) in

218

chromone. In contrast to the pairwise groupings in **1**, we observed stacked columns of molecules of **2** extending along the crystallographic *a* axis, as illustrated in figure 6.1b. Individual molecules within each stack are oriented to minimize the overall dipole, with adjacent molecules related by an inversion center. The offset aryl stacking interactions show an average centroid to centroid distance of 3.590(2) Å which is calculated between two adjacent molecules considering 10 ring atoms of each molecule. The offset of distance is 1.2 Å.

The 6-methoxy chromone **3** crystallized as a monohydrate with the water acting primarily as a hydrogen bonding donor with the nearest chromone molecules. Water is also an acceptor of a CH---O interaction. The two carbonyl oxygen lone pairs of chromone act as acceptors to form two hydrogen bonds with two water molecules with O---O distances of 2.847(2) and 2.850(2) Å. The OH---O hydrogen bonding forms spiral chains following the crystallographic 2_1 screw axis along the monoclinic *b* direction. Another water molecule acts as an acceptor to the H atom adjacent to ring oxygen to form a hydrogen bond with C---O distance of 3.223(2) Å. The methoxy group is a stronger electron donating group (3.7) versus methyl or hydrogen in **2** or **1**.[37] Neighboring chromones stack into columns along the crystallographic *b* direction through aryl stacking distance of 3.524(2) Å (centroid to centroid distance calculated between two adjacent molecules considering 10 ring atoms of each molecules) and offset distance of 1.2 Å. These columns are similar in relative orientation to the previous compounds. Adjacent molecules in each stack are related by crystallographic inversion.

219
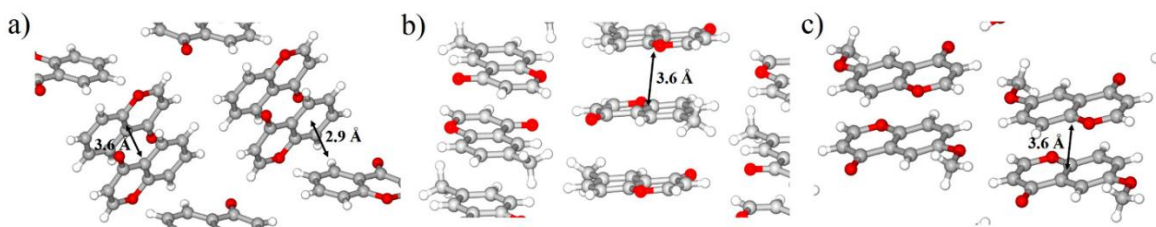
Figure 6.1. Probes for the effects of electron donating groups at the 6-position. (a) Stacking pattern of chromone (**1**) in the crystal lattice highlights the aryl stacking and CH-pi interactions. (b) Orientation of 6-methylchromone (**2**) molecules highlights the aryl stacking interactions. (c) Packing of 6-methoxychromone (**3**) in the crystal highlights the aryl stacking interactions.

Next, we examine the effects of incorporating halides, as electron withdrawing groups at the 6-position. Halogens F, Cl, and Br are known to form variety of non-covalent interactions including hydrogen bonds, halogen bonds, and C-X---л interactions. We observed a markedly different crystal packing features in compounds **4**-**6**, which do not display the electron rich domain of a one molecule packing over an electron poor domain of its neighbor as was typical in the previous structures. In the centrosymmetric structures of **1**-**3**, adjacent molecules are related by crystallographic inversion, and therefore have oppositely directed dipoles. Compounds **4** and **5** both have acentric, chiral packing arrangements, with adjacent molecules in stacks related by unit cell translations. The centroid-halide dipoles of adjacent molecules are oriented in the same direction affording polar structures. Fluorochromone derivative **4** is an unusual example of a small simple achiral molecule that crystallizes in the acentric space group *P*1 (No.1), with one unique molecule per unit cell. It has the strongest electron withdrawing substituent and forms columns of stacked molecules along the crystallographic *a* axis. Within the columns, individual molecules are tilted by 64.55(3)° with respect to the column axis. The columns feature offset pi stacking interactions with centroid-centroid distances of 3.706(1) Å and an offset distance of 1.59 Å. Intercolumnar CH---F hydrogen bonds

220

further stabilize the structure (C2-H2---F1: C-F = 3.206(2) Å, H---F = 2.40(3) Å, <CHF = 135(2) °) (Figure 6.2a). Compounds with larger but less electronegative substituents Cl and Br also showed polar orientation of molecules as in compound **4**. The stacked molecular columns further pack into herringbone-type structures (figure 6.2b and 6.2c). In both Cl and Br derivatives, molecular stacks form columns running along the crystallographic *a* axis with offset aryl stacking interactions with centroid-centroid distances of 3.822(1) Å and 3.9 Å respectively, and with the centroid-centroid offset distance of 1.83 Å. Within the stacks, individual molecules are tilted by 61.15(7)° (Cl) with respect to the stacking axis. We observed the formation of Cl…H, Br…H hydrogen bonds between layers with a distance of 3.527(2) Å (2.90 Å) for Cl1---C9(H9) and 3.0 Å for Br---H respectively. To get further insight into this molecular arrangement, we turned to map the molecular surface using Hirshfeld surface tools.
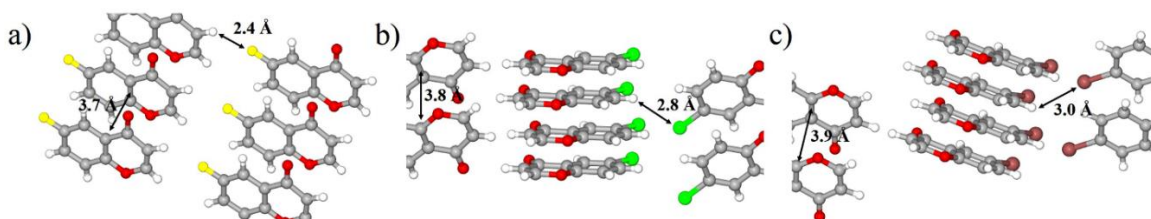
Figure 6.2. Crystal structure of chromones containing electron withdrawing groups at the 6- position. (a) Columnar stacks of 6-fluorochromone arrange along the crystallographic *a* axis (b) Columnar stacks of 6-chlorochromone arrange in herring bone type structure. (c) Columnar stacks of 6-bromochromone arrange in herring bone type structure. (Offset aryl stacking and X…H hydrogen bond distances of each compounds are highlighted)

6.3.2 Hirshfeld surface analysis

Hirshfeld surface analyses were performed in order to understand the nature of packing of molecules in their crystal lattice structure, highlighting the contribution of significant interactions between molecules that are responsible for the molecular

221

arrangement observed in the crystalline state. Two dimensional (2D) fingerprints maps were obtained by calculating the distances from the Hirshfeld surface to the nearest nucleus inside the surface (d_i) to the outside surface (d_e) to analyze the molecular interactions around the nearest neighbor molecules. In 2D maps, green regions shows closer contacts and longer contacts indicated in blue color. The Hirshfeld surfaces of the compounds **1**-**6** were generated over a d_{norm} range -0.5 to 1.5.[38] All surfaces constructed using d_{norn} function were illustrated as transparent hollow maps in order to clearly visualize the benzoannelated γ-pyrone moiety inside the surface. The red spots on the surfaces represent the distances shorter than sum of vdW radii and blue regions correspond to the distances longer than sum of vdW radii. The surfaces created using d_{norm} were used to highlight the intermolecular O…H, C…H, F…H, Cl…H, and Br…H interactions. Hirshfeld surface maps calculated using curvedness function shows large regions of green areas (relatively flat) separated by blue edges represent the large positive curvature of the molecule. Curvedness maps were used to analyze the nature of intermolecular C…C contacts of each compound.

The two dimensional fingerprint maps and corresponding surfaces for the compound **1** depicted in figure 6.3. Hirshfeld analysis suggests that the chromone **1** lattice is stabilized by three major non-covalent interactions: hydrogen bonds (O…H), CH-л interactions (C…H) and aryl-stacking interactions (C…C). There are two major O…H interactions per molecule that contribute to 27.4% to the overall interactions. These two interactions are equivalent by symmetry with an average C=O---C distance of 3.170(2) Å. Figure 6.3d and 6.3e shows the O…H and C…H contacts. The carbonyl oxygen lone pair of one molecule acts as the accepter and the slightly positive H atom

222

bonded to carbon next to the oxygen in the pyran ring acts as the donor. The molecule inside the surface in the figure 6.4f provides a л-face for the molecule on top to donate a CH-л interaction with a distance of 2.899(2) Å. Simultaneously, the aryl groups (ArC-H) act as a hydrogen bond donor to form the second CH-л interaction. The CH-л interactions correspond to 23.1% of total contribution. As expected from literature reports, the aryl-stacking interactions were less prominent than the O…H and C...H interactions.[38] Figure 6.3c shows the full 2D map of the molecule, which also highlights the green area around d_i=d_e~1.8 Å and corresponds to aryl-stacking interactions (8.9% of the total contribution). The curvedness surface in figure 6.3f clearly shows the green flat area and the nearest molecule lying on top with the distance of 3.57 Å, which is well within the distance for the aryl-stacking interaction.
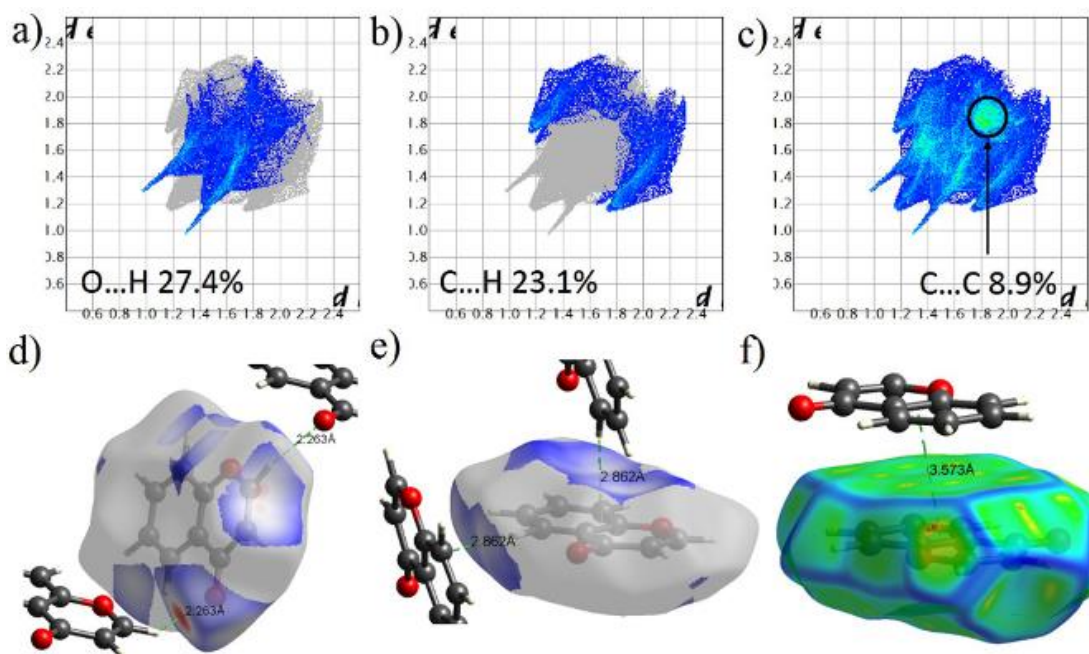
Figure 6.3. Fingerprint plots and surface maps for compound **1**. a) Two dimensional map resolved into O…H/H…O contacts. b) Two dimensional map resolved to show C…H/H…C contacts. c) Full 2D map highlighting the C…C contacts. d) Major O…H/H…O contacts. e) Major C…H/H…C contacts. f) Major C…C contacts.

223

The predominant interactions in compound **2** are hydrogen bonds (O…H) and aryl-stacking (C…C) as shown in figure 6.4. Three adjacent molecules participate in the O…H bonding (figure 6.4c). Two methylene protons acts as hydrogen bond donors to form two O…H interactions with carbonyl oxygen atoms of two adjacent molecules with the C=O---C distances of 3.504(2) and 3.541(2) Å. The third O…H interaction is formed between the H on the pyran ring and the carbonyl oxygen of the nearest molecule with the C=O---C distance of 3.226(2) Å, which is similar to the O…H interaction observed in the compound **1**. The O…H interactions constitute 26.2% of the overall interactions. The two dimensional map in figure 6.4b shows the C…C contacts around the distances of $d_i=d_e\sim1.8$ Å similar to compound **1**. The curvedness map in the figure 6.4d shows two neighboring molecules interact with the single molecule to form two aryl-stacking interactions with the distance of 3.55 and 3.57 Å. The percentage contribution is 16.3%, close to twice as much as calculated for compound **1** which displays only one aryl stacking interaction.

The Hirshfeld analysis suggests that the lattice of compound **3** is stabilized by hydrogen bonds (O…H) and aryl-stacking (C…C) interactions. There are four significant O…H interactions between one molecule of **3** with three molecules of water and another molecule of **3** as indicated by figure 6.5c. The main O…H interactions occur between the oxygen in the methoxy group and a proton from the benzene ring. These forms a stable O…H interaction with the O---C distance of 3.352(1) Å for each O…H interaction. Two H atoms from two water molecules form two O…H interactions with the two lone pairs on the carbonyl oxygen with distances of 2.847(2) and 2.850(2) Å (C=O---O).
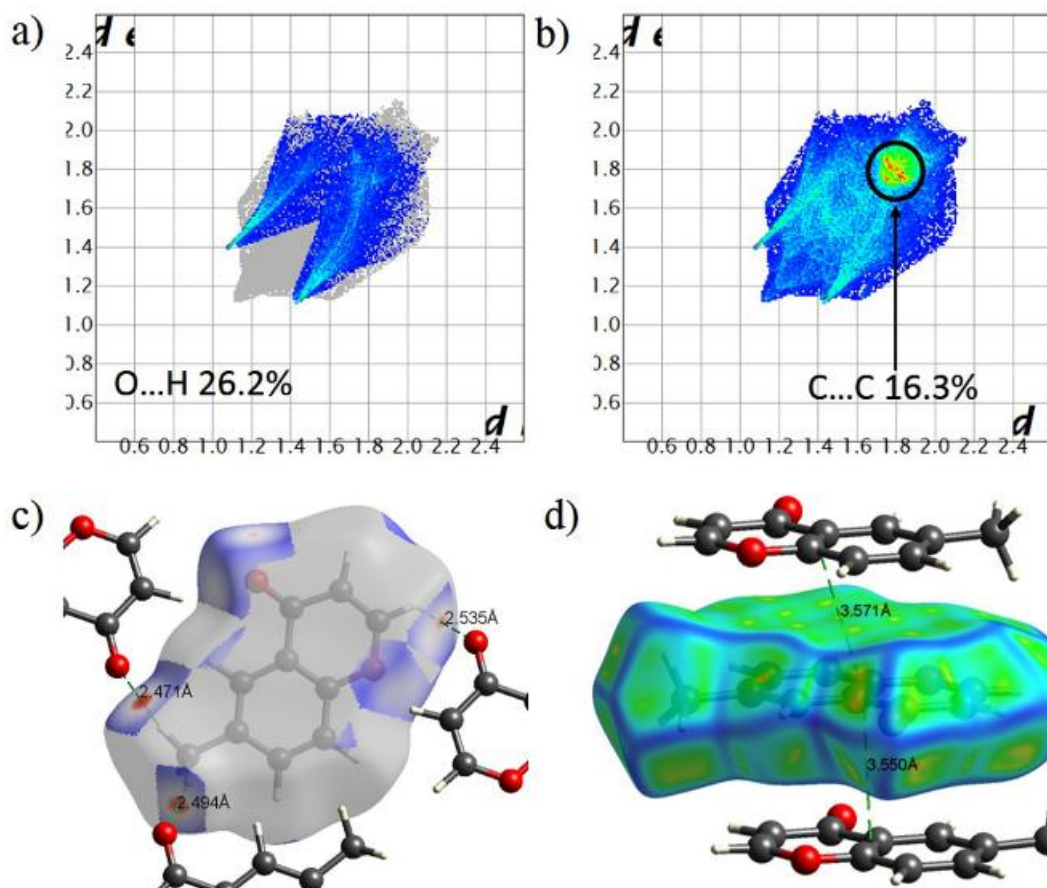
Figure 6.4. Fingerprint plots and surface maps for compound **2**. a) Two dimensional map resolved into O…H/H…O contacts. b) Full 2D map highlighting the C…C contacts. c) Major O…H/H…O contacts between neighboring molecules. d) Major C…C contacts between neighboring molecules.

The oxygen atom from the other water molecule served as the accepter to form another O…H interaction with the proton in the pyran ring with the O---C distance of 3.223(2) Å. All together O…H interactions responsible for 33.4% to the overall stabilizing interactions which is higher compared to molecule **1** and **2**, which have comparatively fewer O…H interactions. The aryl-stacking interactions occurred between two neighboring molecules as indicated by flatness of curvedness map in the figure 6.6d with distances of 3.56 and 3.49 Å. The aryl-stacking (14.7%) has a similar contribution to the overall interaction as molecule **2**.
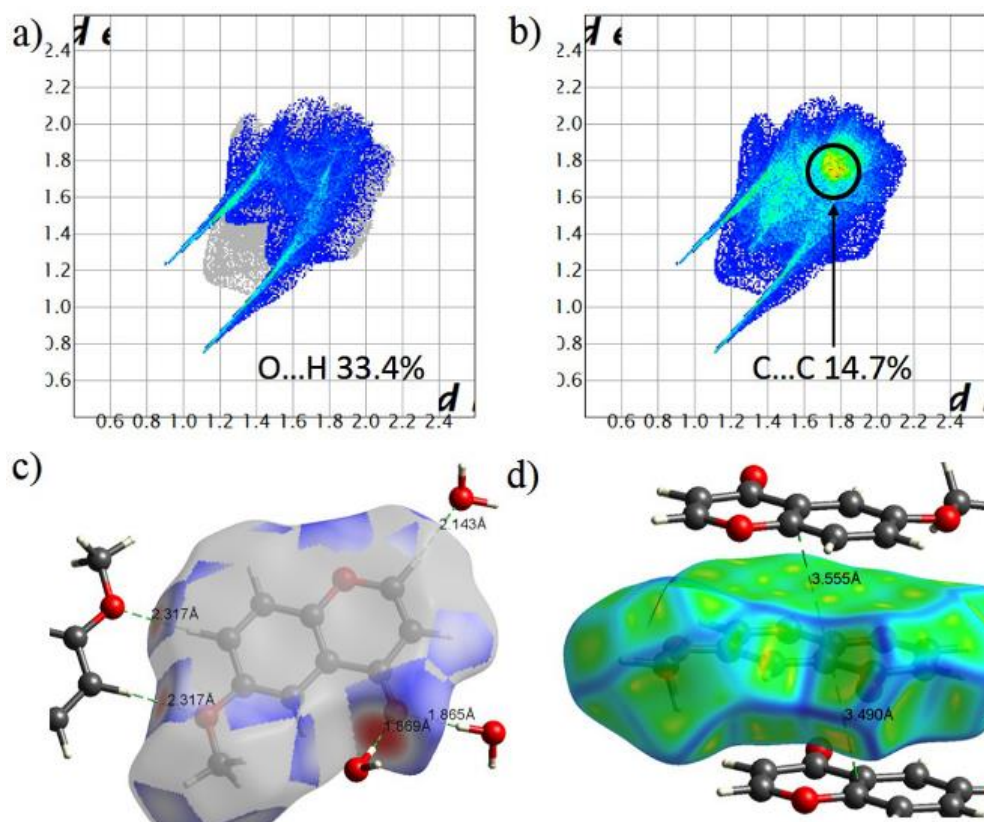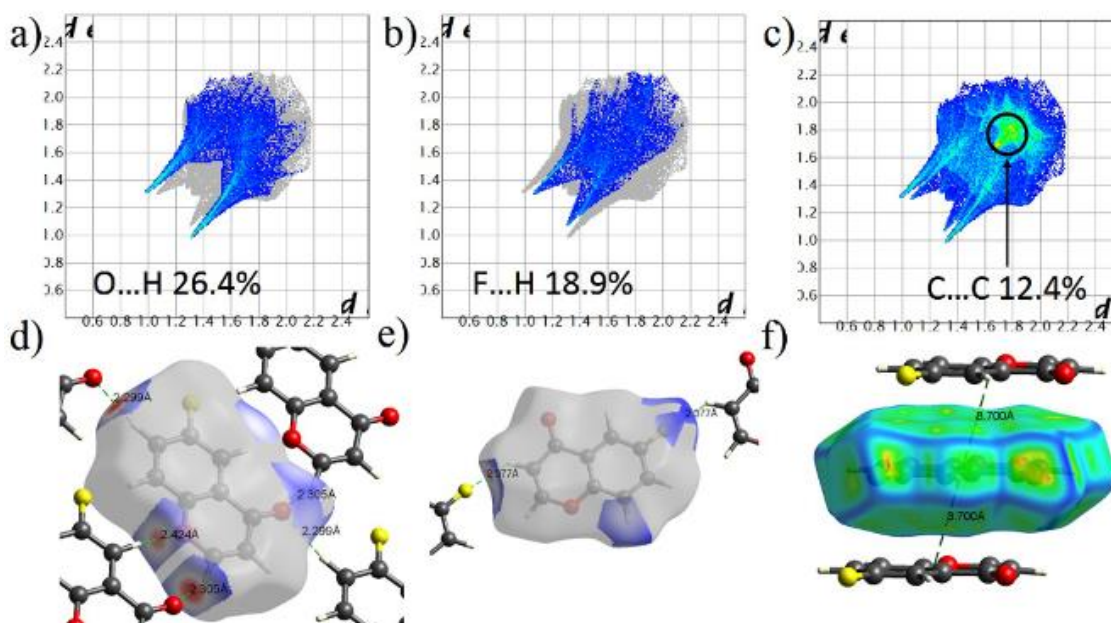
Figure 6.5. Fingerprint plots and surface maps for compounds **3**. a) Two dimensional map resolved into O…H/H…O contacts. b) Full 2D map highlighting the C…C contacts. c) Major O…H/H…O contacts. d) Major C…C contacts.

Figure 6.6 shows the fingerprint plots and surface maps for 6-fluorochromone (**4**). Compound **4** has additional F…H hydrogen bonding interactions in addition to the O…H, and C…C that were observed for compounds **1**-**3**. A single molecule of **4** interacts with three adjacent molecules forming four O…H interactions, contributes significantly to the overall contacts (26.4%). The interaction forms between electron poor H atom on the carbon adjacent to F with the lone pair electron on a neighboring pyran oxygen shows a C---O distances of 3.478(2) Å. The second hydrogen bonding interaction is observed between the electron poor H atom in the pyran ring that interacts with the lone pair of carbonyl oxygen on an adjacent molecule and shows a C=O---C distance of 3.340(2) Å as indicated in the figure 6.6d. In addition, two lone pairs on the carbonyl oxygen of

molecule inside the surface act as acceptors for two C-H hydrogen bonding interactions with two different neighboring molecules displaying C=O---C distances of 3.554(2) and 3.637(2) Å respectively. There are two F…H interactions highlighted in the figure 6.6e which are formed by the H atom close to carbonyl of one molecule with an F atom in the nearest molecule at F---C distance of 3.206(2) Å. The overall contribution of F…H contacts are found to be 18.9%. Two aryl-stacking interactions formed between molecules showed in the curvedness map in figure 6.6f with a distance of 3.7 Å and a contribution of 12.4% little higher than in **2** and **3**.

Figure 6.6. Fingerprint plots and surface maps for compounds **4**. a) Two dimensional map resolved into O…H/H…O contacts. b) Two dimensional map resolved to show F…H/H…F contacts. c) Full 2D map highlighting the C…C contacts. d) Major O…H/H…O contacts. e) Major F…H/H…F contacts. f) Major C…C contacts.

Inspection of the Hirshfeld analysis of compound **5** shows marked differences from the fluorinated analogue **4**. Here, we observed Cl…H hydrogen bonding as the main contributor to the packing with an overall contribution of 23.3 % (figure 6.7a) with the O…H hydrogen bonding motif contributing less (19.3 % in **5** versus 26.4% in **4**). There

227

were two significant Cl…H interactions per molecule with a C---Cl distance of 3.799(2) Å (figure 6.7d). These formed between the Cl atom of one molecule and the H9 of the nearest neighbor molecule. Two hydrogen bonds (O…H) observed between the carbonyl oxygen and H2 atom have similar C=O---C distance of 3.312(3) Å. The offset aryl-stacking interaction also contribute to the overall packing (10.2%) and were show a centroid to centroid distance of 3.82 Å.
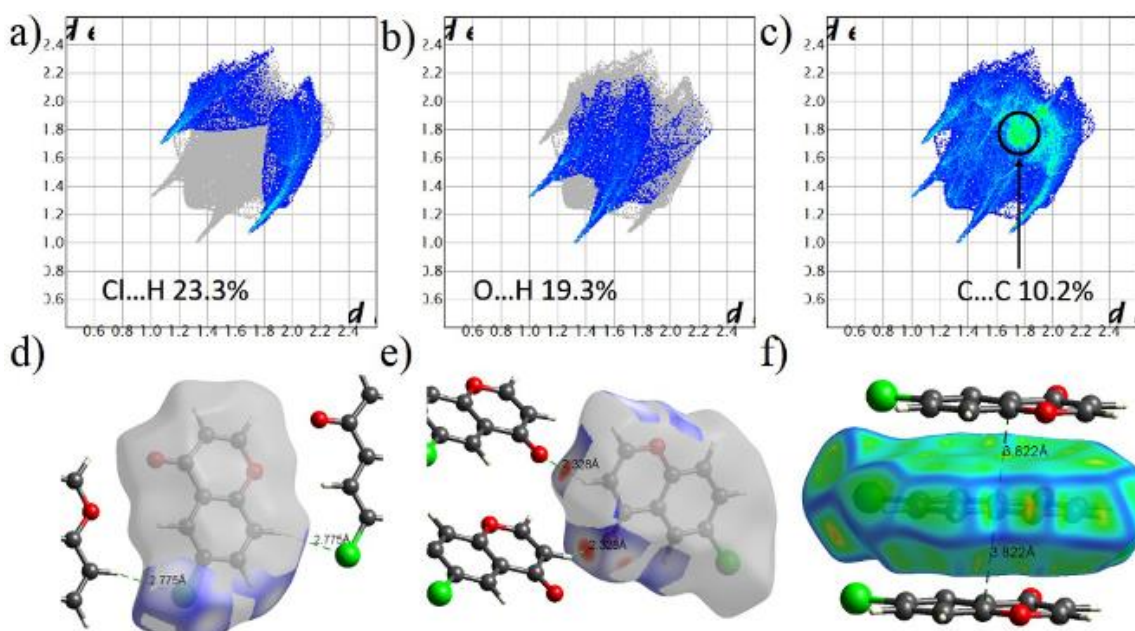
Figure 6.7. Fingerprint plots and surface maps for compounds **5**. a) Two dimensional map resolved to show Cl…H/H…Cl contacts. b) Two dimensional map resolved into O…H/H…O contacts. c) Full 2D map highlighting the C…C contacts. d) Major Cl…H/H…Cl contacts e) Major O…H/H…O contacts. f) Major C…C contacts.

Hirshfeld analysis was carried out on the reported crystal structure of 6-bromochromone **6**, which showed similar herringbone-type packing as the chloro derivative **5**. As expected the lattice forms three major type of interactions with the neighboring molecules. For hydrogen bonding interactions, the Br…H hydrogen bond is the major contributor, with 24.5 % overall contribution. There are two Br…H bonds can

be seen between Br and H4 with a Br---C distances of 3.96 Å. Next, the O…H hydrogen bonds form between carbonyl oxygen and the H3 (figure 6.8e) with the C=O---C distance of 3.32 Å, which contribute 17.8 % to the overall packing. Less prominently, we observed aryl-stacking (C…C) interaction between the pi surfaces of neighboring molecule (figure 6.8f) with a contribution of 9.3% and a distance of 3.92 Å.
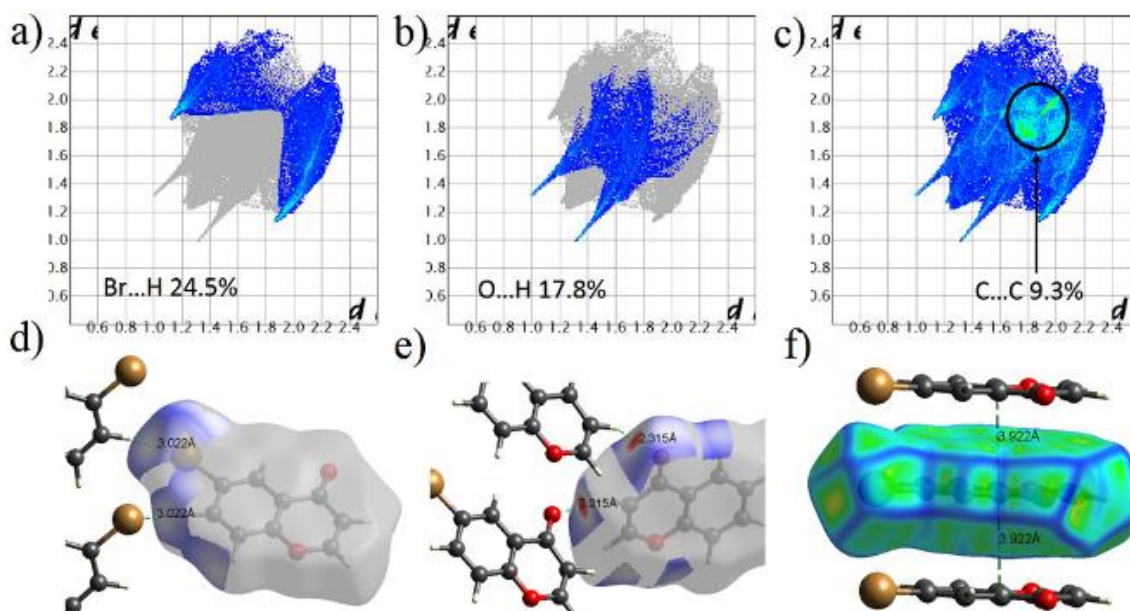
Figure 6.8. Fingerprint plots and surface maps for the 6-bromochromone **6**.[36] a) Two dimensional map resolved to show Br…H/H…Br contacts. b) Two dimensional map resolved into O…H/H…O contacts. c) Full 2D map highlighting the C…C contacts. d) Major Br…H/H…Br contacts e) Major O…H/H…O contacts. f) Major C…C contacts.
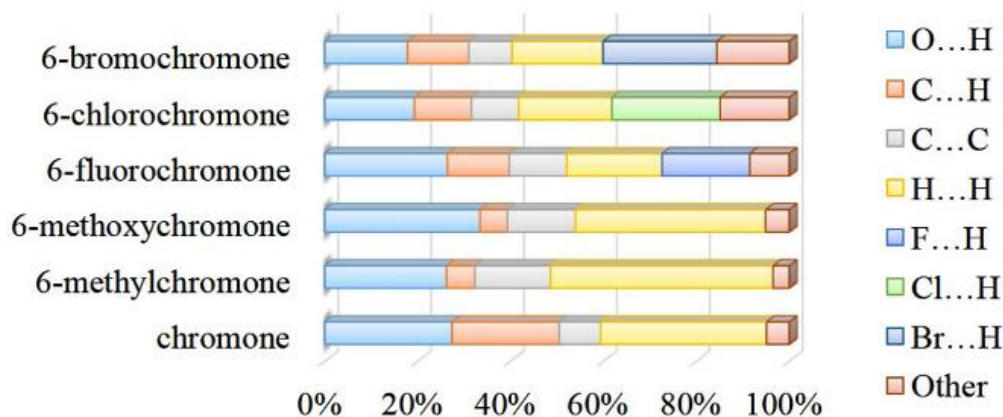
Figure 6.9. Contribution of the various contacts to the Hirshfeld surface.

Figure 6.9 summaries the contribution of all the non-covalent interactions in each compound. Compound 6-methoxychromone showed the highest percentage of O…H contacts (33.4%) where 6-bromochromone has the lowest (17.8%). Among halogen containing compounds 6-bromochromone has the high contribution from X…H contacts (24.5%) while 6-fluorochromone has lowest (18.9%). A survey of halide containing small molecules show that this percentage varies significantly depending on the type of halogen containing compound analyzed.[39,40] We observed a great portion of C…H contacts in the compound chromone (23.1%) and C…C contacts in the compound 6-methylchromone (16.3%). Apart from above the H…H contacts varies 19% to 48% where 6-methylchromone been the highest (47.9%) and 6-bromochromne (19.6%) the lowest.

6.4 Conclusions

In summary, we have systematically investigated the electronic characteristics of simple chromone derivatives through wide selection of electron donating and electron groups at the 6-position. Single crystals of each derivative were successfully grown, their solid-state structures determined by X-ray diffraction and the major packing interactions that help to stabilize each structure and identified. We used Hirshfeld surface analysis to further understand, identify and quantify the interactions that are responsible for different packing patterns seen in the derivatives. According to our Hirshfeld analysis, the majority of stabilizing interactions in chromone **1** consist of O…H hydrogen bonds (27.4%) and CH-л interactions (23.1%). Chromones with electron donating substituents at the 6-position including methyl **2** and methoxy **3**, have O…H hydrogen bonds (26.2%, 33.4%

230

respectively) and offset aryl stacking interactions (16.3%, 14.7% respectively) as the major contributors to the overall packing interactions. In **1-3**, the hydrogen bond donors are relatively weak C-H types. The pairs are oriented with the electron rich aryl group of one chromone oriented over the electron poor aryl group of the neighboring molecule. The analysis outcome of the 6-fluorochromone (**4**) shows a greater portion of stabilizing interactions consist of hydrogen bonds; however, here there are two types of hydrogen bond acceptors with O…H hydrogen bonds contributing slightly more stabilizing interactions (26.4%) than the F…H hydrogen bonds (18.9%). In contrast, in lattice structures of 6-chlorochromone (**5**) and 6-bromochromone (**6**), the halogen contributes the larger percentage of stabilizing hydrogen bonding interactions with Cl…H (23.3%) and Br…H hydrogen bonds (24.5%) versus the O…H hydrogen bond motif (19.3%, 17.8% respectively). In the future, comparison of SCXRD analysis and fingerprints plots generated form Hirshfeld analysis for series of compounds should help to elucidate trends and provide insight into the complex process of crystal formation.

6.5 Experimental

6.5.1 Materials and Methods

Compounds **1** and **4** were purchased from Sigma-Aldrich and compounds **2**, **3**, and **5** were purchased from Indofine Chemical Company. All compounds and solvents were used without further purification. The crystal structure of the compound **6** was previously reported by Staples et al.[36]

6.5.2 Crystallization of ($C_9H_6O_2$) (1), ($C_{10}H_8O_2$) (2), and ($C_{10}H_8O_3$) (H_2O) (3)

Each derivative (50 mg) was dissolved in 0.1 mL chloroform in a scintillation vial. Hexanes were then added dropwise to obtain colorless crystals.

6.5.3 Crystallization of $C_9H_5FO_2$ (4), and $C_9H_5ClO_2$ (5)

Each derivative (50 mg) was heated with 2 mL of acetonitrile in a scintillation vial to obtain a clear solution. The solutions were cooled down to room temperature to obtain colorless crystals.

6.5.4 Single-Crystal Structure Determination

Single crystal X-ray data for all compounds were collected at 100(2) K using Mo Kα radiation (λ = 0.71073 Å). Data for **1** were measured using a Bruker SMART APEX I diffractometer.[37] Data for compounds **2**, **3**, **4**, and **5** were collected using a Bruker D8 QUEST diffractometer equipped with a PHOTON 100 CMOS area detector and an Incoatec microfocus source.[41] The raw area detector data frames were reduced and corrected for absorption effects using the SAINT+ and SADABS programs.[41] Structures were solved by direct methods with SHELXS or SHELXT.[42] Subsequent difference Fourier calculations and full-matrix least-squares refinement against F^2 were performed with SHELXL-2014[42] using OLEX2.[43] All non-hydrogen atoms were refined with anisotropic displacement parameters. Hydrogen atoms were located in Fourier difference maps and either refined freely (**1** and **4**) or as standard riding atoms with refined isotropic displacement parameters (**2**, **3**, **5**). Crystal data for the compounds **1**-**6** are presented in the Table 6.1.

The molecular views of chromones **1**-**6** with corresponding atom numbers are illustrated in the figure 6.10. All the derivatives have the characteristic benzoannelated γ-pyrone moiety, which is composed of benzene fused with a pyran ring. The dihedral angle between the rings range from 0.32° to 2.22° throughout compounds **1**-**6** suggesting a nearly co-planar arrangement. Detailed analysis of the major bond lengths and angles are listed in the table 6.2.
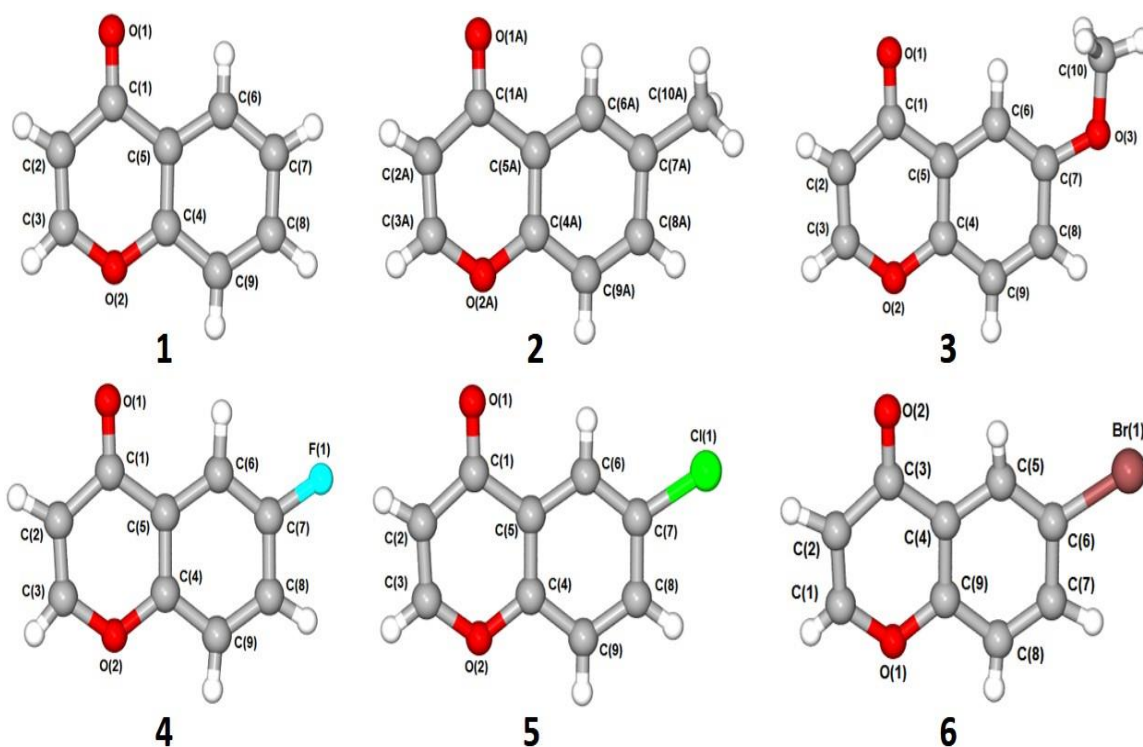
Figure 6.10. Molecular views of the crystal structures with atom numbering: Chromone **1**, 6-methylchromone **2**, 6-methoxychromone **3**, 6-fluorochromone **4**, 6-chlorochromone **5**, and 6-bromochromone **6**.

233

Table 6.2. Comparison of major bond distances and bond angels of compound 1-6.

Entry	C=O	C=C	C-O		C-X	C-C-X	
1	1.232	1.334	1.354 (C3-O2)	1.372 (C4-O2)	0.983 (C7-H)	120.03 (C6-C7-H)	119.91 (C8-C7-H)
2	1.233	1.341	1.356 (C3A-O2A)	1.373 (C4A-O2A)	1.506 (C7A-C10A)	121.63 (C6A-C7A-C10A)	120.29 (C8-C7-C10A)
3	1.247	1.343	1.349 (C3-O2)	1.374 (C4-O2)	1.365 (C7-O3)	124.49 (C6-C7-O3)	114.93 (C8-C7-O3)
4	1.232	1.342	1.357 (C3-O2)	1.378 (C4-O2)	1.357 (C7-F1)	118.63 (C6-C7-F1)	117.98 (C8-C7-F1)
5	1.232	1.339	1.360 (C3-O2)	1.373 (C4-O2)	1.743 (C7-Cl1)	120.30 (C6-C7-Cl1)	117.95 (C8-C7-Cl1)
6	1.238	1.324	1.364 (C1-O1)	1.371 (C9-O1)	1.906 (C6-Br1)	119.88 (C5-C6-Br1)	118.26 (C7-C6-Br1)

The table highlights the variation of bond distances of carbonyl (C=O), olefin (=), and two C-O bonds, within the pyran ring and the bond lengths between the carbon atom in the 6 or 7 position to the corresponding substituent (X) including the bond angles (C-C-X). The C=O bond distances in all the compounds lay in near equality varying only by 0.015 Å between 1.232 Å in compound 3 and 1.247 Å in compound 1. The olefin (=) bond distances also vary by 0.015 Å between 1.349 Å in compound 3 and 1.364 Å in compound 6. The C-O bond in the pyran ring rangers between 1.349 Å and 1.378 Å. The compound 6 has the highest bond distance of 1.906 Å between the C6 atom and the substituent bromine. This supported by the fact that the bromine has the highest atomic radii compared to any other substituent in the series. The compound 4 has a C7-F1 distance of 1.357 Å and the compound 5 has the C7-Cl1 distance of 1.743 Å. The angle

234

C-C-X vary around 120º. The highest deviation from the ideal bond angle fond in the compound 3 where C6-C7-O3 is 124.49º (+4.49º) and C8-C7-O3 114.93º (-5.07º).

6.5.5 Generation of the Hirshfeld surfaces

Molecular Hirshfeld surfaces for compounds **1-6** were constructed using Crystal Explorer 3.1.[44] The Crystallographic Information File (.cif) of each structure was imported into Crystal Explorer and a high resolution Hirshfeld surface was mapped with the functions (a) d_{norm} and (b) curvedness.

6.6 References

(1) Aakeroy, C. B.; Champness, N. R.; Janiak, C. Recent advances in crystal engineering. *CrystEngComm* **2010**, *12*, 22-43.

(2) Braga, D.; Brammer, L.; Champness, N. R. New trends in crystal engineering. *CrystEngComm* **2005**, *7*, 1-19.

(3) Braga, D.; Desiraju, G. R.; Miller, J. S.; Orpen, A. G.; Price, S. L. Innovation in crystal engineering. *CrystEngComm* **2002**, *4*, 500-509.

(4) Desiraju, G. R. Crystal Engineering: A Holistic View. *Angewandte Chemie International Edition* **2007**, *46*, 8342-8356.

(5) Desiraju, G. R. Crystal Engineering: From Molecule to Crystal. *Journal of the American Chemical Society* **2013**, *135*, 9952-9967.

(6) Hollingsworth, M. D. Crystal Engineering: From Structure to Function. *Science* **2002**, *295*, 2410-2413.

(7) Tiekink, E. R. T.: Crystal Engineering. In *Supramolecular Chemistry*; John Wiley & Sons, Ltd, 2012.

(8) Dolain, C.; Maurizot, V.; Huc, I. Protonation-Induced Transition between Two Distinct Helical Conformations of a Synthetic Oligomer via a Linear Intermediate. *Angewandte Chemie International Edition* **2003**, *42*, 2738-2740.

(9) Stadler, A.-M.; Lehn, J.-M. P. Coupled Nanomechanical Motions: Metal-Ion-Effected, pH-Modulated, Simultaneous Extension/Contraction Motions of Double-Domain Helical/Linear Molecular Strands. *Journal of the American Chemical Society* **2014**, *136*, 3400-3409.

(10) Kay, E. R.; Leigh, D. A.; Zerbetto, F. Synthetic Molecular Motors and Mechanical Machines. *Angewandte Chemie International Edition* **2007**, *46*, 72-191.

(11) Lehn, J.-M.: Molecular and Supramolecular Devices. In *Supramolecular Chemistry*; Wiley-VCH Verlag GmbH & Co. KGaA, 2006; pp 89-138.

(12) Makal, T. A.; Li, J.-R.; Lu, W.; Zhou, H.-C. Methane storage in advanced porous materials. *Chemical Society Reviews* **2012**, *41*, 7761-7779.

(13) Tian, J.; Thallapally, P. K.; McGrail, B. P.: Gas Storage and Separation in Supramolecular Materials. In *Supramolecular Chemistry*; John Wiley & Sons, Ltd, 2012.

(14) Liu, J.; Chen, L.; Cui, H.; Zhang, J.; Zhang, L.; Su, C.-Y. Applications of metal-organic frameworks in heterogeneous supramolecular catalysis. *Chemical Society Reviews* **2014**, *43*, 6011-6061.

(15) Wu, C.-D.: Crystal Engineering of Metal-Organic Frameworks for Heterogeneous Catalysis. In *Selective Nanocatalysts and Nanoscience*; Wiley-VCH Verlag GmbH & Co. KGaA, 2011; pp 271-298.

236

(16) Aaker; y, C. B.; Beatty, A. M. <i>Review</i>: Crystal Engineering of Hydrogen-Bonded Assemblies - A Progress Report. *Australian Journal of Chemistry* **2001**, *54*, 409-421.

(17) Desiraju, G. R.: *Crystal engineering: the design of organic solids*; Elsevier, 1989.

(18) Gaspar, A.; Matos, M. J.; Garrido, J.; Uriarte, E.; Borges, F. Chromone: A Valid Scaffold in Medicinal Chemistry. *Chemical Reviews* **2014**, *114*, 4960-4992.

(19) Keri, R. S.; Budagumpi, S.; Pai, R. K.; Balakrishna, R. G. Chromones as a privileged scaffold in drug discovery: A review. *European Journal of Medicinal Chemistry* **2014**, *78*, 340-374.

(20) Verpoorte, R.; Memelink, J. Engineering secondary metabolite production in plants. *Current Opinion in Biotechnology* **2002**, *13*, 181-187.

(21) Ishar, M. P. S.; Singh, G.; Singh, S.; Sreenivasan, K. K.; Singh, G. Design, synthesis, and evaluation of novel 6-chloro-/fluorochromone derivatives as potential topoisomerase inhibitor anticancer agents. *Bioorganic & Medicinal Chemistry Letters* **2006**, *16*, 1366-1370.

(22) Sakamoto, M.; Kanehiro, M.; Mino, T.; Fujita, T. Photodimerization of chromone. *Chemical Communications* **2009**, 2379-2380.

(23) Sakamoto, M.; Yagishita, F.; Kanehiro, M.; Kasashima, Y.; Mino, T.; Fujita, T. Exclusive Photodimerization Reactions of Chromone-2-carboxylic Esters Depending on Reaction Media. *Organic Letters* **2010**, *12*, 4435-4437.

(24) Hanifin, J. W.; Cohen, E. Photoaddition reactions of chromome. *Tetrahedron Letters* **1966**, *7*, 5421-5426.

237

(25) Hanifin, J. W.; Cohen, E. Photoaddition reactions of chromone. *Journal of the American Chemical Society* **1969**, *91*, 4494-4499.

(26) Salpage, S. R.; Donevant, L. S.; Smith, M. D.; Bick, A.; Shimizu, L. S. Modulating the reactivity of chromone and its derivatives through encapsulation in a self-assembled phenylethynylene bis-urea host. *Journal of Photochemistry and Photobiology A: Chemistry* **2016**, *315*, 14-24.

(27) Cohen, M. D.; Schmidt, G. M. J. 383. Topochemistry. Part I. A survey. *Journal of the Chemical Society (Resumed)* **1964**, 1996-2000.

(28) Cohen, M. D.; Schmidt, G. M. J.; Sonntag, F. I. 384. Topochemistry. Part II. The photochemistry of trans-cinnamic acids. *Journal of the Chemical Society (Resumed)* **1964**, 2000-2013.

(29) Schmidt, G. M. J.: Photodimerization in the solid state. In *Pure and Applied Chemistry*, 1971; Vol. 27; pp 647.

(30) McKinnon, J. J.; Jayatilaka, D.; Spackman, M. A. Towards quantitative analysis of intermolecular interactions with Hirshfeld surfaces. *Chemical Communications* **2007**, 3814-3816.

(31) McKinnon, J. J.; Mitchell, A. S.; Spackman, M. A. Hirshfeld Surfaces: A New Tool for Visualising and Exploring Molecular Crystals. *Chemistry – A European Journal* **1998**, *4*, 2136-2141.

(32) Parkin, A.; Barr, G.; Dong, W.; Gilmore, C. J.; Jayatilaka, D.; McKinnon, J. J.; Spackman, M. A.; Wilson, C. C. Comparing entire crystal structures: structural genetic fingerprinting. *CrystEngComm* **2007**, *9*, 648-652.

(33) Spackman, M. A.; McKinnon, J. J. Fingerprinting intermolecular interactions in molecular crystals. *CrystEngComm* **2002**, *4*, 378-392.

(34) Spackman, M. A.; McKinnon, J. J.; Jayatilaka, D. Electrostatic potentials mapped on Hirshfeld surfaces provide direct insight into intermolecular interactions in crystals. *CrystEngComm* **2008**, *10*, 377-388.

(35) Spackman, M. A.; Jayatilaka, D. Hirshfeld surface analysis. *CrystEngComm* **2009**, *11*, 19-32.

(36) Staples, R. J.; Lea, W.: Crystal structure of 6-bromochromone, C9H5BrO2. In *Zeitschrift für Kristallographie - New Crystal Structures*, 2005; Vol. 220; pp 371.

(37) Wells, P. R.: Group Electronegativities. In *Progress in Physical Organic Chemistry*; John Wiley & Sons, Inc., 2007; pp 111-145.

(38) Seth, S. K.; Sarkar, D.; Kar, T. Use of [small pi]-[small pi] forces to steer the assembly of chromone derivatives into hydrogen bonded supramolecular layers: crystal structures and Hirshfeld surface analyses. *CrystEngComm* **2011**, *13*, 4528-4535.

(39) Batsanov, A. S.; Howard, J. A. K.; Albesa-Jové, D.; Collings, J. C.; Liu, Z.; Mkhalid, I. A. I.; Thibault, M.-H.; Marder, T. B. Structural Versatility of Pyrene-2-(4,4,5,5-tetramethyl-[1,3,2]dioxaborolane) and Pyrene-2,7-bis(4,4,5,5-tetramethyl-[1,3,2]dioxaborolane). *Crystal Growth & Design* **2012**, *12*, 2794-2802.

(40) Ling, I.; Alias, Y.; Sobolev, A. N.; Raston, C. L. Hirshfeld surface analysis of phosphonium salts. *CrystEngComm* **2010**, *12*, 4321-4327.

(41) SMART Version 5.631, S. V. a. B. A. X.-r. S., Inc., Madison, Wisconsin, USA.

(42) Sheldrick, G. A short history of SHELX. *Acta Crystallographica Section A* **2008**, *64*, 112-122.

239

(43) Dolomanov, O. V.; Bourhis, L. J.; Gildea, R. J.; Howard, J. A. K.; Puschmann, H. OLEX2: a complete structure solution, refinement and analysis program. *Journal of Applied Crystallography* **2009**, *42*, 339-341.

(44) McKinnon, J. J.; Spackman, M. A.; Mitchell, A. S. Novel tools for visualizing and exploring intermolecular interactions in molecular crystals. *Acta Crystallographica Section B* **2004**, *60*, 627-668.

APPENDIX A

PERMISSION TO REPRINT: CHAPTER II

241

APPENDIX B

PERMISSION TO REPRINT: CHAPTER III

Copyright Clearance Center RightsLink®

Home | Account Info | Help

Title: Modulating the reactivity of chromone and its derivatives through encapsulation in a self-assembled phenylethynylene bis-urea host

Author: Sahan R. Salpage, Logan S. Donevant, Mark D. Smith, Andreas Bick, Linda S. Shimizu

Publication: Journal of Photochemistry and Photobiology A: Chemistry

Publisher: Elsevier

Date: 15 January 2016

Copyright © 2015 Elsevier B.V. All rights reserved.

Logged in as:
Sahan Salpage
Account #:
3001018667

LOGOUT

Order Completed

Thank you very much for your order.

This is a License Agreement between Sahan Salpage ("You") and Elsevier ("Elsevier"). The license consists of your order details, the terms and conditions provided by Elsevier, and the payment terms and conditions.

Get the printable license.

License Number	3847741184036
License date	Apr 14, 2016
Licensed content publisher	Elsevier
Licensed content publication	Journal of Photochemistry and Photobiology A: Chemistry
Licensed content title	Modulating the reactivity of chromone and its derivatives through encapsulation in a self-assembled phenylethynylene bis-urea host
Licensed content author	Sahan R. Salpage, Logan S. Donevant, Mark D. Smith, Andreas Bick, Linda S. Shimizu
Licensed content date	15 January 2016
Licensed content volume number	315
Licensed content issue number	n/a
Number of pages	11
Type of Use	reuse in a thesis/dissertation
Portion	full article
Format	both print and electronic
Are you the author of this Elsevier article?	Yes
Will you be translating?	No
Title of your thesis/dissertation	SYNTHESIS AND UTILITY OF BIS-UREA MACROCYCLES AS NANOREACTORS AND AS LIGANDS FOR METAL ORGANIC MATERIALS
Expected completion date	May 2016
Estimated size (number of pages)	250
Elsevier VAT number	GB 494 6272 12
Permissions price	0.00 USD
VAT/Local Sales Tax	0.00 USD / 0.00 GBP
Total	0.00 USD

ORDER MORE... | CLOSE WINDOW

Copyright © 2016 Copyright Clearance Center, Inc. All Rights Reserved. Privacy statement. Terms and Conditions.
Comments? We would like to hear from you. E-mail us at customercare@copyright.com

242

APPENDIX C

PERMISSION TO REPRINT: CHAPTER VI

Copyright Clearance Center | **RightsLink®** | Home | Account Info | Help
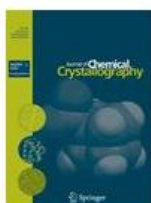
Title:	Crystal Structures and Hirshfeld Surface Analyses of 6-Substituted Chromones
Author:	Sahan R. Salpage
Publication:	Journal of Chemical Crystallography
Publisher:	Springer
Date:	Jan 1, 2016

Copyright © 2016, Springer Science+Business Media New York

Order Completed

Thank you very much for your order.

This is a License Agreement between Sahan Salpage ("You") and Springer ("Springer"). The license consists of your order details, the terms and conditions provided by Springer, and the payment terms and conditions.

Get the printable license.

License Number	3847740923379
License date	Apr 14, 2016
Licensed content publisher	Springer
Licensed content publication	Journal of Chemical Crystallography
Licensed content title	Crystal Structures and Hirshfeld Surface Analyses of 6-Substituted Chromones
Licensed content author	Sahan R. Salpage
Licensed content date	Jan 1, 2016
Type of Use	Thesis/Dissertation
Portion	Full text
Number of copies	2
Author of this Springer article	Yes and you are a contributor of the new work
Title of your thesis / dissertation	SYNTHESIS AND UTILITY OF BIS-UREA MACROCYCLES AS NANOREACTORS AND AS LIGANDS FOR METAL ORGANIC MATERIALS
Expected completion date	May 2016
Estimated size(pages)	250
Total	0.00 USD

CLOSE WINDOW